

DTIC

12

N00014-88-K-2005

**AD-A232 332**

**BROAD AREA DISTRIBUTED GAIN, DISTRIBUTED INDEX  
PROFILE GaAIAs SEMICONDUCTOR LASER DIODES**

James J. Coleman  
University of Illinois  
Department of Electrical and Computer Engineering  
1406 West Green Street  
Urbana, Illinois 61801

DTIC  
ELECTE  
MAR 4 1991  
S D D

14 February 1991

Final Report for Period 15 January 1988 - 14 January 1991

Prepared for

Naval Research Laboratory  
4555 Overlook Avenue SW  
Washington, DC 20375-5000

**DISTRIBUTION STATEMENT A**  
Approved for public release  
Distribution Unlimited

## REPORT DOCUMENTATION PAGE

1a. REPORT SECURITY CLASSIFICATION			1b. RESTRICTIVE MARKINGS		
2a. SECURITY CLASSIFICATION AUTHORITY			3. DISTRIBUTION/AVAILABILITY OF REPORT		
2b. DECLASSIFICATION/DOWNGRADING SCHEDULE					
4. PERFORMING ORGANIZATION REPORT NUMBER(S) N00014-88-K-2005			5. MONITORING ORGANIZATION REPORT NUMBER(S)		
6a. NAME OF PERFORMING ORGANIZATION University of Illinois at Urbana-Champaign		6b. OFFICE SYMBOL (If applicable)	7a. NAME OF MONITORING ORGANIZATION Office of Naval Research		
6c. ADDRESS (City, State, and ZIP Code) Grants and Contracts Office 105 Davenport House, 809 S. Wright St. Champaign, IL 61820 (see back)			7b. ADDRESS (City, State, and ZIP Code) 536 S. Clark Room 286 Chicago, IL 60605-1588		
8a. NAME OF FUNDING/SPONSORING ORGANIZATION Naval Research Laboratory		8b. OFFICE SYMBOL (If applicable)	9. PROCUREMENT INSTRUMENT IDENTIFICATION NUMBER		
8c. ADDRESS (City, State, and ZIP Code) 4555 Overlook Avenue SW Washington, D.C. 20375-5000			10. SOURCE OF FINDING NUMBERS		
			PROGRAM ELEMENT NO.	PROJECT NO.	TASK NO.
					WORK UNIT ACCESSION NO.
11. TITLE (Include Security Classification) BROAD AREA DISTRIBUTED GAIN, DISTRIBUTED INDEX PROFILE GaAlAs SEMICONDUCTOR LASER DIODES					
12. PERSONAL AUTHOR(S) James J. Coleman					
13a. TYPE OF REPORT Final		13b. TIME COVERED FROM 01/15/88 TO 01/14/91		14. DATE OF REPORT (Year, Month, Day) 02/18/91	15. PAGE COUNT 96
16. SUPPLEMENTARY NOTATION					
17. COSATI CODES			18. SUBJECT TERMS (Continue on reverse if necessary and identify by block number)		
FIELD	GROUP	SUB-GROUP	semiconductor lasers, laser arrays, quantum well hetero-structure lasers, impurity induced disordering, buried heterostructure lasers, window lasers, strained layer (over)		
19. ABSTRACT (Continue on reverse if necessary and identify by block number)  See other side					
20. DISTRIBUTION/AVAILABILITY OF ABSTRACT <input checked="" type="checkbox"/> UNCLASSIFIED/UNLIMITED <input type="checkbox"/> SAME AS RPT. <input type="checkbox"/> DTIC USERS			21. ABSTRACT SECURITY CLASSIFICATION Unclassified		
22a. NAME OF RESPONSIBLE INDIVIDUAL James J. Coleman			22b. TELEPHONE (Include Area Code) 217-333-2555	22c. OFFICE SYMBOL	

Abstract: High-power operation of a simple non-planar index-guided quantum well heterostructure periodic laser array structure is described, in which lateral lasing is prevented in a manner that still allows for uniform and continuous front facet light emission. The compositional disordering and compensation effects of MeV oxygen implantation have been applied to form stripe geometry graded barrier quantum well heterostructure lasers. A new broad area as well as narrow stripe window laser structure is described, in which a nonabsorbing window region is formed in the vicinity of the mirror facets by utilizing a selectively etched substrate and the advantageous properties of uniform MOCVD growth on nonplanar substrates. The growth and characterization of strained layer InGaAs-GaAs heterostructure lasers by MOCVD has been addressed. Ethyldimethylindium has been shown to be suitable as a precursor for the growth of indium compounds. The results of time-zero characterization of strained-layer  $\text{In}_x\text{Ga}_{1-x}\text{As-GaAs}$  quantum well heterostructure laser diodes with 70-Å-thick wells and indium mole fractions between 0.08 and 0.42 are reported. High power, in-phase locked operation of a wide aperture array is reported in which the lateral lasing and amplified spontaneous emission, characteristic of wide aperture arrays, are suppressed by a nonplanar active region. The antiguiding behavior of InGaAs-GaAs strained layer lasers has been exploited to form multiple-element oxide-defined-stripe phase-locked high power long wavelength ( $\lambda > 0.95 \mu\text{m}$ ) strained layer quantum well heterostructure diode arrays operating in the in-phase fundamental array mode.

18. Subject Terms (continued)

InGaAs-GaAs heterostructure lasers, metalorganic chemical vapor deposition (MOCVD), phase locked arrays

6c. (continued)

University of Illinois  
Department of Electrical and Computer Engineering  
1406 W. Green  
Urbana, IL 61801

**TABLE OF CONTENTS**

**Table of Contents**.....2

**Report**.....3

**Broad Area Non-planar Laser Arrays**.....3

**Lasers formed by Impurity Induced Disordering**.....3

**Non-planar Window Lasers** .....4

**Strained Layer InGaAs Lasers** .....5

**In-phase Laser Arrays**.....6

**Antiguidded Phase Locked Arrays** .....7

**References and Bibliography** (Publications acknowledged  
    under this grant) ..... 8

**Appendix 1** (Ph.D. theses supported under this grant)..... 10

**Appendix 2** (Reprints of publications acknowledged  
    under this grant) ..... 11

ACQUISITION	
NTIS GRANT	↓
DTIC TAB	□
Unannounced	□
Justification	
By <i>per form 50</i>	
Distribution	
Availability Codes	
Dist	Availability Codes
<b>A-1</b>	



## **REPORT**

### **Broad Area Non-planar Laser Arrays**

We have developed<sup>1-3,7,12</sup> a new broad area laser array structure. The maximum output power for a laser array before catastrophic optical damage occurs is determined primarily by the effective aperture width which is normally limited to a value less than the cavity length, unless lateral lasing and amplified spontaneous emission processes are suppressed. In order to fabricate diodes with a width greater than the laser cavity length, thereby allowing higher total output powers to be obtained, it is necessary to provide some structural change to inhibit lateral lasing. Previously reported methods of inhibiting lateral lasing and amplified spontaneous emission require extra processing steps in addition to the processing required to form the actual array elements, and also result in a portion of the array width which does not contribute to the laser output. We have obtained high-power operation of a simple non-planar index-guided quantum well heterostructure periodic laser array structure in which lateral lasing is prevented in a manner that still allows for uniform and continuous front facet light emission. Growth over a corrugated substrate is utilized for index-guiding and definition of the individual elements, and the resulting non-planar active region structure effectively suppresses lateral lasing and amplified spontaneous emission for the entire array. No additional processing steps after growth, such as proton bombardment, chemical etching, diffusion, epitaxial regrowth, or insulator deposition, which may result in accelerated degradation due to the introduction of material defects, are required.

### **Lasers formed by Impurity Induced Disorder**

We have furthered our studies of using ion implantation to form window lasers and distributed window lasers by impurity induced disordering (IID). As a consequence of the critical role which the implantation mask plays in selective IID, particular attention has been paid to developing techniques necessary to produce a reliable, high voltage, high dose mask. One technique which we developed<sup>9</sup> incorporates an AlGaAs lift-off layer between a metal mask and the sample. Following patterning of the metal layer by conventional techniques and implantation, the AlGaAs layer is selectively etched to remove the metal mask without damage to the underlying epitaxial structure. Alternatively, for low dose or low temperature implantations, a thick photoresist mask over a thin dielectric

(SiO<sub>2</sub> or Si<sub>3</sub>N<sub>4</sub>) lift-off layer may be utilized since the photoresist is able to withstand the implantation. We have characterized<sup>4</sup> the compositional disordering and compensation effects of MeV oxygen implantation. Under specific conditions a single oxygen implantation with subsequent annealing is able to form a semi-insulating region as well as induce compositional disorder in AlAs-GaAs layers 1.25 μm beneath the sample surface.

We have applied<sup>8</sup> this technology to graded barrier quantum well heterostructure lasers. For wider stripe lasers ( $w > 25 \mu\text{m}$ ), the presence of current confinement is apparent in threshold current measurement. Layer disordering has been verified by electron microscopy. As the stripe width is decreased, however, laser threshold currents reach a minimum and then begin to turn up. There are at least two possible reasons for this. The first is that the relatively long oxygen tail introduces distributed optical absorption to some distance into the active region. This would certainly become more critical as the device width is narrowed and possibly preclude this choice of species for IID buried heterostructure lasers. The second reason is that masking for MeV implantation is especially critical and increases in threshold current may result from residual implantation through the mask.

### **Non-planar Window Lasers**

We have successfully developed<sup>6</sup> a new broad area as well as narrow stripe window laser structure. A nonabsorbing window region is formed in the vicinity of the mirror facets by utilizing a selectively etched substrate and the advantageous property of uniform MOCVD growth on nonplanar substrates. Approximately fifty percent more optical power is available from the nonplanar devices than from conventional planar devices. Since the window region is a consequence of the nonplanar substrate, the type of laser structure grown is not restricted nor are sophisticated fabrication techniques or multiple growth steps required as in previously reported window lasers.

In collaboration with others at the University of Illinois, we have investigated<sup>16</sup> the disordering characteristics of GaAs-AlAs superlattices during ion irradiation (750 KeV Kr<sup>+</sup>, 10<sup>16</sup> cm<sup>-2</sup> dose) at various temperatures. Using Rutherford backscattering spectrometry and secondary ion mass spectrometry, it was found that after low temperature implants (235K, 175K and 135K) the superlattice was completely disordered whereas following high temperature implants (300K, 400K and 550K) there is partial retention of the superlattice

layers. These results indicate that by selecting the appropriate implantation temperature, ion implantation may be conducted while minimizing or enhancing compositional disorder. The results also have special significance for understanding the phase diagram of GaAs-AlAs superlattices at low temperatures. These superlattices, as well as others comprised of III-V compounds, are typically grown at temperatures where interdiffusion is negligible. Consequently, the phase diagrams for these systems at the growth temperatures are not well understood since the systems are not in equilibrium. Using ion irradiation to enhance low temperature diffusion processes, the phase diagram can be obtained. Our results provide evidence for a miscibility gap in the GaAs-AlAs phase diagram for temperatures at least as high as 550K.

### **Strained Layer InGaAs Lasers**

We have addressed various issues concerning the growth and characterization of strained layer InGaAs-GaAs heterostructure lasers by MOCVD. The first issue<sup>10</sup> is the use of the metal alkyl ethyldimethylindium (EdMIn) as a precursor for the growth of indium compounds. The more commonly used In-alkyls have been associated with various problems such as low vapor pressure and undesirable parasitic reactions from liquid triethylindium (TEIn) and time varying vapor pressure from solid trimethylindium (TMIn). EdMIn has been suggested as an alternative being a liquid and having a reasonable vapor pressure. It has been suggested however that it is not a stable compound and will evolve into its constituent simple alkyls. Our results show it is useful for laser devices and is stable over time.

We have characterized<sup>11,13,14</sup> a series of strained layer laser devices having a fixed separate confinement quantum well structure and varying In-composition (0.08 - 0.42) in the well. We reported results of time-zero characterization of strained-layer  $\text{In}_x\text{Ga}_{1-x}\text{As}$ -GaAs quantum well heterostructure laser diodes with 70-Å-thick wells and indium mole fractions between 0.08 and 0.42. The emission wavelengths ranged from 0.9  $\mu\text{m}$  to 1.08  $\mu\text{m}$  and agreed well with calculated values. A minimum in threshold current density is observed for devices having an indium fraction of  $\sim 0.25$  in the wells, and devices with well compositions in the range  $\sim 0.16 < x < \sim 0.30$  all operated with low threshold current densities. The data support two design criteria for low threshold operation of strained-layer InGaAs-GaAs quantum well lasers: (1) The electrons should be confined by at least  $\sim 75$  meV in the conduction band, and (2) the

strained-layer active region thickness should not greatly exceed the critical thickness for a sandwiched layer as given by the mechanical equilibrium model of Matthews and Blakeslee.

### **In-phase Laser Arrays**

We have obtained<sup>18</sup> high power, in-phase locked operation of a wide aperture array in which the lateral lasing and amplified spontaneous emission (ASE), characteristic of wide aperture arrays, are suppressed by a nonplanar active region. Phase locked laser arrays have great potential as sources for pumping of Nd:YAG and long distance communication as a result of the high power available and the stabilized far-field patterns. For phased-locked arrays, a characteristic double lobed far-field pattern is generally observed indicating that the device is operating in the highest order array mode with a 180° phase shift between elements. However, by introducing sufficient gain between the elements the device will operate in the lowest order array mode with a 0° phase shift between elements and with a single lobed far-field. The laser device structure utilized for this study is similar to nonplanar periodic laser arrays reported previously. The structure is a AlGaAs-GaAs graded barrier quantum well heterostructure with a 50 Å quantum well grown by metalorganic chemical vapor deposition (MOCVD). The first step in forming the array is wet chemical etching of a periodic pattern of shallow mesa stripes into the substrate (4 μm stripe width, 8 μm center-to-center spacing, and 0.3 μm mesa height). Following etching, the devices are completed by MOCVD growth of the laser structure, and contact metalization. No further processing is required.

The MOCVD growth on a corrugated substrate forms a nonplanar active region, which serves to define the individual emitters, to provide a step in the effective index of refraction for stable mode operation, and to suppress lateral lasing and ASE for high power operation. The average threshold current density of these devices is 264 A/cm<sup>2</sup> and the external efficiency is 33 %. Output power of 400 mW has been measured. The far-field pattern of the device consists of a dominant central lobe at 0° and satellite lobes with angular separations of 5.8-6.0°. The full width at half-maximum of the central lobe is 2.2°. The dominant central lobe centered at 0° indicates that the emitters are largely operating in-phase. Fundamental supermode operation is observed from just above threshold to more than three times threshold (400 mW). Also over this range of currents, the peak height ratio between the central and

satellite peaks remains constant and the peaks do not widen nor change their angular separation. Nonplanar periodic laser arrays with deep mesas (0.6  $\mu\text{m}$ ) do not operate as phase locked arrays as a consequence of a highly nonuniform current distribution. However, shallow mesas allow a more uniform current distribution and thus in-phase locked operation is observed for the shallow mesa devices.

### **Antiguidded Phase Locked Arrays**

Most work to date on semiconductor laser arrays for high power operation has focussed on the evanescent coupling of closely spaced positive-index waveguide elements, where the optical field is mostly confined to the regions of the individual elements, either by gain-guiding or a real index step. In order to achieve phase-locked operation in the fundamental in-phase supermode, arrays of closely spaced index depressions (anti-guides) have been studied in the AlGaAs/GaAs materials system. For these arrays, the antiguides were formed by a two-growth process, resulting in real index steps in the lateral direction. Oxide-defined-stripe gain-guided strained-layer InGaAs-GaAs lasers have recently been shown<sup>19</sup> to be antiguided for narrow stripe widths due to the relatively large depression in the real index caused by injected carriers under the stripe. We have made use of this antiguiding behavior to form<sup>17</sup> multiple-element oxide-defined-stripe phase-locked high power (> 450 mW/uncoated facet) InGaAs-GaAs long wavelength ( $\lambda > 0.95 \mu\text{m}$ ) strained layer quantum well heterostructure diode arrays operating in the in-phase fundamental array mode.

**REFERENCES AND BIBLIOGRAPHY**

Publications acknowledged under this grant:

1. Nonplanar index-guided quantum well heterostructure periodic laser array, C A Zmudzinski, M E Givens, R P Bryan and J J Coleman, *Appl. Phys. Lett.* **53**, 350 (1988)
2. High-power phase-locked InGaAs strained-layer quantum well heterostructure periodic laser array, J N Baillargeon, P K York, C A Zmudzinski, G E Fernandez, K J Beernink and J J Coleman, *Appl. Phys. Lett.* **53**, 457 (1988)
3. High power non-planar quantum well heterostructure periodic laser arrays, M E Givens, C A Zmudzinski, R P Bryan, and J J Coleman, *Appl. Phys. Lett.* **53**, 1159 (1988)
4. Compositional disordering and the formation of semi-insulating layers in AlAs-GaAs superlattices by MeV oxygen implantation, R P Bryan, M E Givens, J L Klatt, R S Averback and J J Coleman, *J. Electronic Materials* **18**, 39 (1989)
5. Operational and design considerations for broad area graded barrier quantum well heterostructure lasers grown by metalorganic chemical vapor deposition for high power applications, M E Givens, C A Zmudzinski, R P Bryan and J J Coleman, *Fiber and Integ. Optics* **7**, 343 (1988)
6. A nonplanar quantum well heterostructure window laser, R P Bryan, L M Miller, T M Cockerill and J J Coleman, *Appl. Phys. Lett.* **54**, 1634 (1989)
7. Optical characteristics of high power non-planar periodic laser arrays, C A Zmudzinski, M E Givens, R P Bryan and J J Coleman, *IEEE J. Quantum Electronics* **QE-25**, 1539 (1989)
8. Impurity induced disordered quantum well heterostructure stripe geometry lasers by MeV oxygen implantation, R P Bryan, J J Coleman L M Miller, M E Givens, R S Averback and J L Klatt, *Appl. Phys. Lett.* **55**, 94 (1989)
9. MeV implantation masking using an aluminum gallium arsenide metal lift-off layer, M M Ghadiri, R P Bryan, L M Miller, T Tang, M E Givens, T A DeTemple and J J Coleman, *J. Appl. Phys.* **66**, 982 (1989)
10. Ethyldimethylindium for the growth of InGaAs-GaAs strained layer lasers by metalorganic chemical vapor deposition, P K York, K J Beernink, J Kim, J J Coleman, G E Fernandez, and C M Wayman, *Appl. Phys. Lett.* **55**, 2476 (1989)
11. Dependence of threshold current density on quantum well composition for strained-layer InGaAs-GaAs lasers by metalorganic chemical vapor deposition, K J Beernink, P K York and J J Coleman, *Appl. Phys. Lett.* **55**, 2585 (1989)

12. High power pulsed operation of an optimized nonplanar corrugated substrate periodic laser diode array, R P Bryan, L M Miller, T M Cockerill, S M Langsjoen and J J Coleman, *IEEE J. Quantum Electron.* **26**, 222 (1990)
13. InGaAs-GaAs strained layer quantum well heterostructure lasers, J J Coleman, P K York and K J Beernink, *SPIE Laser-Diode Technology and Applications II*, **1219**, 32 (1990)
14. Effect of confining layer aluminum composition on AlGaAs-GaAs-InGaAs strained layer quantum well heterostructure lasers, P K York, S M Langsjoen, L M Miller, K J Beernink, J J Alwan and J J Coleman, *Appl. Phys. Lett.* **57**, 843 (1990)
15. Modeling of quantum well lasers for computer aided analysis of optoelectronic integrated circuit, D S Gao, S M Kang, R P Bryan and J J Coleman, *J. Quantum Electron.* **QE-26**, 1206 (1990)
16. Temperature dependence of compositional disordering of GaAs-AlAs superlattices during MeV Kr irradiation, R P Bryan, L M Miller, T M Cockerill, J J Coleman, J L Klatt and R S Averback, *Mater. Research Soc. Proc.* **198**, 79 (1990)
17. InGaAs-GaAs-AlGaAs gain-guided arrays operating in the in-phase fundamental array mode, K J Beernink, J J Alwan and J J Coleman, *Appl. Phys. Lett.* **57**, 2764 (1990)
18. In-phase operation of high power nonplanar periodic laser arrays, R P Bryan, T M Cockerill, L M Miller, T K Tang, T A DeTemple and J J Coleman, *Appl. Phys. Lett.* **58**, 113 (1991)
19. Antiguiding in narrow stripe gain-guided InGaAs-GaAs strained-layer lasers, K J Beernink, J J Alwan and J J Coleman, *J. Appl. Phys.* **69**, 56 (1991)
20. Strained layer quantum well heterostructure lasers, J J Coleman, *Quantum Well Lasers*, P S Zory, Jr. ed. (Academic Press, Inc., Cambridge, MA, in press)
21. Metalorganic chemical vapor deposition of InGaAs-GaAs-AlGaAs strained layer quantum well lasers, P K York, K J Beernink, J Kim, J J Alwan, J J Coleman and C M Wayman, *J. Crystal Growth*, in press

## APPENDIX 1

Ph.D. theses supported under this grant:

High power semiconductor laser arrays by metalorganic chemical vapor deposition, C. A. Zmudzinski, Ph. D. in Electrical and Computer Engineering, 1989

Fabrication of novel semiconductor lasers grown by metalorganic chemical vapor deposition, R. P. Bryan, Ph. D. in Electrical and Computer Engineering, 1990

The growth and characterization of III-V compound semiconductor materials by metalorganic chemical vapor deposition and laser photochemical vapor deposition, P. K. York, Ph. D. in Electrical and Computer Engineering, 1990

**APPENDIX 2**

Reprints of publications acknowledged under this grant:

# Nonplanar index-guided quantum well heterostructure periodic laser array

C. A. Zmudzinski, M. E. Givens, R. P. Bryan, and J. J. Coleman

*Department of Electrical and Computer Engineering and NSF Engineering Research Center for Compound Semiconductor Microelectronics, University of Illinois at Urbana-Champaign, 1406 West Green Street, Urbana, Illinois 61801*

(Received 14 March 1988; accepted for publication 1 June 1988)

Data are presented on nonplanar index-guided quantum well heterostructure periodic laser arrays grown by metalorganic chemical vapor deposition (MOCVD). The nonplanar array structure, formed by a single MOCVD growth over a selectively etched corrugated substrate, not only provides index guiding for the individual array elements, but also suppresses lateral lasing and amplified spontaneous emission for the entire array. As a result, the entire width of the device is utilized for optical emission, and no additional processing steps are required. Devices tested exhibit uniform emission and show no signs of lateral lasing or amplified spontaneous emission for array widths up to 3.3 times the cavity length. The processing required for device fabrication is therefore minimized by taking advantage of the properties of MOCVD growth over nonplanar substrates.

Multiple stripe laser arrays have proven to be a most promising source of high-power emission from semiconductor materials which are suitable for such applications as pumping solid-state neodymium: yttrium aluminum garnet lasers.<sup>1</sup> The maximum total optical power obtainable from a semiconductor laser or laser array is generally limited<sup>2</sup> by catastrophic optical degradation (COD) of the laser facets which occurs at a given facet output power density. Increasing the effective width of the emitting facet by distributing the laser emission over a number of elements in an array decreases the power density, thereby raising the total output power at COD. In most laser structures, the aperture width can only be increased to a value on the order of the cavity length ( $\approx 400 \mu\text{m}$ ), at which point lateral lasing and amplified spontaneous emission mechanisms become large with respect to the desired front facet emission. Lateral lasing and amplified spontaneous emission can be inhibited by isolating suitably narrow active regions of the array either by defining unpumped absorbing regions<sup>3</sup> or by etching deep grooves through the laser structure<sup>4,5</sup> at periodic intervals. However, these solutions result in a fraction of the array width not being utilized for optical output and require additional processing steps.

In this letter, we report the growth and fabrication of a simple nonplanar index-guided quantum well heterostructure periodic laser array structure in which lateral lasing is prevented in a manner that still allows for uniform and continuous front facet light emission. Growth over a periodically patterned substrate<sup>6,7</sup> is utilized to provide an index-guided structure and to define the individual elements of the array. In addition, the resulting nonplanar structure of the array itself serves to inhibit lateral lasing, in contrast to previously utilized methods which require additional fabrication steps. The array is formed simply by etching a corrugated stripe pattern into the substrate surface, growth of the laser structure by metalorganic chemical vapor deposition (MOCVD), and contact metallization. No further processing steps, such as proton bombardment, chemical etching, diffusion, epitaxial regrowth, or insulator deposition, which

may result in accelerated degradation due to the introduction of material defects, are required. Data are presented on the light-current characteristics for both front facet emission and side emission from devices having a total laser width exceeding the cavity length. These data show clearly the suppression of lateral lasing in these structures.

GaAs:Si wafers (100) were prepared for epitaxial growth by photolithographically delineating a periodic array of narrow ( $\approx 4.0 \mu\text{m}$ ) stripes with  $8.0 \mu\text{m}$  center-to-center spacings across the entire substrate surface. Wet chemical etching of the exposed surfaces in a 1:8:80  $\text{H}_2\text{SO}_4:\text{H}_2\text{O}_2:\text{H}_2\text{O}$  solution to the appropriate depth ( $\approx 0.5 \mu\text{m}$ ) left the substrate patterned with a periodic array of narrow mesas and grooves. Stripes were aligned parallel to the (110) direction such that the inclined sidewalls of the mesas consisted primarily of exposed (111)A planes. Following etching, the substrates were cleaned in solvents and HCl prior to deposition of the laser structure. Epitaxial growth was performed at a temperature of  $800^\circ\text{C}$  and a growth rate of  $\approx 3.0 \mu\text{m/h}$  in an atmospheric-pressure MOCVD reactor described previously.<sup>8</sup> The basic structure utilized in this study was an  $\text{Al}_x\text{Ga}_{1-x}\text{As}/\text{GaAs}$  graded barrier quantum well heterostructure (GBQWH) laser<sup>9,10</sup> which consists of a  $0.25 \mu\text{m}$  GaAs buffer layer ( $n = 1 \times 10^{18}$ ), a  $0.5 \mu\text{m}$  linearly graded  $\text{Al}_x\text{Ga}_{1-x}\text{As}$  buffer layer ( $0.0 \leq x \leq 0.85$ ,  $n = 1 \times 10^{18}$ ), a  $1.0 \mu\text{m}$   $\text{Al}_{0.85}\text{Ga}_{0.15}\text{As}$  confining layer ( $n = 1 \times 10^{18}$ ), a  $1200 \text{ \AA}$  parabolically graded  $\text{Al}_x\text{Ga}_{1-x}\text{As}$  layer ( $0.85 \geq x \geq 0.20$ ,  $n = 5 \times 10^{16}$ ), a  $50 \text{ \AA}$  GaAs single quantum well (undoped), a  $1200 \text{ \AA}$  parabolically graded  $\text{Al}_x\text{Ga}_{1-x}\text{As}$  layer ( $0.20 \leq x \leq 0.85$ ,  $p = 1 \times 10^{17}$ ), a  $1.0 \mu\text{m}$   $\text{Al}_{0.85}\text{Ga}_{0.15}\text{As}$  confining layer ( $p = 2 \times 10^{18}$ ), and a  $0.2 \mu\text{m}$  GaAs contact layer ( $p = 3 \times 10^{19}$ ). Growth rates perpendicular to the (100) and (111)A planes are approximately equal such that successive epilayers were deposited uniformly over the nonplanar growth surface. These nearly equal growth rates resulted in an effective widening of the stripe geometry mesas and narrowing of the adjacent grooves as the total epitaxial layer thickness increased, although the corrugated contour

of the growth surface remained essentially unchanged. The structure is illustrated in Fig. 1, which shows a schematic cross section and a scanning electron micrograph of a portion of the laser array. The growth illustrated in Fig. 1 can be contrasted with growth by molecular beam epitaxy (MBE) over similarly patterned substrates, which is highly preferential along particular growth planes and can result in overgrown epilayer contours which differ significantly from the profile of the original growth surface.<sup>6,11</sup> Device wafers were mechanically thinned and polished to  $\approx 125 \mu\text{m}$ , a Ge/Au contact was evaporated and alloyed on the *n* side, and a non-alloyed Ti/Pt/Au contact was evaporated on the *p* side. The samples were then cleaved into bars of various lengths which were diced into individual diode arrays of various widths. The facets of the devices utilized in this study were left uncoated. No further processing or photolithographical steps were required to either define current injection or to prohibit amplified spontaneous emission or lateral lasing action. Devices were tested under pulsed conditions (1.5  $\mu\text{s}$  pulse width/2.0 kHz repetition rate) up to an injected current of 2.0 A. Light output power versus current curves were generated in order to determine  $J_{\text{th}}$  and differential quantum efficiencies. Single-ended output powers were measured using a calibrated silicon photodiode. The light output from the sawn edges was also measured for comparison.

Figure 2 shows a photograph of the video image of a section of an array illustrating laser emission across a large portion of the facet. Note that the light output is extremely uniform across the array of emitters which are spaced by 8.0  $\mu\text{m}$  center to center. High-resolution near-field images indicate that each spot of Fig. 2 is actually two spots originating from individual emitters. The individual emission spots are located at both edges of each mesa at the transitions from (100) to (111)A planar structure and are spaced by 1.5  $\mu\text{m}$ . Far-field patterns in the junction plane show single-lobed

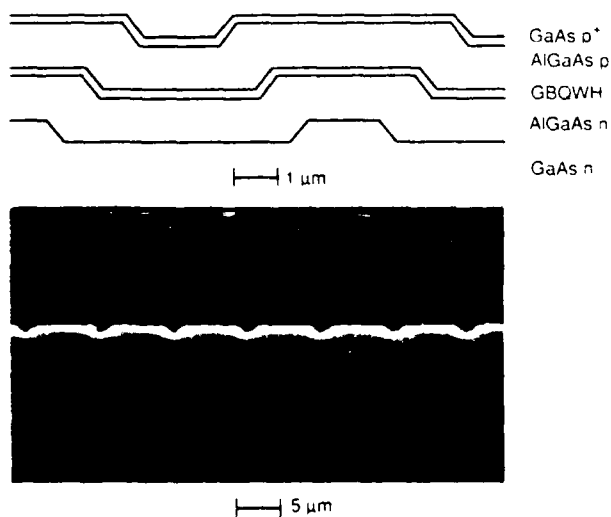


FIG. 1 Schematic diagram and scanning electron micrograph of the periodic nonplanar laser array grown by MOCVD on a corrugated etched substrate. The micrograph illustrates that the epilayers inherit the contours of the etched substrate, resulting in a nonplanar active layer profile which effectively suppresses lateral lasing and amplified spontaneous emission.

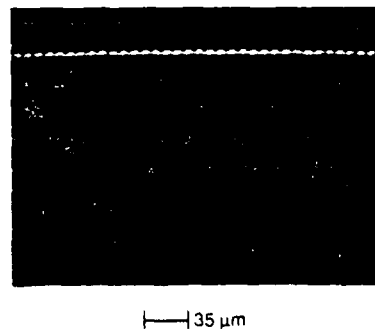


FIG. 2 Photograph of the video image of a large portion of an array fabricated by growth over a corrugated etched substrate. Note that the emission is extremely uniform across the width of the array and that the entire facet contributes to the optical output.

operation with a wide full width at half-maximum angle of 18°, indicating that the elements are not phase locked. The light output power versus current curve of Fig. 3 shows the output from both an uncoated facet and a sawn edge of a typical laser array with a cavity length of 508  $\mu\text{m}$  and a width of 700  $\mu\text{m}$ . The threshold current density was 150 A/cm<sup>2</sup> for this cavity length, with a differential quantum efficiency of 20% per uncoated facet. These results are comparable to 150  $\mu\text{m}$  broad-area lasers having the same structure but grown on planar substrates. There was no observed decrease in efficiency or increase in threshold current density as the width was varied from  $0.5 \times l$  to  $3.3 \times l$ , where  $l$  is the cavity length. The measured light intensity from the cleaved front facets at 2.0 A was typically about 15 times the intensity of light from the sawn edges, independent of device width. In addition, measured side emission spectra possessed a modal structure identical to that of the front facet emission spectra, indicating that the detected side emission was primarily stimulated emission from the front facet which had been scattered into

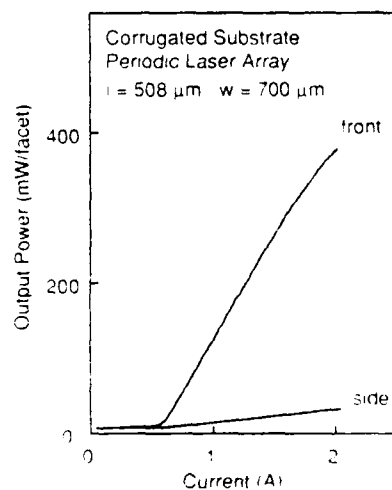


FIG. 3 Light output power vs current characteristics from an uncoated front facet and a sawn edge from a periodic array with a width of 700  $\mu\text{m}$  and a cavity length of 508  $\mu\text{m}$ . The output power from the front facet is more than 15 times the output power from the side even though the device width exceeds the device length, indicating the effective suppression of lateral lasing and amplified spontaneous emission.

the detector as a result of our experimental setup. Therefore, the ratio of front facet emission intensity to side emission intensity is actually greater than that indicated by the  $L-I$  curve of Fig. 3. These data clearly indicate that this simple array structure effectively suppresses amplified spontaneous emission and lateral lasing.

In summary, simple nonplanar index guided quantum well heterostructure periodic laser array structures grown by MOCVD on corrugated etched substrates have been fabricated and tested. These devices show no signs of lateral lasing or amplified spontaneous emission at array widths up to 3.3 times the cavity length. Discrimination against lateral lasing is provided solely by the nonplanar structure of the active region, which is realized by epitaxial growth on a selectively etched substrate patterned with a periodic array of mesa stripes. No additional processing steps, which may contribute to accelerated degradation, are required to inhibit lateral lasing and amplified spontaneous emission. These devices show promise for use in high-power applications where minimal processing is desirable.

The authors would like to gratefully acknowledge T. L. Brock for assistance with mask design and fabrication, and

L. M. Miller and T. K. Higman for helpful discussions and technical support. This work was supported in part by the National Science Foundation Engineering Research Center for Compound Semiconductor Microelectronics (CDR 82-22666), the McDonnell Douglas Corporation, the Naval Research Laboratory (N00014-88-K-2005), and SDIO/IST (DAAL03-87-K-0013).

<sup>1</sup>D. L. Sipes, *Appl. Phys. Lett.* **47**, 74 (1985).

<sup>2</sup>C. H. Henry, P. M. Petroff, R. A. Logan, and F. R. Merritt, *J. Appl. Phys.* **50**, 3721 (1979).

<sup>3</sup>G. L. Harnagel, P. S. Cross, D. R. Scifres, and D. P. Worland, *Electron. Lett.* **22**, 231 (1986).

<sup>4</sup>G. L. Harnagel, P. S. Cross, C. R. Lennon, M. DeVito, and D. R. Scifres, *Electron. Lett.* **23**, 743 (1987).

<sup>5</sup>G. L. Harnagel, P. S. Cross, D. R. Scifres, D. F. Welch, C. R. Lennon, D. P. Worland, and R. D. Burnham, *Appl. Phys. Lett.* **49**, 1418 (1986).

<sup>6</sup>J. S. Smith, P. L. Derry, S. Margalit, and A. Yariv, *Appl. Phys. Lett.* **47**, 712 (1985).

<sup>7</sup>R. D. Dupuis and P. D. Dapkus, *Appl. Phys. Lett.* **33**, 724 (1978).

<sup>8</sup>G. Costrini and J. J. Coleman, *J. Appl. Phys.* **57**, 2249 (1985).

<sup>9</sup>W. T. Tsang, *Appl. Phys. Lett.* **39**, 134 (1981).

<sup>10</sup>L. J. Mawst, M. E. Givens, C. A. Zmudzinski, M. A. Emanuel, and J. J. Coleman, *IEEE J. Quantum Electron.* **QE-23**, 696 (1987).

<sup>11</sup>W. T. Tsang and A. Y. Cho, *Appl. Phys. Lett.* **30**, 293 (1977).

# High-power phase-locked InGaAs strained-layer quantum well heterostructure periodic laser array

J. N. Baillargeon, P. K. York, C. A. Zmudzinski, G. E. Fernández, K. J. Beernink, and J. J. Coleman

NSF Engineering Research Center for Compound Semiconductor Microelectronics and Materials Research Laboratory, University of Illinois at Urbana-Champaign, 1406 West Green Street, Urbana, Illinois 61801

(Received 6 April 1988; accepted for publication 1 June 1988)

Data are presented on high-power strained-layer InGaAs quantum well heterostructure laser arrays. These devices are periodic nonplanar arrays, formed by a single metalorganic chemical vapor deposition growth over a selectively etched corrugated GaAs substrate. The corrugation serves to provide both stripe definition and index guiding while suppressing lateral lasing perpendicular to the stripes. Maximum pulsed optical powers of 2.5 W/facet (width = 1600  $\mu\text{m}$ , length = 440  $\mu\text{m}$ ) for an emission wavelength of 1.03  $\mu\text{m}$  have been obtained from uncoated devices having threshold current densities in the range 290–600 A/cm<sup>2</sup>. Far-field radiation patterns indicate that the arrays are phase locked.

Strained-layer InGaAs quantum well heterostructure laser diodes<sup>1–4</sup> show promise as an alternative to lattice-matched long-wavelength material structures. Multiple-stripe laser diode arrays, as high-power devices, have been shown to be practical for optically pumping solid-state Nd:YAG lasers.<sup>5</sup> The maximum output power of these structures, however, is limited by catastrophic optical degradation (COD) of the laser facets.<sup>6</sup> An effective way to increase the maximum output power at COD is to increase the effective width of the laser facets by distributing the laser emission over many elements in a large-width array. The suppression of lateral lasing, which is a problem for structures having widths greater than the cavity length, can be achieved by defining absorptive regions<sup>7</sup> or by etching grooves between lasing stripes.<sup>8,9</sup> This letter describes the fabrication and operation of a low-threshold high-power nonplanar index-guided InGaAs strained-layer quantum well heterostructure periodic laser array operating at a wavelength greater than 1  $\mu\text{m}$ . This structure<sup>10,11</sup> was realized by a one-step metalorganic chemical vapor deposition (MOCVD) growth over a corrugated GaAs substrate. The corrugation etched in the GaAs substrate results in a nonplanar active region which provides index guiding and suppresses lateral lasing in devices having a width greater than the cavity length. Other than the formation of ohmic contacts to the array, no further processing, such as oxide masking, is required. Data are presented on the light emission characteristics as well as near- and far-field intensity patterns. Pulsed optical powers of 2.5 W/facet (width = 1600  $\mu\text{m}$ , length = 440  $\mu\text{m}$ ) for an emission wavelength of 1.03  $\mu\text{m}$  have been obtained from uncoated devices having threshold current densities of less than 300 A/cm<sup>2</sup>. Far-field radiation patterns indicate the arrays are phase locked.

GaAs:*n* (silicon doped) wafers (100) were patterned by conventional photolithography with a periodic array of 4  $\mu\text{m}$  stripes aligned along the (110) direction and having a center-to-center spacing of 8  $\mu\text{m}$ . Wet chemical etching (H<sub>2</sub>SO<sub>4</sub>:H<sub>2</sub>O:H<sub>2</sub>O) yielded etched grooves approximately 0.5  $\mu\text{m}$  in depth. The epitaxial layers were grown<sup>12</sup> in an atmospheric-pressure metalorganic chemical vapor depo-

sition (MOCVD) reactor using trimethylgallium, trimethylaluminum, trimethylindium, and arsine. The laser structure consists of a 0.25- $\mu\text{m}$ -thick GaAs buffer layer ( $n = 1 \times 10^{18}$ ), 1.25- $\mu\text{m}$ -thick Al<sub>*x*</sub>Ga<sub>1-*x*</sub>As confining layers ( $x = 0.20$ ,  $n = 1 \times 10^{18}$ ,  $p = 1 \times 10^{18}$ ), the quantum well heterostructure active region described below, and a 0.2- $\mu\text{m}$ -thick GaAs cap layer ( $p = 5 \times 10^{19}$ ). The quantum well heterostructure active region is shown schematically in Fig. 1(a) and consists of a single 120-Å-thick In<sub>0.25</sub>Ga<sub>0.75</sub>As strained-layer quantum well centered between 1000-Å-thick GaAs layers. The thickness of the quantum well was adjusted to be less than the critical thickness<sup>13</sup> for this composition. The emission wavelengths for these devices are  $\lambda \sim 1.03 \mu\text{m}$ . The growth rates perpendicular to the (100) and the (111) directions, determined from scanning electron microscope measurements, are not equal, with the growth being greater on the (111) planes. This results in the final structure, shown drawn to scale in Fig. 1(b), with the mesa of the

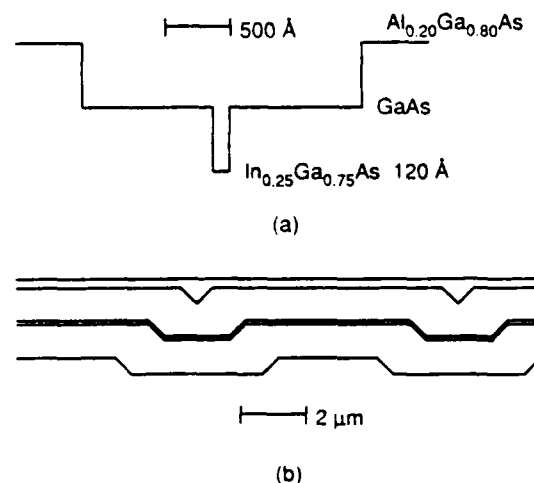


FIG. 1. Scale schematic diagrams of (a) the InGaAs strained-layer quantum well heterostructure active region and (b) the cross section of the periodic nonplanar laser array grown by MOCVD on a corrugated etched GaAs substrate.

active region being  $\sim 5 \mu\text{m}$  in width. After growth, the wafers were mechanically thinned and polished to a thickness of  $125 \mu\text{m}$  and  $n$ -type contacts were formed by evaporating  $250 \text{ \AA}$  Ge/ $2000 \text{ \AA}$  Au on the bottom surface and alloying at a temperature of  $400^\circ\text{C}$  for 15 s. Nonalloyed  $p$ -type contacts of  $300 \text{ \AA}$  Ti/ $500 \text{ \AA}$  Pt/ $2000 \text{ \AA}$  Au were formed on the top surface. No further processing such as oxide defined stripes of facet coatings was implemented. The wafers were then cleaved into bars of various lengths and widths and wire bonded. Pulsed near- and far-field characteristics were measured using  $1.5 \mu\text{s}$  pulses at a 2 kHz repetition rate. Single-ended optical output powers were measured with both calibrated silicon and germanium photodiodes using a 400 ns pulse width and 1 kHz repetition rate.

Threshold current densities for these broad-area InGaAs strained-layer quantum well heterostructure periodic laser arrays ranged between 290 and  $600 \text{ A/cm}^2$ , depending on the length of the laser cavity. Shown in Fig. 2 is the light-current characteristic for a typical uncoated laser array having a cavity length of  $440 \mu\text{m}$  and a width of  $1600 \mu\text{m}$  and a threshold density of  $560 \text{ A/cm}^2$ . The maximum output power observed from a measurement source limited to 40 A was 2.5 W per uncoated facet. Side emission measured for these structures consisted primarily of scattered stimulated emission from the front facet. There is no evidence of significant lateral lasing or amplified spontaneous emission.

Shown in Fig. 3 are near- and far-field emission patterns for an array having a cavity length of  $457 \mu\text{m}$  and a width of  $590 \mu\text{m}$  ( $J_{\text{th}} = 519 \text{ A/cm}^2$ ). Each of the lobes in the near-field emission pattern corresponds to single-lobed emission from a single array element, and emission from adjacent elements appears to be coupled. This is in contrast to similar  $\text{Al}_{0.85}\text{Ga}_{0.15}\text{As-GaAs}$  broad-area graded barrier quantum well heterostructure periodic laser arrays ( $\lambda = 0.82 \mu\text{m}$ )

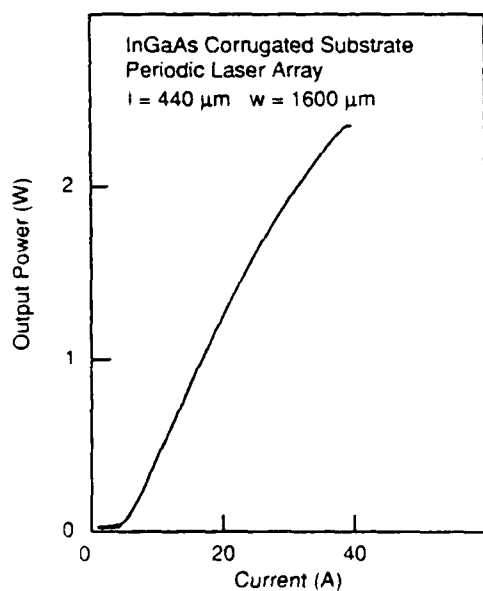
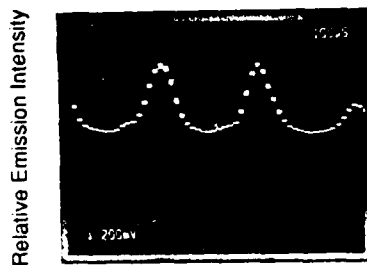
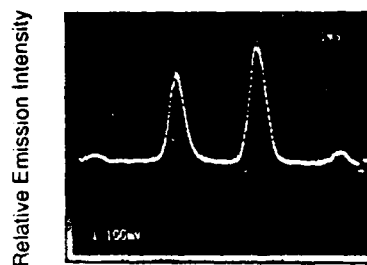


FIG. 2. Light-current characteristic from one facet of an InGaAs strained-layer quantum well heterostructure periodic laser array having a width of  $1600 \mu\text{m}$  and a cavity length of  $440 \mu\text{m}$ . The current source limited maximum output power observed for these laser arrays is 2.5 W per uncoated facet.

InGaAs Corrugated Substrate  
Periodic Laser Array  
 $l = 457 \mu\text{m}$   $w = 590 \mu\text{m}$



Near Field:  $1.25 \times I_{\text{th}}$   $2.17 \mu\text{m/div}$



Far Field:  $1.42 \times I_{\text{th}}$   $2.47 \text{ deg/div}$

FIG. 3. Near-field intensity pattern for two adjacent elements and the far-field radiation pattern for an InGaAs strained-layer quantum well heterostructure periodic laser array. Note the two main lobes (full width at half-maximum  $1.5^\circ$ ) and the two satellite lobes, each separated by  $7.16^\circ$ .

having stronger lateral index guiding which show<sup>11</sup> a double-lobed near-field pattern at each mesa and are not phase locked. These near-field emission patterns are stable up to at least three times threshold. The far-field radiation pattern of Fig. 3 shows the presence of two main lobes (each having a full width at half-maximum of  $1.5^\circ$ ) as well as two satellite lobes. Each lobe is separated from adjacent lobes by  $7.16^\circ$ , in good agreement with  $\theta = 2 \sin^{-1}(\lambda/2d) = 7.38^\circ$  predicted by diffraction theory,<sup>14</sup> where  $d$  is the separation between array elements. These far-field patterns clearly indicate that the array elements are phase locked near the  $180^\circ$  out-of-phase mode across the entire array.

In summary, we have fabricated and tested the first high-power phase-locked  $\text{In}_{1-x}\text{Ga}_x\text{As}$  ( $x = 0.75$ ) index-guided strained-layer quantum well heterostructure periodic laser arrays grown by MOCVD. Operating with an emission wavelength of  $1.03 \mu\text{m}$ , the devices have an observed maximum pulsed power output of 2.5 W per facet and show strong suppression of lateral lasing provided by the non-planar structure of the device. Far-field data indicate phase-locked operation of the array, while near-field measurements show coupling between adjacent elements and stable mode operation up to three times threshold.

The authors would like to gratefully acknowledge T. L. Brock and M. E. Givens for helpful discussions and technical support. This work was supported in part by the National Science Foundation (DMR 83-16981 and CDR 85-22666), the McDonnell Douglas Corporation, the Naval Research Laboratory (N00014-88-K-2005), and SDIO/IST (DAAL03-87-K-0013).

- <sup>1</sup>W. D. Laidig, P. J. Caldwell, Y. F. Lin, and C. K. Peng, *Appl. Phys. Lett.* **44**, 635 (1984).
- <sup>2</sup>W. D. Laidig, Y. F. Lin, and P. J. Caldwell, *Appl. Phys. Lett.* **57**, 33 (1985).
- <sup>3</sup>D. Fekete, K. T. Chan, J. M. Ballantyne, and L. F. Eastman, *Appl. Phys. Lett.* **49**, 1659 (1986).
- <sup>4</sup>S. E. Fisher, D. Fekete, and G. B. Feak, *Appl. Phys. Lett.* **50**, 714 (1987).
- <sup>5</sup>D. L. Sipes, *Appl. Phys. Lett.* **47**, 74 (1985).
- <sup>6</sup>C. H. Henry, P. M. Petroff, R. A. Logan, and F. R. Merritt, *J. Appl. Phys.* **50**, 3721 (1979).
- <sup>7</sup>G. L. Harnagel, P. S. Cross, D. R. Scifres, and D. P. Worland, *Electron. Lett.* **22**, 231 (1986).
- <sup>8</sup>G. L. Harnagel, P. S. Cross, C. R. Lennon, M. DeVito, and D. R. Scifres, *Electron. Lett.* **23**, 743 (1987).
- <sup>9</sup>G. L. Harnagel, P. S. Cross, D. R. Scifres, D. F. Welch, C. R. Lennon, D. P. Worland, and R. D. Burnham, *Appl. Phys. Lett.* **49**, 1418 (1986).
- <sup>10</sup>C. A. Zmudzinski, M. E. Givens, R. P. Bryan, and J. J. Coleman, *Appl. Phys. Lett.* **53**, (1988).
- <sup>11</sup>M. E. Givens, C. A. Zmudzinski, R. P. Bryan, and J. J. Coleman (unpublished data).
- <sup>12</sup>G. Costrini and J. J. Coleman, *J. Appl. Phys.* **57**, 2249 (1985).
- <sup>13</sup>J. W. Matthews and A. E. Blakeslee, *J. Cryst. Growth* **27**, 118 (1974).
- <sup>14</sup>D. R. Scifres, R. D. Burnham, and W. Strieifer, *Electron. Lett.* **18**, 550 (1982).

# High-power nonplanar quantum well heterostructure periodic laser arrays

M. E. Givens, C. A. Zmudzinski, R. P. Bryan, and J. J. Coleman  
*Department of Electrical and Computer Engineering and NSF Engineering Research Center for Compound Semiconductor Microelectronics, University of Illinois at Urbana-Champaign, 1406 West Green Street, Urbana, Illinois 61801*

(Received 3 June 1988; accepted for publication 18 July 1988)

Optical pulsed powers of 8 W from a single uncoated facet and low ( $< 200 \text{ A/cm}^2$ ) threshold current densities have been obtained from 3.1-mm-wide (cavity length =  $483 \mu\text{m}$ ) nonplanar periodic quantum well heterostructure laser diode arrays grown by metalorganic chemical vapor deposition over a selectively etched corrugated substrate. The resulting nonplanar lateral active layer profile provides index guiding and suppresses lateral lasing regardless of device width.

Multiple stripe semiconductor laser diode arrays are a very promising source of high-power emission, suitable for such applications as pumping solid-state Nd:YAG lasers.<sup>1</sup> The maximum output power before catastrophic optical damage<sup>2</sup> occurs is determined primarily by the effective aperture width, which is normally limited to a value less than the cavity length unless lateral lasing and amplified spontaneous emission processes are suppressed. In order to fabricate diodes having a width greater than the laser cavity length, thereby allowing higher total output powers to be obtained, it is necessary to provide some type of structural change to inhibit lateral lasing. Previously reported<sup>3-5</sup> methods of inhibiting lateral lasing and amplified spontaneous emission require extra processing steps in addition to the processing required to form the actual array elements, and also result in a portion of the array width which does not contribute to the laser output. In this letter, we report high-power operation of a simple nonplanar index-guided quantum well heterostructure periodic laser array structure in which lateral lasing is prevented in a manner that still allows for uniform and continuous front facet light emission. Growth over a corrugated substrate<sup>6,7</sup> is utilized for index guiding and definition of the individual elements, and the resulting nonplanar active region structure effectively suppresses lateral lasing and amplified spontaneous emission for the entire array.<sup>8</sup> No additional processing steps after growth, such as proton bombardment, chemical etching, diffusion, epitaxial regrowth, or insulator deposition, which may result in accelerated degradation due to the introduction of material defects, are required. Data are presented on the high-power light-current characteristics and optical near-field measurements for uncoated laser bars with an aperture width of up to 3.1 mm, showing output powers of 8 W per uncoated facet for periodic laser arrays with threshold current densities of  $120\text{--}240 \text{ A/cm}^2$ .

Prior to epitaxial growth, a periodic array of narrow mesa stripes was defined over the surface of a (100) GaAs:*n* (Si-doped) substrate using standard photolithographic and wet chemical etching techniques. The  $\text{Al}_x\text{Ga}_{1-x}\text{As}/\text{GaAs}$  graded barrier quantum well heterostructure (GBQWH)<sup>9,10</sup> laser structure utilized in this study was grown in an atmospheric pressure metalorganic chemical vapor deposition (MOCVD) reactor<sup>11</sup> at a temperature of

$800^\circ\text{C}$ . High composition ( $x = 0.85$ )  $\text{Al}_x\text{Ga}_{1-x}\text{As}$  confining layers surround the GBQWH active layer, which consists of a 50 Å GaAs single quantum well ( $\lambda \sim 8250 \text{ \AA}$ ) centered in a 2450 Å parabolically graded  $\text{Al}_x\text{Ga}_{1-x}\text{As}$  layer ( $0.20 < x < 0.85$ ). Successive epilayers were deposited uniformly over the nonplanar growth surface such that the corrugated contour of the growth surface remained essentially unchanged, as illustrated in Fig. 1, which shows a schematic cross section and a scanning electron micrograph of a portion of the laser array. Device wafers were mechanically thinned and polished, metallized, cleaved into bars of various lengths, and diced into individual diode arrays of various widths. The facets of the devices utilized in this study were left uncoated. No further processing or photolithographic steps were required either to define current injection or to suppress lateral lasing. The devices were mounted *p* side down in indium solder on Cu blocks with multiple wire bonds to contact the *n* side of the device and were tested under pulsed operation (400 ns, 1 kHz).

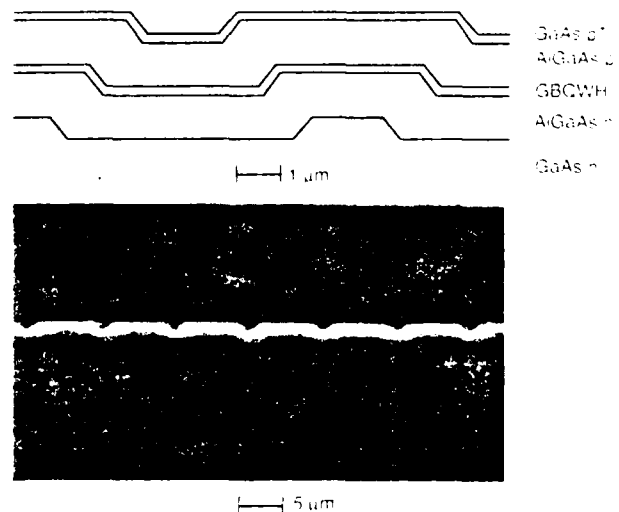


FIG. 1 Schematic diagram and scanning electron micrograph of the periodic nonplanar laser array grown by MOCVD on a corrugated etched substrate. The MOCVD growth over the nonplanar substrate results in a nonplanar active region which suppresses lateral lasing, allowing very wide laser bars.

Figure 2 shows the near-field optical intensity pattern from two adjacent elements of a high-power GBQWH periodic laser array at twice threshold. Note that two lasing spots, spaced by  $1.5 \mu\text{m}$ , are located in each mesa, one near each edge. No lasing action occurs in the grooves. The observed near-field pattern is uniformly distributed over the entire array width and is stable over a wide range of drive currents, retaining its shape from threshold to at least 16 times threshold. Other devices, with wider mesas than the device of Fig. 2 but having the same periodicity, also exhibit two spots in each mesa, spaced accordingly farther apart. The GBQWH periodic laser array structure is essentially a periodic variation of the channel guide structure<sup>7</sup> which has been modeled by Yang *et al.*<sup>12</sup> A comparison of the experimental data with the model<sup>12</sup> suggests that two index-guided waveguides are formed in each mesa, one at each edge, each lasing on the fundamental mode. This is likely since a single-peak fundamental mode of the waveguide structure is never observed, even though that mode is expected to have the lowest threshold gain.<sup>12</sup> The corresponding far-field pattern in the plane of the junction is single lobed, with a relatively wide full width half-maximum angle of  $18^\circ$ , indicating that, while it is possible that the individual emitter pairs are phase locked with each other, adjacent pairs spaced by  $8 \mu\text{m}$  are not phase locked.

For a given cavity length, the threshold current density is essentially independent of device width, as illustrated by the curves of Fig. 3 which show the measured threshold current density for lasers of two different lengths as a function of stripe width. The threshold current density ranges from 120 to  $240 \text{ A/cm}^2$ , depending on the cavity length. As expected, the lasers with a shorter cavity length have a higher threshold current density, as a result of the increased mirror loss for shorter lasers. Conventional semiconductor lasers will not operate when the width exceeds the cavity length, since lateral cavity modes would compete with the desired longitudinal cavity modes. In addition, the threshold current den-

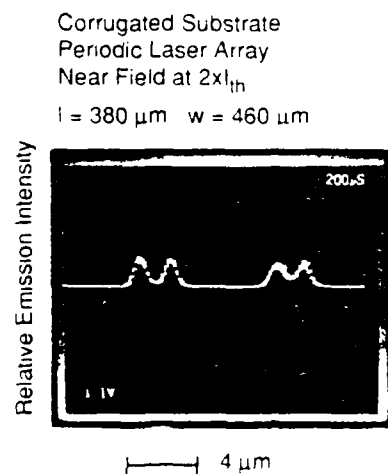


FIG. 2 Near-field intensity pattern of two adjacent elements of the non-planar array indicating two closely spaced emission spots per element. These data suggest that two waveguides are formed on each mesa, one near each edge, and each waveguide operates on the fundamental mode.

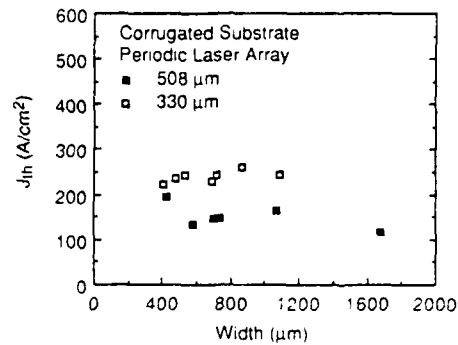


FIG. 3. Measured threshold current density as a function of device width for lasers of two different cavity lengths (330 and  $508 \mu\text{m}$ ). The threshold current density does not increase with device width, indicating the nonplanar active region effectively suppresses lateral lasing and amplified spontaneous emission.

sity for a conventional laser would be expected to increase as the width approaches the length as the lateral modes become dominant. However, the nonplanar structure of the active layer of the periodic arrays described here effectively spoils the lateral cavity by introducing periodic disruption along the lateral path length between the sawn sides of the laser. Thus, the threshold current density does not change with device width, even if the width exceeds the length by a factor of more than 6, as shown by the data of Fig. 4. This figure shows the light output from an uncoated facet as a function of current for a diode with a width equal to 6.4 times the length ( $l = 483 \mu\text{m}$ ,  $w = 3100 \mu\text{m}$ ). The threshold current density is  $170 \text{ A/cm}^2$ , in the expected range of threshold current density for devices with this length ( $483 \mu\text{m}$ ). The maximum observed power (Fig. 4) of  $8 \text{ W}$  per facet for wide devices is limited by the maximum output of our current pulser ( $40 \text{ A}$ ) and not by device degradation. The differential quantum efficiency was not observed to decrease as device width increases, indicating again that this structure inhibits lateral lasing and amplified spontaneous emission. In principle, output powers in excess of  $100 \text{ W}$  per facet could

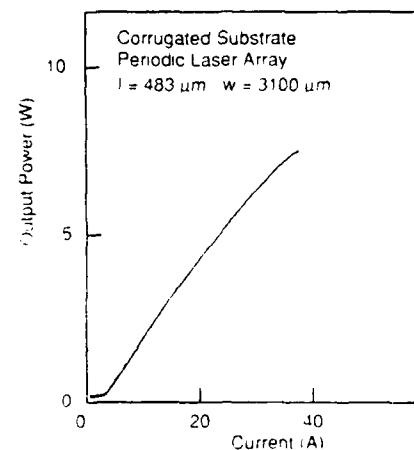


FIG. 4 Light-current characteristic from an uncoated facet of a  $3.1 \text{ mm}$  periodic array (cavity length =  $483 \mu\text{m}$ ). The output power at the catastrophic optical degradation limit is greater than  $8 \text{ W}$  per facet.

be expected from an optimized device, having reflection and antireflection coatings, at currents in excess of 100 A.<sup>4</sup> The low threshold current density of these GBQWH periodic laser array structures results in low threshold currents of 2–3 A for widths up to 3.1 mm. This is considerably lower than the values reported<sup>4,5</sup> for multiple quantum well structures which utilized etched grooves to suppress amplified spontaneous emission and lateral lasing.

In summary, simple nonplanar index-guided graded barrier quantum well heterostructure periodic laser array structures grown by MOCVD on corrugated etched substrates have been fabricated and tested. Current-supply-limited output powers of up to 8 W per uncoated facet from a 3.1-mm-wide bar (cavity length = 483  $\mu\text{m}$ ) and low threshold current densities of 120–240 A/cm<sup>2</sup> have been obtained for pulsed operation. Near-field data suggest that two index-guided waveguides are formed in each mesa, one at each edge, each lasing on the fundamental mode. Discrimination against lateral lasing is provided solely by the nonplanar structure of the active region, and no increase in threshold current density or decrease in efficiency is observed for lasers with a width up to 6.4 times the cavity length. No additional processing steps are required to inhibit lateral lasing and amplified spontaneous emission. This structure is very desirable because of the simple fabrication processes involved and the demonstrated potential for high-power operation.

The authors would like to gratefully acknowledge T. L.

Brock for assistance with mask design and fabrication and L. M. Miller and T. King Higman for helpful discussions and technical support. This work was supported in part by the National Science Foundation Engineering Research Center for Compound Semiconductor Microelectronics, the McDonnell Douglas Corporation, the Naval Research Laboratory (N00014-88-K-2005), and SDIO/IST (DAAL 03-87-K-0013).

<sup>1</sup>D. L. Sipes, *Appl. Phys. Lett.* **47**, 74 (1985).

<sup>2</sup>C. H. Henry, P. M. Petroff, R. A. Logan, and F. R. Merritt, *J. Appl. Phys.*, **50**, 3721 (1979).

<sup>3</sup>G. L. Harnagel, P. S. Cross, D. R. Scifres, and D. P. Worland, *Electron. Lett.* **22**, 231 (1986).

<sup>4</sup>G. L. Harnagel, P. S. Cross, C. R. Lennon, M. DeVito, and D. R. Scifres, *Electron. Lett.* **23**, 743 (1987).

<sup>5</sup>G. L. Harnagel, P. S. Cross, D. R. Scifres, D. F. Welch, C. R. Lennon, D. P. Worland, and R. D. Burnham, *Appl. Phys. Lett.* **49**, 1418 (1986).

<sup>6</sup>J. S. Smith, P. L. Derry, S. Margalit, and A. Yariv, *Appl. Phys. Lett.* **47**, 712 (1985).

<sup>7</sup>R. D. Dupuis and P. D. Dapkus, *Appl. Phys. Lett.* **33**, 724 (1978).

<sup>8</sup>C. A. Zmudzinski, M. E. Givens, R. P. Bryan, and J. J. Coleman, *Appl. Phys. Lett.* **53**, 350 (1988).

<sup>9</sup>W. T. Tsang, *Appl. Phys. Lett.* **39**, 134 (1981).

<sup>10</sup>L. J. Mawst, M. E. Givens, C. A. Zmudzinski, M. A. Emanuel, and J. J. Coleman, *IEEE J. Quantum Electron.* **QE-23**, 696 (1987).

<sup>11</sup>G. Costrini and J. J. Coleman, *J. Appl. Phys.* **57**, 2249 (1985).

<sup>12</sup>J. J. Yang, R. D. Dupuis, and P. D. Dapkus, *J. Appl. Phys.* **53**, 7218 (1982).

# Compositional Disordering and the Formation of Semi-insulating Layers in AlAs-GaAs Superlattices by MeV Oxygen Implantation

R. P. BRYAN, M. E. GIVENS, J. L. KLATT, R. S. AVERBACK and J. J. COLEMAN

Materials Research Laboratory  
University of Illinois at Urbana—Champaign  
1406 W. Green St., Urbana, IL 61801-2991

Data are presented demonstrating the use of MeV oxygen ion implantation and subsequent annealing procedures to induce compositional disordering and to create a semi-insulating region simultaneously within an AlAs-GaAs superlattice. High dose oxygen implantation yields a compositionally disordered region 3500 Å wide centered 1.25 μm below the surface of the superlattice, as determined by secondary ion mass spectrometry (SIMS) analysis. More extensive disordering of the superlattice occurs at lower implantation temperatures. Current-voltage measurements indicate the formation of a semi-insulating layer which is thermally stable to at least 850° C. The semi-insulating properties of the implanted superlattice are assigned to the disorder-enhanced formation of Al-O pairs and the substitutional introduction of deep level states.

**Key words:** Compositional disordering, oxygen ion implantation, semi-insulating layer, AlAs-GaAs superlattice

## INTRODUCTION

Impurity induced compositional disordering of III-V compound semiconductor epitaxial structures exhibits immense potential for the microfabrication of unique optical and electronic devices.<sup>1-13</sup> Compositional disordering of thin layer AlAs-GaAs superlattices (SLs) has most commonly been induced with the electrically active impurities Zn and Si which are introduced into the crystal by either diffusion or ion implantation. For many applications, however, the incorporation of electrically active impurities may be undesirable and recent reports indicate that compositional disordering can be induced through implantation of the lattice constituents Ga, Al, and As,<sup>5-4</sup> or other electrically inactive impurities, such as Kr, B, and F.<sup>5,6</sup>

Ion implantation has also been utilized in the formation of semi-insulating regions in bulk epitaxial layers suitable for optoelectronic device applications.<sup>14</sup> Proton bombardment, the most widely applied technique, relies on the formation of a high density of defects during the implantation to induce localized compensation of GaAs resulting in a region of nonconducting material. However, high temperature annealing serves to repair this damage and, therefore, restore the GaAs to its uncompensated conducting state. Alternately, Favennec *et al.*<sup>15</sup> have demonstrated that implantation of high doses of oxygen into *n*-type GaAs yields highly resistive material which is thermally stable at anneal temperatures up to 900° C. Several mechanisms<sup>15-20</sup> have been proposed to explain the compensation effects in oxygen implanted GaAs, without consensus. Nonetheless, oxygen implantation has been used in the fabrication of such electrical and optical devices

as laser diodes, field effect transistors, heterostructure bipolar transistors, and optical waveguides.<sup>21-24</sup>

In this paper, MeV implantation of oxygen into an AlAs-GaAs SL is shown to result in induced compositional disordering and the formation of a semi-insulating layer at a depth of ~1.25 μm. The degree of induced disorder was examined for several different doses ( $10^{15}$  cm<sup>-2</sup>,  $10^{16}$  cm<sup>-2</sup>, and  $10^{17}$  cm<sup>-2</sup>) and for two different implant temperatures (room temperature and 250° C). It has been shown<sup>11,25-27</sup> that by increasing the temperature at which the implantation occurs, the doping efficiency increases and the net damage generated decreases. Therefore the amount of damage produced during the implantation may be varied to an extent independently of the dose. The compositional structure of the SL was studied by secondary ion mass spectroscopy (SIMS) for the as-grown, implanted, and annealed cases. Depth profiles indicate no detectable compositional disordering for doses below  $10^{17}$  cm<sup>-2</sup>. For a dose of  $10^{17}$  cm<sup>-2</sup>, partial disordering is evident prior to annealing for both the room temperature and 250° C implanted samples, although it is more extensive in the room temperature implanted sample. Following annealing, the room temperature implanted sample exhibits enhanced disordering resulting in complete intermixing of adjacent layers over a range of ~3500 Å. In contrast, annealing of the 250° C implanted sample produces no further disordering.

The electrical properties of the semi-insulating region formed during the implant were inferred from current-voltage measurements of mesa delineated *p-n* diodes fabricated in the AlAs-GaAs SL. Following implantation ( $10^{17}$  cm<sup>-2</sup> oxygen dose, unannealed), substantial increases in both the forward turn-on and reverse break-down voltages of the diodes are observed. The insulating characteristics

(Received July 11, 1988; revised September 25, 1988)

of the implanted samples are slightly enhanced following annealing. These data indicate the formation of both a thermally stable semi-insulating layer and a compositionally disordered region formed in an AlAs-GaAs SL by high energy oxygen ion implantation and annealing.

## EXPERIMENT

The superlattice structure examined in this study was grown by atmospheric pressure metalorganic chemical vapor deposition<sup>28</sup> (MOCVD) at a temperature of 800° C on Si-doped (100) GaAs substrates having a carrier concentration of  $2 \times 10^{18} \text{ cm}^{-3}$ . The structure consisted of a 0.25  $\mu\text{m}$  GaAs undoped buffer layer underlying an 50 period undoped SL, each period consisting of 200Å AlAs and 200Å GaAs yielding a total SL thickness of 2  $\mu\text{m}$ . As a consequence of the high growth temperature, the average background *p*-type carrier concentration of the superlattice was approximately  $10^{18} \text{ cm}^{-3}$ . Ion implantation was performed using a Van de Graaff accelerator at a fixed beam energy (1 MeV), current (120 nA), and sample chamber pressure ( $6 \times 10^{-4}$  Torr) with the beam focused into a 3 mm diameter spot. The dose was varied between  $10^{15}$  and  $10^{17} \text{ cm}^{-2}$ . The large amount of radiation damage for these high doses prevents any significant channeling<sup>29</sup> of the oxygen ions. During implantation, the samples were maintained at either room temperature or 250° C. Capless anneals of the implanted samples were performed in the MOCVD reactor under arsine overpressure at 850° C for 45 min. The depth profiles of <sup>16</sup>O and <sup>27</sup>Al were measured with a Cameca ims-3f SIMS microanalyzer using Cs<sup>+</sup> primary ions. The compositional structure of the SL was examined by measuring the Al profile, as opposed to that of Ga, because the negative ion sensitivity<sup>30</sup> of the system is greater for <sup>27</sup>Al than for <sup>69</sup>Ga. *P*-type contacts (Cr/Au) were made to the surface of the SL and alloyed *n*-type contacts (AuGe) were made to the substrate. Electrical measurements of etched circular mesas with 200  $\mu\text{m}$  diameter contact areas were made using a digitizing semiconductor parameter analyzer (HP4145B).

## RESULTS AND DISCUSSION

### Compositional Disorder

The SIMS profiles of <sup>27</sup>Al in the unimplanted SL sample, for both as-grown and annealed (850° C, 45 min) material, are shown in Fig. 1. The amplitude of the oscillations of the Al signal do not decrease with depth, indicating that resolution sufficient to delineate clearly the 200Å layers is maintained throughout the 2  $\mu\text{m}$  of the SL. Consistent with previous results,<sup>31</sup> the 850° C anneal was insufficient to induce thermal disordering of the SL. SIMS depth profiles of <sup>27</sup>Al in the SL samples which were implanted at room temperature with doses of either  $10^{15}$  or  $10^{16} \text{ cm}^{-2}$  show no evidence of any disorder-

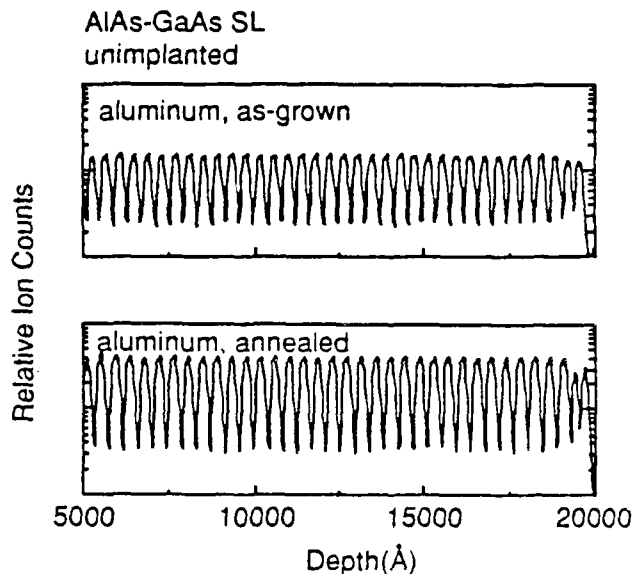


Fig. 1 — <sup>27</sup>Al depth profiles by SIMS of an unimplanted, as-grown and then annealed (850° C, 45 min) AlAs (200Å)-GaAs (200Å) SL.

ing of the SL layers for these doses. Similar <sup>27</sup>Al profiles are obtained when the superlattices were implanted with the same doses at a temperature of 250° C.

For the highest dose studied ( $10^{17} \text{ cm}^{-2}$ ), the <sup>27</sup>Al profiles of the SL exhibit clear evidence of compositional disordering, even prior to annealing, for both the room temperature and 250° C implants, as shown in Figs. 2 and 3. The decrease seen in the <sup>27</sup>Al sig-

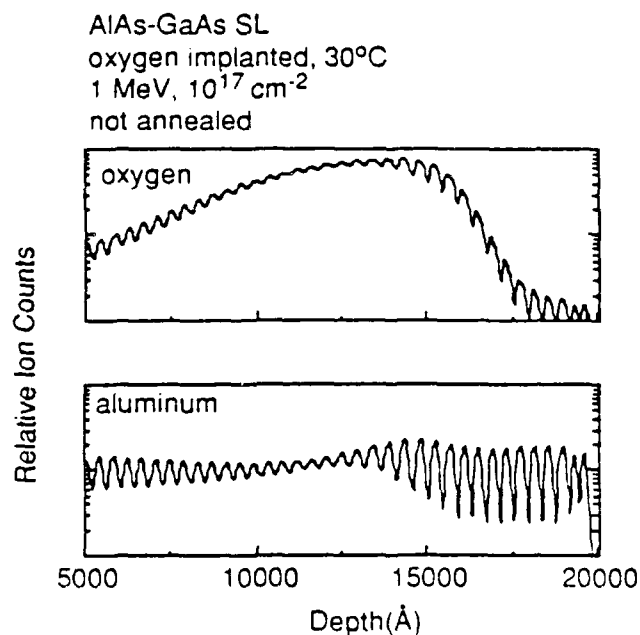


Fig. 2 — <sup>16</sup>O and <sup>27</sup>Al depth profiles by SIMS for an unannealed AlAs (200Å)-GaAs (200Å) SL implanted with 1 MeV oxygen to a dose of  $10^{17} \text{ cm}^{-2}$  at room temperature. Partial compositional disordering is evident in the <sup>27</sup>Al signal at  $\sim 125 \mu\text{m}$ . The region of partial disordering is not aligned with the highest concentration of oxygen.

*0.125 μm*

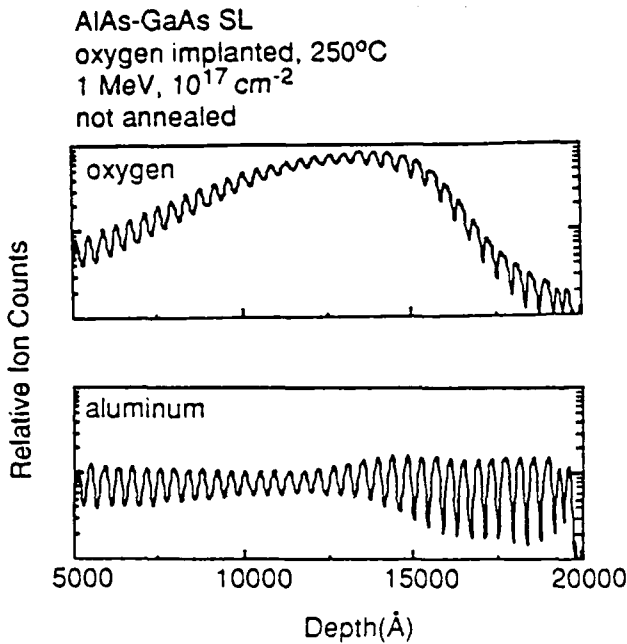


Fig. 3 — Depth profiles of  $^{16}\text{O}$  and  $^{27}\text{Al}$  by SIMS for an unannealed AlAs (200Å)-GaAs (200Å) SL implanted with 1 MeV oxygen to a dose of  $10^{17} \text{ cm}^{-2}$  at 250°C. Partial compositional disordering is evident in the  $^{27}\text{Al}$  signal at  $\sim 1.25 \mu\text{m}$ . The region of partial disordering is not aligned with the highest concentration of oxygen.

nal oscillations is not the result of degradation of the SIMS resolution with depth, as evidenced by the recovery of the oscillation intensity at greater depths. The location of the partially disordered region does not coincide with that of the peak oxygen concentration, but is slightly removed toward the surface of the epilayer and aligned with the region of greatest damage as determined from a computer simulation.<sup>12</sup> The measured degree of disorder is greater for the room temperature implanted sample than for the 250°C implanted sample, consistent with the higher levels of damage induced during the room temperature implant.<sup>11,25-27</sup> The oscillations seen in the  $^{16}\text{O}$  signal are an artifact of the matrix effect associated with the SIMS technique in which the  $^{16}\text{O}$  sensitivity is increased in the AlAs layers. The projected range of the implanted oxygen ions is observed to be  $1.3 \mu\text{m}$ , consistent with data reported<sup>23-22</sup> for similar 1 MeV oxygen implants into GaAs.

No disordering was observed in SIMS depth profiles of the SL implanted at either room temperature or 250°C, at a dose of  $10^{19} \text{ cm}^{-2}$ , and annealed at 850°C for 45 min. Profiles of samples implanted with a dose of  $10^{17} \text{ cm}^{-2}$  at both room temperature and 250°C and similarly annealed are shown in Figs. 4 and 5. For the sample implanted at 250°C, the partial disorder present prior to annealing is seen to remain essentially unchanged following annealing. The profiles of Fig. 4 for the  $10^{17} \text{ cm}^{-2}$  sample implanted at room temperature, however, clearly show that the 850°C annealing results in further disordering of the SL to the point of complete in-

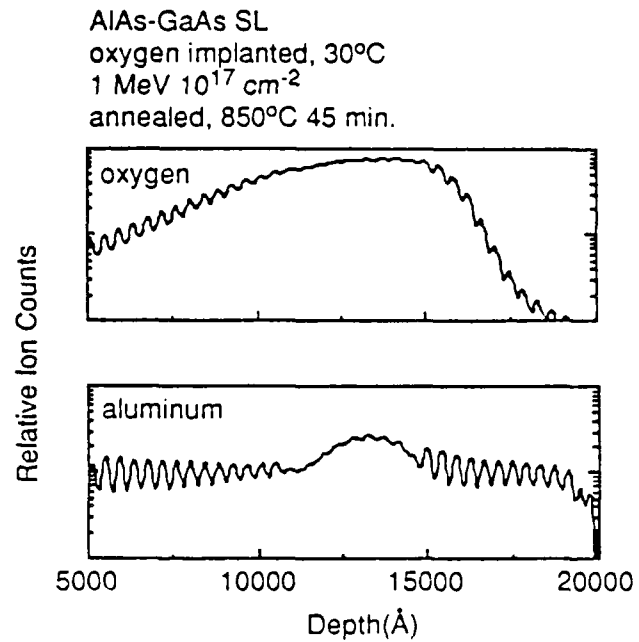


Fig. 4 —  $^{16}\text{O}$  and  $^{27}\text{Al}$  depth profiles by SIMS for an AlAs (200Å)-GaAs (200Å) SL implanted with 1 MeV oxygen to a dose of  $10^{17} \text{ cm}^{-2}$  at room temperature and annealed at 850°C for 45 min. A region  $\sim 3500\text{Å}$  of complete disordering is observed at  $\sim 1.25 \mu\text{m}$ .

termixing of the GaAs and AlAs layers over a region 3500Å in width. No redistribution of the oxygen profile is observed in the SL, in contrast to the redistribution reported<sup>34</sup> following annealing (900°C, 20 min) of bulk GaAs implanted with oxygen at 1 MeV. The cause of the small rise in the Al signal within the disordered region is not yet clearly

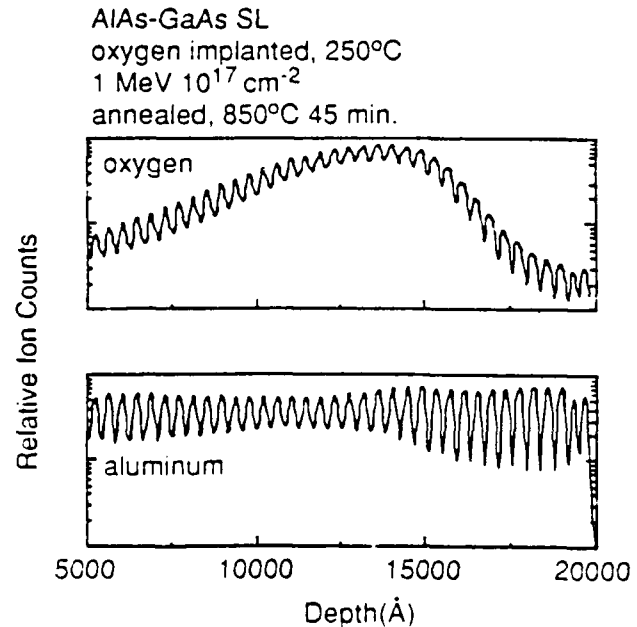


Fig. 5 — SIMS depth profiles of  $^{16}\text{O}$  and  $^{27}\text{Al}$  depth profiles of an AlAs (200Å)-GaAs (200Å) SL implanted with 1 MeV oxygen to a dose of  $10^{17} \text{ cm}^{-2}$  at 250°C and annealed at 850°C for 45 min. Partial compositional disordering is evident in the  $^{27}\text{Al}$  signal profile.

understood. This rise tracks the peak of the oxygen concentration and, therefore, may be due to an increase in Al sensitivity as a consequence of the high oxygen concentration and the mixed matrix.

In summary, for doses of  $10^{16}$   $\text{cm}^{-2}$  or less no disordering is observed in either the as-implanted or the annealed samples. Partial disorder is seen prior to annealing in the  $10^{17}$   $\text{cm}^{-2}$  implanted samples for both implant temperatures with more extensive disordering evident for the room temperature implant, which induces the higher level of damage. Subsequent annealing has little effect on the  $10^{17}$   $\text{cm}^{-2}$ ,  $250^\circ\text{C}$  implanted sample but results in greatly enhanced disordering for the  $10^{17}$   $\text{cm}^{-2}$ , room temperature implanted sample to the point of total intermixing of the GaAs and AlAs layers over a region approximately 3500Å wide. No evidence of oxygen redistribution was noted following annealing for any of the doses used. This indicates that the oxygen induced disordering seen here is not dependent on fast diffusion of the implanted species during the anneal, as is the case for Si implantation.<sup>2,12-13</sup> Rather, the atomic mixing processes (*i.e.* ion beam mixing, radiation enhanced diffusion) taking place during the implantation allow sufficient disruption of the lattice to produce partial disordering. Further disorder occurs during subsequent annealing, presumably by defect motion, although the details of the disordering process have not yet been investigated.

#### Carrier Compensation

The forward and reverse current-voltage (I-V) characteristics of an as-grown SL and an unannealed, oxygen implanted SL ( $10^{17}$   $\text{cm}^{-2}$ , room temperature) are compared in Fig. 6. The I-V characteristic of the as-grown sample exhibits a forward turn-on voltage of 2 V and a reverse breakdown voltage of 10 V. For the implanted sample, both the forward turn-on and reverse breakdown voltages

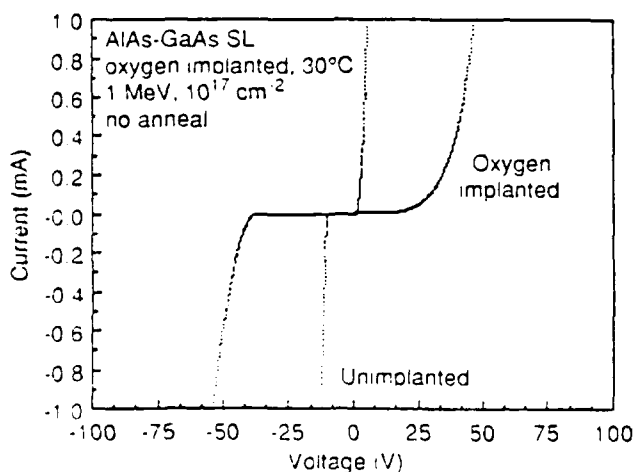


Fig 6 — Forward and reverse I-V characteristics of an unimplanted, unannealed AlAs (200Å)-GaAs (200Å) SL (inner curve) and the unannealed SL implanted with 1 MeV oxygen to a dose of  $10^{17}$   $\text{cm}^{-2}$  at room temperature (outer curve).

increase substantially, the former increasing from 2 V to 30 V and the latter from 10 V to 41 V. It has been reported<sup>16</sup> that the high density of defects generated in bulk GaAs implanted with a moderate dose ( $10^{15}$   $\text{cm}^{-2}$ ) of oxygen acts as a conduction path for carriers. Only after repair of the implantation induced damage during annealing is a semi-insulating region obtained.<sup>16</sup> The data of Fig. 6, however, show that a semi-insulating layer is formed in a SL prior to annealing. These SL samples were implanted with higher doses than those of Ref. 16 and should contain a greater density of defects. Thus, the mechanism for defect conduction observed in bulk GaAs does not occur in an AlAs-GaAs SL.

The forward and reverse I-V characteristics of annealed ( $850^\circ\text{C}$ , 45 min) samples, both implanted ( $10^{17}$   $\text{cm}^{-2}$ , room temperature) and unimplanted, are shown in Fig. 7. The forward turn-on and reverse breakdown voltages of these annealed samples are only slightly higher than those of the unannealed samples. For the unimplanted sample, the forward turn-on voltage increased from 2 to 4 V and the reverse breakdown voltage increased from 10 to 11 V, while for the implanted sample, the values increased from 30 to 78 V and from 41 to 99 V in the forward and reverse bias conditions, respectively. The electric field in the SL at which breakdown occurs for the annealed, implanted sample is approximately  $4 \times 10^5$  V/cm. These data demonstrate for formation of a highly resistive region within a SL epilayer, via oxygen implantation, which exhibits good semi-insulating properties that are stable under high temperature annealing.

Although the compensation mechanism active in oxygen implanted AlGaAs layers is not clearly understood, it has been proposed that the compensation is due to complexes involving oxygen and defects created during the implantation.<sup>15-20</sup> In GaAs, oxygen can introduce both deep donor and deep acceptor states. A deep donor level is generated when

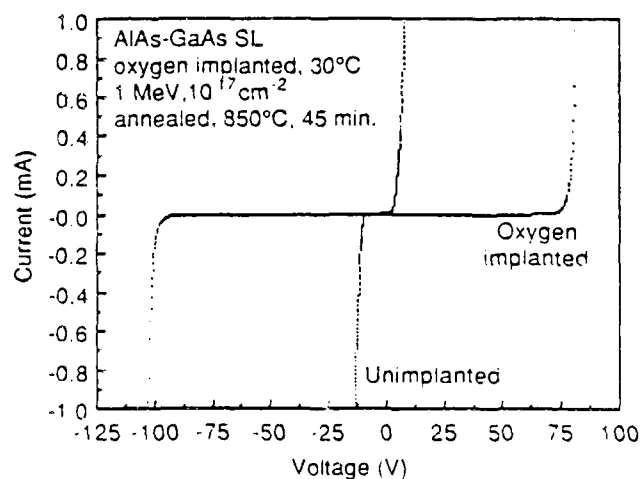


Fig 7 — I-V characteristics for annealed ( $850^\circ\text{C}$  for 45 min) samples of an unimplanted AlAs (200Å)-GaAs (200Å) SL (inner curve) and a SL implanted at room temperature with 1 MeV oxygen to a dose of  $10^{17}$   $\text{cm}^{-2}$  (outer curve).

oxygen substitutes on an arsenic site ( $O_{As}$ ) in the GaAs lattice, while a complex of a substitutional  $O_{As}$  and an arsenic vacancy ( $V_{As}$ ), or a different complex involving the defects generated during the oxygen implantation, results in a deep acceptor level. It is possible that a complex pairing of Al and O species may also form a deep level trap in AlGaAs material. It has previously been reported<sup>35</sup> that for AlGaAs possessing a constant concentration of oxygen, the electron concentration decreases as the aluminum concentration increases. The layer intermixing process induced during the  $10^{17}$  cm<sup>-2</sup> room temperature implant, and enhanced during the subsequent anneal, results in a redistribution of aluminum from regions of high concentration (the AlAs layers of the SL) into regions previously devoid of aluminum (the GaAs layers of the SL). Migration of Al atoms into the GaAs layers having a high concentration of O atoms should allow the formation of additional Al-O pairs, thereby improving the semi-insulating characteristics of the layer. The increase in material resistivity reported here may be caused by a reduction in carrier concentration due to the enhanced formation of deep level Al-O complexes in the AlGaAs regions which comprise the intermixed interfaces of the disordered or partially disordered AlAs-GaAs SLs.

### CONCLUSIONS

The data presented demonstrate the use of oxygen ion implantation and subsequent annealing procedures to simultaneously induce compositional disordering and create a semi-insulating region within an AlAs-GaAs SL. A deep (1.25  $\mu$ m) disordered region is produced by the damage generated by a 1 MeV oxygen implantation at a dose of  $10^{17}$  cm<sup>-2</sup>. A correspondence between induced disordering and lattice damage is evidenced by the alignment of the disordered region with the calculated peak of the damage profile in the epilayer and the partial disordering seen in the unannealed, as-implanted sample. The presence of more extensive disorder in the room temperature implanted samples, which have a greater level of induced damage than those implanted at 250°C, also supports this observation. The I-V characteristics of the SL indicate that the oxygen implant generates a compensated, semi-insulating layer which is thermally stable at the annealing temperature required to disorder completely a region of the SL. As the damage related to the implantation is assumed to have been repaired during the high temperature anneal, the insulating properties of the implanted layer are assigned to a chemically induced compensation related to the formation of Al-O pairs and deep levels.

### ACKNOWLEDGEMENTS

The authors would like to gratefully acknowledge J. Baker and B. Clymer for valuable discussions and

technical assistance. This work has been funded by the National Science Foundation (DMR 86-12860), the Naval Research Laboratory (N00014-88-K-2005) and the Department of Energy Basic Energy Sciences (DE-AC02-76ER01198).

### REFERENCES

1. W. D. Laidig, N. Holonyak, Jr., M. D. Camras, K. Hess, J. J. Coleman, P. D. Dapkus, and J. Bardeen, *Appl. Phys. Lett.* **38**, 776 (1981).
2. T. Venkatesan, S. A. Schwarz, D. M. Hwang, R. Bhat, M. Koza, H. W. Yoon, P. Mei, Y. Arakawa, and A. Yariv, *Appl. Phys. Lett.* **49**, 701 (1986).
3. M. D. Camras, J. J. Coleman, N. Holonyak, Jr., K. Hess, P. D. Dapkus, and C. G. Kirkpatrick, *Inst. Phys. Conf. Ser.* **65**, 233 (1982).
4. J. J. Coleman, P. D. Dapkus, C. G. Kirkpatrick, M. D. Camras, and N. Holonyak, Jr., *Appl. Phys. Lett.* **40**, 904 (1982).
5. P. Gavrilovic, D. G. Deppe, K. Meehan, N. Holonyak, Jr., J. J. Coleman, and R. D. Burnham, *Appl. Phys. Lett.* **47**, 130 (1985).
6. Y. Hirayama, Y. Suzuki, and H. Okamoto, *Jpn. J. Appl. Phys.* **24**, 1498 (1985).
7. J. Cibert, P. M. Petroff, D. J. Werder, S. J. Pearton, A. C. Gossard, and J. H. English, *Appl. Phys. Lett.* **49**, 223 (1986).
8. K. Kash, B. Tell, P. Grabbe, E. A. Dobisz, H. G. Craighead, and M. C. Tamargo, *J. Appl. Phys.* **63**, 190 (1988).
9. K. Ishida, K. Marsui, T. Fukunaga, T. Takamori, and H. Nakashima, *Jpn. J. Appl. Phys.* **25**, L690 (1986).
10. P. Gavrilovic, K. Meehan, L. J. Guido, N. Holonyak, Jr., V. Eu, M. Feng, and R. D. Burnham, *Appl. Phys. Lett.* **47**, 903 (1985).
11. E. A. Dobisz, B. Tell, H. G. Craighead, and M. C. Tamargo, *J. Appl. Phys.* **60**, 4150 (1986).
12. S. A. Schwarz, T. Venkatesan, D. M. Hwang, H. W. Yoon, R. Bhat, and Y. Arakawa, *Appl. Phys. Lett.* **50**, 281 (1987).
13. K. Matsui, J. Kobayashi, T. Fukunaga, K. Ishida, and H. Nakashima, *Jpn. J. Appl. Phys.* **25**, L651 (1986).
14. A. G. Foyt, W. T. Lindley, C. M. Wolfe, and J. P. Donnelly, *Solid-State Electron.* **12**, 209 (1969).
15. P. N. Favenec, *J. Appl. Phys.* **47**, 2532 (1976).
16. X.-C. Deng, *Nucl. Instrum. and Methods Phys. Res.* **209-210**, 657 (1983).
17. B. Deveaud and P. N. Favenec, *Inst. Phys. Conf. Ser.* **45**, 492 (1979).
18. T. Itoh, T. Tsuchiya, and M. Takeuchi, *Jpn. J. Appl. Phys.* **15**, 2277 (1976).
19. R. S. Bhattacharya, A. K. Rai, and P. P. Pronko, *Phys. Stat. Sol. A* **78**, 283 (1983).
20. E. V. K. Rao, N. Duhamel, P. N. Favenec, and H. L'Hardon, *J. Appl. Phys.* **49**, 3898 (1978).
21. J. M. Blum, J. C. McGroddy, P. G. McMullin, K. K. Shih, A. W. Smith, and J. F. Ziegler, *IEEE J. Quantum Electron.* **QE-11**, 413 (1975).
22. V. I. Kolyshkin and E. L. Portnoi, *Sov. Tech. Phys. Lett.* **4**, 260 (1978).
23. P. M. Asbeck, D. L. Miller, R. J. Anderson, and F. H. Eisen, *IEEE Electron Device Lett.* **EDL-5**, 310 (1984).
24. W. Lee and C. G. Fonstad, *IEEE Electron Device Lett.* **EDL-8**, 217 (1987).
25. J. S. Harris, F. H. Eisen, B. Welch, J. D. Haskell, R. D. Pashley, and J. W. Mayer, *Appl. Phys. Lett.* **21**, 601 (1972).
26. J. S. Williams and M. W. Austin, *Appl. Phys. Lett.* **36**, 994 (1980).
27. D. V. Morgan, F. H. Eisen, and A. Ezis, *IEE Proc.* **128-1**, 109 (1981).
28. J. J. Coleman and P. D. Dapkus, in *Gallium Arsenide Technology*, ed. by D. K. Ferry, Howard W. Sams, Indianapolis, IN, 1985, p. 79.
29. T. Asano, R. D. Atanassov, H. Ishiwara, S. Furukawa, *Jpn. J. Appl. Phys.* **20**, 901 (1981).

30. H. A. Storms, K. F. Brown, and J. D. Stein, *Anal. Chem.* **49**, 2023 (1977).
31. W. D. Laidig, N. Holonyak, Jr., J. J. Coleman, and P. D. Dapkus, *J. Electron. Mater.* **11**, 1 (1982).
32. J. P. Biersack and L. G. Haggmark, *Nucl. Instr. and Meth.* **174**, 257 (1980).
33. T. Asano and P. L. F. Hemment, *Solid-State Electron.* **23**, 1089 (1980).
34. P. N. Favennec, B. Deveaud, M. Salvi, A. Martinez, and C. Armand, *Electron. Lett.* **18**, 202 (1982).
35. R. H. Wallis, M.-A. di Forte Poisson, M. Bonnet, G. Beuchet, and J.-P. Duchemin, *Inst. Phys. Conf. Ser.* **56**, 73 (1981).

## Operational and Design Considerations for Broad Area Graded Barrier Quantum Well Heterostructure Lasers Grown by Metalorganic Chemical Vapor Deposition for High Power Applications

M. E. GIVENS  
C. A. ZMUDZINSKI  
R. P. BRYAN  
J. J. COLEMAN

Materials Research Laboratory and  
NSF Engineering Research Center for Compound Semiconductor  
Microelectronics  
University of Illinois at Urbana-Champaign  
1406 West Green Street  
Urbana, Illinois 61801

*Abstract* Graded barrier quantum well heterostructure (GBQWH) broad area lasers have been shown to be capable of high power pulsed and cw operation. In this article, we consider several operational characteristics and design issues associated with broad area graded barrier quantum well heterostructure lasers grown by metalorganic chemical vapor deposition. In particular, the effect of junction heating on emission wavelength for cw device operation and the effects of various buffer layer structures on the material properties and device characteristics of GBQWH structures are addressed. Typical results for high power operation of uncoated broad area laser diodes are also outlined.

### Introduction

Graded barrier quantum well heterostructure (GBQWH) lasers<sup>1, 2</sup> exhibit extremely low threshold current densities and high quantum efficiencies due to the two-dimensional density of states of the quantum well active layer and the excellent optical and carrier confinement provided by the compositional grading of the barriers.<sup>3-5</sup> These structures are therefore suitable for use in high power applications where low drive currents and high power conversion efficiencies, which result in reduced heat generation in devices operated under cw conditions, are desirable. The lower threshold current density inherent to the GBQWH structure, in comparison to conventional double heterostructure (DH) lasers,<sup>6</sup> allows operation of devices with accordingly wider stripe geometries (150  $\mu\text{m}$  in this study, as compared to 50  $\mu\text{m}$  in the DH study), but having the same threshold current at much higher power levels before device heating leads to reductions in output

Received: April 13, 1988; accepted: May 24, 1988

power and undesirable temperature-induced shifts in the emission wavelength. In addition, the larger near-field emission spot size of broad area GBQWH lasers, due to the wider stripe geometry utilized and confinement of the optical field in a large optical cavity, results in a relatively narrow output beam and reduces the output power density at the facets, allowing higher total output powers at the point of catastrophic optical degradation.<sup>7</sup> In this article, heat generation and dissipation in GBQW lasers are addressed, along with some design considerations to reduce the former and enhance the latter.

During high power operation, diode heating effects can cause a significant shift in laser emission wavelength as the output power level is increased and can eventually lead to enhanced device degradation, thereby shortening the operational lifetime, or even result in abrupt thermally induced catastrophic failure. It is necessary to take such thermal effects into account when designing high power cw lasers for stable operation at specific wavelengths, such that heat dissipation can be maximized. In this work, thermally induced wavelength shifts as a function of output power for high power broad area GBQWH laser diodes grown by metal-organic chemical vapor deposition (MOCVD)<sup>8</sup> are described. Comparison of emission spectra at various pulsed and cw output power levels and ambient temperatures is presented, allowing estimates of average laser diode internal operating temperatures to be made. The effect of various types of buffer layers on the material quality of epitaxial layers of high composition ( $x = 0.85$ )  $\text{Al}_x\text{Ga}_{1-x}\text{As}$  laser material grown by MOCVD on horizontal Bridgman (HB) and liquid encapsulated Czochralski (LEC) substrates is also reviewed. Details of the various prelayers and their effects on the device performance of GBQWH lasers having high composition  $\text{Al}_x\text{Ga}_{1-x}\text{As}$  confining layers are described. Finally, high power data are presented on the operational characteristics of various broad area GBQWH laser structures, and correlations between device performance and assorted GBQWH design parameters are noted.

### Dependence of Emission Wavelength on Operating Temperature and Output Power

It has been shown that heat generated by nonradiative processes in a semiconductor laser raises the junction temperature of any laser diode structure, thereby inhibiting stimulated emission and reducing the total optical output power.<sup>9</sup> Junction heating also results in a temperature-dependent red-shift in emission energy to longer wavelengths,<sup>10, 11</sup> which is undesirable in applications where high power operation at a specific wavelength is required or where wavelength stability over a wide range of output powers is desired. In this section, the variation in emission wavelength of wide stripe broad area GBQWH lasers as a function of pulsed and cw output power is noted, and the effects of structural design and device processing on the magnitude of this thermally induced wavelength shift are discussed. Comparison of laser emission spectra for pulsed and cw operation of devices at various power levels and ambient temperatures allows an estimate to be made of the average internal operating temperature of the laser diode active region.

The devices utilized in this study were grown by MOCVD at 800°C in an atmospheric pressure vertical reactor described previously.<sup>12</sup> The basic  $\text{Al}_x\text{Ga}_{1-x}\text{As}/\text{GaAs}$  laser structure consisted of a 0.5- $\mu\text{m}$  GaAs buffer layer ( $n =$

$1 \times 10^{18}$ ), a 0.5- $\mu\text{m}$  linearly graded  $\text{Al}_x\text{Ga}_{1-x}\text{As}$  buffer layer ( $0.0 \leq x \leq 0.85$ ,  $n = 1 \times 10^{18}$ ), a 1.5- $\mu\text{m}$   $\text{Al}_{0.85}\text{Ga}_{0.15}\text{As}$  confining layer ( $n = 1 \times 10^{18}$ ), a 1,200- $\text{\AA}$  parabolically graded  $\text{Al}_x\text{Ga}_{1-x}\text{As}$  layer ( $0.85 \geq x \geq 0.20$ ,  $n = 5 \times 10^{16}$ ), a 50- $\text{\AA}$  GaAs single quantum well (undoped), a 1,200- $\text{\AA}$  parabolically graded  $\text{Al}_x\text{Ga}_{1-x}\text{As}$  layer ( $0.20 \leq x \leq 0.85$ ,  $p = 1 \times 10^{17}$ ), a 1.5- $\mu\text{m}$   $\text{Al}_{0.85}\text{Ga}_{0.15}\text{As}$  confining layer ( $p = 2 \times 10^{18}$ ), and a 0.2- $\mu\text{m}$  GaAs contact layer ( $p = 3 \times 10^{19}$ ). The use of such high aluminum composition confining layers ( $x = 0.85$ ) allows more heat to be generated in the device without a detrimental temperature rise at the active layer junction due to the high thermal conductivity of  $\text{Al}_x\text{Ga}_{1-x}\text{As}$  at higher values of  $x$ .<sup>13</sup> Broad area oxide-defined stripe geometry ( $w = 150 \mu\text{m}$ ) devices were fabricated using standard photolithographic and wet chemical etching techniques. Alloyed Ge/Au contacts were utilized on the n-side, and nonalloyed Ti/Pt/Au contacts were evaporated on the p-side. The facets of the devices utilized in this study were left uncoated. Diodes were mounted p-side down in indium solder on Cu blocks and wire bonded to contact the n-side ( $R_{\text{series}} = 0.9 \Omega$ ). Devices were tested under pulsed (1.5- $\mu\text{sec}$  pulse width/2.0 kHz repetition rate) and cw conditions at various operating temperatures ( $\geq 24^\circ\text{C}$ ) in a variable temperature test fixture. L-I curves were generated in order to determine broad area threshold current densities ( $J_{\text{th}}$ ) and differential quantum efficiencies, and single-ended output powers were measured using a calibrated silicon photodiode.

Figure 1 shows the emission spectra of a diode operated at 450 mA (pulsed) at fixture temperatures of both  $24^\circ$  and  $68^\circ\text{C}$  and at 700 mA (pulsed and cw) at a fixture temperature of  $24^\circ\text{C}$ . Typical diodes operated at cw output power levels up to 235 mW per uncoated facet. Comparison of the pulsed spectra at  $24^\circ\text{C}$  for currents of 450 and 700 mA reveals no observable shift in the peak emission wavelength (8,205  $\text{\AA}$ ) with increasing current, indicating no appreciable increase in the internal junction temperature under these low duty cycle pulsed conditions. The spectra of the same diode operated cw at 700 mA and a fixture temperature of  $24^\circ\text{C}$ , however, shows a red-shift of +120  $\text{\AA}$  to a peak emission wavelength of 8,325  $\text{\AA}$ . Diodes operated under pulsed conditions at 450 mA and a fixture temperature of  $68^\circ\text{C}$  also exhibit a peak wavelength of 8,325  $\text{\AA}$ , suggesting an internal junction temperature rise of approximately  $44^\circ\text{C}$  (to  $68^\circ\text{C}$ ) for the case of 700 mA cw operation.

These data illustrate some of the consequences of thermal energy generation in a GBQWH laser structure operated under high power cw conditions, as reflected in a rise in diode internal operating temperature and a corresponding red-shift in emission wavelength. Under pulsed operation at the low duty cycles (0.3%) and with the simple heat sinking employed in this study, it is evident that the small amount of heat generated in these GBQWH devices at high output power levels is easily dissipated such that associated increases in internal temperature or shifts in emission wavelength are undetectable. Under cw operation, however, the amount of heat generated can be significant, resulting in an apparent  $44^\circ\text{C}$  increase in diode junction temperature ( $\Delta E = 3 \text{ meV}$ ) as deduced from a measured increase in laser wavelength of 120  $\text{\AA}$  from 8,205  $\text{\AA}$  to 8,325  $\text{\AA}$ . Device heating at this level can result in accelerated material degradation and reduced cw operational lifetimes. The importance of incorporating structural features that facilitate heat dissipation in the design of GBQWH structures and the need to provide external mechanisms for efficient heat sinking are, therefore, demonstrated. It is imperative to address such issues when designing semiconductor laser diode

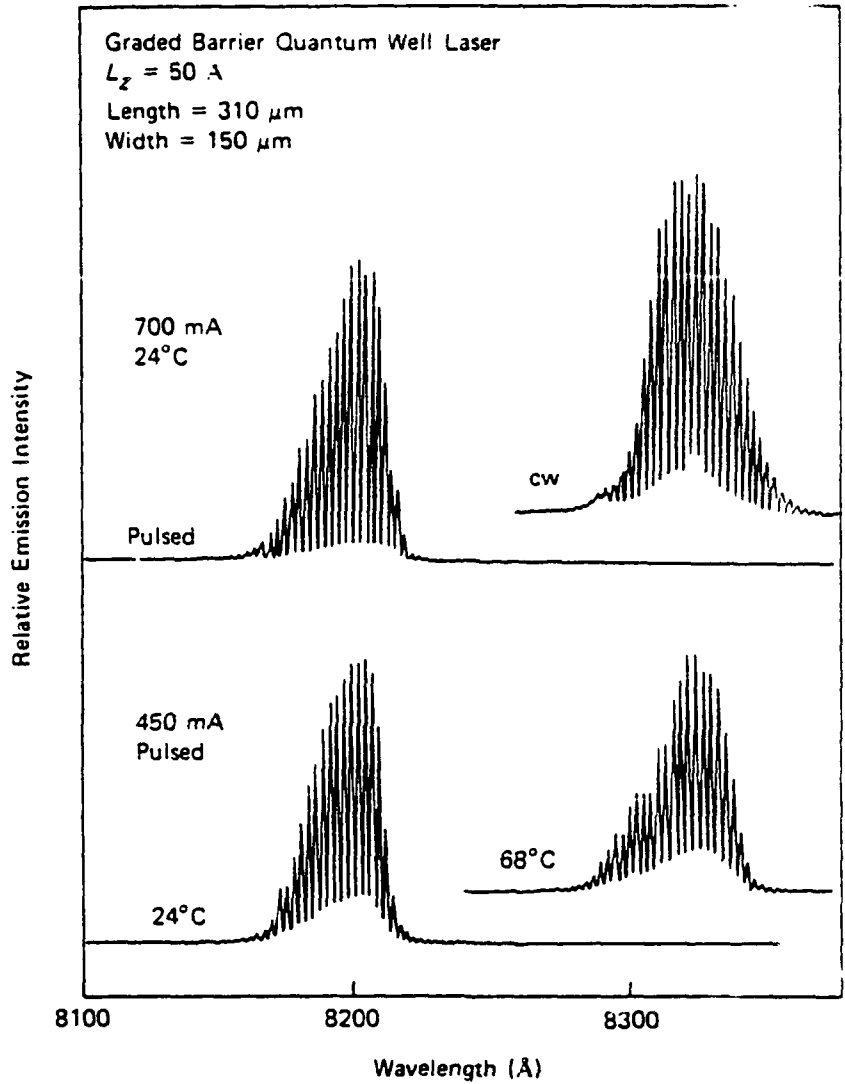


**Figure 1.** Laser spectra of a diode operated at 450 mA (pulsed) at temperatures of both 24°C and 68°C and at 700 mA (pulsed and cw) at 24°C. Comparison of the 24°C pulsed spectra at 450 and 700 mA indicates that there is no observable shift in the peak emission wavelength (8.205 Å). The spectra of the same diode operated cw at 700 mA, however, has red-shifted by 120 Å due to diode junction heating, yielding a peak wavelength of 8.325 Å.

systems intended for high power cw applications where stable emission wavelengths over a wide power range and long operational lifetimes are required.

### The Effect of Various Buffer Layer Structures

During the epitaxial growth process, defects present in the crystal substrate are inherited as climbing dislocations into subsequently deposited  $\text{Al}_x\text{Ga}_{1-x}\text{As}$  epilayers, especially those of higher Al composition<sup>14</sup> and propagate vertically through the growing layers, eventually emerging on the surface of the structure. These defects act as nonradiative recombination centers and contribute to optical field scattering, thereby raising the threshold current<sup>15</sup> if they propagate through the active layer of a device. When operated under high levels of current injection for prolonged periods, such defects may develop into larger defect networks, dark line defects, which act as localized sites of nonradiative recombination and result in localized heating.<sup>16</sup> Laser structures utilized in high power applications that possess such defects in high enough densities exhibit radically shortened operational lifetimes and decreased reliability due to thermally induced degradation and catastrophic failure. Typically, GaAs substrates are obtained from crystals grown by either the liquid-encapsulated Czochralski (LEC) or horizontal Bridgman (HB) technique. LEC substrates are available in larger diameter circular geometries, ideal for automated processing, making them preferable from a production standpoint. However, LEC crystals also tend to be of lower overall quality and possess much higher dislocation densities than the HB crystals currently available, rendering devices grown on LEC wafers susceptible to the difficulties described above.

In this section, the effect of various buffer layer structures on the material quality of high composition  $\text{Al}_x\text{Ga}_{1-x}\text{As}$  laser material grown by MOCVD, as reflected in the device characteristics of GBQWH lasers, is outlined. The previously described GBQWH structures having high composition ( $x \approx 0.85$ ) confining layers were grown simultaneously on both high quality HB and relatively lower quality LEC (100) GaAs:Si substrates at a temperature of 800°C. The four buffer layer structures studied consisted of 0.5  $\mu\text{m}$  GaAs plus: (1) no additional buffer structure (NOBUF), (2) a 0.5- $\mu\text{m}$  compositionally graded  $\text{Al}_x\text{Ga}_{1-x}\text{As}$  buffer (CGB) layer ( $0.0 \leq x \leq 0.85$ ), (3) a three-period superlattice buffer (3XSLB), each period consisting of 100 Å AlAs/100 Å GaAs, and (4) a 20-period superlattice buffer (20XSLB), each period consisting of 100 Å AlAs/100 Å GaAs. Following MOCVD growth, broad area oxide-defined stripe lasers with various cavity lengths were fabricated and broad area threshold current densities were taken from pulsed (2.0  $\mu\text{sec}$  pulse width/2.0 kHz repetition rate) L-I characteristics.

In Figure 2 the broad area threshold current density data for GBQW devices grown on HB substrates with each of the four types of buffer layers is plotted as a function of cavity length. As reported previously,<sup>5</sup> the type of prelayer has essentially no effect on  $J_{th}$  when HB substrates are utilized. In Figure 3,  $J_{th}$  versus cavity length data is plotted for the same structures grown simultaneously on LEC substrates. As for the HB case, the buffer layer type has little or no effect on the diode threshold current. In addition, these devices exhibited a mean  $J_{th} \approx 250$  A/cm<sup>2</sup>, which is the same as that of the HB-grown devices and indicative of high optical quality material. The similar thresholds exhibited for the two substrate

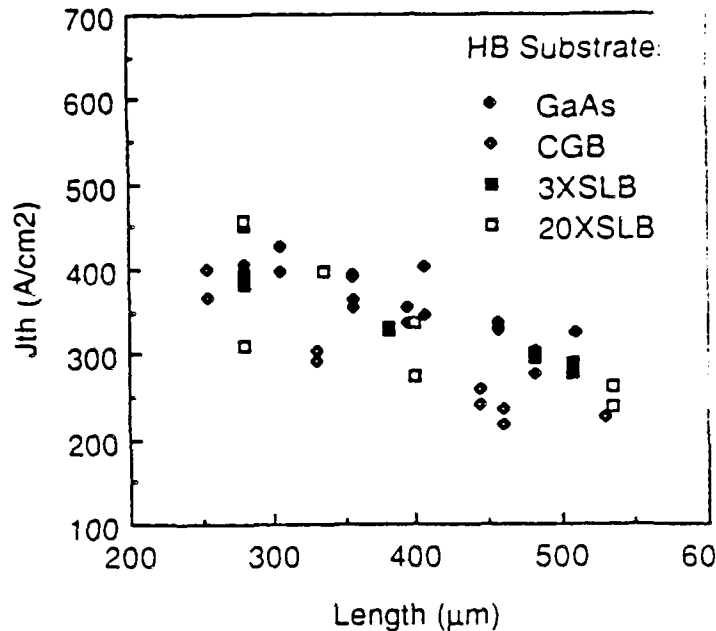
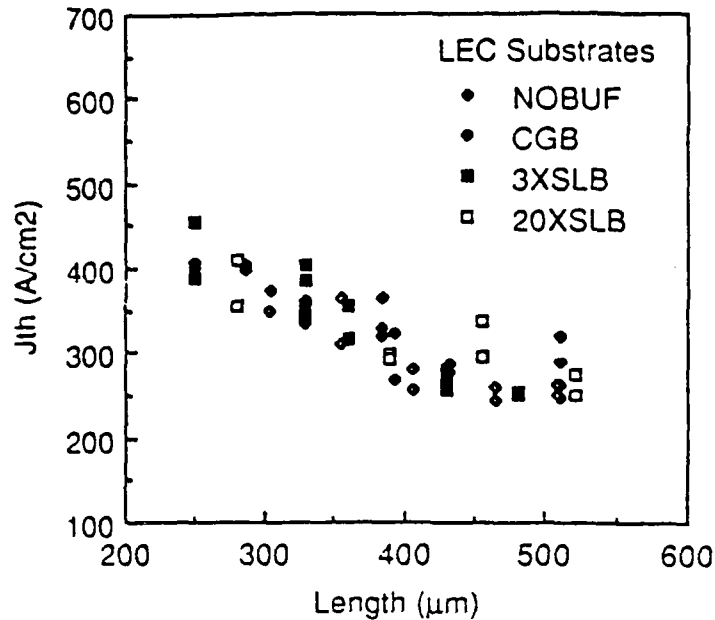


Figure 2. Broad area threshold current density ( $J_{th}$ ) as a function of cavity length for GBQW lasers grown on high quality/low dislocation density HB substrates with the various buffer layer structures indicated.

types was unexpected due to the fact that the as-grown GBQWH epilayer structures appeared visibly roughened and degraded for the LEC case, especially for those with NOBUF, when compared with the corresponding HB-grown structures, which were all smooth and specular, even under magnification. A related study<sup>17</sup> on the effect of these same buffer layers on the dislocation density of bulk high composition ( $x = 0.85$ ) epilayers also indicates a much higher defect density and lower overall crystal quality for those epitaxial structures grown on LEC substrates when the less sophisticated prelayers are utilized, whereas the proper choice of buffer layer can result in equivalently low etch pit densities (EPD) and smooth surface morphologies for both the LEC and HB cases. Laser device performance does not seem to be linked to EPD or surface morphology for these LEC-grown GBQWH structures, however, and all devices exhibit essentially the same threshold current, independent of the type of buffer layer and/or substrate utilized.

The results of this section can be summarized as follows. First, it has been observed that the threshold current density of GBQW laser structures grown by MOCVD on high quality/low dislocation density HB substrates is independent of the type of underlying buffer layer utilized. This is in contrast to previous reports<sup>18, 19</sup> in which the threshold current density of similar laser structures grown by MBE was highly dependent on the type of prelayer used. The introduction of a CGB<sup>18</sup> or SLB<sup>19</sup> was shown to result in at least a 50 percent reduction in  $J_{th}$  for these MBE-grown devices. No such reduction is noted for the MOCVD-grown devices



**Figure 3.** Broad area threshold current density ( $J_{th}$ ) as a function of cavity length for GBQW lasers grown on low quality/high dislocation density LEC substrates during the same growth run as the devices characterized by Figure 2. Note that the threshold current of these lasers is not only independent of the type of buffer layer utilized but is also as low as that of devices grown on HB substrates (Fig. 2) for all prelayer types.

in this study, a fact attributed to basic differences between the MBE and MOCVD growth processes.<sup>17</sup>

It has also been shown that the pulsed threshold current density of GBQWH lasers grown by MOCVD is independent of not only the type of underlying buffer layer but also the type (HB or LEC) and dislocation density of the substrate used. This indicates that laser structures grown by MOCVD exhibit a relative insensitivity to material defect density as compared to that exhibited by structures grown by MBE. From a pragmatic standpoint, it has been demonstrated that MOCVD can be utilized to grow high quality GBQWH lasers on commercially desirable LEC substrates having characteristics comparable to identical structures grown on HB substrates. Such devices are suitable for high power applications requiring low threshold current operation and minimal dependence of device characteristics on bulk material dislocation density.

### Typical High Power Laser Results

Higher output power levels can be obtained from laser diodes operated under pulsed conditions than from diodes operated cw for low duty cycle and low pulse frequency conditions. It has been shown<sup>20</sup> that the maximum peak output power for pulsed operation increases inversely as the square root of the pulse width for pulse durations shorter than a few microseconds. For longer pulse widths, the

maximum pulsed output power asymptotically approaches the cw value. In this section, typical data on the high current pulsed response of broad area GBQWH laser devices are presented and correlated with various structural parameters. These GBQWH structures were essentially identical to the structures described earlier, except they possessed single quantum well active layers with either  $L_z = 30 \text{ \AA}$  or  $L_z = 50 \text{ \AA}$  and  $\text{Al}_x\text{Ga}_{1-x}\text{As}$  confining layers with aluminum compositions of either  $x = 0.60$  or  $x = 0.85$ . The dependence of both output power at a given reference current and single-ended output power at the point of catastrophic degradation on these device parameters is also noted.

Broad area ( $w = 150 \text{ }\mu\text{m}$ ) oxide-defined stripe lasers were operated under pulsed (6.0  $\mu\text{sec}$  pulse width/2.0 kHz repetition rate) conditions and driven by high injection currents (2–3 A). The average single-ended output power measured from structures having  $x = 0.60$  confining layers and a 50- $\text{\AA}$  quantum well was 350 mW per uncoated facet at a drive current of 2.2 A. Catastrophic optical degradation of the facets typically occurred at an output of 385 mW per facet. After being driven to the point of mirror degradation, devices still operated, albeit with output power levels reduced by a factor of two at any given injection current. Structures having  $x = 0.60$  confining layers but a 30- $\text{\AA}$  quantum well yielded an average output power of 335 mW per facet for a 2.2 A pulsed drive current, with catastrophic mirror degradation again occurring at 385 mW per facet. The small reduction ( $\approx 4\%$ ) seen in output power at a given current level is a result of the small increase in device threshold current density associated with the smaller well size utilized, 30  $\text{\AA}$  as compared to 50  $\text{\AA}$ , which slightly reduces the carrier collection efficiency of the GBQWH structure.<sup>21</sup>

Improved high power broad area characteristics were obtained by increasing the aluminum mole fraction in the confining layers to  $x = 0.85$ . These devices, which also had 50- $\text{\AA}$  quantum wells, exhibited extremely low threshold current densities ( $J_{th} \leq 200 \text{ A/cm}^2$ ) and external differential quantum efficiencies of 45 percent. The exponential temperature dependence of the threshold current density ( $T_0$ ) was 150 K, measured up to an operating temperature of 80°C. These devices exhibited output powers of 430 mW per facet at a pulsed drive current of 1.5 A and up to 585 mW per facet at 2.2 A. Gradual degradation of the facets began to occur, however, at output powers above 500 mW per facet. The significant increase realized in output power for these GBQWH structures results from the incorporation of such high aluminum composition confining layers, which yields increased optical and carrier confinement in the GBQWH active region, thereby reducing the threshold current density and increasing the differential quantum efficiency of the devices. These high power data for the various GBQW structures are summarized in Table 1.

**Table 1.**  
Summary of High Power Uncoated Laser Data for Various Combinations of  
Quantum Well Width and  $\text{Al}_x\text{Ga}_{1-x}\text{As}$  Confining Layer Composition

$\text{Al}_x\text{Ga}_{1-x}\text{As}$ Confining Layer Composition	Quantum Well Width	Peak Power (mW/facet @ 2.2 A)	Power @ Catastrophic Optical Degradation (mW/facet)
$x = 0.60$	50 $\text{\AA}$	350	>385
$x = 0.60$	30 $\text{\AA}$	330	>385
$x = 0.85$	50 $\text{\AA}$	585	>500

## Conclusions

In this article, we considered various performance aspects and design issues underlying the operation of broad area graded barrier quantum well heterostructure lasers grown by metalorganic chemical vapor deposition. We examined thermally induced red-shifts in the peak emission wavelength of wide stripe broad area GBQWH devices as a function of cw output power. Comparison of laser emission spectra for both pulsed and cw operation of devices at various output power levels and ambient temperatures allowed an estimate to be made of the average internal operating temperature of the laser diode active region. We have also demonstrated that the device characteristics of GBQWH lasers grown by MOCVD are independent of not only the type of underlying buffer layer but also the type (HB or LEC) and dislocation density of the substrate used. This indicates a relative insensitivity of device performance to material defect density for structures grown by MOCVD as compared to those grown by MBE. We have also fabricated and tested single stripe broad area devices that exhibit peak output powers of up to 585 mW per uncoated facet under pulsed operation. The output power at a given drive current and the peak power at the point of catastrophic optical degradation have been shown to depend on the details of the GBQWH structural design. Optimization of the quantum well active layer thickness and  $\text{Al}_x\text{Ga}_{1-x}\text{As}$  confining layer composition resulted in increased output power levels due to the minimized threshold current density and increased power conversion efficiency realized for these devices.

## Acknowledgments

The authors would like to gratefully acknowledge L. J. Mawst and M. A. Emanuel for historical purposes, and L. M. Miller and Y. S. Moroz for helpful discussions and technical support. This work was supported in part by the National Science Foundation (DMR 83-16981 and CDR 85-22666), the McDonnell Douglas Corporation, the U.S. Naval Research Laboratory (N00014-88-K-2005), and the U.S. Army Night Vision and Electro-Optics Laboratory (DAAK 20-84-K-0225).

## References

1. W. T. Tsang, "A graded-index waveguide separate-confinement laser with very low threshold and a narrow Gaussian beam," *Appl. Phys. Lett.*, **39**, 134 (1981).
2. L. J. Mawst, M. E. Givens, C. A. Zmudzinski, M. A. Emanuel, and J. J. Coleman, "Optimization and characterization of index-guided visible  $\text{Al}_x\text{Ga}_{1-x}\text{As}/\text{GaAs}$  graded barrier quantum well laser diodes," *J. Quantum Electron.*, **QE-23**, 696 (1987).
3. W. T. Tsang, "Extremely low threshold  $\text{Al}_x\text{Ga}_{1-x}\text{As}$  graded-index waveguide separate-confinement heterostructure lasers grown by molecular beam epitaxy," *Appl. Phys. Lett.*, **40**, 217 (1982).
4. L. J. Mawst, M. E. Givens, C. A. Zmudzinski, M. A. Emanuel, and J. J. Coleman, "Complementary self-aligned laser arrays by metalorganic chemical vapor deposition," *J. Appl. Phys.*, **60**, 2633 (1986).
5. M. E. Givens, L. J. Mawst, C. A. Zmudzinski, M. A. Emanuel, and J. J. Coleman, "Effect of compositionally graded and superlattice buffer layers on the device performance of graded barrier quantum well heterostructure laser diodes," *Appl. Phys. Lett.*, **50**, 301 (1987).
6. M. Sakamoto and Y. Kato, "High power (710 mW cw) single-lobe operation of broad area  $\text{Al}_x\text{Ga}_{1-x}\text{As}$  double heterostructure lasers grown by metalorganic chemical vapor deposition," *Appl. Phys. Lett.*, **50**, 869 (1987).

7. C. H. Henry, P. M. Petroff, R. A. Logan, and F. R. Merritt. "Catastrophic damage of  $\text{Al}_x\text{Ga}_{1-x}\text{As}$  double-heterostructure laser material." *J. Appl. Phys.*, **50**, 3721 (1979).
8. J. J. Coleman and P. D. Dapkus. "Metalorganic chemical vapor deposition." *Gallium Arsenide Technology*, D. K. Ferry, (Howard W. Sams and Co., Indianapolis), p. 79 (1985).
9. R. F. Broom. "Transient temperature distribution in diode lasers and the time duration of the output pulse at 300 K." *IEEE J. Quantum Electron.*, **QE-4**, 135 (1968).
10. C. H. Gooch. "The thermal properties of gallium arsenide laser structures." *IEEE J. Quantum Electron.*, **QE-4**, 140 (1968).
11. T. L. Paoli. "A new technique for measuring the thermal impedance of junction lasers." *IEEE J. Quantum Electron.*, **QE-11**, 498 (1975).
12. G. Costrini and J. J. Coleman. "Conditions for uniform growth of GaAs by metalorganic chemical vapor deposition in a vertical reactor." *J. Appl. Phys.*, **57**, 2249 (1985).
13. M. A. Afromowitz. "Thermal conductivity of  $\text{Ga}_{1-x}\text{Al}_x\text{As}$  alloys." *J. Appl. Phys.*, **44**, 1292 (1973).
14. M. Shinohara, T. Ito, and Y. Imamura. "Generation and propagation of defects into molecular beam epitaxially grown GaAs from an underlying GaAs substrate." *J. Appl. Phys.*, **58**, 3449 (1985).
15. C. H. Henry and D. V. Lang. "Nonradiative capture and recombination by multiphonon emission in GaAs and GaP." *Phys. Rev. B*, **15**, 989 (1977).
16. B. C. De Loach, Jr., B. W. Hakki, R. L. Hartman, and L. A. D'Asaro. "Degradation of cw GaAs double-heterostructure lasers at 300 K." *Proc. IEEE*, **61**, 1042 (1973).
17. M. E. Givens, J. J. Coleman, C. A. Zmudzinski, R. P. Bryan, M. A. Emanuel, and L. M. Miller. "The effect of various buffer layer structures on the material quality and dislocation density of high composition  $\text{Al}_x\text{Ga}_{1-x}\text{As}$  laser material grown by metalorganic chemical vapor deposition." *J. Appl. Phys.*, **63**, 5092 (1988).
18. T. Hayakawa, T. Suyama, M. Kondo, T. Takahashi, S. Yamamoto, and T. Hijikata. "Improvements in  $\text{Al}_x\text{Ga}_{1-x}\text{As}$  laser diodes grown by molecular beam epitaxy using a compositionally graded buffer layer." *Appl. Phys. Lett.*, **49**, 191 (1986).
19. O. Wada, T. Sanada, M. Kuno, and T. Fujii. "Very low threshold current ridge-waveguide  $\text{Al}_x\text{Ga}_{1-x}\text{As}/\text{GaAs}$  single-quantum-well lasers." *Electron. Lett.*, **21**, 1025 (1985).
20. H. Imai, M. Morimoto, H. Sudo, T. Fujiwara, and M. Takusagawa. "Catastrophic degradation of  $\text{Ga}_{1-x}\text{Al}_x\text{As}$  DH laser diodes." *Appl. Phys. Lett.*, **33**, 1011 (1978).
21. P. Blood, E. D. Fletcher, K. Woodbridge, and P. J. Hulyer. "Short wavelength (visible) quantum well lasers grown by molecular beam epitaxy." *Physica B*, **129**, 465 (1985).

# Nonplanar quantum well heterostructure window laser

R. P. Bryan, L. M. Miller, T. M. Cockerill, and J. J. Coleman

Compound Semiconductor Microelectronics Laboratory and W. L. Everitt Laboratory, University of Illinois at Urbana-Champaign, 1406 West Green Street, Urbana, Illinois 61801

(Received 14 December 1988; accepted for publication 13 February 1989)

Data are presented on a nonplanar graded barrier quantum well heterostructure window laser formed by a single metalorganic chemical vapor deposition (MOCVD) growth. By utilizing a selectively etched substrate, a transparent window region is formed in the vicinity of the facets thereby relaxing the maximum power limit imposed by catastrophic optical degradation. The ultimate output power available from such devices is approximately 50% higher than from devices with the same structure but grown on unetched substrates. The processing required for device fabrication is minimized by taking advantage of the properties of MOCVD growth on nonplanar substrates.

Many of the degradation mechanisms of semiconductor lasers may be attributed to the presence of the active layer at the mirror facets.<sup>1,2</sup> During high-power operation optical absorption in the active region near the facets, which is enhanced by a high surface recombination velocity, leads to local heating in the region and may result in catastrophic optical degradation (COD). Furthermore, at lower intensity levels augmented generation of defects and facet oxidation degrade device performance. These degradation mechanisms may be eliminated or reduced by incorporating a nonabsorbing region between the active region and the mirror facets. The window region<sup>1</sup> reduces the local heating at the facets and decreases the optical intensity at a given output power by broadening the beam. Previously reported schemes<sup>3-9</sup> to produce window lasers require sophisticated fabrication processes or multiple growth steps. The diffused window stripe laser<sup>3-5</sup> requires precise control over its diffusion, the crank transverse junction stripe (TJS) laser<sup>6</sup> requires sophisticated selective etching, the V-channeled substrate inner stripe (VSIS) laser<sup>7</sup> and the large optical cavity buried heterostructure (LOC-BH) window laser<sup>8,9</sup> require two growth steps. Such complexities of the fabrication procedure reduce the laser yield, lower the device reliability, and limit the device structure.

In this letter we report the growth and fabrication of a simple nonplanar quantum well heterostructure window laser. In order to produce a nonabsorbing region in the vicinity of the facets at the active region, long mesas are etched in the substrate prior to growth. As a result of uniform<sup>10-12</sup> metalorganic chemical vapor deposition (MOCVD) growth over nonplanar surfaces, the active region is displaced toward the surface in the vicinity of the facets. Consequently, the optical field traverses the higher band-gap nonabsorbing confining layer in the vicinity of the mirror facets. Since the window region is a result of the nonplanar substrate, the type of laser structure grown is not restricted nor are sophisticated fabrication techniques or multiple growth steps required as in previously described window lasers. Data are presented on the light-current characteristics of devices with and without window regions which demonstrate a nearly 50% increase in the maximum output power. Near-field and far-field radiation patterns perpendicular to the junction which are pre-

sented clearly show a broadening of the optical field due to the window region.

GaAs:Si (100) substrates were prepared prior to epitaxial growth by delineating narrow mesa stripes (25  $\mu\text{m}$  wide and 510  $\mu\text{m}$  apart) with standard photolithography and wet chemical etching (1:8:30  $\text{H}_2\text{SO}_4\text{:H}_2\text{O}_2\text{:H}_2\text{O}$ ). The mesas, after growth, define the window region of the lasers. A graded barrier quantum well (GBQW) heterostructure laser<sup>13,14</sup> was grown in an atmospheric pressure MOCVD reactor<sup>15,16</sup> at a temperature of 800 °C. The laser structure consists of a 0.25  $\mu\text{m}$  GaAs:*n* buffer layer, a 0.5  $\mu\text{m}$  linearly graded ( $0.0 \leq x \leq 0.85$ )  $\text{Al}_x\text{Ga}_{1-x}\text{As}$ :*n* buffer layer, a 1.0  $\mu\text{m}$   $\text{Al}_{0.85}\text{Ga}_{0.15}\text{As}$ :*n* confining layer, a 1200 Å parabolically graded ( $0.85 \geq x \geq 0.20$ )  $\text{Al}_x\text{Ga}_{1-x}\text{As}$ :*n* layer, a 50 Å GaAs:*n* quantum well, a 1200 Å parabolically graded ( $0.20 \leq x \leq 0.85$ )  $\text{Al}_x\text{Ga}_{1-x}\text{As}$ :*p* layer, a 1.0  $\mu\text{m}$   $\text{Al}_{0.85}\text{Ga}_{0.15}\text{As}$ :*p* confining layer, and a 0.2  $\mu\text{m}$  GaAs:*p*<sup>+</sup> contact layer. The MOCVD growth is highly uniform<sup>10-12</sup> over the nonplanar substrate such that the substrate contours are maintained in the laser structure as illustrated in Fig. 1, which is a schematic cross section of the laser structure in the vicinity of the mirror facets. A planar substrate was loaded into the MOCVD reactor along with the etched substrate in order to directly compare the characteristics of

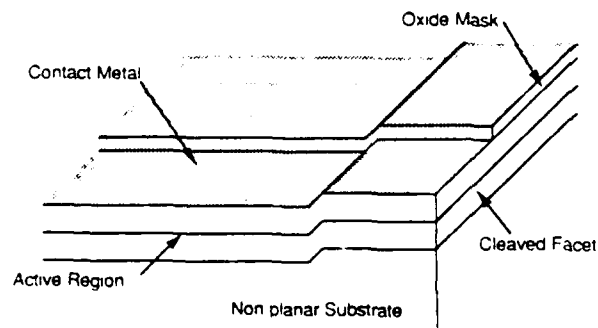


FIG. 1. Schematic of a nonplanar GBQW window laser grown by MOCVD on an etched substrate. The MOCVD growth follows the contours of the substrate resulting in a nonplanar active region and a nonabsorbing window region formed from the  $\text{Al}_{0.85}\text{Ga}_{0.15}\text{As}$  confining layer between the active region and the mirror facet.

the two structures. Following MOCVD growth, wide ( $w = 150 \mu\text{m}$ ) and narrow ( $w = 8 \mu\text{m}$ ) oxide-defined stripe lasers were fabricated. Alloyed Ge/Au contacts were formed on the back of the substrate and nonalloyed Cr/Au contacts were formed on top of the structure. The window lasers were formed by cleaving bars along the length of the mesas and then scribing the bars into individual devices, thereby producing a device with a  $510\text{-}\mu\text{m}$ -long laser cavity and a  $0.6 \mu\text{m}$  step to a  $\sim 12 \mu\text{m}$  window region. The facets of the devices utilized in this study were left uncoated. No sophisticated fabrication processes or multiple growth steps were required to form the window region. Devices were tested under pulsed conditions (300 ns pulses, 1 kHz repetition rate). Output power was measured using a calibrated silicon photodiode and the near- and far-field radiation patterns were measured using a silicon photodiode array.

Figure 2 shows the light output power versus pulsed current curves for a wide stripe window laser and a conventional wide stripe laser both with a cavity length of  $510 \mu\text{m}$ . The window stripe lasers emitted up to  $1244 \text{ mW}$  per uncoated facet whereas the conventional wide stripe lasers failed due to COD at  $842 \text{ mW}$ . Narrow stripe window lasers ( $I_{\text{th}} = 140 \text{ mA}$ ) emitted  $393 \text{ mW}$  per uncoated facet compared to  $280 \text{ mW}$  per facet from conventional narrow stripe lasers ( $I_{\text{th}} = 75 \text{ mA}$ ). Near-field and far-field radiation patterns perpendicular to the junction at  $1.75 I_{\text{th}}$  of a narrow stripe window laser and a conventional narrow stripe laser are shown in Figs. 3 and 4, respectively. The optical field has broadened in the window region as indicated by the wider near-field full width at half maximum (FWHM) ( $1.2 \mu\text{m}$ ) and narrower far-field FWHM ( $25^\circ$ ) of the window laser compared with the near-field FWHM ( $0.8 \mu\text{m}$ ) and far-field FWHM ( $35^\circ$ ) of the conventional laser. The mesa step separates the GBQW layer in the window region from the GBQW layer in the light-emitting region by  $0.6 \mu\text{m}$ . Based on calculations of the optical field in the light-emitting region, the optical intensity is reduced by more than four orders of magnitude across the  $0.6 \mu\text{m}$  from its peak value in the active region. We have also experimentally observed that the majority of the light from the window lasers is emitted

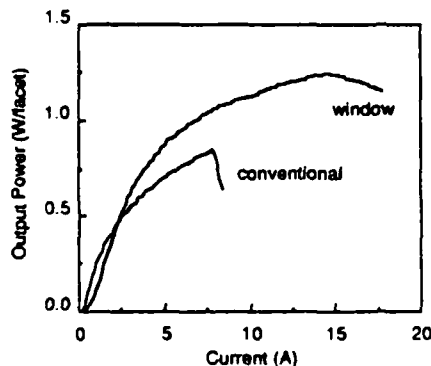


FIG. 2. Light output power vs pulsed current characteristics from a wide stripe ( $150 \mu\text{m}$ ) uncoated facet of a window laser compared to that of a conventional laser both with a cavity length of  $510 \mu\text{m}$ . The maximum output power from the window laser is nearly 50% greater than the maximum output power from the conventional laser.

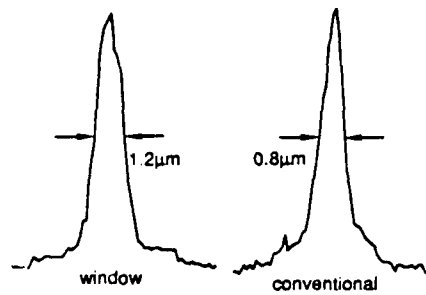


FIG. 3. Near-field radiation pattern perpendicular to the junction at  $1.75 I_{\text{th}}$  from a narrow stripe ( $8 \mu\text{m}$ ) uncoated facet of a window laser compared to that of a conventional laser both with a cavity length of  $510 \mu\text{m}$ . The FWHM of the window laser is  $1.2 \mu\text{m}$  whereas the FWHM of the conventional laser is  $0.8 \mu\text{m}$ . The data indicate that the optical field broadens in the window region.

from the lower confining layer of the window region. Consequently, we propose that the majority of the optical field propagates in the lower confining layer as an unguided mode in the window region (although some of the mode would couple into the waveguide formed by the GBQW layer in the window region but the coupling would be poor). The absence of an optical waveguide leads to incomplete coupling between the optical field in the window region and the optical field in the light-emitting region. To account for the incomplete coupling of the fields we have incorporated coupling coefficients in an expression for the threshold current ( $I_{\text{th}}$ )<sup>17</sup>:

$$I_{\text{th}} = \frac{w}{\beta} \left( \alpha L + \frac{1}{2} \ln \frac{1}{R_1 C_1 R_2 C_2} \right), \quad (1)$$

where  $w$  is the width of the stripe,  $\beta$  is the differential gain coefficient,  $\alpha$  is the loss coefficient,  $L$  is the length of the device,  $R_{1,2}$  are the mirror reflectivities, and  $C_{1,2}$  are the coupling coefficients. By comparing threshold current data of devices with and without window regions we have calculated the coupling coefficient as 0.4. A limited coupling coefficient is expected with the narrow active region of GBQW lasers.

In conclusion, nonplanar GBQW window lasers have

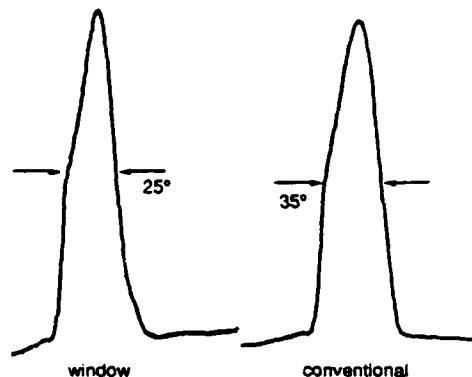


FIG. 4. Far-field radiation pattern perpendicular to the junction at  $1.75 I_{\text{th}}$  from a narrow stripe ( $8 \mu\text{m}$ ) uncoated facet of a window laser compared to that of a conventional laser both with a cavity length of  $510 \mu\text{m}$ . The FWHM of the window laser is  $25^\circ$  whereas the FWHM of the conventional laser is  $35^\circ$ .

been fabricated with standard photolithography and wet chemical etching by using the advantageous property of uniform MOCVD growth on nonplanar substrates. Since the window region is formed as a consequence of the nonplanar substrate nearly any structure may be utilized as the laser structure. A 50% improvement in the maximum output power is achieved from the nonplanar window lasers compared with conventional planar lasers. Improved coupling, a smaller increase in the threshold current, and better quantum efficiencies while still limiting COD may be realized by forming only one window region and applying a high-reflectivity coating on the opposite facet.

The authors gratefully acknowledge valuable discussions with C. A. Zmudzinski and M. E. Givens. This work has been supported in part by the National Science Foundation Engineering Research Center for Compound Semiconductor Microelectronics (CDR 82-22666), the Naval Research Laboratory (N00014-88-K-2005), and SDIO/IST (DAAL03-87-K-0013).

<sup>1</sup>D. P. Cooper, C. H. Gooch, and R. J. Sherwell, *IEEE J. Quantum Electron.* **QE-2**, 329 (1966).

- <sup>2</sup>C. H. Henry, P. M. Petroff, R. A. Logan, and F. R. Merritt, *J. Appl. Phys.* **50**, 3721 (1979).
- <sup>3</sup>H. Yonzeu, M. Ueno, T. Kamejima, and I. Hayashi, *IEEE J. Quantum Electron.* **QE-15**, 775 (1979).
- <sup>4</sup>Y. Suzuki, Y. Horikoshi, M. Kobayashi, and H. Okamoto, *Electron. Lett.* **20**, 383 (1984).
- <sup>5</sup>R. L. Thornton, D. F. Welch, R. D. Burnham, T. L. Paoli, and P. S. Cross, *Appl. Phys. Lett.* **49**, 1572 (1986).
- <sup>6</sup>H. Kumabe, T. Tanaka, S. Nita, Y. Seiwa, T. Sogo, and S. Takamiya, *Jpn. J. Appl. Phys.* **21**, 347 (1982).
- <sup>7</sup>S. Yamamoto, H. Hayashi, T. Hayakawa, N. Miyauchi, S. Yano, and T. Hijikata, *Appl. Phys. Lett.* **42**, 406 (1983).
- <sup>8</sup>H. Blauvelt, S. Margalit, and A. Yariv, *Appl. Phys. Lett.* **40**, 1029 (1982).
- <sup>9</sup>J. Ungar, N. Bar-Chaim, and I. Ury, *Electron. Lett.* **22**, 279 (1986).
- <sup>10</sup>C. A. Zmudzinski, M. E. Givens, R. P. Bryan, and J. J. Coleman, *Appl. Phys. Lett.* **53**, 350 (1988).
- <sup>11</sup>M. E. Givens, C. A. Zmudzinski, R. P. Bryan, and J. J. Coleman, *Appl. Phys. Lett.* **53**, 1159 (1988).
- <sup>12</sup>K. M. Dzurko, E. P. Menu, C. A. Beyler, J. S. Osinski, and P. D. Dapkus, *Appl. Phys. Lett.* **54**, 105 (1989).
- <sup>13</sup>W. T. Tsang, *Appl. Phys. Lett.* **39**, 134 (1981).
- <sup>14</sup>L. J. Mawst, M. E. Givens, C. A. Zmudzinski, M. A. Emanuel, and J. J. Coleman, *IEEE J. Quantum Electron.* **QE-23**, 696 (1987).
- <sup>15</sup>L. M. Miller and J. J. Coleman, *CRC Crit. Rev. Solid State Mater. Sci.* **15**, 1 (1988).
- <sup>16</sup>G. Costrini and J. J. Coleman, *J. Appl. Phys.* **57**, 2249 (1985).
- <sup>17</sup>H. Kressel and J. K. Butler, *Semiconductor Lasers and Heterostructure LED's* (Academic, New York, 1977), p. 269.

# Optical Characteristics of High-Power Nonplanar Periodic Laser Arrays

CHARLES A. ZMUDZINSKI, STUDENT MEMBER, IEEE, MICHAEL E. GIVENS, ROBERT P. BRYAN, AND JAMES J. COLEMAN, SENIOR MEMBER, IEEE

**Abstract**—Optical characteristics of high-power nonplanar periodic laser arrays are presented and analyzed. The nonplanar arrays, grown by metalorganic chemical vapor deposition, consist of a periodic array of mesas and grooves, which provides index guiding and prevents lateral lasing. The near- and far-field patterns are shown to be a strong function of the laser structure, particularly of the confining layer composition and effective index step. The near-field pattern determined by the structure affects the external differential quantum efficiency of these arrays relative to similar planar active region devices. Laser emission was generally confined to the mesa regions. A simple model is used as an aid to explain the observed near- and far-field patterns and to identify the mechanisms which confine the optical field to the mesa or groove region.

## I. INTRODUCTION

MULTIPLE-stripe laser arrays have proven to be a most promising source of high-power emission from semiconductor materials which are suitable for such applications as pumping solid-state Nd:YAG lasers [1]. Lateral lasing and amplified spontaneous emission in wide laser arrays can be suppressed by etching deep grooves at periodic intervals [2], [3] or by forming a nonplanar active region by metalorganic chemical vapor deposition (MOCVD) on an etched GaAs substrate [4], [5]. Either technique allows very wide lasers to be fabricated which emit over essentially the entire width of the facet. For nonplanar periodic laser arrays, the sharp bends in the active region provide large scattering losses for the lateral cavity modes, with no extra processing required to prevent lateral lasing. The purpose of this paper is to describe the characteristics of high-power nonplanar corrugated substrate laser arrays grown by MOCVD on etched GaAs substrates. An advantage of using MOCVD for the growth of these lasers is that the growth over the etched substrate follows the contour of the substrate more closely than with other growth methods [4]–[6].

In this paper, we discuss the fabrication, optical characteristics, and design considerations of nonplanar index-guided quantum well heterostructure periodic laser arrays which are suitable for high-power applications requiring

optical power in excess of 10 W. In particular, we discuss the effects of fabrication parameters such as confining layer aluminum composition, active region structure, and the width of mesas and grooves on the threshold current, efficiency, and near- and far-field patterns of the laser array. We have experimentally observed a strong dependence of the near- and far-field patterns on the confining layer composition  $x_i$  of graded barrier quantum well heterostructure (GBQWH) [7], [8] periodic laser arrays, which in turn affects the external differential quantum efficiency of the laser arrays. In Section II, the fabrication process for the periodic laser arrays is described. Experimental results for lasers with various structures will be presented in Section III. In Section IV, a discussion of the experimental data is presented, and the results of this paper are summarized in Section V.

## II. LASER FABRICATION

The fabrication of nonplanar periodic laser arrays has been described previously [4], [5]. The resulting structure is shown in Fig. 1. The important features of the structure are the nonplanar active region with a series of grooves and mesas and a bent region connecting the grooves and mesas, which serves to provide index guiding and prevent lateral lasing and amplified spontaneous emission [4], [5]. Epitaxial growth was performed in an atmospheric pressure MOCVD reactor described previously [9]. Three different  $\text{Al}_i\text{Ga}_{1-i}\text{As}/\text{GaAs}$  GBQWH [7], [8] laser wafers were prepared on etched GaAs substrates for this study. All three structures consist of a  $0.25\ \mu\text{m}$  GaAs buffer layer ( $n = 1 \times 10^{18}$ ), a  $0.5\ \mu\text{m}$  linearly graded  $\text{Al}_i\text{Ga}_{1-i}\text{As}$  buffer layer ( $0.0 \leq x \leq x_i$ ,  $n = 1 \times 10^{18}$ ), a  $1.0\ \mu\text{m}$   $\text{Al}_i\text{Ga}_{1-i}\text{As}$  confining layer ( $n = 1 \times 10^{18}$ ,  $x = x_i$ ), a  $1200\ \text{\AA}$  parabolically graded  $\text{Al}_i\text{Ga}_{1-i}\text{As}$  layer ( $x_i \geq x \geq 0.20$ ,  $n = 5 \times 10^{16}$ ), a  $50\ \text{\AA}$  GaAs single quantum well (undoped), a  $1200\ \text{\AA}$  parabolically graded  $\text{Al}_i\text{Ga}_{1-i}\text{As}$  layer ( $0.20 \leq x \leq x_i$ ,  $p = 1 \times 10^{17}$ ), a  $1.0\ \mu\text{m}$   $\text{Al}_i\text{Ga}_{1-i}\text{As}$  confining layer ( $p = 2 \times 10^{18}$ ,  $x = x_i$ ), and a  $0.2\ \mu\text{m}$  GaAs contact layer ( $p = 3 \times 10^{19}$ ). The first two wafers, one with  $x_i = 0.85$  and one with  $x_i = 0.40$ , labeled wafer I and wafer II, respectively, were grown, with a mesa width of approximately  $3.6\ \mu\text{m}$ , a groove width of about  $3.2\ \mu\text{m}$ , and a bent region width of approximately  $0.6\ \mu\text{m}$ , resulting in a center-to-center spacing between adjacent mesas or grooves of  $8\ \mu\text{m}$ . Wafer III has the same structure as wafer I, except the

Manuscript received October 6, 1988; revised January 18, 1989. This work was supported in part by the National Science Foundation Engineering Research Center for Compound Semiconductor Microelectronics under Grant CDR 82 22666 and in part by the Naval Research Laboratory under Contract N00014-88-K 2005.

The authors are with the Compound Semiconductor Microelectronics Laboratory, University of Illinois at Urbana-Champaign, Urbana, IL 61801. IEEE Log Number 8927326.

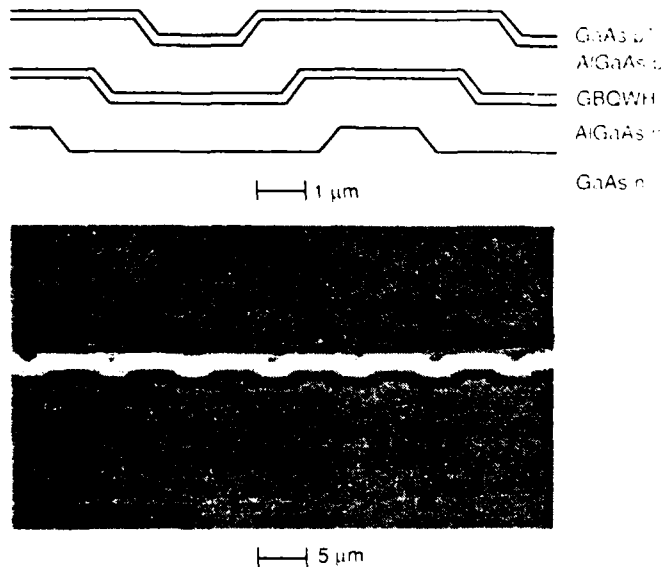


Fig. 1. Schematic and scanning electron micrograph of a nonplanar array fabricated from wafer I. The array of mesas and grooves, along with the bent region, forms an index-guided structure which prevents lateral lasing.

TABLE I  
STRUCTURE OF THE THREE WAFERS IN THIS STUDY, THRESHOLD CURRENT DENSITIES OF NONPLANAR LASERS FROM EACH WAFER, AND DIFFERENTIAL QUANTUM EFFICIENCIES OF NONPLANAR LASERS, AND BROAD-AREA PLANAR LASERS FROM EACH WAFER

Wafer No.	Structure	$J_{th}$ ( $l = 508 \mu\text{m}$ )	Efficiency (non-planar/planar)
I	$x_c = 0.85$	158 A/cm <sup>2</sup>	31 % / 55 %
	GBQWH		
	$w_{\text{mesa}} = 3.6 \mu\text{m}$ $w_{\text{groove}} = 3.2 \mu\text{m}$		
II	$x_c = 0.40$	557 A/cm <sup>2</sup>	29 % / 44 %
	GBQWH		
	$w_{\text{mesa}} = 3.6 \mu\text{m}$ $w_{\text{groove}} = 3.2 \mu\text{m}$		
III	$x_c = 0.85$	223 A/cm <sup>2</sup>	21 % / 43 %
	GBQWH		
	$w_{\text{mesa}} = 2.8 \mu\text{m}$ $w_{\text{groove}} = 3.9 \mu\text{m}$		

width of the mesa is  $2.8 \mu\text{m}$ , smaller than the width of the groove, which is  $3.9 \mu\text{m}$ . The center-to-center spacing was kept at  $8 \mu\text{m}$ . Table I summarizes the structure of each of the three wafers and includes some experimental results, which will be discussed in the following sections. Device wafers were mechanically thinned and polished, and ohmic contacts were deposited on the p- and n-sides of the wafer. The samples were then cleaved into bars of various lengths, which were diced into individual diode arrays of various widths. The entire width of the laser bar is pumped. The facets of the devices utilized in this study were left uncoated. For comparison, broad-area  $150 \mu\text{m}$  wide oxide stripe lasers were fabricated and tested from

unetched planar wafers grown with each of the etched wafers.

### III. EXPERIMENTAL RESULTS

In this section, experimental results from each of the three wafers are described. First, the longitudinal mode spectra are discussed. Then the threshold current density and the differential quantum efficiencies of the various lasers are compared. In particular, the effect of the nonplanar substrate on efficiency is evaluated by comparison to the broad area planar lasers grown on unetched substrates. The near-field intensity patterns, both below and above threshold, are compared. The far-field patterns from the three laser structures are also described.

The longitudinal mode spectrum of nonplanar arrays was determined using a grating spectrometer. The emission of lasers from wafer I was  $8270 \text{ \AA}$ , as expected from a single  $50 \text{ \AA}$  GaAs quantum well with  $\text{Al}_{0.2}\text{Ga}_{0.8}\text{As}$  barriers [10]. A single group of longitudinal modes was observed from all but a few of the lasers. A few lasers had two groups of modes oscillating, and spatially resolved spectral measurements indicate that each array element oscillates on only one of the two groups of modes. This anomaly may be associated with well thickness variations across the wafer associated with the nonplanar growth and is sometimes observed in planar broad-area lasers as well. The lasers from wafer II emit at  $8260 \text{ \AA}$ , again corresponding to the quantum well transition for a single  $50 \text{ \AA}$  GaAs quantum well with  $\text{Al}_{0.2}\text{Ga}_{0.8}\text{As}$  barriers. The lasers from wafer III emit at  $8390 \text{ \AA}$ , indicating that the actual quantum well thickness for wafer III may be greater than  $50 \text{ \AA}$  [10].

The data in Table I show the average threshold current density of corrugated substrate lasers from each wafer and the external differential quantum efficiency (both facets) for both corrugated substrate lasers and broad-area planar lasers with cavity length  $l = 508 \mu\text{m}$  from each of the three wafers. As expected, the threshold current density of lasers from wafers I and III is lower than the threshold current density of lasers from wafer II due to the higher aluminum composition confining layers of the lasers from wafers I and III. Note that the broad-area planar lasers from wafer III have a slightly higher threshold current density and lower quantum efficiency than the broad-area planar lasers from wafer I, indicating a slight variation in the starting material of lasers from wafers I and III. The preferred structure for high-power low-threshold-current operation is the laser structure with  $x_c = 0.85$  because of the very low threshold current density and high differential quantum efficiency of these lasers. For each laser structure, the external differential quantum efficiency of planar broad-area lasers is higher than the efficiency of nonplanar lasers, but not by the same factor. In addition, the threshold current density of the lasers on etched substrates is lower than the threshold current density of lasers on planar substrates. This indicates that the current is not uniformly injected across the width of the laser, so that one should not use the total width of the device to calcu-

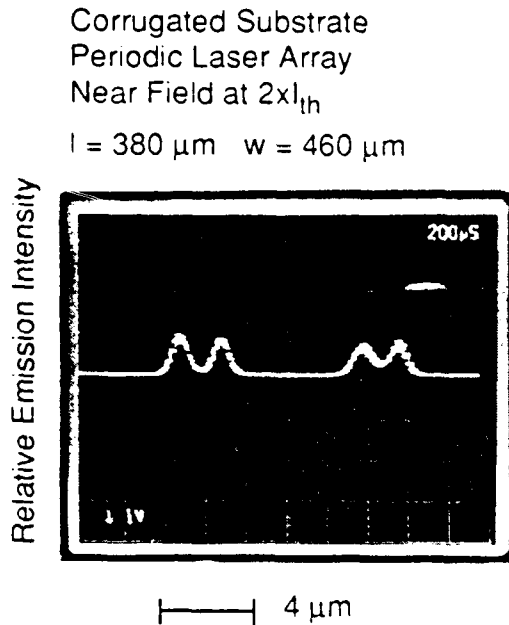


Fig. 2. Near-field pattern for a laser from wafer I. The observed emission is from the mesa, with two peaks on the mesa. The emission from the groove is two orders of magnitude lower than the emission from the mesa and is not detected in this near-field pattern.

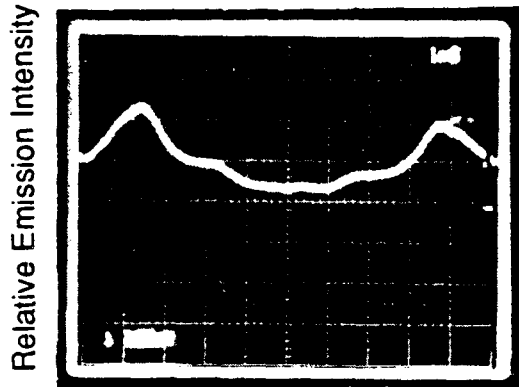
late the cross sectional area. The effect of the nonplanar structure on efficiency is more pronounced for wafers I and III than for wafer II, and when the near-field patterns of these nonplanar arrays is examined below, the reason for the reduced efficiencies relative to broad-area lasers will become apparent.

Fig. 2 shows the near-field optical intensity pattern from two adjacent elements of a high-power GBQWH periodic laser array from wafer I at twice the threshold. Note that two lasing spots, spaced by  $1.5 \mu\text{m}$ , are located in each mesa, one near each edge. No lasing action in the grooves is indicated by the near-field pattern of Fig. 2; however, if the sensitivity of the near-field measurement is increased, lasing action is detected in the groove region, with two peaks per groove. We estimate the emission from the grooves to be about two orders of magnitude lower than in the mesa, and we determined that the emission wavelength in the groove is the same as in the mesa using a spatially resolved measurement to measure the emission wavelength in the mesa and groove regions. Since the emission wavelength is the same in both the mesa and groove regions, the quantum well thickness is the same in the mesa and groove regions. The very low emission from the grooves is responsible for the decreased efficiency of nonplanar lasers relative to planar broad-area lasers from the same growth run since the groove region is pumped with current just as the mesa region is. The observed 44 percent reduction in efficiency relative to broad-area lasers is not as large as might be expected since the stimulated emission in the groove with its shorter carrier lifetime will compete effectively for nearby carriers subject to the slower spontaneous emission outside the mesa. The observed near-field pattern of Fig. 2 is stable over a wide

range of drive currents, retaining its shape from threshold to at least 16 times threshold. The spontaneous emission near-field intensity pattern far below threshold ( $0.1 \times I_{th}$ ) was also measured for these devices, and the intensity of the emission from the mesas was about 30 percent higher than the intensity in the grooves. A shallow dip in intensity at the center of the mesa was observed, which eventually grew into the double peak pattern in the mesa shown in Fig. 2. These observations indicate there is a slight gain variation between the mesa and groove regions. This gain variation may be a result of nonuniform current injection, as evidenced by the lower measured threshold current density when it is assumed that the current is uniformly distributed across the device. From the threshold current density of lasers on planar substrates, one can estimate the nonuniformity in current between the mesa and the groove by requiring the current density in the mesa at threshold to be equal to the threshold current density of a broad-area laser with a planar active region and also requiring the total current to be equal to the threshold current of the laser on the etched substrate. From our data, using the above conditions, we estimate that the current density in the mesa is 30 percent higher than in the grooves. A scanning electron micrograph of the growth on etched substrates indicates that the layer thickness varies in the bent region [6], with the layer being thinner near the mesa than near the groove. The thinner quantum well near the mesa forms a barrier for electrons [11], [12], helping to confine carriers to the mesa. A similar barrier is not formed near the groove. This nonuniformity of growth rate in the bent region [6] will probably cause a slightly higher carrier concentration in the mesa. The gain variation is probably exaggerated by the fact that the mesa region is a perfect (100) surface, whereas the groove region is not. The far-field pattern of a laser from wafer I is shown in Fig. 3, showing two broad peaks at  $\pm 9^\circ$  and a minimum, but not a zero, at  $0^\circ$ . The depth of the minimum at  $0^\circ$  varies somewhat from diode to diode. The adjacent mesa elements spaced by  $8 \mu\text{m}$  are not coupled, as indicated by the two broad peaks with full width half maximum angles of about  $7^\circ$  observed in the far-field pattern of Fig. 3.

The near-field pattern of lasers from wafer II is more complicated, with three small peaks in the groove and a small peak in the bent region, accounting for the five small peaks between the large single peaks in the mesa, as shown in Fig. 4. The reduction in efficiency of corrugated substrate lasers from wafer II relative to the corresponding broad-area planar lasers is not as pronounced as for wafer I since some emission is observed in the grooves of the lasers from wafer II. The spontaneous emission pattern at  $0.1 \times I_{th}$  of lasers from wafer II indicates the gain in both the mesa and the groove regions are approximately equal, and some spontaneous emission is also observed in the bent regions. The far-field pattern of lasers from wafer II exhibits narrow lobes (full width half maximum =  $1.2^\circ$ ) at  $\pm 3^\circ$ , as shown in Fig. 5. The spacing between peaks of  $6^\circ$  is close to the expected value of  $5.9^\circ$  calcu-

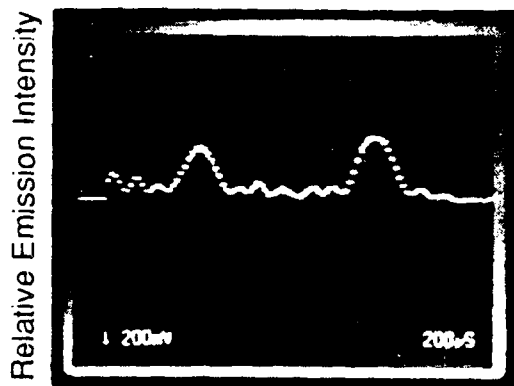
Corrugated Substrate  
Periodic Laser Array  
Far Field at  $1.1 \times I_{th}$   
 $l = 330 \mu\text{m}$   $w = 80 \mu\text{m}$   
GBQWH  $x = 0.85$



2.47 deg/div

Fig. 3. Far-field pattern of a laser from wafer I. The double-lobed pattern has two peaks at  $\pm 9^\circ$  and a minimum at  $0^\circ$ , but the minimum at  $0^\circ$  is not a null in intensity.

Corrugated Substrate  
Periodic Laser Array  
Near Field at  $1.2 \times I_{th}$   
 $l = 305 \mu\text{m}$   $w = 230 \mu\text{m}$   
GBQWH  $x = 0.40$



4  $\mu\text{m}$

Fig. 4. Near-field pattern for a laser from wafer II. The larger peak corresponds to the mesa, while the three smaller peaks in the center correspond to the groove, and the other two small peaks between the mesas are emission from the bent region.

lated from simple diffraction theory assuming in-phase coupling between adjacent elements and a center-to-center spacing of  $8 \mu\text{m}$  at a wavelength of  $8260 \text{ \AA}$  [13]. The error is probably due to the emission from the grooves.

Corrugated Substrate  
Periodic Laser Array  
Far Field at  $2.1 \times I_{th}$   
 $l = 500 \mu\text{m}$   $w = 240 \mu\text{m}$   
GBQWH  $x = 0.40$

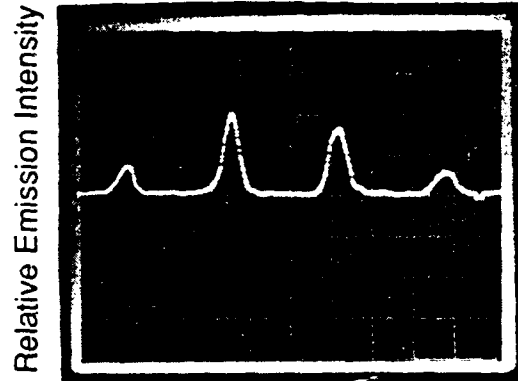


Fig. 5. Far-field pattern of a laser from wafer II. The narrow lobes with a full width half maximum angle of  $\sim 1.2^\circ$  indicate the elements are phase locked, in contrast to the lasers from wafer I.

The far-field data clearly imply that the adjacent elements spaced by  $8 \mu\text{m}$  in lasers from wafer II are phase locked, in contrast to the laser elements spaced by  $8 \mu\text{m}$  in lasers from wafer I, which are uncoupled.

The spontaneous emission intensity pattern at  $0.1 \times I_{th}$  of lasers from wafer III is not as uniform as for lasers from wafer I, with the spontaneous emission being about three times more intense in the mesa than in the groove region. As observed in lasers from wafer I, a slight dip is observed in the spontaneous emission pattern at the center of the mesa of lasers from wafer III. The near-field pattern above threshold is confined primarily to the mesas, with strongly attenuated laser emission from the grooves and two peaks per mesa, just as observed in lasers from wafer I. An even smaller percentage of the facet contributes to the output power because the mesas are smaller in wafer III than in wafer I, so the relative reduction in efficiency between nonplanar lasers and broad-area lasers is even larger for wafer III, as shown in Table I. Finally, the far-field pattern of lasers from wafer III is similar to the observed patterns of lasers from wafer I, except the null at  $0^\circ$  is barely noticeable in these lasers, resulting in a very broad far-field pattern with a full width half maximum angle of about  $20^\circ$ . These data show that the adjacent elements spaced by  $8 \mu\text{m}$  are uncoupled.

Despite the reduced efficiency of the nonplanar arrays relative to the broad-area planar lasers, an output power of  $8 \text{ W/uncoated}$  facet from the nonplanar lasers has been observed since the nonplanar lasers can be made very wide [4], [5]. It would be desirable to excite the grooves of the lasers with the GBQWH structure of wafers I and III in order to increase the efficiency and thus further increase the output power from nonplanar laser arrays. The following section offers an analysis of the experimental data

given in this section, which aids in the understanding of these lasers arrays and may lead to a solution which will allow more uniform emission across the width of the array.

#### IV. DISCUSSION

In an effort to explain the widely varying near-field patterns of the lasers from the different wafers, we developed a simple analytical model of these arrays. This periodic laser array structure is essentially a periodic variation of the channel guide structure [14], which has been modeled by Yang *et al.* [15]. For simplicity, we assumed a uniform gain distribution across the entire array, so only the real part of the index of refraction is used in the calculation. The spontaneous emission patterns below threshold indicate this is a good assumption well below threshold for lasers from wafer II, a fair assumption for lasers from wafer I, and a poor assumption for lasers from wafer III. Since this assumption is not always valid below threshold and is in general not valid above threshold [16], the calculated fields presented here cannot be taken as definitive, but the calculation does provide information which helps to determine the waveguiding mechanism for the various array structures. Fig. 6 shows a schematic and assumed real refractive index profile of one period of the structure. The  $x$  direction is defined to be perpendicular to the junction, and the  $y$  direction is parallel to the junction. We derived the real refractive index profile of Fig. 6 using the *effective index approximation* [15]–[18] as follows. First, the effective index is found in the mesa and groove regions by solving for the effective index  $n_e$  for the structure perpendicular to the junction:

$$d^2F/dx^2 + k_0^2[n^2(x) - n_e^2]F = 0 \quad (1)$$

where  $k_0$  is the free space propagation constant,  $n(x)$  is the refractive index as a function of position with  $x = 0$  at the center of the active region, and  $F$  describes the  $x$  dependence of the  $y$  component of the electric field, assuming TE polarization. The index of refraction of AlGaAs was taken to be a linear function of aluminum composition, with  $n = 3.1$  for a 0.85 aluminum mole fraction,  $n = 3.51$  for a 0.20 aluminum mole fraction, and  $n = 3.36$  for a 0.40 aluminum mole fraction [19]. The index in the middle of the bent region is assumed to be the refractive index of Al<sub>0.85</sub>Ga<sub>0.15</sub>As ( $x = x_1$ ),  $n_1$ , at the laser wavelength, so  $n_1 = 3.1$  for wafers I and III and  $n_1 = 3.36$  for wafer II. The solution of (1) gave  $n_e = 3.28$  for wafers I and III and  $n_e = 3.4$  for wafer II. A measure of the index step is  $n_1 - n_e$ , which is much larger for lasers with  $x_1 = 0.85$  than for lasers with  $x_1 = 0.40$ . The smaller index step of lasers from wafer II ( $x_1 = 0.40$ ) allows the adjacent elements to couple, explaining the much sharper far-field peaks of those lasers. A transition region of index is assumed for the edges of the bent regions, and this index profile is calculated as

$$n_{\text{eff}}(y) = n_e - \Delta n_{\text{eff}}(y). \quad (2)$$

This approximate method for calculating the effective in-

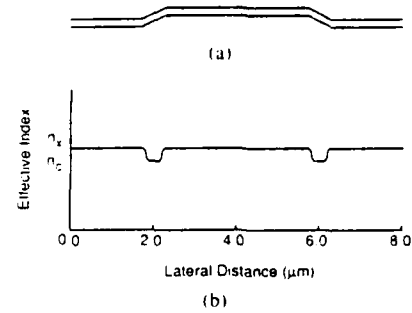


Fig. 6. (a) Schematic of the active region. (b) Refractive index profile used to calculate the optical modes of the laser. The  $x$  direction is perpendicular to the junction, and the  $y$  direction is lateral to the junction. The center region corresponds to the mesa region, while the edges correspond to the groove, and  $n_1$  and  $n_e$  are defined in the text.

dex in the bent region is derived from first-order perturbation theory [20], which approximates the perturbation to the effective index as

$$\Delta n_{\text{eff}}(y) = \langle F | \Delta n(x) | F \rangle \quad (3)$$

where  $\Delta n(x)$  is the change in refractive index at the point  $y$  in the bent region due to the displacement of the waveguide by a distance along the  $x$  direction of  $\Delta x = y \tan \theta$  where  $\theta$  is the angle the bent region makes with the  $y$  axis and  $F$  is the unperturbed solution of (1). The refractive index profile of Fig. 6 is used to solve for the lateral field variations by solving the one-dimensional field equation

$$d^2G/dy^2 + k_0^2[n_{\text{eff}}^2(y) - n_e^2]G = 0 \quad (4)$$

where  $n_e$  is the effective index for the lateral waveguide along the  $y$  direction and  $G$  contains the  $y$  dependence of the electric field. The boundary conditions of (4) require both the field and the derivative of the field to be continuous at the period boundaries. The near-field intensity is taken to be the electric field squared. The far-field pattern for a single element is calculated in the usual way, using the Fourier transform of the near-field pattern, and the inclination factor is taken to be equal to  $\cos \theta$  [21]. The far-field pattern was not calculated for lasers from wafer II since the elements were phase locked.

The calculated near-field pattern of the  $m = 1$  mode of one period for lasers from wafer I is shown in Fig. 7. As expected, the emission is only expected in the mesa, in agreement with the measured data of Fig. 2. The degree of confinement to the mesa was relatively independent of mode number, other modes are also virtually confined to the mesa. This calculation shows that a difference in width between the mesa and the groove will tend to confine the optical field to the wider of the two regions, assuming gain-guiding effects are negligible. For a mesa width of  $3.6 \mu\text{m}$  and a groove width of  $3.2 \mu\text{m}$ , the field is virtually confined to the mesa for lasers from wafer I since the index step for  $x_1 = 0.85$  lasers is relatively large. In addition, the observed gain variations between the groove and mesa as determined by the spontaneous emission data for lasers from wafer I will tend to confine the field to the mesa since the gain was slightly higher in the mesa than

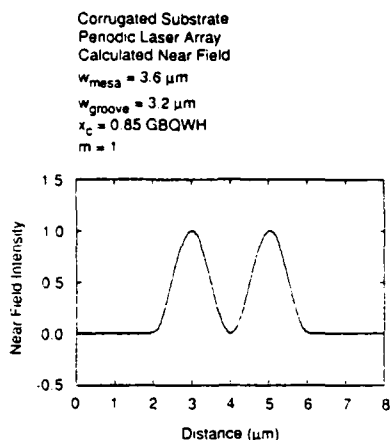


Fig. 7. Calculated near-field pattern of the  $m = 1$  mode for an  $r_c = 0.85$  GBQWH laser with a mesa width of  $3.6 \mu\text{m}$  and a groove width of  $3.2 \mu\text{m}$  (wafer I). The center region corresponds to the mesa, and the outer regions correspond to the groove, as indicated by Fig. 6. The emission is strongly confined to the wider mesa region.

in the groove. From a comparison of the efficiency and threshold current density of lasers on etched substrates with the lasers on planar substrates from wafer I, we estimate that 56 percent of the total current is injected into the groove, with 44 percent injected into the mesa. As a result, we conclude that two effects are responsible for the confinement of laser emission to the mesas for lasers from wafer I. First, the larger width of the mesa relative to the groove tends to confine the field to the mesa region. Second, slight gain guiding, indicated in the below threshold spontaneous emission pattern, will tend to confine the field to the mesa.

The gain variation between the mesa and groove is a result of the nonuniform current injection between the mesa and groove, as indicated by the threshold current density comparison between planar lasers and etched substrate lasers, as described above. The relatively small variation in current density between the mesa and the groove can lead to a situation in which the gain in the mesa is much larger than the gain in the groove since the gain is highly sensitive to the number of carriers injected into the quantum well [22]. We have solved (4) using a complex effective index to estimate the effects of gain variations on the near-field pattern. If the gain in the mesa is four times the gain in the groove, the optical field will be confined to the mesa if the gain coefficient in the mesa is assumed to be greater than  $\sim 200 \text{ cm}^{-1}$ . Given this result, it is easy to believe that the variation in current density estimated from our data can cause a large enough variation in gain to confine the optical field to the mesa. See, for example, [22, Figs. 2 and 3].

For lasers from wafer III, the effect of gain guiding, which tends to confine the field to the mesa of lasers from wafer III, dominates over the effect of having a wider groove width than mesa width, which tends to confine the optical field to the groove. These data indicate that the variation in gain induced by nonuniform current injection is responsible for the confinement of the optical field to the mesa. The larger gain variation between the mesas and grooves of lasers from wafer III may result from the

fact that the larger grooves in wafer III deviate more from a perfect (100) surface than the smaller grooves in lasers from wafer I. The shape of the growth in the groove depends on the relative sizes of the grooves and mesas [6].

The far-field pattern calculated from the near-field pattern of Fig. 7 (the  $m = 1$  mode) is shown in Fig. 8, with peaks at  $\pm 9^\circ$  and a zero normal to the facet. Since the measured far-field pattern of lasers from wafers I and III does not have a zero at  $0^\circ$ , the  $m = 1$  mode of a waveguide confined to the mesa is not an adequate description of the laser. Although there is no structural variation in the center of the mesa to form two waveguides in the mesa, a carrier-induced reduction of the index of refraction at the center of the mesa, where the optical field is a minimum, can form two waveguides in the mesa [23]. The far field implies that two coupled waveguides are formed on the mesa. If two coupled waveguides are formed, it is possible for them to couple in or out of phase [24]. The observed far-field pattern probably results from a superposition of the in-phase mode, which has a single peak at  $0^\circ$ , and the out-of-phase mode, which has two peaks at  $\pm 16^\circ$  and a null at  $0^\circ$ , for a center-to-center spacing of  $1.5 \mu\text{m}$  [13], which is the distance between the peaks on the mesa. The variation of the depth of the minimum at  $0^\circ$  for different diodes results from a variation in the fraction of power in each of the two modes. We have observed that it is more difficult to force a zero in the center of a smaller mesa since the entire mesa experiences gain. Thus, for lasers from wafer III with smaller mesas, the in-phase mode is expected to dominate, and the minimum at  $0^\circ$  is washed out [24].

For lasers from wafer II, the calculation shows that the smaller real index step  $\Delta n_{\text{eff}}(y)$  between the mesa or groove regions and the bent regions results in reduced sensitivity of the near field to asymmetry between the mesa and the groove. For a laser from wafer II with the same mesa and groove widths as for the lasers from wafer I, the calculated near-field pattern of both the  $m = 0$  mode and the  $m = 1$  mode has substantial emission in the grooves. The  $m = 0$  mode is shown in Fig. 9. This calculation agrees qualitatively with the observed reduced emission in the grooves relative to the mesas of lasers from wafer II. There may also be a nonuniformity in gain between the mesa and groove regions, but the spontaneous emission near-field pattern indicates that the gain variation is not as great as in lasers from wafers I and III. A waveguide similar to the one described in Fig. 6 is formed in the bent regions, and this emission was also observed in lasers from wafer II.

There are many allowed higher-order modes of the real index waveguide described by the profile of Fig. 6, and the mode which is selected will be determined by the relative threshold gains of the various allowed modes. The refractive index profile of Fig. 6 can be used as a starting point in a self-consistent calculation [25] of the optical near-field pattern when it is safe to assume there are no gain or carrier-induced index variations across the width of the array. The starting profile should include the gain variation between the mesa and groove which is present

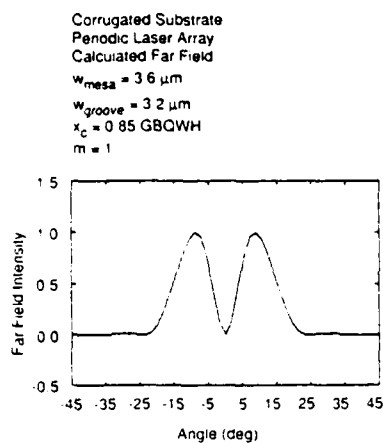


Fig. 8. Calculated far-field pattern for the near-field pattern of Fig. 7, for lasers from wafer I. The two peaks at  $\pm 9^\circ$  agree with the measured data of Fig. 3, but the null at  $0^\circ$  does not agree, which indicates that two coupled modes are oscillating on the mesa, not the  $m = 1$  mode

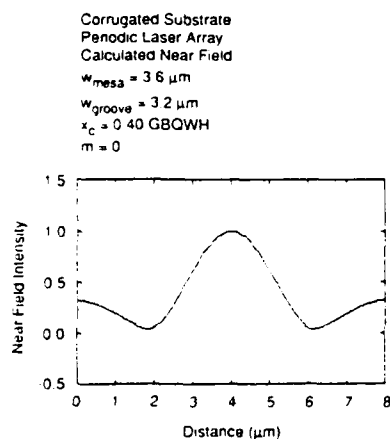


Fig. 9. Calculated near-field pattern of the  $m = 0$  mode for an  $x_c = 0.40$  GBQWH laser with a mesa width of  $3.6 \mu\text{m}$  and a groove width of  $3.2 \mu\text{m}$  (wafer II). More emission occurs in the grooves than in the calculated near-field pattern of Fig. 7 because of the smaller index step  $n_c$ .

below threshold for wafers I and III and should also contain gain and index variations in the bent regions caused by different growth rates in the bent regions [6]. As the current is increased, the allowed lateral modes will begin to appear, the actual refractive index profile will deviate from the original profile of Fig. 6, and new lateral gain and index variations will be established, which will make it possible to calculate the modal threshold gains and determine the actual near-field pattern. For example, in lasers from wafer I, the two-waveguide structure which seems to be present on the mesa, as indicated by the far-field patterns of those lasers, is probably formed by self-stabilizing effects [23] since a dip in the optical field is observed well below threshold. This dip is formed as the  $m = 1$  mode of the starting index profile of Fig. 6 grows. Furthermore, the stability of the near-field patterns is probably due to the same self-stabilizing effects [23]. Similarly, the  $m = 2$  mode in the groove of lasers from wafer II develops into three stable self-focused waveguides in the groove of lasers from wafer II, which would account for the multiple peaks observed in the grooves of

lasers from wafer II. These self-consistent calculations, along with mode gain calculations, must be carried out in order to explain why the different laser structures select different modes. Such calculations are beyond the scope of this work.

## V. CONCLUSION

In conclusion, we have investigated the effects of the structural parameters on the operating characteristics of nonplanar laser arrays fabricated by MOCVD by comparing the characteristics of lasers from three different wafers. The lowest threshold current density and highest efficiency are obtained from lasers having a GBQWH structure and a high confining layer aluminum composition of  $x_c = 0.85$ . The efficiency of nonplanar lasers relative to broad-area lasers fabricated from the same wafer depends on the near-field pattern and is lowest if emission is totally suppressed in either the mesas or the grooves. There are two effects which will confine the emission to the mesa region or the groove region. First, the emission will tend to be confined to the wider of the two regions because of real index-guiding effects, which are calculated in Section IV. This effect is more pronounced for lasers with high aluminum composition confining layers because of the larger effective index step for such lasers. Second, the emission will tend to be confined to a region of higher gain. The effect of gain variations between the mesa and groove regions is more important than the effect of having different widths in the mesa and groove regions, as evidenced by the lasers from wafer III, which emit in the mesa region despite the fact that the mesa region is narrower than the groove region. The relative emission between the mesa and groove regions is very sensitive to variations in current injection into the mesa and groove regions since the gain is a highly sensitive function of injection current in single-quantum-well lasers [22]. The lateral index step which confines the optical field to the mesa is a strong function of the confining layer aluminum composition  $x_c$ . The larger index step in lasers with a high confining layer aluminum composition of  $x_c = 0.85$  prevents coupling between elements, but the lower index step for devices with  $x_c = 0.40$  allows the elements to be phase locked, explaining the sharp peaks observed in the far-field pattern of such lasers. In order to design a laser which will emit with equal intensity in both the mesa and groove and thus maximize the efficiency of the laser, it is necessary to control the relative widths of the mesa and groove regions and the relative gain distribution between the groove and mesa.

## ACKNOWLEDGMENT

The authors would like to acknowledge gratefully T. L. Brock for assistance with mask design and fabrication and L. M. Miller and T. K. Higman for helpful discussions and technical support.

## REFERENCES

- [1] D. L. Sipes, "Highly efficient neodymium-yttrium aluminum garnet laser end pumped by a semiconductor laser array," *Appl. Phys. Lett.*, vol. 47, pp. 74-76, July 15, 1985.

- [2] G. L. Harmagel, P. S. Cross, C. R. Lennon, M. DeVito, and D. R. Scifres, "Ultra-high-power quasi-CW monolithic laser diode arrays with high power conversion efficiency," *Electron. Lett.*, vol. 23, pp. 743-744, July 2, 1987.
- [3] G. L. Harmagel, P. S. Cross, D. R. Scifres, D. F. Welch, C. R. Lennon, D. P. Worland, and R. D. Burnham, "High-power quasi-cw monolithic laser diode linear arrays," *Appl. Phys. Lett.*, vol. 49, pp. 1418-1419, Nov. 24, 1986.
- [4] C. A. Zmudzinski, M. E. Givens, R. P. Bryan, and J. J. Coleman, "Nonplanar index-guided quantum well heterostructure periodic laser array," *Appl. Phys. Lett.*, vol. 53, pp. 350-352, Aug. 1, 1988.
- [5] M. E. Givens, C. A. Zmudzinski, R. P. Bryan, and J. J. Coleman, "High power nonplanar quantum well heterostructure periodic laser arrays," *Appl. Phys. Lett.*, vol. 53, pp. 1159-1161, Sept. 26, 1988.
- [6] K. M. Dzurko, E. P. Menu, C. A. Beyler, J. S. Osinski, and P. D. Dapkus, "Temperature engineered growth of low-threshold quantum well lasers by metalorganic chemical vapor deposition," *Appl. Phys. Lett.*, vol. 54, pp. 105-107, Jan. 9, 1989.
- [7] W. T. Tsang, "A graded-index separate-confinement laser with very low threshold current and a narrow gaussian beam," *Appl. Phys. Lett.*, vol. 39, pp. 134-137, July 15, 1981.
- [8] S. D. Hersee, M. Baldy, P. Assemat, B. DeCremoux, and J. P. Duchemin, "Very low threshold GRIN-SCH GaAs/AlGaAs laser structure grown by OM-VPE," *Electron. Lett.*, vol. 18, pp. 870-871, Sept. 30, 1982.
- [9] G. Costrini and J. J. Coleman, "Conditions for uniform growth of GaAs by metalorganic chemical vapor deposition in a vertical reactor," *J. Appl. Phys.*, vol. 57, pp. 2249-2252, Mar. 15, 1985.
- [10] L. J. Mawst, M. E. Givens, C. A. Zmudzinski, M. A. Emanuel, and J. J. Coleman, "Optimization and characterization of index-guided visible AlGaAs/GaAs graded barrier quantum well laser diodes," *IEEE J. Quantum Electron.*, vol. QE-23, pp. 696-703, June 1987.
- [11] E. Kapon, M. C. Tamargo, and P. M. Hwang, "Molecular beam epitaxy of GaAs/AlGaAs superlattice heterostructure on nonplanar substrates," *Appl. Phys. Lett.*, vol. 50, pp. 347-349, Feb. 9, 1987.
- [12] E. Kapon, C. P. Yun, J. P. Harbison, and N. G. Stoffel, "Patterned quantum well semiconductor injection laser grown by molecular beam epitaxy," *Appl. Phys. Lett.*, vol. 52, pp. 607-609, Feb. 22, 1988.
- [13] D. R. Scifres, R. D. Burnham, and W. Streiter, "Lateral grating array high power cw visible semiconductor laser," *Electron. Lett.*, vol. 18, pp. 549-550, June 24, 1982.
- [14] R. D. Dupuis and P. D. Dapkus, "Single-longitudinal mode cw room-temperature Ga<sub>0.4</sub>Al<sub>0.6</sub>As channel-guide lasers grown by metalorganic chemical vapor deposition," *Appl. Phys. Lett.*, vol. 33, pp. 724-726, Oct. 15, 1978.
- [15] J. J. Yang, R. D. Dupuis, and P. D. Dapkus, "Theoretical analysis of single-mode AlGaAs-GaAs double heterostructure lasers with channel guide structure," *J. Appl. Phys.*, vol. 53, pp. 7218-7223, Nov. 1982.
- [16] J. K. Butler and D. Botez, "Mode characteristics of nonplanar double heterojunction and large-optical-cavity laser structure," *IEEE J. Quantum Electron.*, vol. QE-18, pp. 952-961, June 1982.
- [17] W. Streiter and E. Kapon, "Application of the equivalent-index method to DH diode lasers," *Appl. Opt.*, vol. 18, pp. 3724-3725, Nov. 15, 1979.
- [18] J. Buus, "The effective index method and its application to semiconductor lasers," *IEEE J. Quantum Electron.*, vol. QE-18, pp. 1083-1089, July 1982.
- [19] H. C. Casey and M. B. Panish, *Heterostructure Lasers Part A: Fundamental Principles*. Orlando, FL: Academic, 1978.
- [20] N. C. Frateschi and A. R. B. De Castro, "Perturbation theory for the wave equation and the 'effective refractive index' approach," *IEEE J. Quantum Electron.*, vol. QE-22, pp. 12-15, Jan. 1986.
- [21] D. R. Scifres, R. D. Burnham, and W. Streiter, "Experimental and analytic studies of coupled multiple stripe diode lasers," *IEEE J. Quantum Electron.*, vol. QE-15, pp. 917-922, Sept. 1979.
- [22] B. Saint-Cricq, F. Lozes-Dupuy, and G. Vassiliell, "Well width dependence of gain and threshold current in GaAlAs single quantum well lasers," *IEEE J. Quantum Electron.*, vol. QE-22, pp. 625-630, May 1986.
- [23] D. Mehuys, R. J. Lang, M. Mittelstein, J. Salzman, and A. Yariv, "Self-stabilized nonlinear lateral modes of broad area lasers," *IEEE J. Quantum Electron.*, vol. QE-23, pp. 1909-1920, Nov. 1987.
- [24] E. Figueroa, T. L. Holcomb, K. Burghard, D. Bullock, C. B. Morrison, I. M. Zinkiewicz, and G. A. Evans, "Modeling of the optical characteristics for twin-channel laser (TCL) structures," *IEEE J. Quantum Electron.*, vol. QE-22, pp. 2141-2149, Nov. 1986.
- [25] Y. Tzu, K. Chen, S. Wang, J. R. Whinnery, and A. Dienes, "Eigenmode analysis of phase locked semiconductor laser arrays," *Appl. Phys. Lett.*, vol. 48, pp. 16-18, Jan. 6, 1986.



**Charles A. Zmudzinski** (S'83-M'85-S'86) was born in South Bend, IN, on February 2, 1962. He received the B.S. degree in electrical engineering from the University of Notre Dame, Notre Dame, IN, in 1984 and the M.S. degree in electrical engineering from the University of Illinois at Urbana-Champaign, Urbana, in 1986.

He is presently working towards the Ph.D. degree in electrical engineering at the University of Illinois. His research has concentrated on the design and fabrication of high-power semiconductor lasers grown by MOCVD.



**Michael E. Givens** was born in Sterling, IL, on February 26, 1963. He received the B.S. and M.S. degrees in electrical engineering from the University of Illinois at Urbana-Champaign, Urbana, in 1985 and 1988, respectively.

He is currently working towards the Ph.D. degree in electrical engineering as a Research Assistant in the National Science Foundation Engineering Research Center for Compound Semiconductor Microelectronics at the University of Illinois. His research has focused on the epitaxial crystal growth of compound semiconductors by MOCVD with a concentrated interest in the growth, development, and characterization of Al<sub>x</sub>Ga<sub>1-x</sub>As/GaAs semiconductor laser diode structures.



**Robert P. Bryan** was born in Lisle, IL, on August 23, 1965. He received the B.S. degree in electrical engineering with highest honors and the M.S. degree in electrical engineering from the University of Illinois at Urbana-Champaign, Urbana, in 1986 and 1988, respectively.

Currently, he is working towards the Ph.D. degree in electrical engineering under an AT&T Doctoral Fellowship at the National Science Foundation Engineering Research Center for Compound Semiconductor Microelectronics at the University of Illinois. His research concentrates on the development and materials characterization of semiconductor laser structures.



**James J. Coleman** (S'73-M'76-SM'80) received the B.S., M.S., and Ph.D. degrees in electrical engineering from the University of Illinois at Urbana-Champaign, Urbana, in 1972, 1973, and 1975, respectively.

At Bell Laboratories, Murray Hill, NJ (1976-1978), he studied the materials properties of InGaAsP grown by liquid phase epitaxy (LPE) and helped to develop proton-isolated room temperature CW lasers operating at wavelengths near 1.3 μm. At Rockwell International, Anaheim, CA (1978-1982), he contributed to the development of the MOCVD growth method and to the processing and testing of various CW room temperature, low-threshold AlGaAs/GaAs laser devices such as the self-aligned laser and the narrow diffused stripe laser. By extension of the MOCVD growth process to large numbers of ultrathin (10-200 Å) layers and to all binary AlAs/GaAs structures, he was able to make unique quantum well heterostructures and superlattices which show two-dimensional optical and electronic transport effects. He is presently a Professor of Electrical Engineering at the University of Illinois at Urbana-Champaign (1982 to present). He and his students are involved in the study of optical processes and electronic transport in various structures, such as quantum well heterostructures, superlattices, real-space transferred electron devices, and laser arrays. He has authored or coauthored more than 125 technical papers and holds two patents.

Prof. Coleman has served on the program committees of the 1983, 1984, and 1988 International Electron Devices Meetings, the 1984 International Semiconductor Laser Conference, the 1986 International Conference on Metalorganic Vapor Phase Epitaxy, and the 1987 Southwest Optics Conference. He was the Guest Editor of the IEEE JOURNAL OF QUANTUM ELECTRONICS Special Issue on Quantum Well Heterostructures and Superlattices. He was the recipient of a Beckman Research Award in 1982. He is a member of the American Physical Society, the Electrochemical Society, and Sigma Xi.

# Impurity induced disordered quantum well heterostructure stripe geometry lasers by MeV oxygen implantation

R. P. Bryan, J. J. Coleman, L. M. Miller, M. E. Givens, R. S. Averback, and J. L. Klatt  
*Materials Research Laboratory, University of Illinois, 1406 West Green Street, Urbana, Illinois 61801*

(Received 15 March 1989; accepted for publication 3 May 1989)

Data are presented on stripe geometry AlGaAs-GaAs graded barrier quantum well heterostructure lasers formed by MeV oxygen implantation and annealing. Low-dose implants are found to suppress lateral carrier diffusion but do not result in compositional disordering. High-dose implants form both a semi-insulating and a compositionally disordered region leading to index-guided buried-heterostructure laser operation. However, the concentration of oxygen which spreads laterally under the implantation mask during high-dose implants is sufficient to partially compensate the stripe region for narrow stripe widths and thereby significantly increases the threshold current.

In recent years, considerable interest has been shown in impurity-induced compositional disordering of III-V compound semiconductor devices especially in efforts directed towards fabricating index-guided buried-heterostructure (BH) lasers.<sup>1</sup> It has been previously reported that a compositionally averaged region may be formed by either diffusion<sup>2</sup> or implantation<sup>3-7</sup> of species such as Zn, Si, Ga, Al, and O into AlGaAs-GaAs heterostructures. Implantation has also been employed to eliminate leakage current in laser structures by the chemical and damage effects of O, Fe, and H implantation.<sup>8-12</sup> In this letter we report the fabrication of BH graded barrier quantum well (GBQW) lasers by MeV oxygen ion implantation in which we utilize the compositionally disordering and semi-insulating characteristics of oxygen-implanted AlGaAs layers. We observe that low-dose implants ( $10^{14}$ – $10^{16}$  cm<sup>-2</sup>) are sufficient to eliminate leakage current in laser devices by the formation of a semi-insulating region but insufficient to induce compositional disordering, thus resulting in gain-guided laser operation. High-dose implants ( $10^{17}$  cm<sup>-2</sup>) are able to induce compositional disordering and hence index-guided laser operation but, as a consequence of the lateral distribution of oxygen under the implantation mask, also partially compensate the stripe region thereby greatly increasing the threshold current for narrow stripe widths ( $< 5 \mu\text{m}$ ).

A GBQW heterostructure laser<sup>13,14</sup> was grown in an atmospheric pressure metalorganic chemical vapor deposition (MOCVD) reactor<sup>15</sup> at a temperature of 800 °C on a Si-doped GaAs:*n* (100) substrate. The laser structure consists of a 0.25  $\mu\text{m}$  GaAs:*n* buffer layer, a 0.5  $\mu\text{m}$  linearly graded (0.05  $x$ :0.85) Al<sub>1-*x*</sub>Ga<sub>*x*</sub>As:*n* buffer layer, a 1.0  $\mu\text{m}$  Al<sub>0.85</sub>Ga<sub>0.15</sub>As:*n* confining layer, a 1200 Å parabolically graded (0.85  $x$ :0.20) Al<sub>1-*x*</sub>Ga<sub>*x*</sub>As:*n* layer, a 50 Å GaAs:*n* quantum well, a 1200 Å parabolically graded (0.20  $x$ :0.85) Al<sub>1-*x*</sub>Ga<sub>*x*</sub>As:*p* layer, a 0.85  $\mu\text{m}$  Al<sub>0.85</sub>Ga<sub>0.15</sub>As:*p* confining layer, a 0.2  $\mu\text{m}$  GaAs:*p* contact layer, and a 0.1  $\mu\text{m}$  Al<sub>0.60</sub>Ga<sub>0.40</sub>As:*p* implantation mask lift-off layer. Following MOCVD growth, the sample was patterned with a variable stripe width Pb/Cr/Au (1.25  $\mu\text{m}$ /0.035  $\mu\text{m}$ /0.53  $\mu\text{m}$ ) metal implantation mask by conventional photolithography and lift-off techniques. Ion implantation was performed using a Van de Graaff accelerator

at a fixed beam energy (1 MeV), current (100 nA), and implant temperature (26 °C) resulting in the structure shown in Fig. 1. The dose for different samples was varied between  $10^{14}$  and  $10^{17}$  cm<sup>-2</sup>. Following implantation, the Al<sub>0.60</sub>Ga<sub>0.40</sub>As lift-off layer was selectively etched away<sup>16</sup> in hydrochloric acid, removing the metal mask in the process, but without damaging the underlying structure. Capless anneals of the implanted samples were performed in the MOCVD reactor under an arsine overpressure at 850 °C for 45 min. SiO<sub>2</sub>-defined stripe geometry lasers of various widths were also fabricated from the same MOCVD grown wafer, for comparison to the oxygen-implanted lasers. Alloyed Ge/Au contacts were formed on the back of the substrate and nonalloyed Cr/Au contacts were formed on top of the structure. Uncoated devices were tested by using a 2 kHz pulsed current with a pulse length of 1.5  $\mu\text{s}$ . Output power was measured using a calibrated silicon photodiode and the near- and far-field radiation patterns were measured using a silicon photodiode array as input into a digitizing oscilloscope.

In Fig. 2, the threshold current ( $I_{th}$ ) versus stripe width for high-dose ( $10^{17}$  cm<sup>-2</sup>) oxygen-implanted stripe lasers (cavity length 457  $\mu\text{m}$ ) is shown as solid circles. For comparison, the threshold current versus stripe width for 406- $\mu\text{m}$ -long SiO<sub>2</sub>-defined oxide stripe lasers made from the same starting material is also plotted as open circles in Fig. 2. In the range of stripe widths from 50 to 6  $\mu\text{m}$ , the threshold

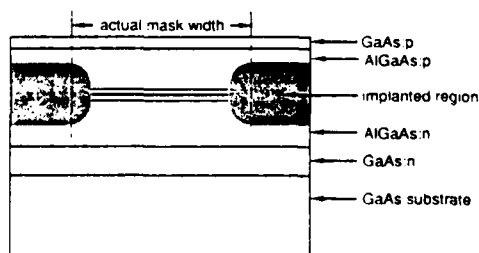


FIG. 1. Schematic cross section of the graded barrier quantum well heterostructure laser grown by MOCVD used in this study. The region of the oxygen implantation, including the extent of lateral spreading of the oxygen under the implantation mask, defines an effective stripe width.

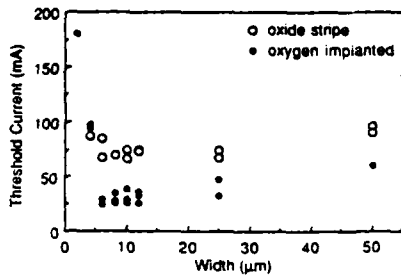


FIG. 2. Threshold current vs stripe width for both oxygen-implanted graded barrier quantum well heterostructure lasers ( $10^{17} \text{ cm}^{-2}$  dose, closed circles) and  $\text{SiO}_2$ -defined stripe lasers (open circles). The cavity length of the oxygen implanted lasers is  $457 \mu\text{m}$  and the length of the  $\text{SiO}_2$  defined stripe lasers is  $406 \mu\text{m}$ .

current of the oxygen-implanted stripe lasers decreases slightly. However, for narrower stripe widths ( $< 5 \mu\text{m}$ ), the threshold current of these lasers rises rapidly with decreasing stripe width. The threshold current of the conventional oxide-defined stripe lasers is higher overall and decreases approximately linearly with decreasing stripe width down to the narrower stripe widths after which it is nearly independent of width. Although the cavity lengths of the oxide-defined stripe lasers and the oxygen-implanted lasers of Fig. 2 are different, this difference leads only to a negligible ( $\sim 5\%$ ) error in the oxide stripe laser threshold currents. The emission wavelength ( $\lambda = 8220 \text{ \AA}$ ) is the same for both the oxygen-implanted lasers and the  $\text{SiO}_2$ -defined lasers. In the high-dose ( $10^{17} \text{ cm}^{-2}$ ) oxygen-implanted lasers, fundamental mode operation is observed in the near-field and far-field radiation patterns from laser threshold to more than five times the threshold current as illustrated in Fig. 3, which shows the near-field and far-field patterns for a high-dose oxygen-implanted laser ( $8 \mu\text{m}$  width,  $457 \mu\text{m}$  length). The

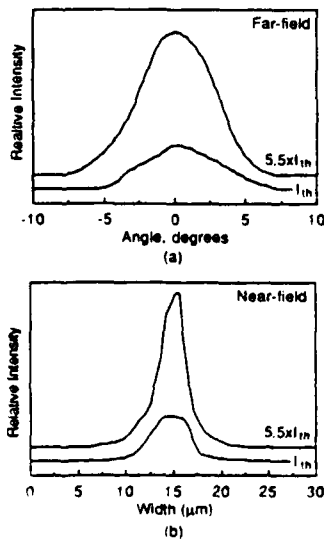


FIG. 3 (a) Near-field and (b) far-field radiation patterns at threshold (27 mA) and 5.5 times threshold (150 mA) for an oxygen-implanted graded barrier quantum well heterostructure laser ( $10^{17} \text{ cm}^{-2}$  dose, length  $457 \mu\text{m}$ , width  $8 \mu\text{m}$ ). The small amount of structure evident in the data is an artifact of the digitation.

small amount of structure evident in the data of Fig. 3 is an artifact of the digitation. At lower implant doses, the  $I_{\text{th}}$  versus stripe width data are essentially the same as those shown in Fig. 2. However, no evidence of index-guided laser operation is observed in the near-field and far-field patterns for samples irradiated at lower doses or in the  $\text{SiO}_2$ -defined stripe lasers.

As we reported previously, high-dose oxygen implantations ( $\sim 10^{17} \text{ cm}^{-2}$ ) are necessary<sup>7</sup> to induce compositional disordering in AlGaAs-GaAs heterostructures. Lower dose implants show no evidence<sup>7</sup> of any compositional intermixing as observed by secondary-ion mass spectrometry (SIMS) measurements. Thus, it is entirely expected that index guiding is observed only in the high-dose ( $10^{17} \text{ cm}^{-2}$ ) implanted samples. Favennec<sup>17</sup> has demonstrated that implantation of high doses of oxygen into  $n$ -type GaAs yields highly resistive material which is thermally stable at anneal temperatures up to  $900^\circ\text{C}$ . In our earlier work<sup>7</sup> and in the work by Pearton *et al.*<sup>18</sup> similar effects in  $p$ -type and  $n$ -type AlGaAs, attributed to deep level Al-O complexes, were reported. As a consequence, the effective stripe width of lasers fabricated by oxygen implantation is significantly smaller than corresponding  $\text{SiO}_2$  defined stripe lasers since lateral current spreading is eliminated by the semi-insulating properties of the oxygen implantation. In these studies we have found that even a low dose ( $10^{14} \text{ cm}^{-2}$ ) of oxygen implanted into highly doped AlGaAs layers is sufficient to make the layers semi-insulating. It follows that the effective semi-insulating region of higher dose oxygen implantations will encroach into the masked region of a sample due to the lateral spread of the implant species under the mask. Hence, the total effective stripe of oxygen-implanted devices is significantly smaller than the width delineated by the implantation mask, as shown in Fig. 1. As a result, the oxygen-implanted laser devices have a lower threshold current than corresponding  $\text{SiO}_2$ -defined stripe lasers.<sup>10</sup> For very high dose implantations and narrow stripe widths, the spread of the oxygen under each edge of the mask will overlap under the stripe giving rise to a substantial increase in the threshold current as observed in the oxygen-implanted laser threshold data for stripe widths below  $5 \mu\text{m}$  shown in Fig. 2.

In this letter we have presented data on stripe geometry AlGaAs-GaAs BH GBQW lasers fabricated by MeV oxygen implantation. In order to obtain index-guided laser operation, high-dose ( $10^{17} \text{ cm}^{-2}$ ) implantations, which intermix the AlGaAs-GaAs layers outside of the stripe and eliminate lateral current spreading, are required. The index-guided lasers thus formed operate in the fundamental lateral mode from the lasing threshold to over five times the threshold current. However, the high-dose implants are accompanied by a significant lateral distribution of oxygen under the implantation mask. For the dose required to induce compositional disordering, the lateral spread of implanted oxygen partially compensates a significant portion of the laser stripe for narrow stripe widths ( $< 5 \mu\text{m}$ ) and, consequently, the threshold current increases substantially for these widths. Low-dose implants are found to compensate carriers and thereby suppress lateral carrier diffusion but are insufficient to induce compositional disordering.

The authors gratefully acknowledge valuable discussions with T. M. Cockerill and C. A. Zmudzinski and technical assistance from B. E. Clymer. This work has been supported in part by the Naval Research Laboratory (N00014-88-K-2005), the National Science Foundation (DMR 86-12860 and CDR 85-22666), and the Department of Energy Basic Energy Sciences (DE-AC02-76ER01198). R. P. Bryan is supported in part by an AT&T Doctoral Fellowship.

- <sup>1</sup>P. Gavrilovic, D. G. Deppe, K. Meehan, N. Holonyak, Jr., J. J. Coleman, and R. D. Burnham, *Appl. Phys. Lett.* **47**, 130 (1985).  
<sup>2</sup>W. D. Laidig, N. Holonyak, Jr., M. D. Camras, K. Hess, J. J. Coleman, P. D. Dapkus, and J. Bardeen, *Appl. Phys. Lett.* **38**, 776 (1981).  
<sup>3</sup>J. J. Coleman, P. D. Dapkus, C. G. Kirkpatrick, M. D. Camras, and N. Holonyak, Jr., *Appl. Phys. Lett.* **40**, 904 (1982).  
<sup>4</sup>T. Venkatesan, S. A. Schwarz, D. M. Hwang, R. Bhat, M. Koza, H. W. Yoon, P. Mei, Y. Arakawa, and A. Yariv, *Appl. Phys. Lett.* **49**, 701 (1986).  
<sup>5</sup>J. Cibert, P. M. Petroff, D. J. Werder, S. J. Pearton, A. C. Gossard, and J. H. English, *Appl. Phys. Lett.* **49**, 223 (1986).

- <sup>6</sup>K. Kash, B. Tell, P. Grabbe, E. A. Dobisz, H. G. Craighead, and M. C. Tamargo, *J. Appl. Phys.* **63**, 190 (1988).  
<sup>7</sup>R. P. Bryan, M. E. Givens, J. L. Klatt, R. S. Averback, and J. J. Coleman, *J. Electron. Mater.* **18**, 39 (1989).  
<sup>8</sup>J. M. Blum, J. C. McGroddy, P. G. McMullin, K. K. Shih, A. W. Smith, and J. F. Ziegler, *IEEE J. Quantum Electron.* **QE-11**, 413 (1975).  
<sup>9</sup>V. I. Kolyshkin and E. L. Portnoi, *Sov. Tech. Phys. Lett.* **4**, 260 (1978).  
<sup>10</sup>F. Xiong, T. A. Tombrello, H. Wang, T. R. Chen, H. Z. Chen, H. Morkoç, and A. Yariv, *Appl. Phys. Lett.* **54**, 730 (1989).  
<sup>11</sup>D. P. Wilt, B. Schwartz, B. Tell, E. D. Beebe, and R. J. Nelson, *Appl. Phys. Lett.* **44**, 290 (1984).  
<sup>12</sup>A. G. Foyt, W. T. Lindley, C. M. Wolfe, and J. P. Donnelly, *Solid-State Electron.* **12**, 209 (1969).  
<sup>13</sup>W. T. Tsang, *Appl. Phys. Lett.* **39**, 134 (1981).  
<sup>14</sup>L. J. Mawst, M. E. Givens, C. A. Zmudzinski, M. A. Emanuel, and J. J. Coleman, *IEEE J. Quantum Electron.* **QE-23**, 696 (1987).  
<sup>15</sup>L. M. Miller and J. J. Coleman, *CRC Crit. Rev. Solid State Mater. Sci.* **15**, 1 (1988).  
<sup>16</sup>M. M. Ghadiri, R. P. Bryan, L. M. Miller, T. Tang, M. E. Givens, T. A. DeTemple, and J. J. Coleman (unpublished data).  
<sup>17</sup>P. N. Favennec, *J. Appl. Phys.* **47**, 2532 (1976).  
<sup>18</sup>S. J. Pearton, M. P. Iannuzzi, C. L. Reynolds, Jr., and L. Peticolas, *Appl. Phys. Lett.* **52**, 395 (1988).

# MeV implantation masking using an aluminum gallium arsenide metal liftoff layer

M. M. Ghadiri,<sup>a)</sup> R. P. Bryan, L. M. Miller, T. Tang, M. E. Givens, T. A. DeTemple, and J. J. Coleman

Compound Semiconductor Microelectronics Laboratory, University of Illinois at Urbana-Champaign, 1406 West Green Street, Urbana, Illinois 61801

(Received 22 November 1988; accepted for publication 22 March 1989)

An alternative masking method for high-voltage ion implantation masking of compound semiconductors which incorporates an additional AlGaAs layer between a Pb/Cr/Au metal mask and the sample to be implanted is described. Following patterning by conventional techniques and implantation, the AlGaAs layer is selectively etched to remove the metal mask without damaging the underlying epitaxial structure.

Ion implantation is a standard technique in the fabrication process of advanced microelectronic devices as a consequence of the inherent capability to accurately control the introduction of dopants and to induce compositional disordering<sup>1</sup> of heterostructures. High-energy (MeV) implants have recently become important in several optoelectronic applications, such as semiconductor lasers, optical waveguides, and integrated optics.<sup>2,3</sup> Masking layers are necessary in order to selectively control the area into which ions are introduced. Metals such as Al, dielectrics such as SiO<sub>2</sub> and Si<sub>3</sub>N<sub>4</sub>, and photoresists are commonly used as mask materials.<sup>4,5</sup> The use of a metal mask may present difficulties due to chemical bonding between the metal and the GaAs. Furthermore, the substances and processes necessary for removal of the mask may damage the structure. Implantation at high doses and energy may result in target temperature increases which induce chemical changes in photoresist masks, effectively reducing the thickness of the photoresist and making removal difficult. Because a thick layer of dielectric will often crack, dielectric masks are not reliable for high-energy implantation applications. In order to surmount these difficulties associated with masking for high-energy ion implantation, we have developed a novel method to fabricate a reliable, easily removed implantation mask. As an integral part of the process, the heterostructure sample is grown with an additional high composition AlGaAs metal liftoff layer above the desired structure. To define the device geometry, a thick metal mask is patterned by a conventional photoresist liftoff process. Following implantation the AlGaAs layer is selectively etched away, removing the metal mask in the process but without damaging the underlying structure.

In order to highlight the characteristics of this process, a special sample was prepared by atmospheric pressure metalorganic chemical vapor deposition.<sup>6,7</sup> The structure, grown on a (100) GaAs:*n* substrate, consists of a 0.5 μm GaAs buffer layer, a 500 Å AlAs layer, a 0.5 μm GaAs layer, and a 1 μm Al<sub>0.6</sub>Ga<sub>0.4</sub>As layer. The AlAs layer is included for reference as a marker. This marker layer facilitates a comparison of the cross section before and after selective

etching of the AlGaAs metal liftoff layer. The AlGaAs layer is much thicker for these demonstration samples than is necessary for post-implantation mask removal in order to be clearly visible in scanning electron micrographs. The process has been successfully implemented for AlGaAs layers of less than 1000 Å. The Al content of the AlGaAs has been chosen as  $x = 0.60$  to yield a short post-implantation etching time while minimizing oxidation of the AlGaAs layer.

The processing steps described here do not place a limitation on the materials used to form the metal mask. However, we have compared several materials combinations on the basis of stopping power, difficulty of evaporation of layers of sufficient thickness, ease of liftoff, and expense. We have found that a multilayer metal mask consisting of Pb/Cr/Au best meets the requirements listed above. A mask of pure gold, in addition to being expensive, is difficult to process due to inconsistencies associated with using a conventional liftoff process to define the mask pattern. Similarly, a pure lead mask has been found to be porous, allowing penetration of the implanted species into undesired areas. The Pb/Cr/Au combination provides the required stopping power with a thinner Au layer. Figure 1 is a scanning electron micrograph cross section of a masked region of the sam-

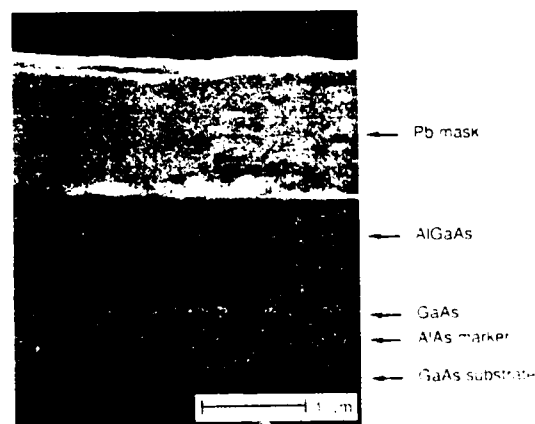


FIG. 1. Scanning electron micrograph cross-section image of an AlGaAs-GaAs heterostructure with an evaporated Pb-Cr-Au metal mask. The AlAs layer serves as a marker. For demonstration purposes the Al<sub>0.6</sub>Ga<sub>0.4</sub>As metal liftoff layer is much thicker than necessary.

<sup>a)</sup> Permanent address: Parkland College, Champaign, IL 61821

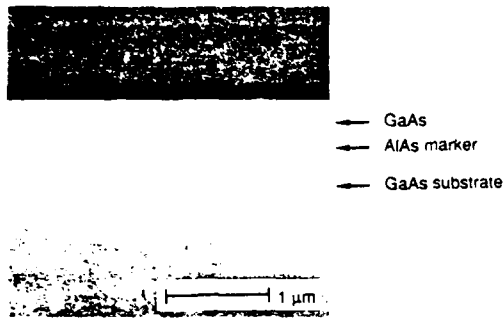


FIG. 2. Scanning electron micrograph cross-section image of the sample of Fig. 1 after the AlGaAs metal liftoff layer has been selectively removed. In the process, the metal mask is also completely removed without disturbing the underlying GaAs layer.

ple after deposition of the Pb/Cr/Au (12000 Å/300 Å/1000 Å) mask by conventional thermal evaporation and photoresist liftoff. Following the implantation, the removal of the metal mask and the AlGaAs cap layer is accomplished simply by etching the sample in hydrochloric acid for 5 min. As shown in Fig. 2, both the metal mask and the AlGaAs cap layer are completely removed. The HCl completely etches the AlGaAs metal liftoff layer, undercutting the metal mask, and causing the metal mask to lift off. The removal of the implantation mask takes place without damage to the surface of the underlying structure, since HCl selectively etches AlGaAs. Examination of the surfaces under lower-power

optical microscopy shows clear featureless surfaces after etching.

In summary, we have described a novel process to fabricate a reliable, easily removed mask for high-energy and high-dose ion implantation. The sample to be implanted is grown with an additional AlGaAs metal liftoff layer as the surface layer, upon which a metal mask is patterned by conventional photoresist liftoff techniques. Following implantation, the AlGaAs metal liftoff layer and the metal mask are removed by selectively etching the AlGaAs with HCl. Due to the selective nature of HCl the underlying epitaxial structure is left undamaged during the removal of the metal mask.

This work was supported by the National Science Foundation Engineering Research Center for Compound Semiconductor Microelectronics (CDR-85-22666), Material Research Laboratory (DMR-86-12860), and the Naval Research Laboratory (N00014-88-K-2005).

- <sup>1</sup>J. J. Coleman, P. D. Dapkus, C. G. Kirkpatrick, M. D. Camras, and N. Holonyak, Jr., *Appl. Phys. Lett.* **40**, 904 (1982).
- <sup>2</sup>B. Monemar and J. M. Blum, *J. Appl. Phys.* **48**, 1529 (1972).
- <sup>3</sup>P. D. Townsend, *Proc. SPIE* **401**, 295 (1983).
- <sup>4</sup>K. V. Vaidyanathan, R. A. Jullens, C. L. Anderson, and H. L. Dunlap, *Solid-State Electron.* **26**, 717 (1983).
- <sup>5</sup>D. J. Elliott, *Proc. SPIE* **174**, 153 (1979).
- <sup>6</sup>G. Costrini and J. J. Coleman, *J. Appl. Phys.* **57**, 2249 (1985).
- <sup>7</sup>L. M. Miller and J. J. Coleman, *CRC Crit. Rev. Solid State Mater. Sci.* **15**, 1 (1988).

( $g_{\text{GaAs}}$ ), and the TMGa vapor pressure ( $p_G$ ) allows calculation<sup>23</sup> of the vapor pressure of EDMIn,  $p_I$ , from

$$g = k(p_G F_G + p_I F_I) = g_{\text{GaAs}} + g_{\text{InAs}} \quad (1)$$

and, eliminating the chamber-dependent geometrical growth constant  $k$ ,

$$g = g_{\text{GaAs}} (1 + p_I F_I / p_G F_G). \quad (2)$$

The InGaAs growth rate  $g$  obtained from TEM data for these samples is  $\sim 93 \text{ \AA}/\text{min}$ .  $F_I$  and  $F_G$  are the EDMIn and TMGa mass flow rates and the vapor pressure of TMGa<sup>24</sup> at  $-10^\circ\text{C}$  is 39.33 Torr. From these data we calculate a vapor pressure for EDMIn of 0.56 Torr at  $11^\circ\text{C}$ . This is consistent with the reported values of  $0.7^{19}$  Torr at  $18^\circ\text{C}$  and  $0.85^{17}$  Torr at  $17^\circ\text{C}$ . The composition for these InGaAs layers ( $x = 0.25$ ) was then extracted from the molar ratio of the column III constituents  $x = p_I F_I / (p_I F_I + p_G F_G)$ .

Quantum well thickness as a function of growth time is shown in Fig. 1 for samples having nominally 40, 70, 80, 100, 120, and 140  $\text{\AA}$  wells. There were two separate growth runs for each of the 80 and 120  $\text{\AA}$  quantum wells. From these data it is clear that the growth rate of InGaAs using EDMIn is linear with growth time, indicating complete saturation of the vapor. Additionally, the repeatability of a particular structure is evidenced by the two sets of 80 and 120  $\text{\AA}$  quantum wells. Growth rates for identical samples grown at 575, 625, and  $675^\circ\text{C}$  did not appear to vary with temperature.

This collection of samples was grown over a six month period to evaluate the long-term stability of EDMIn. There has been some speculation that EDMIn may rapidly decompose into its constituents, namely, TMIIn and TEIn, within the bubbler over time or when introduced into the source gas lines if maintained at a higher temperature than the bubbler. This would probably lead to run-to-run irreproducibility and long-term instability caused by an evolving vapor pressure. Fry *et al.*<sup>17</sup> observed with mass spectrometry, however, that EDMIn consists of only a single compound, with no trace of TMIIn or TEIn. We have observed stable InGaAs growth rates over a six month period for the growth conditions described above, as illustrated in Fig. 2. During this time period a large number of other InGaAs heterostructure samples were also grown. These data indicate that EDMIn

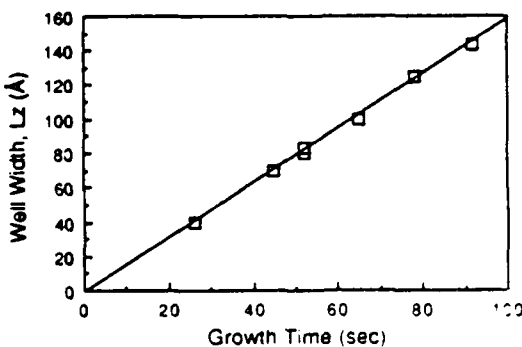


FIG. 1. In<sub>0.25</sub>Ga<sub>0.75</sub>As quantum well width vs layer growth time at  $625^\circ\text{C}$ . The growth rate for each of these wells was  $93 \text{ \AA}/\text{min}$  for EDMIn and TMGa mass flow rates of 44.2 and 2 sccm, respectively.

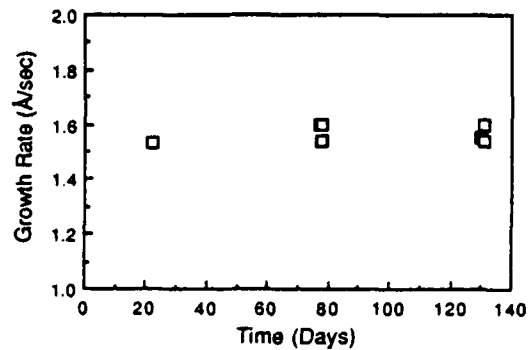


FIG. 2. In<sub>0.25</sub>Ga<sub>0.75</sub>As growth rates over the period of approximately six months for EDMIn and TMGa mass flow rates of 44.2 and 2 sccm, respectively.

has a stable vapor pressure over the time frame studied and it seems likely, based on our continued use of EDMIn, that it has a stability similar to that observed for TMGa and TMAI.

In general, the growth rate is linear with the column III precursor mass flow rate<sup>23</sup> in the diffusion-limited growth regime ( $T > 575^\circ\text{C}$ ). In a subsequent<sup>25</sup> and otherwise identical laser series, the quantum well thickness was kept constant at 70  $\text{\AA}$  while the composition was varied from In<sub>0.07</sub>Ga<sub>0.93</sub>As to In<sub>0.42</sub>Ga<sub>0.58</sub>As by changing the EDMIn mass flow rate from  $\sim 11$  to 102 sccm. The emission wavelengths for these lasers matched those predicted from composition and thickness data using the vapor pressure data obtained here for EDMIn. This implies linearity in growth rate also with flow rate for EDMIn.

The performance of these structures as lasers is a key indicator of the quality of the EDMIn source. We have seen no clear difference in laser threshold current densities for strained-layer lasers grown with either TMIIn or EDMIn and routinely observe values in the range of  $200\text{--}400 \text{ A}/\text{cm}^2$  for these single-well structures. The lowest threshold current density observed for all of the single-well strained-layer lasers we have fabricated is  $127 \text{ A}/\text{cm}^2$  (955  $\mu\text{m}$  cavity, 100  $\text{\AA}$  In<sub>0.25</sub>Ga<sub>0.75</sub>As well) from a laser grown using EDMIn. Threshold current densities for various cavity lengths for this same laser structure are shown in Fig. 3.

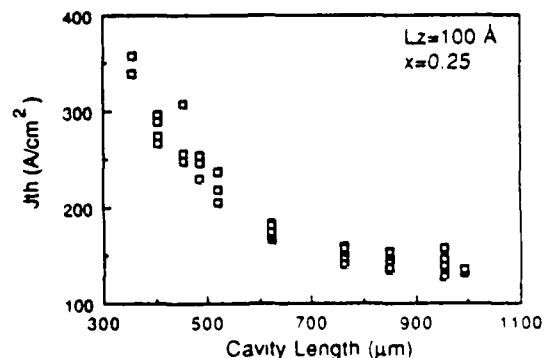


FIG. 3. Threshold current densities for various cavity lengths for an In<sub>0.25</sub>Ga<sub>0.75</sub>As-GaAs-Al<sub>0.3</sub>Ga<sub>0.7</sub>As separate-confinement strained-layer laser with a 100  $\text{\AA}$  quantum well.

# Ethyldimethylindium for the growth of InGaAs-GaAs strained-layer lasers by metalorganic chemical vapor deposition

P. K. York, K. J. Beernink, J. Kim, J. J. Coleman, G. E. Fernández, and C. M. Wayman  
*Materials Research Laboratory, University of Illinois at Urbana-Champaign, 1406 West Green Street,  
Urbana, Illinois 61801*

(Received 31 July 1989; accepted for publication 26 September 1989)

The growth and characterization of strained  $\text{In}_{0.25}\text{Ga}_{0.75}\text{As-GaAs-Al}_{0.20}\text{Ga}_{0.80}\text{As}$  quantum well lasers grown by metalorganic chemical vapor deposition using ethyldimethylindium (EDMIn) are described. A vapor pressure of 0.56 Torr at 11 °C has been extracted from the growth rates of thin InGaAs layers by transmission electron microscopy. Data on reproducibility in quantum well size are presented which indicate long-term stability in the EDMIn vapor pressure. Laser performance in samples grown with EDMIn is equivalent to, and in some cases better than, those grown with trimethylindium.

Recently, interest in strained-layer InGaAs-GaAs-AlGaAs materials has risen dramatically as a consequence of the demonstration of high performance<sup>1-11</sup> and long-lived<sup>8-11</sup> lasers. The consistency with which these lasers can be grown by metalorganic chemical vapor deposition (MOCVD) seems to be limited only by the reproducibility of the vapor pressure of the indium precursor. Many groups<sup>12-15</sup> have been successful in the use of trimethylindium (TMIn), which is a solid, at both atmospheric and low pressure, generally by operating the source and associated gas lines at elevated temperatures. However, TMIn is known<sup>16,19</sup> to convert from a powder to very large crystals over the period of a few months, thereby continually reducing the surface area available for sublimation. This reduction in surface area can make it difficult to maintain a saturated vapor for high flow rates or over long growth runs. This results in a lower effective vapor pressure, leading to a reduction in growth efficiency as well as poor composition control and irreproducibility. Ethyldimethylindium (EDMIn) is a relatively new organometallic source that has been reported<sup>16,17</sup> as a potential replacement for TMIn. The compound is comprised of an indium atom bonded to two methyl radicals ( $\text{CH}_3$ ) and a single ethyl radical ( $\text{C}_2\text{H}_5$ ), and has a vapor pressure<sup>17</sup> similar to TMIn. In contrast to TMIn, EDMIn is a liquid at room temperature, presumably free of the problems associated with solid sources. Others<sup>18</sup> have used the liquid triethylindium (TEIn), primarily at reduced pressure because of its tendency to parasitically react with the hydrides. A major advantage of EDMIn over TEIn is that it has a vapor pressure that is approximately an order of magnitude<sup>17</sup> higher. Bulk  $\text{In}_{0.41}\text{Ga}_{0.47}\text{As-InP}$  structures grown with EDMIn have been characterized<sup>16,17</sup> structurally, optically, and electrically and were found to have properties similar to samples grown with TMIn. To our knowledge, no one has reported the growth of quantum wells or device structures using EDMIn. We describe here the growth of  $\text{GaAs-Al}_{0.20}\text{Ga}_{0.80}\text{As}$  quantum well lasers with a strained  $\text{In}_{0.25}\text{Ga}_{0.75}\text{As}$  active region grown by MOCVD using EDMIn as the indium precursor. Data on reproducibility in quantum well size are presented which indicate long term stability in the EDMIn source vapor pressure. Additionally, we have extracted a vapor pressure for EDMIn which is consistent with values<sup>17,19</sup> found by others.

Epitaxial crystal growth was carried out in a vertical reaction chamber at atmospheric pressure using trimethylgallium (TMGa, -10 °C), trimethylaluminum (TMAI, 20 °C), and EDMIn (11 °C). A single bottle of EDMIn was used in this study and was purchased from Morton International-CVD, Woburn, MA. No special selection, specification, additional preparation, or purification was used. Diethylzinc and silane were used for *p*- and *n*-type dopants, respectively. A total hydrogen mass flow rate of 10.2 slpm gave a chamber gas velocity of 3.7 cm/s. The  $\text{In}_{0.25}\text{Ga}_{0.75}\text{As}$  layers were grown with TMGa and EDMIn mass flow rates of 2 and 44.2 sccm, respectively, and a V/III ratio of 147.

The laser structures described in these experiments are separate confinement quantum well heterostructures with a strained InGaAs active region. The growth consists of a 0.25  $\mu\text{m}$  *n*<sup>+</sup>-GaAs buffer layer grown on a (100) GaAs:*n*<sup>+</sup> substrate, 1.5  $\mu\text{m}$   $\text{Al}_{0.20}\text{Ga}_{0.80}\text{As}$  confining layers, a 2000 Å GaAs carrier collection and optical confinement region surrounding the active layer, and a 0.2  $\mu\text{m}$  GaAs *p*<sup>+</sup> cap layer. Each laser structure incorporates a single  $\text{In}_{0.25}\text{Ga}_{0.75}\text{As}$  quantum well with a thickness ranging between 40 and 140 Å. The buffer layer and the confining layers were grown at 720 °C while the temperature was lowered during the growth of the GaAs separate confinement region to 625 °C for the InGaAs quantum well. After growth of the structure, broad-area lasers were fabricated with oxide-defined 150  $\mu\text{m}$  stripes, cleaved into individual diodes, and tested under pulsed conditions (1.5  $\mu\text{s}$  pulse width, 2 kHz repetition rate).

Due to the constraint on InGaAs layer thicknesses (< 200 Å) imposed by misfit strain at indium compositions above 0.20,<sup>20</sup> bulk crystal measurements of composition and growth rates are not possible. Initial rough composition data and growth rates using EDMIn were obtained for thick layers of near lattice-matched InGaAs-InP. Subsequently, transmission electron microscopy (TEM) was used to determine the quantum well thicknesses for the present laser structures. Cross-sectional specimens were prepared using standard thinning and mounting techniques and examined ([110] bright field)<sup>21,22</sup> with a Philips 420 electron microscope. No threading or misfit dislocations have been observed in any of these cross-sectional specimens. Accurate knowledge of the InGaAs layer thickness, GaAs growth rate

In summary, we have investigated the growth of strained-layer quantum well lasers using EDMIn as the indium precursor. There is no indication that any parasitic gas phase reactions that would deplete the EDMIn from the gas stream are occurring. This is evidenced by linearity in the growth rates with growth time and flow rate. Also, the reproducibility in growth rates of  $\text{In}_{0.25}\text{Ga}_{0.75}\text{As}$  demonstrates long-term stability in the vapor pressure of this source, presumably due to the fact that the source is a liquid. This indicates that ethyldimethylindium is stable and does not rapidly decompose into the potential constituents, trimethylindium and triethylindium. Laser performance for samples grown with EDMIn is equivalent to, and in some cases better than those grown with TMIIn.

The authors are grateful to A. Melas, L. M. Miller, M. K. Suits, and K. Kuehl for helpful discussions and technical assistance. This work was supported by the Naval Research Laboratory (N00014-88-K-2005), the National Science Foundation (DMR 86-12860 and CDR 85-22666), and the Charles Stark Draper Laboratory (DLH 285419).

<sup>1</sup>W. D. Laidig, P. J. Caldwell, Y. F. Lin, and C. K. Peng, *Appl. Phys.* **44**, 653 (1984).

<sup>2</sup>D. Fekete, K. T. Chan, J. M. Ballantyne, and L. F. Eastman, *Appl. Phys. Lett.* **49**, 1659 (1986).

<sup>3</sup>Y. J. Yang, K. Y. Hsieh, and R. M. Kolbas, *Appl. Phys.* **51**, 215 (1987).

<sup>4</sup>J. N. Baillargeon, P. K. York, C. A. Zmudzinski, G. E. Fernández, K. J. Beernink, and J. J. Coleman, *Appl. Phys. Lett.* **53**, 457 (1988).

<sup>5</sup>P. K. York, K. J. Beernink, G. E. Fernández, and J. J. Coleman, *Appl. Phys. Lett.* **54**, 499 (1989).

<sup>6</sup>D. P. Bour, G. A. Evans, and D. B. Gilbert, *J. Appl. Phys.* **65**, 3340 (1989).

<sup>7</sup>J. S. Major, Jr., L. J. Guido, K. C. Hsieh, N. Holonyak, Jr., W. Stutius, P. Gavrilovic, and J. E. Williams, *Appl. Phys. Lett.* **54**, 913 (1989).

<sup>8</sup>W. Stutius, P. Gavrilovic, J. E. Williams, K. Meehan, and J. H. Zarrabi, *Electron. Lett.* **24**, 1493 (1988).

<sup>9</sup>S. E. Fischer, R. G. Waters, D. Fekete, J. M. Ballantyne, Y. C. Chen, and B. Soltz, *Appl. Phys. Lett.* **54**, 1861 (1989).

<sup>10</sup>R. Waters, P. K. York, K. J. Beernink, and J. J. Coleman (unpublished data).

<sup>11</sup>K. J. Beernink, P. K. York, J. J. Coleman, R. Waters, J. Kim, and C. M. Wayman, *Appl. Phys. Lett.* **55**, 2167 (1989).

<sup>12</sup>A. Mircea, R. Azoulay, L. Dugrand, R. Mellet, K. Rao, and M. Sacilotti, *J. Electron. Mater.* **13**, 603 (1984).

<sup>13</sup>C. P. Kuo, J. S. Jan, R. M. Cohen, J. Dunn, and G. B. Stringfellow, *Appl. Phys. Lett.* **44**, 550 (1984).

<sup>14</sup>K. W. Carey, *Appl. Phys. Lett.* **64**, 89 (1985).

<sup>15</sup>R. Meyer, D. Grützmacher, H. Jürgensen, and P. Balk, *J. Cryst. Growth* **93**, 285 (1988).

<sup>16</sup>J. Knauf, D. Schmitz, G. Strauch, H. Jürgensen, and M. Heyen, *J. Cryst. Growth* **93**, 34 (1988).

<sup>17</sup>K. L. Fry, C. P. Kuo, C. A. Larsen, R. M. Cohen, and G. B. Stringfellow, *J. Electron. Mater.* **15**, 91 (1986).

<sup>18</sup>J. P. Duchemin, M. Bonnet, G. Beuchet, and F. Koelsch, *Inst. Phys. Conf. Ser. No. 45*, Ch. 1, 10 (1979).

<sup>19</sup>Morton International-CVD, Andreas Melas (private communication).

<sup>20</sup>J. W. Matthews and A. E. Blakeslee, *J. Cryst. Growth* **27**, 118 (1974).

<sup>21</sup>S. J. Jeng, C. M. Wayman, G. Costrini, and J. J. Coleman, *Mater. Lett.* **2**, 359 (1984).

<sup>22</sup>K. K. Fung, P. K. York, G. E. Fernández, J. A. Eades, and J. J. Coleman, *Philos. Mag. Lett.* **57**, 221 (1988).

<sup>23</sup>D. H. Reep and S. K. Ghandi, *J. Electrochem. Soc.* **130**, 675 (1983).

<sup>24</sup>M. J. Ludowise, *J. Appl. Phys.* **58**, R31 (1985).

<sup>25</sup>K. J. Beernink, P. K. York, and J. J. Coleman, *Appl. Phys. Lett.* (to be published).

# Dependence of threshold current density on quantum well composition for strained-layer InGaAs-GaAs lasers by metalorganic chemical vapor deposition

K. J. Beernink, P. K. York, and J. J. Coleman

Compound Semiconductor Microelectronics Laboratory and Materials Research Laboratory, University of Illinois, 1406 West Green Street, Urbana, Illinois 61801

(Received 31 July 1989; accepted for publication 26 September 1989)

A series of separate confinement  $\text{In}_x\text{Ga}_{1-x}\text{As}$ -GaAs ( $0.08 < x < 0.42$ ) strained-layer quantum well lasers with 70 Å well thickness has been grown by metalorganic chemical vapor deposition. Data are presented on emission wavelengths and threshold current densities ( $J_{th}$ ) as a function of composition. A minimum in  $J_{th}$  of 140 A/cm<sup>2</sup> was observed for devices with  $\text{In}_{0.24}\text{Ga}_{0.76}\text{As}$  wells. The dependence of  $J_{th}$  on well composition is explained by a balance between strain effects and carrier confinement in the quantum well.

The use of lattice-mismatched thin layer structures in which the strain is accommodated elastically allows for greater flexibility in the design of semiconductor devices. One example is the utilization of strained-layer InGaAs active regions in AlGaAs/GaAs heterostructure laser diodes to increase the available range of wavelengths to  $\lambda \sim 1.1 \mu\text{m}$ .<sup>1-11</sup> Reports of high-power arrays,<sup>4,6</sup> cw reliability testing,<sup>7,8</sup> and low threshold current devices<sup>5,9-11</sup> indicate a strong future for strained-layer InGaAs-GaAs-AlGaAs laser diodes. The potential use of these strained-layer lasers in the 0.9–1.1  $\mu\text{m}$  wavelength range for such applications as pumping  $\text{Er}^{3+}$ -doped optical fiber amplifiers,<sup>12</sup> Nd:YAG lasers, and other solid-state hosts calls for the characterization of these structures to determine the range of practical compositions and well sizes for a particular application. In this letter we report wavelengths and threshold current densities of broad-area separate confinement heterostructure (SCH) strained-layer InGaAs quantum well laser diodes with 70 Å well thickness and indium fractions ranging from 0.08 to 0.42. The emission wavelengths of these devices agree well with values calculated from a model which accounts for strain and quantum size effects. A minimum in threshold current density  $J_{th}$  is observed for wells with an indium fraction of  $\sim 0.25$ , and devices with well compositions in a range  $0.16 < x < 0.30$  around this "optimum" composition also operated with acceptably low threshold current densities. The trend in  $J_{th}$  is explained by a balance between carrier confinement in the quantum well and strain effects.

The laser structures described here were grown by<sup>13</sup> metalorganic chemical vapor deposition (MOCVD) at atmospheric pressure in a vertical geometry reactor using ethyldimethylindium,<sup>14</sup> trimethylgallium, trimethylaluminum, and arsine. Silane and diethylzinc were used for *n*- and *p*-type dopants, respectively. Each structure consists of a 0.25- $\mu\text{m}$ -thick GaAs:*n*<sup>+</sup> buffer layer grown on a (100) GaAs:*n*<sup>+</sup> substrate, *n*- and *p*-type 1.5- $\mu\text{m}$ -thick  $\text{Al}_{0.20}\text{Ga}_{0.80}\text{As}$  confining layers surrounding a single  $\text{In}_x\text{Ga}_{1-x}\text{As}$  ( $0.08 < x < 0.42$ ) undoped strained-layer quantum well centered in a 0.2- $\mu\text{m}$ -thick GaAs carrier collection layer, and a 0.2  $\mu\text{m}$  GaAs:*p*<sup>+</sup> contact layer. Six different laser structures were grown sequentially with nominal  $\text{In}_x\text{Ga}_{1-x}\text{As}$  well compositions of  $x = 0.08, 0.16, 0.20, 0.24, 0.33,$  and 0.42.

Standard processing was used to fabricate 150- $\mu\text{m}$ -wide

oxide-defined stripes on each sample. The substrates were lapped and polished to a thickness of approximately 125  $\mu\text{m}$ , and *n*-type contacts were formed by evaporating 250 Å Ge/2000 Å Au and alloying for 10 s at 400 °C. Nonalloyed 300 Å Cr/1500 Å Au contacts were evaporated on the *p* side. Various cavity lengths were formed by cleaving, and the resulting bars were cleaved into individual diodes for testing. Devices were tested under pulsed conditions (1.5  $\mu\text{s}$  pulse width, 2 kHz repetition rate) at room temperature.

The emission wavelengths of devices with 815- $\mu\text{m}$ -long cavities are shown as circles in Fig. 1. Devices with the largest indium fraction in this study ( $\text{In}_{0.42}\text{Ga}_{0.58}\text{As}$  wells) emitted only very weak spontaneous emission for drive currents up to 2 A and we were unable to measure the wavelength of this light. There is good agreement between the measured wavelengths and the calculated values represented by the line in Fig. 1. The calculation of wavelength follows that of Pan *et al.*,<sup>15</sup> and accounts for both quantum size effects and the strain-induced shift of the InGaAs band-gap energy. The unstrained band gap used in these calculations is<sup>16</sup>

$$E_g(\text{In}_x\text{Ga}_{1-x}\text{As}) = 1.42 - 1.615x + 0.555x^2 \text{ eV.}$$

All other material parameters were from Ref. 15. A 70/30 split of the heterojunction discontinuity between conduction and valence bands was assumed in the calculation.

The measured threshold current density  $J_{th}$  as a function of well composition for 815- $\mu\text{m}$ -long devices is shown in Fig. 2. Note that all devices with  $\text{In}_{0.42}\text{Ga}_{0.58}\text{As}$  wells failed

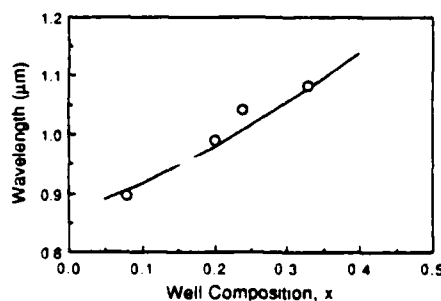


FIG. 1. Calculated and experimental emission wavelengths for  $150 \times 815 \mu\text{m}^2$  devices with 70 Å  $\text{In}_x\text{Ga}_{1-x}\text{As}$  quantum wells.

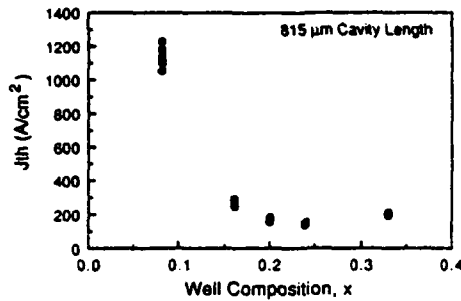


FIG. 2. Threshold current density  $J_{th}$  as function of well composition for  $150 \times 815 \mu\text{m}^2$  devices with  $70 \text{ \AA}$   $\text{In}_x\text{Ga}_{1-x}\text{As}$  quantum wells.

to reach threshold at 2 A, which places  $J_{th}$  for these devices at a value greater than  $1.6 \text{ kA/cm}^2$ , which is off the scale of Fig. 2. The trend in this figure is the same for all cavity lengths tested. Figure 3 shows the variation of  $J_{th}$  with cavity length for devices with  $\text{In}_{0.20}\text{Ga}_{0.80}\text{As}$  wells. These devices exhibit the usual increase in  $J_{th}$  with decreasing cavity length as a result of proportionally increasing end losses.

The minimum in  $J_{th}$  versus composition of  $140 \text{ A/cm}^2$  at an indium fraction of approximately 0.25 in Fig. 2 is explained by the consideration of two effects. For low indium fraction in the wells, the carriers are poorly confined, while for high indium fractions the effects of strain result in increased  $J_{th}$ . The two competing effects are shown in Fig. 4. For low indium fraction in the wells, the confining energy  $\Delta E_{conf}$  between the bound state of electrons in the conduction band and the GaAs barriers is small.  $\Delta E_{conf}$  is shown versus well composition in Fig. 4(a), and was calculated from the same model as the wavelengths of Fig. 1. From a simple argument concerning carrier distributions, it is reasonable to expect that a confining energy of at least a few  $kT$  ( $\sim 75 \text{ meV}$ ) is necessary to have good carrier confinement in the well. Smaller confining energies result in a significant portion of the electron population in the active region having energies greater than the barrier height, and a corresponding higher density of electrons in the barriers. Similar considerations apply to the confinement of holes in the valence band, but the higher density of states reduces the effect. Since the barriers have a much larger volume than the well, a significantly larger current density would then be required to supply the necessary carriers to the barriers to reach a threshold carrier density in the well. For devices with  $\text{In}_{0.08}\text{Ga}_{0.92}\text{As}$  wells, the electrons are poorly confined since  $\Delta E_{conf}$  ( $\sim 30$

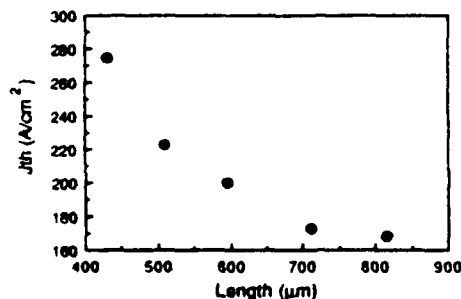


FIG. 3. Cavity length dependence of threshold current density for  $150\text{-}\mu\text{m}$ -wide stripe broad-area devices with  $70 \text{ \AA}$   $\text{In}_{0.20}\text{Ga}_{0.80}\text{As}$  quantum wells. Devices with other well compositions exhibited the same behavior.

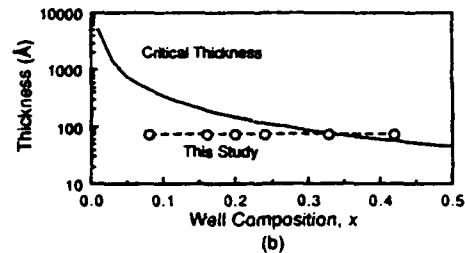
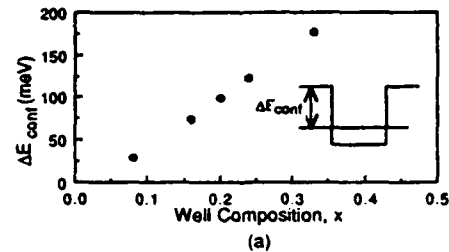


FIG. 4. Factors influencing  $J_{th}$ : (a) calculated confining energy  $\Delta E_{conf}$  for electrons in the conduction band and (b) critical thickness calculated for  $\text{In}_x\text{Ga}_{1-x}\text{As}$  layer sandwiched between GaAs layers (solid line). Quantum well thicknesses for this study (open circles) are shown for comparison.

$\text{meV}$ ) is only of the order of  $kT$ . For these devices,  $J_{th}$  of  $1.1 \text{ kA/cm}^2$  is very high compared to  $J_{th}$  of  $265 \text{ A/cm}^2$  for devices with  $\text{In}_{0.16}\text{Ga}_{0.84}\text{As}$  wells and a confining energy of  $75 \text{ meV}$ . As the indium fraction in the wells is increased and the well is made deeper, the state is better confined, and this operates to decrease  $J_{th}$ . The results for low indium fraction in the wells agree qualitatively with those of Hersee *et al.*<sup>17</sup> for AlGaAs-GaAs graded refractive index separate confinement heterostructure quantum well lasers where a steep increase in  $J_{th}$  was observed as the aluminum fraction in the barriers was reduced below 15%.

$J_{th}$  continues to decrease for wells with indium content up to  $\sim 0.25$ . As the indium fraction of the wells increases beyond this point, the effects of strain begin to adversely affect the laser performance for the  $70\text{-}\text{\AA}$ -wide wells of this study. Figure 4(b) shows the critical thickness  $h_c$  calculated for a sandwiched layer from the mechanical equilibrium model of Matthews and Blakeslee.<sup>18,19</sup> Circles corresponding to the  $70 \text{ \AA}$  wells of this study are also shown for comparison to the critical thickness. For  $70\text{-}\text{\AA}$ -thick wells with indium fraction below  $\sim 0.25$ , the strained active region thickness is well below the critical thickness as calculated from this model. For higher indium mole fractions in the well, the thickness of the active region approaches or exceeds the calculated critical thickness, and the deleterious effects of the strain become evident as  $J_{th}$  increases. This may be the result of dislocations in the strained-layer active region which act as nonradiative recombination centers.

For the  $70\text{-}\text{\AA}$ -thick wells of this study, the lowest threshold current density is observed for devices with  $\sim 0.25$  indium in the well. The combination of well composition and thickness for these devices is such that the electrons are adequately confined in the well ( $\Delta E_{conf} \sim 160 \text{ meV}$ ), and the thickness of the strained-layer active region is comfortably below the critical thickness. Note that for all devices with well compositions in the range from  $x \sim 0.16$  to  $x \sim 0.33$ ,  $\Delta E_{conf}$  is greater than  $75 \text{ meV}$ , and the well thickness is be-

low the calculated critical thickness. The performance of devices in this range ( $\sim 0.16$ – $\sim 0.33$ ) did not differ dramatically from those with the "optimal" composition, and only outside this range is there a sharp increase in  $J_{th}$ . Since the above discussion of carrier confinement and strain effects would apply to any combination of well size and composition, we expect other strained-layer quantum well lasers with confining energies greater than 75 meV and strained-layer thicknesses below the critical thickness to perform well. This suggests that there is some freedom in the choice of well thicknesses and compositions that will yield low threshold, high efficiency operation at a given design wavelength.

The thickness of the  $\text{In}_{0.33}\text{Ga}_{0.67}\text{As}$  well is very near (within 5%) the calculated critical thickness for that composition, and although they are less efficient than devices having a lower indium fraction in the wells, these devices still performed well.  $J_{th}$  for  $150 \times 815 \mu\text{m}$  devices with  $\text{In}_{0.33}\text{Ga}_{0.67}\text{As}$  active regions was  $202 \text{ A/cm}^2$  (and  $310 \text{ A/cm}^2$  for  $150 \times 470 \mu\text{m}$  devices). Although, as discussed above, it is desirable to remain below the critical thickness in order to achieve the lowest thresholds and highest efficiencies, this is consistent with previous results in our laboratory<sup>7</sup> which show that high performance lasers can be grown with strained-layer active region thicknesses slightly greater than the critical thickness predicted by Matthews and Blakeslee's mechanical equilibrium model.

In summary, we have reported results of time-zero characterization of strained-layer  $\text{In}_x\text{Ga}_{1-x}\text{As}$ -GaAs quantum well heterostructure laser diodes with 70-Å-thick wells and indium mole fractions between 0.08 and 0.42. The emission wavelengths ranged from 0.9 to  $1.08 \mu\text{m}$  and agreed well with calculated values. A minimum in threshold current density is observed for devices having an indium fraction of  $\sim 0.25$  in the wells, and devices with well compositions in the range  $\sim 0.16 < x < \sim 0.30$  all operated with low threshold current densities. The data support two design criteria for low threshold operation of strained-layer  $\text{InGaAs}$ -GaAs quantum well lasers: (1) The electrons should be confined by at least  $\sim 75 \text{ meV}$  in the conduction band and (2) the strained-layer active region thickness should not greatly ex-

ceed the critical thickness for a sandwiched layer as given by the mechanical equilibrium model of Matthews and Blakeslee.

The authors are grateful to R. P. Bryan, L. M. Miller, S. M. Langsjoen, M. K. Suits, and K. Kuehl for helpful discussions and technical support. This work was supported by the Naval Research Laboratory (N00014-88-K-2005), the National Science Foundation (DMR 86-12860 and CDR 85-22666), and the Charles Stark Draper Laboratory (DLH 285419).

<sup>1</sup>W. D. Laidig, P. J. Caldwell, Y. F. Lin, and C. K. Peng, *Appl. Phys. Lett.* **44**, 653 (1984).

<sup>2</sup>D. Fekete, K. T. Chan, J. M. Ballantyne, and L. F. Eastman, *Appl. Phys. Lett.* **49**, 1659 (1986).

<sup>3</sup>Y. J. Yang, K. Y. Hsieh, and R. M. Kolbas, *Appl. Phys. Lett.* **51**, 215 (1987).

<sup>4</sup>J. N. Baillargeon, P. K. York, C. A. Zmudzinski, G. E. Fernández, K. J. Beernink, and J. J. Coleman, *Appl. Phys. Lett.* **53**, 457 (1988).

<sup>5</sup>P. K. York, K. J. Beernink, G. E. Fernández, and J. J. Coleman, *Appl. Phys. Lett.* **54**, 499 (1989).

<sup>6</sup>D. P. Bour, P. Stabile, A. Rosen, W. Janton, L. Elbaum, and D. J. Holmes, *Appl. Phys. Lett.* **54**, 2637 (1989).

<sup>7</sup>K. J. Beernink, P. K. York, J. J. Coleman, R. G. Waters, J. Kim, and C. Wayman, *Appl. Phys. Lett.* **55**, 2167 (1989).

<sup>8</sup>S. E. Fischer, R. G. Waters, D. Fekete, J. M. Ballantyne, Y. C. Chen, and B. Soltz, *Appl. Phys. Lett.* **54**, 1861 (1989).

<sup>9</sup>J. S. Major, Jr., L. J. Guido, K. C. Hsieh, N. Holonyak, Jr., W. Stutius, P. Gavrilovic, and J. E. Williams, *Appl. Phys. Lett.* **54**, 913 (1989).

<sup>10</sup>S. D. Offsey, W. J. Schaff, P. J. Tasker, H. Ennen, and L. F. Eastman, *Appl. Phys. Lett.* **54**, 2527 (1989).

<sup>11</sup>S. E. Fischer, D. Fekete, G. B. Feak, and J. M. Ballantyne, *Appl. Phys. Lett.* **50**, 714 (1987).

<sup>12</sup>R. I. Laming, M. C. Farries, P. R. Morkel, L. Reekie, and D. N. Payne, *Electron. Lett.* **25**, 12 (1989).

<sup>13</sup>G. Costrini and J. J. Coleman, *J. Appl. Phys.* **57**, 2249 (1985).

<sup>14</sup>K. L. Fry, C. P. Kuo, C. A. Larsen, R. M. Cohen, G. B. Stringfellow, and A. Melas, *J. Electron. Mater.* **15**, 91 (1986).

<sup>15</sup>S. H. Pan, H. Shen, Z. Hang, F. H. Pollak, W. Zhuang, Q. Xu, A. P. Roth, R. A. Masut, C. Lacelle, and D. Morris, *Phys. Rev. B* **38**, 3375 (1988).

<sup>16</sup>S. Adachi, *J. Appl. Phys.* **53**, 8775 (1982).

<sup>17</sup>S. D. Hersee, B. de Cremoux, and J. P. Duchemin, *Appl. Phys. Lett.* **44**, 476 (1984).

<sup>18</sup>J. W. Matthews and A. E. Blakeslee, *J. Cryst. Growth* **27**, 118 (1974).

<sup>19</sup>I. J. Fritz, S. T. Picraux, L. R. Dawson, T. J. Drummond, W. D. Laidig, and N. G. Anderson, *Appl. Phys. Lett.* **46**, 967 (1985).

# **High-Power Pulsed Operation of an Optimized Nonplanar Corrugated Substrate Periodic Laser Diode Array**

**R. P. Bryan  
L. M. Miller  
T. M. Cockerill  
S. M. Langsjoen  
J. J. Coleman**

**Reprinted from  
IEEE JOURNAL OF QUANTUM ELECTRONICS  
Vol. 26, No. 2, February 1990**

## High-Power Pulsed Operation of an Optimized Nonplanar Corrugated Substrate Periodic Laser Diode Array

R. P. BRYAN, L. M. MILLER, T. M. COCKERILL, S. M. LANGSJOEN, AND J. J. COLEMAN

**Abstract**—High-power pulsed operation of 14.1 W per uncoated facet from an optimized 3 mm wide (510  $\mu\text{m}$  cavity length) nonplanar corrugated substrate periodic laser diode array is reported. Single-step metalorganic chemical vapor deposition growth over a selectively etched corrugated substrate provides suppressed lateral lasing and amplified spontaneous emission with a minimal number of processing steps. Higher external differential quantum efficiency, slope efficiency, and output power result from a design optimization with regard to the widths of the mesas and grooves of the corrugated substrate.

**M**ONOLITHIC multiple-stripe laser arrays have great potential as sources for high-power, high-efficiency operation. Applications for such devices include pumping of neodymium:yttrium aluminum garnet lasers [1], high-speed optical recording, and long-distance transmission. Although the maximum output optical power attainable from multiple-stripe laser diodes has increased dramatically in recent years, high-power operation is limited [2] by catastrophic optical degradation (COD). By increasing the aperture width of a laser diode, the intensity decreases for a given output power and, therefore, the total power at which COD occurs is increased. However, the maximum aperture width is generally restricted to being less than the cavity length because, as the width of the laser is made larger than the cavity length, lateral lasing and amplified spontaneous emission (ASE) become significant and the desired front facet emission is reduced. Lateral lasing and ASE can be suppressed by forming isolated regions of emitters thereby disrupting the propagation of the lateral modes. Previously reported [3]–[4] methods for achieving isolation require processing steps in addition to those required to form the actual array elements and also result in a portion of the array width which does not contribute to the laser output. In this letter we report optimized high-power, high-efficiency operation of a nonplanar multiple-stripe corrugated substrate laser array utilizing a graded-barrier quantum well (GBQW) [5], [6] structure. Metalorganic chemical vapor deposition

(MOCVD) growth on a corrugated substrate is utilized [7]–[10] to form a nonplanar active region which effectively inhibits lateral lasing and ASE for the entire array. No additional processing steps, which may result in accelerated degradation due to the introduction of material defects, are required. Data presented within on the high-power pulsed operation (14.1 W per uncoated facet) of an optimized 3 mm wide corrugated substrate laser array represent a substantial improvement in device performance characteristics over previously obtained results on similar structures [7], [8], [11]. We report an increased maximum output power and linear power density; a highly uniform emission intensity across the structure; and a 40 percent improvement in the slope efficiency and differential quantum efficiency.

The GBQW structures were grown using an atmospheric MOCVD [12] system at 800°C following corrugated substrate preparation described previously [7]. The structure consists of a (100) GaAs:n substrate and buffer layer, a linearly graded AlGaAs:n layer, 1.0  $\mu\text{m}$  Al<sub>0.85</sub>Ga<sub>0.15</sub>As confining layers, a 2400 Å Al<sub>x</sub>Ga<sub>1-x</sub>As parabolically graded ( $x = 0.85$  to 0.20) region, a 50 Å GaAs quantum well, and a GaAs:p<sup>+</sup> contact layer. The corrugated contours of the etched substrate are maintained throughout the epitaxial growth providing uniform formation of the active region (see Fig. 1) [7]–[9]. The nonplanar active region disrupts the propagation of the lateral cavity modes and no additional processing or photolithographic steps are necessary to either define current injection or to inhibit ASE or lateral lasing after the MOCVD growth. For comparison, 150  $\mu\text{m}$  wide oxide stripe broad area lasers were fabricated from planar structures grown concurrently with each of the nonplanar substrates. The devices were mounted p side down in indium solder on Cu blocks with multiple Au wires to contact the n side and were tested using a 1 kHz pulsed current with a pulse duration of 225 ns. The facets of the devices described in this letter were left uncoated.

A typical near-field optical intensity pattern from a section of the nonplanar laser array is illustrated in Fig. 2. Shown also in Fig. 2 for reference as a dashed line is the relative size and position of the laser active region. The observed near-field pattern is uniformly distributed over the entire array width and is stable over a wide range of drive currents. Note that the emission is entirely from a double peak on each mesa [8], [9]. As a consequence of the negligible emission from the grooves there is a reduction in the efficiency [9] of nonplanar lasers relative to

Manuscript received July 27, 1989; revised October 2, 1989. This work was supported in part by Strategic Defense Initiative Organization/IST under Contract DAAL03-87-K-0013 by the Naval Research Laboratory under Contract N00014-88-K-2005, and by the National Science Foundation Engineering Research Center for Compound Semiconductor Microelectronics under Contract CDR 85-22666. The work of R. P. Bryan was supported in part by an AT&T Doctoral Fellowship. The work of T. M. Cockerill was supported in part by a Hughes Fellowship.

The authors are with the Compound Semiconductor Microelectronics Laboratory and the W. L. Everitt Laboratory, University of Illinois at Urbana-Champaign, Urbana, IL 61801.

IEEE Log Number 8932611

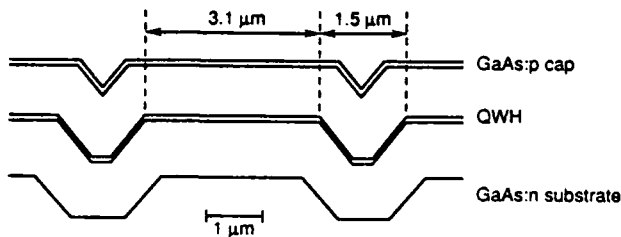


Fig. 1. Schematic diagram of the nonplanar periodic laser array grown by MOCVD on a corrugated etched substrate. The uniform MOCVD growth over the nonplanar substrates results in a nonplanar active region which suppresses lateral lasing and ASE, and is conducive to the simple fabrication of very wide laser arrays.

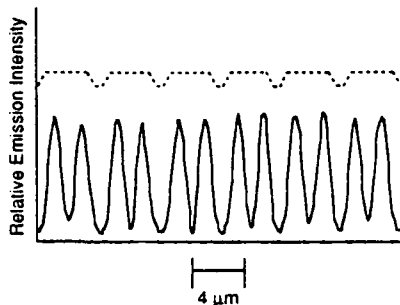


Fig. 2. Near-field intensity pattern at  $2 \times I_{th}$  from a section of a nonplanar periodic laser array of width 1 mm and cavity length 510  $\mu\text{m}$ . The widths of the mesas and the grooves are 3.1 and 0.5  $\mu\text{m}$ , respectively. Shown also for reference as a dashed line is the relative position of the laser active region. The intensity pattern illustrates the two emission peaks per mesa and also the uniformity of the intensity across the device.

planar lasers which is less, however, than expected from geometric considerations. Although Waters *et al.* [11] attributed the reduced emission in the grooves of their devices (200  $\mu\text{m}$  wide mesas and grooves) to an etching problem, we propose an alternative explanation for narrow-stripe structures. Theoretical modeling [13] of these structures indicates a nonuniform current distribution resulting from the nonplanar geometry and differing hole and electron mobilities. This, along with the difference [9] in the recombination lifetimes in the mesa region (stimulated) and the groove region (spontaneous), results in a strong predilection for emission to occur on the mesas rather than in the grooves.

Increasing the width of the mesas should also increase the quantum efficiency of the devices; however, there exists an upper limit of the width ( $\sim 4 \mu\text{m}$ ) of the mesas, above which the lateral mode is no longer stabilized. Optimization of the overlap between the current distribution and the optical field should also increase the quantum efficiency. For this structure, the overlap of the optical field with the carrier distribution is greater for a fundamental lateral mode than for a doubled peak mode if one assumes a uniform carrier distribution across the mesas. Consequently, a reduction of the confining layer composition [14] with the corresponding decrease in the lateral index step should favor oscillation in a fundamental mode. However, a lower confining layer composition results in an increased threshold current density. Thus, an opti-

mized structure would consist of grooved regions that are as small as possible while still providing disruption of lateral lasing and ASE, and of mesa regions that are as large as possible while still favoring stable lateral mode operation.

The data in Table I show the upper and lower bounds of the average threshold current density of the nonplanar laser arrays, the external differential quantum efficiency (both facets), and the light-current ( $L-I$ ) slope efficiency for nonplanar lasers for three different mesa and groove width geometries along with the concurrently grown planar lasers. The upper bound of the threshold current density was calculated using the area of only the mesa regions and the lower bound was calculated using the complete surface area of the devices. For each laser structure the quantum efficiency and the  $L-I$  slope efficiency of the planar broad area lasers is higher than the efficiency of the nonplanar lasers. As expected from the discussion above, the structure having the smallest relative groove width most closely approaches the broad area efficiency.

Fig. 3 shows the  $L-I$  curve from an uncoated facet of a typical laser array with a cavity length of 510  $\mu\text{m}$ , a width of 3000  $\mu\text{m}$ , a mesa width of 3.1  $\mu\text{m}$ , and a groove width of 0.5  $\mu\text{m}$ . The maximum observed power of 14.1 W per facet of these devices is limited by the maximum output of our current pulser (40 A) and not by device degradation. In principle, output powers in excess of 150 W per facet could be expected from a device having reflection and antireflection coatings [3]. The low threshold current density of these laser arrays results in a significantly lower threshold current (2–3 A) for widths up to 3 mm compared to values reported [3], [4] for multiple quantum well structures which utilized etched grooves to suppress ASE and lateral lasing.

In summary, optimized nonplanar multiple-stripe corrugated substrate laser array structures grown by MOCVD have been shown to inhibit lateral lasing and ASE as a consequence of the nonplanar active region. The external differential quantum efficiency and light-current slope efficiency of the optimized corrugated substrate laser array represent a 40 percent improvement compared to previously reported devices [7], [8], [11]. The highest efficiency devices are obtained from laser arrays having the smallest grooves while still disrupting lateral lasing and ASE. This is a consequence of laser emission dominant on the mesa, which is a result of the geometry and the nonuniform current distribution. Furthermore, the typical maximum attainable output power (14.1 W for a 3 mm aperture at 40 A) and linear power density exceeds our nonoptimized devices (8 W for a 3 mm aperture at 40 A) and the best device reported by Waters *et al.* [11] (9.2 W for a 2 mm aperture at 40 A). The optimized structure also resulted in a highly uniform emission intensity across the device ( $\pm 6$  percent of the average value) which is a marked improvement compared to our nonoptimized devices ( $\pm 15$  percent) and the best device of Waters *et al.* [11] ( $\pm 30$  percent). Higher emission uniformity as well as stable near-field patterns may be attributed to index-

TABLE I

Mesa Width ( $\mu\text{m}$ )	Groove Width ( $\mu\text{m}$ )	Threshold Current Density ( $\text{A}/\text{cm}^2$ )		Quantum Efficiency (Percent)		Slope Efficiency ( $\text{W}/\text{A}$ )	
		Upper	Lower	Planar	Nonplanar	Planar	Nonplanar
3.6	3.2	351	158	55	31	0.8	0.5
2.8	3.9	629	223	43	21	0.7	0.3
3.1	0.5	246	166	55	44	0.8	0.7

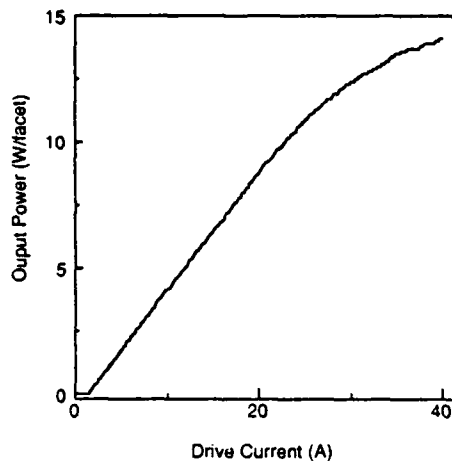


Fig. 3. Light output power versus drive current from a single uncoated facet of a 3 mm periodic laser array with a cavity length of  $510 \mu\text{m}$ . The widths of the mesas and the grooves are  $3.1$  and  $0.5 \mu\text{m}$ , respectively. The maximum output power of  $14.1 \text{ W}$  is limited by the current source and not COD.

guided operation [7], [9] in the small-period devices compared to gain-guiding operation of large-period devices [11].

#### REFERENCES

- [1] D. L. Sipes, "Highly efficient neodymium: yttrium aluminum garnet laser end pumped by a semiconductor laser array," *Appl. Phys. Lett.*, vol. 47, pp. 74-76, 1985.
- [2] C. H. Henry, P. M. Petroff, R. A. Logan, and F. R. Merritt, "Catastrophic damage of  $\text{Al}_x\text{Ga}_{1-x}\text{As}$  double-heterostructure laser material," *J. Appl. Phys.*, vol. 50, pp. 3721-3732, 1979.
- [3] G. L. Hamagel, P. S. Cross, C. R. Lennon, M. DeVito, and D. R. Scifres, "Ultra-high-power quasi-CW monolithic laser diode arrays with high power conversion efficiency," *Electron. Lett.*, vol. 23, pp. 743-744, 1987.
- [4] G. L. Hamagel, P. S. Cross, D. R. Scifres, D. F. Welch, C. R. Lennon, D. P. Worland, and R. D. Burnham, "High-power quasi-CW monolithic laser diode linear arrays," *Appl. Phys. Lett.*, vol. 49, pp. 1418-1419, 1986.
- [5] W. T. Tsang, "A graded-index separate-confinement laser with very low threshold current and a narrow Gaussian beam," *Appl. Phys. Lett.*, vol. 39, pp. 134-137, 1981.
- [6] L. J. Mawst, M. E. Givens, C. A. Zmudzinski, M. A. Emanuel, and J. J. Coleman, "Optimization and characterization of index-guided visible  $\text{AlGaAs}/\text{GaAs}$  graded barrier quantum well laser diodes," *IEEE J. Quantum Electron.*, vol. QE-23, pp. 696-703, 1987.
- [7] C. A. Zmudzinski, M. E. Givens, R. P. Bryan, and J. J. Coleman, "Nonplanar index-guided quantum well heterostructure periodic laser array," *Appl. Phys. Lett.*, vol. 53, pp. 350-352, 1988.
- [8] M. E. Givens, C. A. Zmudzinski, R. P. Bryan, and J. J. Coleman, "High-power nonplanar quantum well heterostructure periodic laser arrays," *Appl. Phys. Lett.*, vol. 53, pp. 1159-1161, 1988.
- [9] C. A. Zmudzinski, M. E. Givens, R. P. Bryan, and J. J. Coleman, "Optical characteristics of high-power nonplanar periodic laser arrays," *IEEE J. Quantum Electron.*, vol. 25, pp. 1539-1546, 1989.
- [10] T. Suyama, T. Hayakawa, K. Takahashi, and S. Yamamoto, "Semiconductor laser array device," U.S. Patent 4 737 959, Apr. 12, 1988.
- [11] R. G. Waters, R. J. Dalby, and M. A. Emanuel, "Full-aperture, high-power semiconductor laser," *Appl. Phys. Lett.*, vol. 54, pp. 2534-2535, 1989.
- [12] L. M. Miller and J. J. Coleman, "Metalorganic chemical vapor deposition," *CRC Crit. Rev. Solid State Mater. Sci.*, vol. 15, pp. 1-26, 1988.
- [13] S. M. Lee, S.-L. Chuang, R. P. Bryan, and J. J. Coleman, unpublished data.
- [14] D. E. Ackley and G. Hom, "Twin-channel substrate-mesa-guide injection lasers fabricated by organometallic vapor phase epitaxy," *Appl. Phys. Lett.*, vol. 42, pp. 653-656, 1983.

# PROCEEDINGS REPRINT

 SPIE—The International Society for Optical Engineering

*Reprinted from*

## Laser-Diode Technology and Applications II

16-19 January 1990  
Los Angeles, California



Volume 1219

©1990 by the Society of Photo Optical Instrumentation Engineers  
Box 10, Bellingham, Washington 98227 USA. Telephone 206/676-3290.

## InGaAs-GaAs strained layer quantum well heterostructure lasers

J. J. Coleman, P. K. York and K. J. Beernink

Materials Research Laboratory and  
Compound Semiconductor Microelectronics Laboratory  
University of Illinois, 1406 West Green Street, Urbana, IL 61801

and

R. G Waters

McDonnell-Douglas Electronic Systems Company, 350 Executive Blvd, Elmsford, NY 10523

### ABSTRACT

InGaAs-GaAs strained layer quantum well heterostructure lasers offer availability of emission wavelengths in the range of 0.9-1.1  $\mu\text{m}$  otherwise largely inaccessible with semiconductor diode lasers. We describe here InGaAs-GaAs strained layer lasers and laser arrays grown by atmospheric pressure metalorganic chemical vapor deposition (MOCVD). The growth conditions for preparing these strained layer structures by MOCVD are presented and time zero characterization of oxide defined stripe broad area lasers as a function of InGaAs layer composition and thickness, relative to the critical thickness, will be outlined. Various structures, grown throughout the 0.9-1.1  $\mu\text{m}$  wavelength range and having In mole fractions from  $x=0-0.50$ , are shown to have low broad area threshold current densities ( $J_{\text{th}} < 200 \text{ A/cm}^2$ ) and other characteristics of unstrained quantum well heterostructure lasers. Recent results indicating highly reliable cw operation of oxide stripe strained quantum well heterostructure lasers are reviewed.

### 2. INTRODUCTION

The use of lattice-mismatched thin layer structures in which the strain is accommodated elastically, such as the utilization of strained layer InGaAs active regions in AlGaAs/GaAs heterostructure laser diodes, allows extension of the available range of emission wavelengths to  $\lambda \sim 1.1 \mu\text{m}^{1-12}$ . The potential use of these strained layer lasers in the 0.9  $\mu\text{m}$  - 1.1  $\mu\text{m}$  wavelength range for such applications as pumping rare earth doped optical fiber amplifiers<sup>13</sup> requires the characterization of these structures to determine the range of practical compositions and well sizes for a particular application. The key practical issue for these laser devices is the relative stability of the strained layer. When the strained layer active region of these devices is sufficiently thin, the mismatch strain is accommodated elastically, and the strained layer remains commensurate with the substrate. Above a compositionally dependent critical thickness<sup>14,15</sup>, however, it becomes energetically favorable for the strained layer to relax, forming misfit dislocations which degrade device performance. There is disagreement<sup>16</sup> over the actual value of the critical thickness, with some materials study data supporting the mechanical equilibrium model<sup>14</sup> of Matthews and Blakeslee, while other results are in better agreement with the values predicted by the energy balance model<sup>15</sup> of People and Bean. In this work we have studied the time zero laser characteristics of broad area separate confinement heterostructure (SCH) strained layer InGaAs quantum well laser diodes with a fixed 70  $\text{\AA}$  well thickness and indium fractions ranging from 0.08 to 0.42, and a fixed well In-composition ( $x = 0.25$ ) and quantum well thicknesses of 100, 125, and 143  $\text{\AA}$ .

### 3. STRUCTURE, EPITAXIAL GROWTH AND PROCESSING

The laser structures described here were grown<sup>17</sup> by metalorganic chemical vapor deposition (MOCVD) at atmospheric pressure in a vertical geometry reactor using ethyldimethylindium<sup>18</sup> (EDMIn), trimethylgallium (TMGa), trimethylaluminum (TMAI), and arsine. Silane and diethylzinc were used for *n*- and *p*-type dopants, respectively. Each structure consists of a 0.25- $\mu\text{m}$ -thick GaAs:*n*<sup>+</sup> buffer layer grown on a (100) GaAs:*n*<sup>+</sup> substrate, *n*- and *p*-type 1.5- $\mu\text{m}$ -thick Al<sub>0.20</sub>Ga<sub>0.80</sub>As confining layers, an active region, and a 0.2- $\mu\text{m}$  GaAs:*p*<sup>+</sup> contact layer, as shown in Fig. 1a. The separate confinement quantum well heterostructure active region, shown in Fig. 1b, consists of an In<sub>*x*</sub>Ga<sub>1-*x*</sub>As (*x* ~ 0.08-0.42) undoped

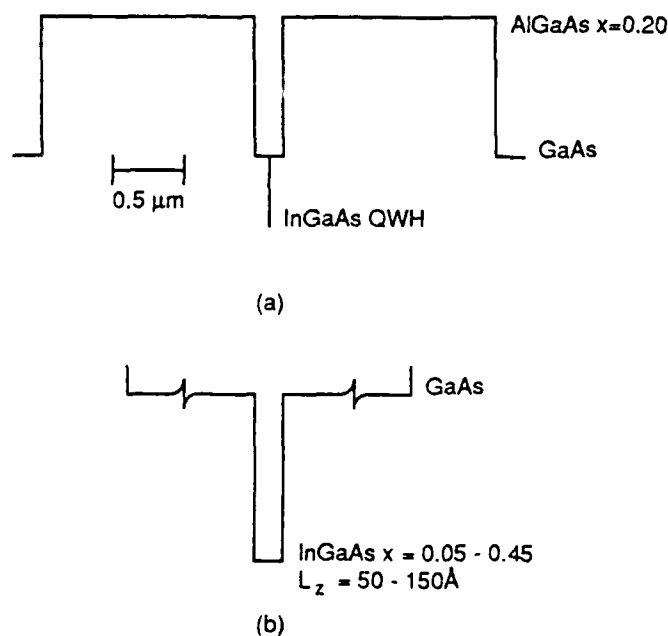


Figure 1

strained layer quantum well centered in a 0.2- $\mu\text{m}$ -thick GaAs carrier collection layer. The compositions of the  $L_z = 70\text{\AA}$  quantum wells were determined from the vapor pressure for EDMIn, obtained from the growth rate of the quantum wells, and the vapor pressure of TMGa. The thicknesses of the  $x \sim 0.25$  quantum wells for the three samples were measured by transmission electron microscopy using standard thinning and mounting techniques<sup>19</sup> and were found to be 100, 125, and 143  $\text{\AA}$ . No threading or misfit dislocations were observed in these cross-section specimens. Standard processing was used to fabricate 150  $\mu\text{m}$  wide oxide-defined stripes on each sample. Various cavity lengths were formed by cleaving, and the resulting bars were cleaved into individual diodes for testing. Devices were tested under pulsed conditions (1.5  $\mu\text{sec}$  pulse-width, 2 kHz repetition rate) at room temperature. Standard processing was also used to define 60  $\mu\text{m}$  wide oxide-defined stripes for cw life-testing. These uncoated devices, 600  $\mu\text{m}$  long, were mounted junction up on a copper heat sink.

### 4. RESULTS

Shown in Fig. 2 is the critical thickness for InGaAs strained layers on GaAs versus In-composition according to the models of Matthews and Blakeslee<sup>14</sup> (dashed line) and Peoples and Bean<sup>15</sup> (solid line).

Shown also for reference in Fig. 2 are data points corresponding to this work for six 70Å quantum well laser structures having varying composition (squares) and for three  $x \sim 0.25$  laser structures having varying well widths (circles). The measured threshold current density,  $J_{th}$ , as a function of well composition in the range  $x = 0.10-0.40$  ( $L_z = 70\text{\AA}$ , length 815  $\mu\text{m}$ ) is shown in Fig. 3. All of the devices

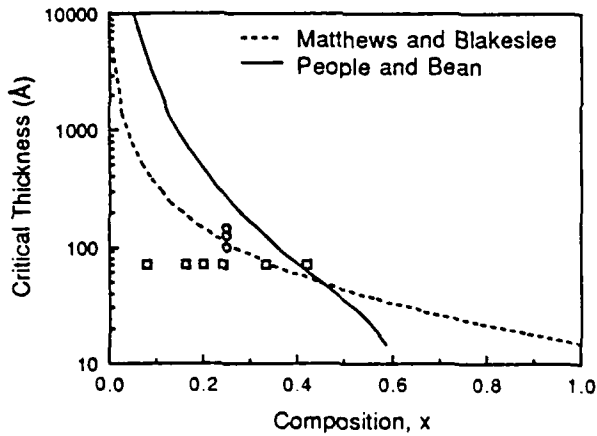


Figure 2

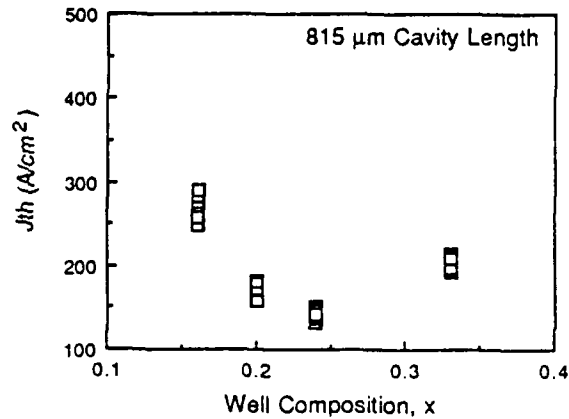


Figure 3

with compositions outside this range had threshold values greater than 1 kA/cm<sup>2</sup>. The minimum in  $J_{th}$  versus composition of 140 A/cm<sup>2</sup> at an indium fraction of approximately 0.25 in Fig. 3 is defined by poor carrier confinement for low indium fraction in the wells and the deleterious effects of strain at higher indium fractions in these fixed well size structures. The result at either limit is manifest as an increased  $J_{th}$ . The results for low indium fraction in the wells agree qualitatively with those of Hersee<sup>20</sup> for AlGaAs-GaAs graded refractive index separate confinement heterostructure quantum well lasers.

Shown in Fig. 4 is threshold current density versus quantum well thickness for four cavity lengths of three laser structures having a well composition of  $x \sim 0.25$  and thicknesses near the Matthews and Blakeslee critical thickness. These lasers show time zero laser threshold current density increasing with thickness from below 150 A/cm<sup>2</sup> ( $L_z = 100\text{\AA}$ , length 950  $\mu\text{m}$ ) to more than 300 A/cm<sup>2</sup>. Life-testing on these three structures was performed at constant power on 60  $\mu\text{m}$  oxide stripe devices operating cw at 60 mW per uncoated facet. The results of the life-test of lasers with  $L_z=100\text{\AA}$  are shown in Fig. 5. All of the devices

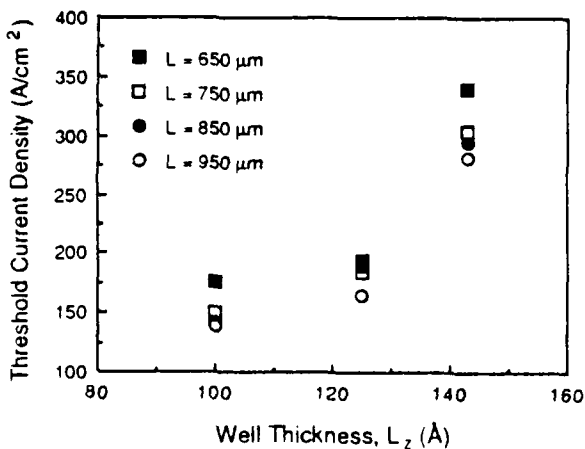


Figure 4

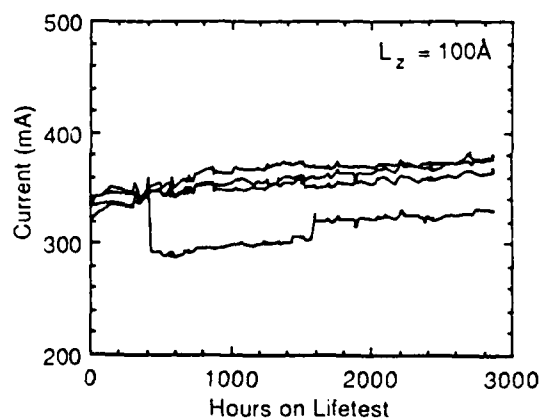


Figure 5

fabricated from this material are still operating with only a gradual increase in current, comparable to other InGaAs strained layer lasers reported earlier<sup>21-23</sup>. In contrast, the performance of the 143 Å quantum well devices exceeded the current doubling limit in under 100 hours. The performance of devices with 125 Å wells was intermediate between these two extremes. These data suggest that the maximum practical thickness for In<sub>0.25</sub>Ga<sub>0.75</sub>As quantum well active regions is more accurately predicted by the model of Matthews and Blakeslee, and well below the value of ~ 265 Å predicted by People and Bean for this composition.

## 5. SUMMARY

In summary, we have reviewed results of time-zero characterization of strained layer In<sub>x</sub>Ga<sub>1-x</sub>As-GaAs quantum well heterostructure laser diodes with 70-Å-thick wells and indium mole fractions between 0.08 and 0.42 and with nominal In<sub>0.25</sub>Ga<sub>0.75</sub>As well compositions and 100, 125, and 143 Å well thicknesses.. The data support the design criteria for low threshold operation of strained layer InGaAs-GaAs quantum well lasers that the indium composition in the well must be sufficient for effective carrier confinement in the conduction band, and the strained layer active region thickness should not greatly exceed the critical thickness given by the mechanical equilibrium model of Matthews and Blakeslee. Within these design constraints, long lived, very low threshold strained layer lasers ( $\lambda \sim 1 \mu\text{m}$ ) are realizable.

## 6. ACKNOWLEDGEMENTS

The authors wish to thank S. Yellen, R. Soltz, R.P. Bryan, G.E. Fernández, L.M. Miller, S.M. Langsjoen, M.K. Suits and K. Kuehl for technical assistance. We are also grateful to C. Krebs and S. Whiteley for continued support. This work was supported by the McDonnell-Douglas Electronics Systems Company, the Naval Research Laboratory (N00014-88-K-2005), the National Science Foundation (DMR 86-12860 and CDR 85-22666), and the Charles Stark Draper Laboratory (DLH 285419).

## 7. REFERENCES

1. W.D. Laidig, P.J. Caldwell, Y.F. Lin, and C.K. Peng, *Appl. Phys. Lett.* **44**, 653 (1984).
2. D. Fekete, K.T. Chan, J.M. Ballantyne, and L.F. Eastman, *Appl. Phys. Lett.* **49**, 1659 (1986).
3. Y.I. Yang, K.Y. Hsieh, and R.M. Kolbas, *Appl. Phys. Lett.* **51**, 215 (1987).
4. J.N. Baillargeon, P.K. York, C.A. Zmudzinski, G.E. Fernández, K.J. Beernink, and J.J. Coleman, *Appl. Phys. Lett.* **53**, 457 (1988).
5. P.K. York, K.J. Beernink, G.E. Fernández, and J.J. Coleman, *Appl. Phys. Lett.* **54**, 499 (1989).
6. D.P. Bour, P. Stabile, A. Rosen, W. Janton, L. Elbaum, and D.J. Holmes, *Appl. Phys. Lett.* **54**, 2637 (1989).
7. K.J. Beernink, P.K. York, J.J. Coleman, R.G. Waters, J. Kim, and C. Wayman, *Appl. Phys. Lett.* **55**, 2167 (1989).
8. K.J. Beernink, P.K. York, and J.J. Coleman, *Appl. Phys. Lett.* **55**, in press (1989)
9. S.E. Fischer, R.G. Waters, D. Fekete, J.M. Ballantyne, Y.C. Chen, and B. Soltz, *Appl. Phys. Lett.* **54**, 1861 (1989).
10. J.S. Major, Jr., L.J. Guido, K.C. Hsieh, N. Holonyak, Jr., W. Stutius, P. Gavrilovic, and J.E. Williams, *Appl. Phys. Lett.* **54**, 913 (1989).

11. S.D. Offsey, W.J. Schaff, P.J. Tasker, H. Ennen, and L.F. Eastman, *Appl. Phys. Lett.* **54**, 2527 (1989).
12. S.E. Fischer, D. Fekete, G.B. Feak, and J.M. Ballantyne, *Appl. Phys. Lett.* **50**, 714 (1987).
13. R. I. Laming, M.C. Farries, P.R. Morkel, L. Reekie, and D.N. Payne, *Electron. Lett.* **25**, 12 (1989).
14. J.W. Matthews and A.E. Blakeslee, *J. Cryst. Growth* **27**, 118 (1974).
15. R. People and J.C. Bean, *Appl. Phys Lett.* **47**, 322 (1985).
16. P.L. Gourley, I.J. Fritz, and L.R. Dawson, *Appl. Phys. Lett.* **52**, 377 (1988) *and references therein.*
17. G. Costrini and J.J. Coleman, *J. Appl. Phys.* **57**, 2249 (1985).
18. P.K. York, K.J. Beernink, J. Kim, J.J. Coleman, G.E. Fernández, and C. M. Wayman, *Appl. Phys. Lett.* **55**, 2476 (1989)
19. S.J. Jeng, C.M. Wayman, G. Costrini, and J.J. Coleman, *Materials Lett.* **2**, 359 (1984).
20. S.D. Hersee, B. de Cremoux, and J.P. Duchemin, *Appl. Phys. Lett.* **44**, 476 (1984).
21. W. Stutius, P. Gavrilovic, J.E. Williams, K. Meehan, and J.H. Zarrabi, *Electron. Lett.* **24**, 1493 (1988).
22. S.E. Fischer, R.G. Waters, D. Fekete, J.M. Ballantyne, Y.C. Chen, and B. Soltz, *Appl. Phys. Lett.* **54**, 1861 (1989)
23. R.G. Waters, P.K. York, K.J. Beernink, and J.J. Coleman, *Appl. Phys. Lett.* **55**, in press (1989)

# Effect of confining layer aluminum composition on AlGaAs-GaAs-InGaAs strained-layer quantum well heterostructure lasers

P. K. York, S. M. Langsjoen, L. M. Miller, K. J. Beernink, J. J. Alwan, and J. J. Coleman  
*Compound Semiconductor Microelectronics Laboratory and Materials Research Laboratory,  
University of Illinois, 208 North Wright Street, Urbana, Illinois 61801*

(Received 4 May 1990; accepted for publication 15 June 1990)

Data are presented on laser threshold current density and emission wavelength of strained-layer InGaAs-GaAs-Al<sub>x</sub>Ga<sub>1-x</sub>As single quantum well lasers having confining layer aluminum compositions in the range 0.20 < x < 0.85. A decrease in threshold current density with increasing confining layer composition is related to the increased confinement factor of the waveguide structure. An increase in the laser emission wavelength is observed as a consequence of reduced bandfilling.

The existence of elastically accommodated strain in thin layers of InGaAs sandwiched by bulk (Al)GaAs brings about several important modifications to the InGaAs energy band structure. These changes can lead to improved performance<sup>1-3</sup> in strained quantum well lasers as compared to conventional, unstrained quantum well lasers. Most notable are expectations of a lower transparency current and therefore lower threshold current density,<sup>1</sup> and an increase in the modulation bandwidth<sup>4,5</sup> through superior differential gain.<sup>4-7</sup> These features arise primarily through a strain-induced decrease in the in-layer-plane effective hole mass and consequently a reduced valence-band density of states, but may be somewhat offset by a greater tendency for nonradiative recombination mechanisms in lower band-gap alloys such as InGaAs.<sup>8</sup> Excellent performance has been reported recently by many authors<sup>9-18</sup> with a variety of confining layer AlGaAs compositions, carrier collection (barrier) layer (Al)GaAs compositions, InGaAs quantum well active regions, and growth parameters, both by metalorganic chemical vapor deposition (MOCVD)<sup>10,14,16-18</sup> and molecular beam epitaxy.<sup>9,11,15</sup> In this letter, we show data that define the relationship of the laser threshold current density and emission wavelength of strained-layer InGaAs-GaAs-Al<sub>x</sub>Ga<sub>1-x</sub>As single quantum well lasers to aluminum composition (0.20 < x < 0.85) in the confining layers. We observe a decrease in threshold current density with increasing confining layer composition related to the increased confinement factor of the waveguide structure. These observations are then directly correlated to an increase in the laser emission wavelength as a consequence of bandfilling effects, which is pronounced in these quantum wells due to the reduced InGaAs density of states.

The laser structures here were grown by MOCVD at atmospheric pressure in a vertical geometry reaction chamber using trimethylgallium (-10 °C), trimethylaluminum (20 °C), trimethylindium (17 °C) or ethyldimethylindium<sup>17</sup> (11 °C), and arsine. The structures are shown schematically in Fig. 1 and consist of a 0.25 μm GaAs:n<sup>+</sup> buffer layer grown on a (100) GaAs:n<sup>+</sup> substrate, 1.5 μm Al<sub>x</sub>Ga<sub>1-x</sub>As confining layers, where x varies between 0.20 and 0.85, 0.10 μm GaAs carrier collection and optical confinement barrier layers on either side of an elastically

strained In<sub>y</sub>Ga<sub>1-y</sub>As active region, and a 0.20 μm GaAs:p<sup>+</sup> (2 × 10<sup>19</sup> cm<sup>-3</sup>) contact cap layer. The n-type confining and GaAs barrier layers were doped 1 × 10<sup>18</sup> cm<sup>-3</sup> and 1 × 10<sup>16</sup> cm<sup>-3</sup>, respectively, using silane. The p-type barrier layers were doped 5 × 10<sup>17</sup> cm<sup>-3</sup> with diethylzinc (20 °C). The 0.20 and 0.40 p-type confining layers were doped 1 × 10<sup>18</sup> cm<sup>-3</sup> with diethylzinc and the 0.60 and 0.85 confining layers were carbon autodoped to ~1 × 10<sup>18</sup> cm<sup>-3</sup>. The buffer and confining layers were grown at 800 °C while the InGaAs active region was grown at 625 °C. The temperature was lowered to 720 °C at the start of the GaAs:n barrier layer and raised to 800 °C after the end of the GaAs:p barrier layer to avoid long pauses at the quantum well interfaces. The temperature was also ramped from 720 to 625 °C (625 to 720 °C) during the growth of the GaAs:n (GaAs:p) barrier layer. The GaAs:p<sup>+</sup> cap layer was grown at 650 °C to facilitate the incorporation of zinc for a low-resistance ohmic contact.

Two sets of In<sub>0.25</sub>Ga<sub>0.75</sub>As single quantum well laser structures were grown, one with 70 Å wells and one with 100 Å wells. Both of these well sizes are less than the critical thickness of ~105 Å predicted by<sup>19</sup> the Matthews and Blakeslee model. Each set is comprised of four growths, identical except for the confining layer aluminum composition, which is 0.20, 0.40, 0.60, or 0.85. Compositions of these strained InGaAs layers were initially estimated by the molar ratio of the column III constituents in conjunction<sup>17</sup> with accurate transmission electron microscopy layer thicknesses. Accuracy of the composition was

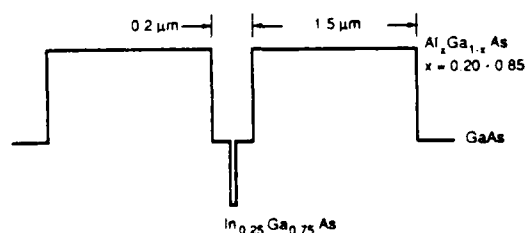


FIG. 1. Schematic diagram of a separate confinement laser structure with a single strained 70 or 100 Å In<sub>0.25</sub>Ga<sub>0.75</sub>As quantum well, GaAs carrier collection layers, and Al<sub>x</sub>Ga<sub>1-x</sub>As confining layers having x = 0.20, 0.40, 0.60, or 0.85.

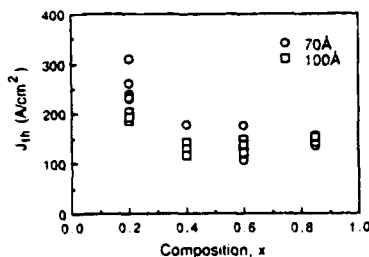


FIG. 2. Laser threshold current density vs aluminum confining layer composition  $x$  for separate confinement lasers with 70 Å (circles) or 100 Å (squares)  $\text{In}_{0.25}\text{Ga}_{0.75}$  quantum wells. The diode cavity lengths are  $\sim 800 \mu\text{m}$  for each laser.

confirmed by comparing actual laser emission wavelengths to calculated ones. Calculation of the wavelength is similar to that of Pan *et al.*<sup>20</sup> and accounts for both quantum size effects and the strained-induced shift of the InGaAs band-gap energy, assuming a 70/30 split of the heterojunction discontinuity between the conduction and valence bands. This method is self-consistent, although the absolute value of the composition may be slightly off due to approximations in the model and some uncertainty in the band structure parameters required for the calculations.

Broad-area devices were fabricated with oxide-defined 150- $\mu\text{m}$ -wide stripes, cleaved into devices of various lengths, and tested under pulsed conditions (1.5  $\mu\text{s}$  pulse width, 2 kHz repetition rate). The threshold current densities  $J_{\text{th}}$  for both the 70 Å (circles) and the 100 Å (squares)  $\text{In}_{0.25}\text{Ga}_{0.75}\text{As}$  single quantum well lasers are plotted as a function of the aluminum composition in the confining layers in Fig. 2. The cavity lengths for these diodes are  $\sim 800 \mu\text{m}$  to avoid short-cavity effects.<sup>21</sup>  $J_{\text{th}}$  decreases significantly as the composition is increased from 0.20 to 0.85 in the confining layers. This trend was observed for all cavity lengths tested (300–800  $\mu\text{m}$ ). A decrease in threshold current density with confining layer composition is expected from the increase in the optical confinement factor  $\Gamma$  due to the lower refractive index in layers with higher aluminum composition. This is evidenced by the usual expression for the threshold current density in the low current range where the gain is a linear function of current density:

$$J_{\text{th}} = \frac{J_0}{\eta_i} + \frac{1}{\Gamma} \left[ \left( \frac{1}{\eta\beta} \right) \left( \frac{1}{L} \ln \frac{1}{R} + \alpha_i \right) \right]. \quad (1)$$

Here,  $J_0$  is the transparency current ( $\text{A}/\text{cm}^2$ ),  $\eta_i$  is the internal quantum efficiency,  $\beta$  is the gain coefficient ( $\text{cm}/\text{A}$ ),  $L$  is the laser diode cavity length,  $R$  is the facet reflectivity, and  $\alpha_i$  represents the internal optical loss ( $\text{cm}^{-1}$ ). The optical confinement factors were calculated for each of the eight structures using a five-slab waveguide model<sup>22</sup> taking into account the index of refraction of each of the confining and barrier layers at the appropriate emission wavelength. Calculated values for the inverse of the optical confinement factor are plotted as a function of the confining layer composition in Fig. 3. The optical confinement factor varies<sup>22</sup> roughly linearly with the quantum well size, as indicated by the larger values for the 100 Å well. It can

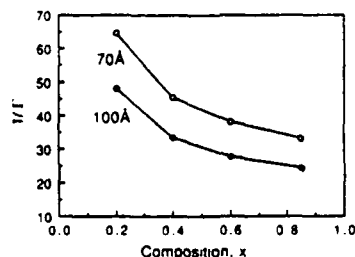


FIG. 3. Calculated values for the inverse optical confinement factor  $\Gamma^{-1}$  vs aluminum confining layer composition  $x$  for separate confinement lasers with 70 Å (open circles) or 100 Å (filled circles)  $\text{In}_{0.25}\text{Ga}_{0.75}$  quantum wells.

be seen by comparing Figs. 2 and 3 that the decrease in the threshold current density essentially follows the decrease in  $\Gamma^{-1}$ .

A decrease in threshold current density is accompanied in these structures by an increase in the laser emission wavelength, which ranged between 9700 and 10 100 Å for the 70 Å wells and 10 200 and 10 500 Å for the 100 Å wells. The emission wavelengths shifted to longer values, with the total shift being 300–400 Å, from values observed for lasers with  $\text{Al}_{0.20}\text{Ga}_{0.80}\text{As}$  confining layers to those observed for lasers with  $\text{Al}_{0.85}\text{Ga}_{0.15}\text{As}$  confining layers. The transition energies corresponding to these emission wavelengths are, therefore, decreasing with increasing aluminum composition, as shown in Fig. 4 for both the 70 and 100 Å  $\text{In}_{0.25}\text{Ga}_{0.75}\text{As}$  quantum well lasers. The electron effective mass  $m_e^*(y)$  in  $\text{In}_y\text{Ga}_{1-y}\text{As}$  decreases for increasing indium content which brings about a reduced conduction-band density of states as compared to GaAs. Consequently, band filling becomes pronounced<sup>16</sup> for increasing carrier injection levels, shifting the laser transition energy  $E$  up from the quantum well bound state energy. For a quantum well of thickness  $L_z$ , the change in laser transition energy  $\Delta E$  caused by bandfilling can be described in terms of the observed change in the quantum well current density. The injected density  $n$  and the threshold current density are of course related by

$$J_{\text{th}} = qnL_z/\tau. \quad (2)$$

The emission energy is determined by the positions of the quasi-Fermi levels which, in turn, are determined from

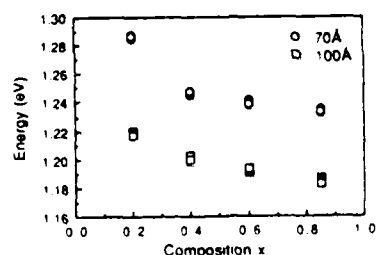


FIG. 4. Laser transition energy vs aluminum confining layer composition  $x$  for separate confinement lasers with 70 Å (circles) or 100 Å (squares)  $\text{In}_{0.25}\text{Ga}_{0.75}$  quantum wells.

$$n = \int \rho(E) f(E - E_F) dE, \quad (3)$$

where  $f(E - E_F)$  is the Fermi function and  $\rho(E)$  is the quantum well heterostructure density of states function, which is<sup>23</sup> independent of energy for the first quantum state and proportional to  $1/L_z$ . From these equations it can be easily determined that a change in threshold current density associated with a change in confinement factor results in a corresponding well-defined change in emission energy, independent of quantum well size, as shown in Fig. 4.

In summary, we have determined the relationship of the InGaAs-GaAs-AlGaAs quantum well laser threshold current density and transition energy to the aluminum composition  $x$  of the confining layers for  $x = 0.20$ – $0.85$ . The threshold current density decreases for increasing  $x$  due to the increased confinement factor in the optical waveguide. Furthermore, the laser emission wavelength increases with decreasing  $J_{th}$  as a direct consequence of the reduced bandfilling for lower quantum well threshold current densities.

The authors are grateful to M. K. Suits and K. Kuehl for helpful discussions and technical support. This work was supported by the Naval Research Laboratory (N00014-88-K-2005), the National Science Foundation (DMR 86-12860 and CDR 85-22666), and the Charles Stark Draper Laboratory (DLH285419). K. J. Beernink is supported in part by a NDSEG fellowship.

<sup>1</sup>E. Yablonovitch and E. O. Kane, *J. Lightwave Technol.* **6**, 1292 (1988).

<sup>2</sup>G. C. Osbourn, R. M. Biefeld, and P. L. Gourley, *Appl. Phys. Lett.* **41**, 172 (1981).

<sup>3</sup>N. G. Anderson, W. D. Laidig, R. M. Kolbas, and Y. C. Lo, *J. Appl. Phys.* **60**, 2363 (1986).

<sup>4</sup>K. Y. Lau, S. Xin, W. I. Wang, N. Bar-Chaim, and M. Mittelstein, *Appl. Phys. Lett.* **55**, 1173 (1989).

<sup>5</sup>I. Suemune, L. A. Coldren, M. Yamanishi, and Y. Kan, *Appl. Phys. Lett.* **53**, 1378 (1988).

<sup>6</sup>J. LaCourse, B. Yu, W. Rideout, P. K. York, K. J. Beernink, and J. J. Coleman, *Proceedings of the Technical Digest Optical Fiber Conference, WJ4* (Optical Society of America, Washington, D.C., 1990).

<sup>7</sup>W. Rideout, B. Yu, J. LaCourse, P. K. York, K. J. Beernink, and J. J. Coleman, *Appl. Phys. Lett.* **56**, 706 (1990).

<sup>8</sup>N. K. Dutta, *J. Appl. Phys.* **54**, 1236 (1983).

<sup>9</sup>W. D. Laidig, P. J. Caldwell, Y. F. Lin, and C. K. Peng, *Appl. Phys. Lett.* **44**, 653 (1984).

<sup>10</sup>D. Feketa, K. T. Chan, J. M. Ballantyne, and L. F. Eastman, *Appl. Phys. Lett.* **49**, 1659 (1986).

<sup>11</sup>R. M. Kolbas, N. G. Anderson, W. D. Laidig, Y. Sin, Y. C. Lo, K. Y. Hsieh, and Y. J. Yang, *IEEE J. Quantum Electron.* **24**, 1605 (1988).

<sup>12</sup>R. G. Waters, P. K. York, K. J. Beernink, and J. J. Coleman, *J. Appl. Phys.* **67**, 1132 (1990).

<sup>13</sup>K. J. Beernink, P. K. York, J. J. Coleman, R. G. Waters, J. Kim, and C. M. Wayman, *Appl. Phys. Lett.* **55**, 2167 (1989).

<sup>14</sup>D. P. Bour, D. B. Gilbert, L. Elbaum, and M. G. Harvey, *Appl. Phys. Lett.* **53**, 2371 (1988).

<sup>15</sup>C. Shieh, H. Lee, J. Mantz, D. Ackley, and R. Engelmann, *Electron. Lett.* **25**, 1226 (1989).

<sup>16</sup>D. Hall, J. S. Major, Jr., N. Holonyak, Jr., P. Gavrilovic, K. Meehan, W. Stutius, and J. E. Williams, *Appl. Phys. Lett.* **55**, 752 (1989).

<sup>17</sup>P. K. York, K. J. Beernink, J. Kim, J. J. Coleman, G. E. Fernández, and C. M. Wayman, *Appl. Phys. Lett.* **55**, 2476 (1989).

<sup>18</sup>K. J. Beernink, P. K. York, and J. J. Coleman, *Appl. Phys. Lett.* **55**, 2585 (1989).

<sup>19</sup>J. A. Matthews and A. E. Blakeslee, *J. Cryst. Growth* **27**, 118 (1974).

<sup>20</sup>S. H. Pan, H. Shen, Z. Hang, F. H. Pollak, W. Zhuang, Q. Xu, A. P. Roth, R. A. Masut, C. Lacelle, and D. Morris, *Phys. Rev. B* **38**, 3375 (1988).

<sup>21</sup>P. S. Zory, A. R. Reisinger, L. J. Mawst, G. Costrini, C. A. Zmudzinski, M. A. Emanuel, M. E. Givens, and J. J. Coleman, *Electron. Lett.* **22**, 475 (1986).

<sup>22</sup>H. C. Casey, Jr., M. B. Panish, W. O. Schlosser, and T. L. Paoli, *J. Appl. Phys.* **45**, 322 (1974).

<sup>23</sup>J. T. Verdeyen, *Laser Electronics*, 2nd ed. (Prentice Hall, Englewood Cliffs, N.J., 1989).

# Modeling of Quantum-Well Lasers for Computer-Aided Analysis of Optoelectronic Integrated Circuits

DAVID S. GAO, S. M. (STEVE) KANG, FELLOW, IEEE, ROBERT P. BRYAN,  
AND JAMES J. COLEMAN, SENIOR MEMBER, IEEE

**Abstract**—A two-port circuit model for quantum-well (QW) lasers has been developed from rate equations. With emphasis on the physical principles, the phenomena of the recombination process of electron-hole pairs and the light wave resonance in the active region have been incorporated into this new model. Our model has been implemented into a circuit simulator and validated with measured dc and transient laser characteristics. The frequency effects on the modulation properties of QW lasers have been studied and analyzed using a small-signal model. Simulation results show excellent agreement with experimental data.

## I. INTRODUCTION

SEMICONDUCTOR lasers (especially quantum-well lasers) are desirable sources in optoelectronic integrated circuits for optical communication systems and optical interconnections in large computer systems. Thus, the detailed analysis of the characteristics of semiconductor lasers as light sources is crucial to the design of optoelectronic integrated circuits (OEIC) and systems. Circuit simulation could be a powerful tool for the design and analysis of optical interconnections [1]. Therefore, accurate circuit models for optical devices such as semiconductor lasers are necessary for the analysis of dynamic properties of OEIC circuits and systems.

The issue of modeling the semiconductor laser with circuit elements has been addressed by several authors. Previously reported laser models are limited to conventional double heterostructure lasers [2]–[6]. There is a need for a suitable model for quantum-well lasers, which represents a more logical choice of semiconductor laser technology for integrated optoelectronic circuits [7], [8].

In this paper, we propose a new circuit model for quantum-well lasers derived from rate equations. For the large-signal model, the gain function and the carrier density

have been calculated from positions of quasi-Fermi levels in the active region. Both the spontaneous and the stimulated emission currents are modeled with appropriate nonlinear circuit elements. In order to allow the optical resonator of a quantum-well laser to be represented by an equivalent circuit which consists of dependent current sources and *RC* components, active Fabry-Perot resonator analysis is used in deriving an analytical formula to describe the relation between the photon density in the optical cavity and the output light intensity. The output light power is expressed in terms of an output node voltage in the circuit simulation. As a result, the rate equations of a quantum-well laser can be represented by a two-port coupling circuit. A similar small-signal model has also been derived from the same set of equations and assumptions, which is useful in the analysis of modulation properties of quantum-well lasers in the frequency domain.

## II. ANALYSIS OF RATE EQUATIONS

In general, circuit simulators are based upon constitutive relationships of circuit element models for the individual devices comprising the integrated circuit. Device modeling for circuit simulation is an indispensable link between new technology and computer-aided circuit analysis. The basis of circuit modeling is to transform the fundamental theories of device physics into a form which is solvable by the circuit simulation program. The circuit simulation environment imposes certain requirements on the formulation of model equations. All nonlinear elements adopted in the model must be described by analytical closed-form functions of circuit variables which have at least continuous first-order derivatives. Any given model, such as the quantum-well laser model, should also be compatible with other models in a circuit simulation environment. Therefore, certain assumptions are necessary to satisfy these requirements.

### A. Rate Equations

The electrical and optical properties of the active region of a quantum-well laser can be described by the well-known rate equations [9], [10]. A general-purpose circuit

Manuscript received August 7, 1989; revised February 20, 1990. This work was supported by the National Science Foundation Engineering Research Center for Compound Semiconductor Microelectronics under Contract NSF CDR 85-22666, by the National Science Foundation under Contract ECD 89-43116, by the Joint Services Electronics Program under Contract N00014-84-C-0149, and by the Naval Research Laboratory under Contract N00014-18-K-2005. R. P. Bryan was supported in part by an AT&T Doctoral Fellowship.

The authors are with the Department of Electrical and Computer Engineering and the Center for Compound Semiconductor Microelectronics, University of Illinois, Urbana-Champaign, Urbana, IL 61801.

IEEE Log Number 9035992

simulator can solve a large set of first-order differential equations with node voltages as state variables. Since the rate equations consist of only first-order differential equations, they can be solved by a circuit simulation program provided that the rate equations can be represented by an equivalent circuit model with proper mapping of physical quantities into circuit variables. The single-mode rate equations are expressed as

$$\frac{dn_e}{dt} = \frac{J}{qNL_z} - \beta n_e^2 - \Gamma g_m c' S \quad (1)$$

$$\frac{dS}{dt} = \beta B n_e^2 + \Gamma g_m c' S - \frac{S}{\tau_{ph}} \quad (2)$$

Readers are referred to Table I for the variable definitions. In general the photon density  $S$ , charge density  $n_e$  and optical gain  $g_m$  are functions of their lateral positions in the optical waveguide. But, in (1) and (2), these three quantities simply represent the corresponding average values.

Equation (1) requires that the current flow into the active region, minus the current lost to spontaneous and stimulated emissions, is equal to the time rate of change for the charge density in this region. Similarly, (2) requires that the time rate of change for the average photon density in the Fabry-Perot resonator is equal to the sum of spontaneous emission and stimulated emission minus the absorption in the active region.

Since most of the radiative recombination in a laser is likely to occur in the region of the quantum-well under the metal contact, we assume that the volume of the active region can be approximated by the dimensions of the quantum-well under the metal contact. The portion of the optical field outside of the active region is accounted for by the confinement factor  $\Gamma$ .

### B. Spontaneous and Stimulated Emissions

To construct a circuit model, it is important to find analytical expressions for all nonlinear model elements. In (1) and (2), the spontaneous emission term has quadratic dependence on carrier density when dominated by the direct band-to-band electron-hole recombination.  $B$  can be determined from experimental data [11]. It is necessary then to find an analytical form for  $n_e$ , the carrier density.

In our quantum-well laser model, we assume that the coupling between adjacent wells is weak, the potential barrier is sufficiently high, then the quantum well can be described as a one-dimensional ( $z$  direction) square well. Then the quantized subband energy levels can be approximated as the energy level derived from a one-dimensional infinitely deep potential well model. If the bulk band energies can be approximated to be parabolic in the  $x$  and  $y$  directions, the densities of states in the conduction and the valence bands are step like. If only the lowest order quantum transitions are considered, the electron

TABLE I  
DEFINITIONS OF TERMS

Terminology	Definitions
$c$	speed of light in vacuum
$c'$	speed of light in the lasing medium
$E_{c1}$	energy level of the first conduction subband in the quantum-well
$E_{v1}$	energy level of the first valence subband in the quantum-well
$E_{fc}$	quasi-Fermi level in the conduction band
$E_{fv}$	quasi-Fermi level in the valence band
$E_g$	energy bandgap of the laser material
$E_q$	energy gap between two subbands
$E_{ph}$	photon energy
$g_m$	optical gain
$h$	Planck constant divided by $2\pi$
$J$	injected current density
$k$	Boltzman constant
$L$	length of the laser
$L_z$	thickness of a single quantum-well
$m_c^*$	effective mass in the conduction band
$m_e$	mass of an electron
$m_v^*$	effective mass in the valence band
$N$	number of quantum-wells
$n_e$	charge density in the quantum-well
$\pi$	refractive index
$q$	charge of an electron
$S$	photon density
$W$	width of the metal contact on the laser
$\beta$	spontaneous emission coupling coefficient
$\Gamma$	optical confinement factor
$B$	conventional band-to-band recombination coefficient
$\epsilon_0$	permittivity of free space
$\omega$	radian frequency
$\tau_{ph}$	photon life time

density in the quantum well is determined by

$$n_e = \frac{m_c^* kT}{\pi \hbar^2 L_z} \ln \left[ 1 + \exp \frac{E_{fc} - E_{c1}}{kT} \right] \quad (3)$$

In (3) the charge density is now expressed in terms of quasi-Fermi levels and the spontaneous emission term is also described in terms of quasi-Fermi energies.

The stimulated emission term in (1) can be expressed as  $\Gamma c' g_m S$ , which depends linearly on the photon density present in the active region. The confinement factor  $\Gamma$  depends on the geometry and the material composition of the laser, and will be discussed in the next section. The optical gain  $g_m$  is a complicated function which depends not only on the geometry and material composition of the device, but also on the driving current. A key step of this work is the derivation of a closed-form analytic expression for  $g_m$ . Instead of assuming that the optical gain  $g_m$  depends linearly on the carrier density, we have calculated  $g_m$  in order to provide a stronger connection to the physical phenomena of quantum-well lasers. Originally, this method was developed by Lasher and Stern [12] to calculate transitions in bulk GaAs material and later extended by several authors to transitions in a quantum well [9], [13], [14]. In our calculation band-to-band stimulated recombination is assumed to be dominant between the first electron and heavy hole states and the light hole effect is neglected. When the recombination is dominated by the band-to-band recombination, the optical gain derived under  $k$ -selection rules is given by

$$g_m = \int \rho_{red} M^2 (f_c(E_{cv}, E') - f_v(E_{cv}, E')) dE \quad (4)$$

Here  $\rho_{\text{red}}$  is the reduced density of states,  $|M|$  is the transition matrix element,  $f_c(E_{fc}, E'_c)$  and  $f_v(E_{fv}, E'_v)$  are the Fermi distribution functions in the conduction and valence bands, respectively, and  $E'_c$  and  $E'_v$  are given as

$$E'_c = \frac{m_v^*}{m_c^* + m_v^*} (E_{\text{ph}} - E_g) \quad (5)$$

and

$$E'_v = \frac{m_c^*}{m_c^* + m_v^*} (E_{\text{ph}} - E_g) \quad (6)$$

where  $E_g$  is the bandgap of the material and  $E_{\text{ph}}$  is the photon energy. The photon energy  $E_{\text{ph}} = \hbar\omega$  is determined by the material and the structure of the laser, and is an input parameter to our model. The value of  $E_{\text{ph}}$  can be either extracted from the actual device measurement data or from a device simulator. The reduced density of states function  $\rho_{\text{red}}$  in two-dimension (2-D) form is given by

$$\rho_{\text{red}} = \frac{1}{\pi \hbar^2 L_z} \cdot \frac{m_c^* m_v^*}{m_c^* + m_v^*} \quad (7)$$

This reduced density of states function (2-D) is independent of the energy. Following the method proposed by Kane [15], the matrix element  $|M|$  can be approximated as a constant. Therefore, the gain function in (4) is calculated to be

$$g_m = \frac{2\pi q^2}{\epsilon_0 m_e^* c \bar{n} \hbar E_{\text{ph}}} \cdot \frac{m_c^* m_v^*}{m_c^* + m_v^*} \cdot |M|^2 \cdot [f_c(E_{fc}, E'_c) - f_v(E_{fv}, E'_v)]. \quad (8)$$

Here  $|M|^2$ , the square of the dipole matrix element of the transition between band edges, is given by

$$|M|^2 \approx 1.33 K_m m_e E_q. \quad (9)$$

In (8), the optical gain is now expressed as a function of quasi-Fermi levels.

$E_q$  is an experimentally derived input parameter to the model; when experimental data are not available, it is calculated in the model from the infinite potential well approximation under the lasing condition [14]

$$E_q < E_{fc} - E_{fv}. \quad (10)$$

The adjustable parameter  $K_m$  takes into account different polarizations of the dipole moment as well as other effects of the transition [14], [16]. When  $K_m$  is equal to one, (9) represents the matrix element of the dipole moment of a TE wave between the band edges. Although  $K_m$  is an adjustable parameter, it would be inappropriate to take a value much larger than two [16].

### C. External Applied Voltage

In the previous section, the charge density  $n$ , and the optical gain  $g_m$  are expressed in terms of two quasi-Fermi levels. But, Fermi levels are not physically observable quantities; furthermore, circuit simulation programs pri-

marily use node voltages as circuit variables. We assume that the potential difference between two quasi-Fermi levels is equal to the applied voltage.

If the quantum well is made of intrinsic material and the charge neutrality condition is valid locally, the quasi-Fermi level in the conduction band can be calculated from

$$[(1 + e^{E_{fc}/kT})^\mu + 1] e^{E_{fc}/kT} = e^{qV_n - E_q/kT} \quad (11)$$

where  $\mu = m_c/m_v$  and  $V_n$  is the nominal voltage across the active region. Applying the Newton-Raphson method to (11),  $E_{fc}$  can be found numerically. Then  $E_{fv}$  is given as

$$E_{fv} = E_{fc} - qV_n. \quad (12)$$

Since both  $E_{fc}$  and  $E_{fv}$  can be expressed in terms of the applied voltage, (3) and (8) now can be expressed as functions of the applied voltage.

It is difficult to find a closed-form solution of  $E_{fc}$  directly from (11). An empirical formula, derived by using a data fitting method, is expressed as

$$E_{fc} = \begin{cases} -0.6755 + 0.4871V_n & \text{if } V_n < 1.1 \\ -0.2077 - 0.4253V_n + 0.4895V_n^2 \\ \quad - 0.03359V_n^3 - 0.007999V_n^4 & \text{otherwise.} \end{cases} \quad (13)$$

This empirical formula is valid over the range of  $-1$  to  $3.5$  V. Since the energy bandgap of GaAs is  $1.424$  eV, it is not expected that the quasi-Fermi levels will reach a level much above the energy bandgap. Therefore, this empirical formula is well-suited for modeling of a GaAs-based quantum-well laser. Values of parameters, which have been used in the computation, are given in Table II.

Fig. 1 illustrates the gain  $g_m$  as a function of the applied voltage across the active region. It shows that the gain, actually a loss, is nearly a constant in the low applied voltage region. As the applied voltage becomes larger than a certain threshold voltage,  $g_m$  increases quickly as a large population inversion is created in the active region. However, when the applied voltage becomes still larger, a second threshold voltage is reached and the gain saturates. Because the optical gain depends also on the wavelength of the photon, further increases in charge density in the quantum-well only generate higher energy electron-hole pairs. The probability for stimulated recombination of these electron-hole pairs by low-energy photons is small. Thus they contribute little to increasing the optical gain for that particular wavelength.

### D. Photon Density in the Active Region

For most semiconductor lasers, the cavity structure of the active region can be considered as a Fabry-Perot resonator. It is necessary to include this effect into (1) and (2) to provide a self-consistent analysis. The wave propagated inside the laser cavity is not a plane wave in general; it is very difficult to derive a closed-form analytical formula based on a nonplane wave. For a first-order ap-

TABLE II  
THE PARAMETERS FOR GAIN CALCULATION

Parameters	Value
index of refraction $n$	3.55
wavelength $\lambda$	3350 Å
$m_c$	0.067 $m_0$
$m_v$	0.45 $m_0$
recombination energy $E_r$	1.482 eV
temperature $T$	300° K

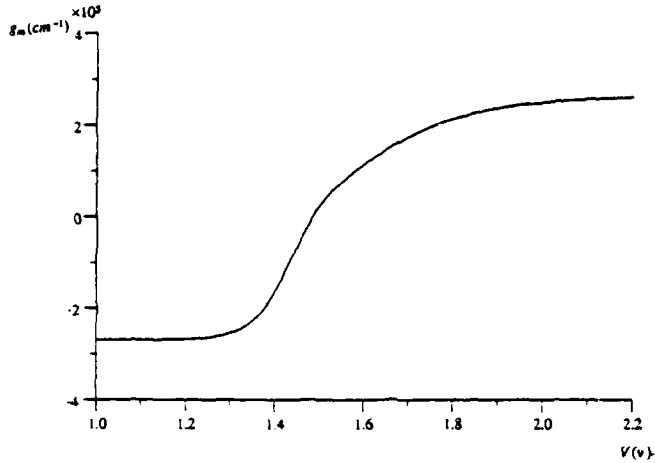


Fig. 1. Optical gain versus applied voltage.

proximation, we use a plane wave (TEM) approximation. Based upon this, a simplified method can be applied to analyze the Fabry-Perot resonator (see the Appendix). The average photon density in the laser cavity is given by [17], [18]

$$S = \left[ \frac{(e^{gL} - 1)[(1 - R_2)(1 + R_1 e^{gL}) + (1 - R_1)(1 + R_2 e^{gL})]}{gL(1 - R_1 R_2 e^{2gL})} - 2 \right] \frac{r_{sp}}{gc'} \quad (14)$$

Here  $R_1$  and  $R_2$  are the respective back-facet and front facet reflectivities, and  $L$  is the cavity length. The gain index is given by

$$g = \Gamma(g_m - \alpha_i) \quad (15)$$

where  $\alpha_i$  is the intrinsic index of loss of the quantum-well. The spontaneous emission rate in (14), is expressed as

$$r_{sp} = \beta B n_2^2 \quad (16)$$

The average photon density  $S$  is not an observable physical quantity and thus is not suitable as a circuit variable. The output light power  $P_{out}$  carries the physical information from a laser, and therefore is represented by a circuit variable. Based upon the plane-wave assumption, the output light power  $P_{out}$  from a laser amplifier can be expressed as

$$P_{out} = \frac{r_{sp} E_{ph} WNL_c}{2g} \frac{(1 - R_2)(e^{gL} - 1)(R_1 e^{gL} + 1)}{(1 - R_1 R_2 e^{2gL})} \quad (17)$$

A detailed derivation is shown in the Appendix. For quantum-well lasers without facet coatings, the reflectivities at both ends of a laser are equal, i.e.,  $R_1 = R_2 = R$ . Above the threshold condition the loss will be approximately equal to the gain

$$gL = \ln \left( \frac{1}{R} \right) \quad (18)$$

Then the output light power can be expressed as

$$P_{out} = (W \cdot NL_c) gL \frac{E_{ph} c'}{4} \cdot S \quad (19)$$

The expression for average light power emitted from the front facet is given by

$$P_{avg} = \frac{c' WNL_c E_{ph}}{4} \cdot S \quad (20)$$

If the values of adjustable parameters are chosen properly, then the effects of unequal facet reflectivity can be taken into account in (19). The issues of modeling of non-uniform longitudinal distributions of charge density and the more rigorous formula of wave propagation in a Fabry-Perot resonator remain open for further investigation.

### III. THE LARGE-SIGNAL CIRCUIT MODEL

A useful model for a quantum-well laser should 1) find the current-voltage ( $I$ - $V$ ) characteristics of each nonlinear function in the electrical continuity equation, 2) express rate equations in terms of appropriate circuit vari-

ables, 3) represent rate equations by conventional circuit elements, and 4) find equivalent circuit elements for parasitic effects not expressed by single-mode rate equations. From the discussion in Section II, requirements 1) and 2) have been mostly met. We now address requirements 3) and 4).

#### A. The Equivalent Circuit

To derive an equivalent circuit from the rate equations, proper circuit variables must be chosen. For the electrical continuity equation, (1), this means expressing every nonlinear function as a function of node voltages. Due to the fact that the laser output power  $P_{out}$  is the main physical quantity which carries the information to the system,  $P_{out}$  was chosen to be a special circuit variable. Selecting the light output power as a circuit variable is equivalent to defining it as an "optical voltage" in the circuit simulation program.

Equations (3) and (8) can now be expressed as functions of the applied voltage by using (12) and (13). By including the volume of the active region and normalizing

the electrical continuity equation accordingly, the recombination current caused by spontaneous emission can be expressed as

$$I_{sp} = qNL_z WLBn_z^2 \quad (21)$$

Equation (21) describes the  $I$ - $V$  characteristics of the nonlinear resistor representing the spontaneous emission current. The recombination current from stimulated emission can be derived as follows:

$$I_{st} = 4 \left( \frac{q}{E_{ph}} \right) L\Gamma g_m P_{avg} \quad (22)$$

in which the  $I$ - $V$  characteristic of a nonlinear resistor represents the stimulated emission current, with  $g_m$  expressed by the applied voltage.  $\Gamma$  is the confinement factor of the optical waveguide and is a function of the structure and material composition of the laser. In our model, the confinement factor is an input parameter. When the value of  $\Gamma$  is not specified by the user, it is calculated by a simple formula [9] in our model,

$$\Gamma = 0.3 \cdot \frac{L_z}{1000} \quad (23)$$

By applying the chain rule to the derivative of charge density  $n_z$ , the term representing the time rate of change of the charge density can be expressed as a product of  $C_n$  and  $dV/dt$ , with  $C_n$  expressed as

$$C_n = qN_z WL \frac{dn_z(V_n)}{dV_n} \quad (24)$$

Physically, this term represents the charge storage effect in the active region. Rearranging the two sides of the electrical continuity rate equation, (1), the radiative recombination current  $I_r$  in the quantum-well region, can be expressed as

$$I_r = I_{sp}(V_n) + I_{st}(V_n, P_{out}) + C_n \frac{dV_n}{dt} \quad (25)$$

Thus the electrical continuity rate equation is now translated into an equivalent circuit.

The procedure for modeling the optical continuity equation, (2), is similar. For computational accuracy, the intermediate variable  $P_{avg}$ , which can be coupled to the output port by a coupling coefficient, is adopted instead of the actual  $P_{out}$ . Applying (20) to (1) and (2) to replace  $S$  with  $P_{avg}$  and normalizing (2) with respect to the volume of the active region,  $P_{avg}$  can be calculated from

$$\alpha_{sp} I_{sp} - \alpha_{st} I_{st} = \frac{P_{avg}}{R_l} - C_{op} \frac{dP_{avg}}{dt} \quad (26)$$

Here the coupling coefficients are defined as  $\alpha_{sp} = \beta(E_{ph}/qL)$  and  $\alpha_{st} = E_{ph}/qL$ .  $I_{sp}$  and  $I_{st}$  have been defined in (21) and (22), respectively. Both  $\alpha_{sp} I_{sp}$  and  $\alpha_{st} I_{st}$  can be modeled as a pair of current controlled current sources in the optical portion of the equivalent circuit.

The light absorption effect in the cavity is represented by an equivalent resistance

$$R_l = \frac{c' \tau_{ph}}{4} \quad (27)$$

where  $\tau_{ph}$  is the photon lifetime in the optical cavity.  $\tau_{ph}$  can be calculated from the following simple equation:

$$\tau_{ph} = K_r \cdot \frac{1}{\alpha_{loss} c'} \quad (28)$$

where  $\alpha_{loss}$  is the loss coefficient in the laser cavity. Because it is difficult [14] to determine  $\alpha_{loss}$  for the active region without knowing the phase information of the light wave, an adjustable parameter  $K_r$  is introduced which should be chosen as close to one as possible.  $C_{op}$  represents the photon storage effects in the Fabry-Perot resonator and is given as

$$C_{op} = \frac{4K_{co}}{c'} \quad (29)$$

The adjustable parameter  $K_{co}$  accounts for the effects of photon storage outside the defined active region. Equations (25) and (26) are represented by the equivalent circuit inside the dashed lines of Fig. 2.

When the input current is below the threshold, the  $I$ - $V$  characteristic of a laser diode is similar to that of an ordinary diode indicating that the nonradiative recombination process is similar for both. Therefore, the nonradiative recombination current is modeled as an ideal diode which is in parallel with the model for the active region. The series resistor  $R_s$  in Fig. 2 represents the voltage drop outside the depletion region. The depletion and diffusion capacitances of a conventional diode have also been included by a capacitance  $C_d$  in parallel to the ideal diode model.

Although only single-mode rate equations have been adapted in our model, the spontaneous emission into modes other than the lasing mode can also be taken into account by using another equivalent circuit driven by a dependent source shown in Fig. 2, where  $\alpha'_{sp} = \beta_{avg}(E_{ph}/qL)$  is the coupling coefficient,  $\beta_{avg}$  is the effective spontaneous emission coupling efficient for nonlasing modes being detected, and is determined experimentally. It is assumed that the average loss and the photon storage effect in nonlasing modes are the same as those of the lasing mode, i.e.,  $R'_l = R_l$  and  $C'_{op} = C_{op}$ . Since the total light output power is the superposition of the two optical voltages, the output port consists of two voltage controlled voltage sources in series.

## B. Limiting Scheme for Simulation

General-purpose circuit simulators apply Newton-Raphson method to find solutions of nonlinear elements in the differential equations. Unfortunately, this method does not guarantee the right solution among a set of multiple solutions, especially for the rate equations for lasers. Since lasers are inherently positive feedback devices, there

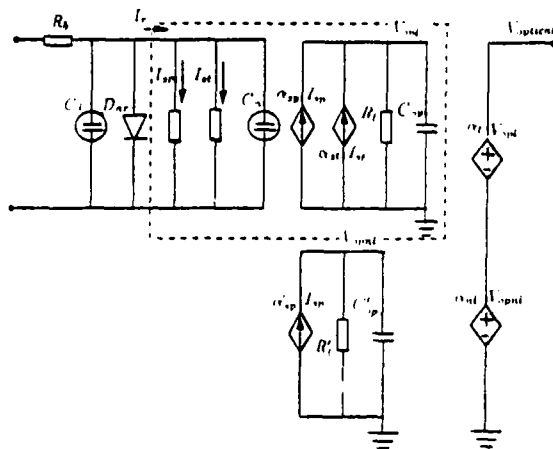


Fig. 2. The equivalent circuit of the quantum-well laser.

are other solutions which are numerically more stable than the solution of the real lasing point. Without any special selection, the output voltage of the laser model may become negative, which is nonphysical. In the steady state, physical mechanisms limit the gain such that it will never become larger than the loss. In a numerical calculation, however, gain being larger than loss is a stable solution to rate equations and results in a negative optical output voltage. Thus, it is necessary to prevent the value of the optical gain  $g_m$  from reaching a value larger than the loss. The following heuristic method has been used in our model.

If ( $V_{n_{new}} > V_{limit}$  and  $V_{optical} < 0$ ) then

$$V_n = V_{n_{old}} + (V_{limit} - V_{n_{old}}) \left( 1 - \frac{V_{limit} - V_{n_{old}}}{V_{n_{new}} - V_{n_{old}}} \right)$$

otherwise

$$V_n = V_{n_{new}} \quad (30)$$

Here  $V_{n_{new}}$  and  $V_{n_{old}}$  are values of  $V_n$  at the present and the previous iteration steps, and  $V_{limit}$  is the value of  $V_n$  which makes the gain equal to the loss. This method effectively forces the circuit simulator to find the right solution point of the rate equations.

One important aspect in numerical computation is checking the numerical errors. Since the output power is defined as one of the circuit variables in circuit simulation, it is necessary to consider its numerical accuracy. Because the output from a semiconductor laser is in the range of milliwatts (mW), we use it as the unit for the laser output to keep the range of numerical errors approximately to the same order for all circuit variables.

Some previous semiconductor laser models have been incorporated indirectly into circuit simulators through their input files, which greatly limits the accuracy, flexibility, and generalization of the model. We chose to implement our model directly into a general-purpose circuit simulator (SMILE [20]). The input format of our QW laser model is the same as those of other active device models.

TABLE III  
THE PARAMETERS OF THE QW LASER MODEL

Model Parameters	Value
laser length $L$	584 ( $\mu\text{m}$ )
laser width	150 ( $\mu\text{m}$ )
quantum-well width	51.0 ( $\text{\AA}$ )
wavelength $\lambda$	9350 ( $\text{\AA}$ )
intrinsic loss $\alpha_i$	14.5 ( $\text{cm}^{-1}$ )
radiative recombination coefficient $B$	$3.4 \times 10^{-11}$ ( $\text{cm}^3 \text{s}^{-1}$ )
coupling coefficient $\beta$	$1.0 \times 10^{-2}$
reflectivity $R$	0.3
quantum-well energy	1.482 (eV)
$R_0$	3.2 ( $\Omega$ )
nonradiative recombination current $I_0$	$7.36 \times 10^{-11}$ (mA)
ideality factor $n$	2.11
depletion capacitance $C_0$	139.0 (pF)
$K_r$	0.9
$K_m$	1.0
$K_{sp}$	31.0

The user defines the connection to the input and the output nodes of the laser diode and specifies the parameters in the input cards of the circuit simulator. If not enough parameters have been specified, the model takes default values automatically or calculates them from the given values.

#### IV. SIMULATION RESULTS

Our model has been tested extensively. The simulation outputs are compared with a wide range of published data and our own experimental results. With a suitable choice of adjustable parameters, the model predictions can provide an excellent match with experimental data. In this section, the simulation results are compared with measured dc and transient curves from a broad-area graded-barrier quantum-well heterostructure laser grown by metalorganic chemical vapor deposition (MOCVD) [21]. The parameter values are listed in Table III.

The dc curves are measured using a voltage source connected to the laser diode through a 50  $\Omega$  series resistor as shown in Fig. 3(a). Fig. 3(b) shows the circuit for the transient measurement system which includes the stray parasitics. The dc  $I$ - $V$  curve is shown in Fig. 4(a) and the  $L$ - $I$  curve is shown in Fig. 4(b). The solid lines indicate experimental data while the dashed lines indicate simulation data. Fig. 4(a) and (b) show that simulation dc curves match the experimental data extremely well. The only discrepancy in the  $L$ - $I$  curve occurs at the threshold current where the simulation curve shows a sharper corner than the experimental data. This discrepancy may result from the approximation of the lasing condition in the derivation of  $P_{out}$  and  $S$  relations.

With a more accurate analysis of the Fabry-Perot resonator, a better simulation curve may be obtainable. If the spontaneous emission coupling coefficient  $\beta$  is chosen to be larger than 0.2, then a better fit of the  $L$ - $I$  curve can be achieved even with the current model. However, it is generally agreed that  $\beta$  should not be larger than 0.1 [22]. Further investigation is needed to determine whether such a large value of  $\beta$  can be obtained from the amplification of nonlasing modes, namely, superradiance. Fig. 5 shows

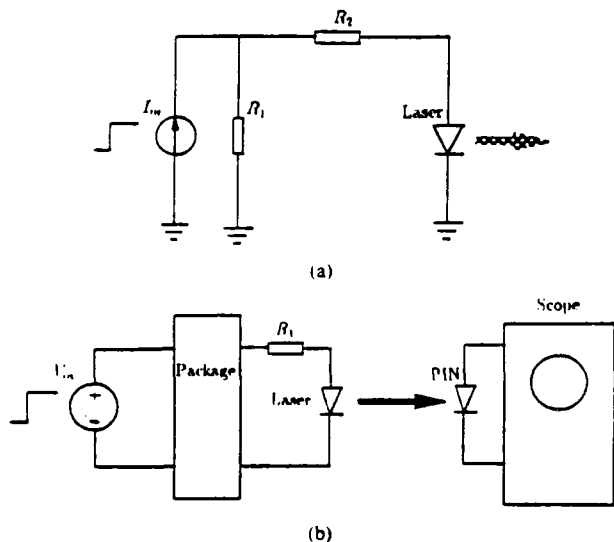


Fig. 3. (a) The experimental setup for the measurement of dc characteristics of the QW laser. (b) The experimental setup for the measurement of transient characteristics of the QW laser.

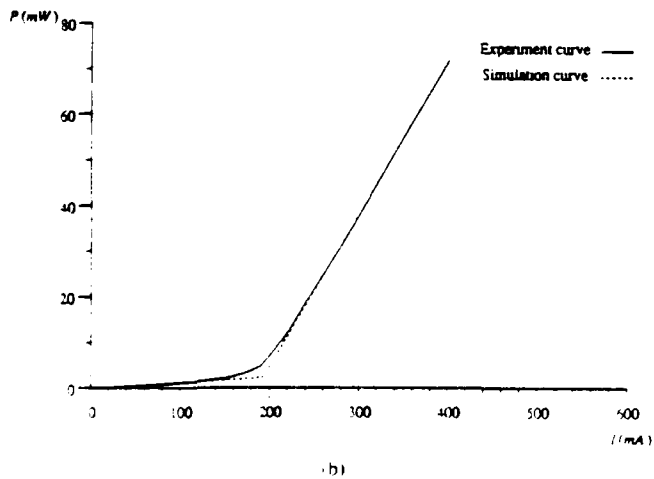
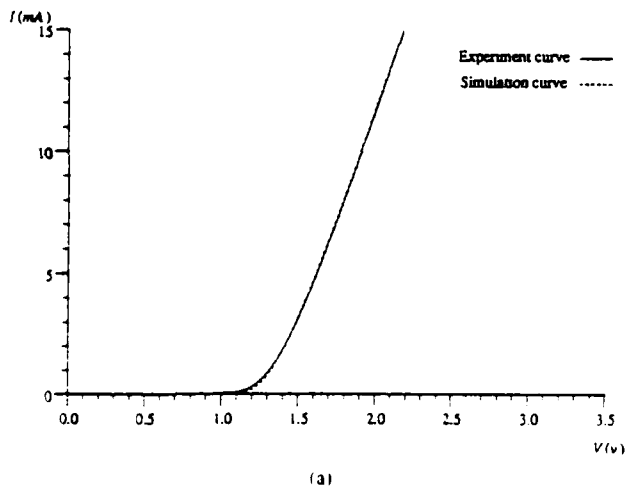


Fig. 4. (a) The dc  $I$ - $V$  characteristic of a quantum-well laser. (b) The dc  $P$ - $I$  characteristic of a quantum well laser.

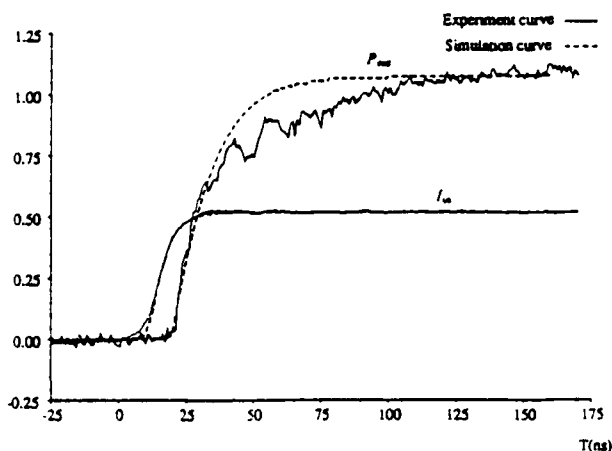


Fig. 5. Comparison of experimental and simulation transient characteristics of a QW laser.

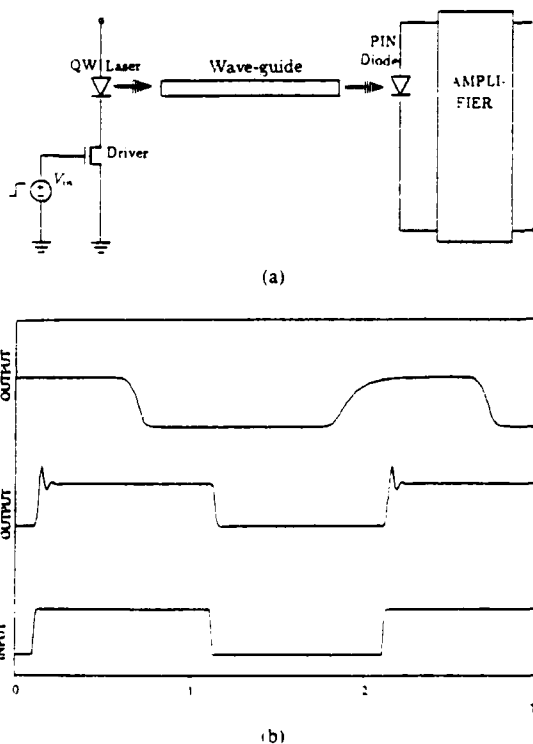


Fig. 6. (a) A circuit of an optical interconnection with a QW laser as the light source, a MODFET as the driver, and a p-i-n diode as the detector. (b) Simulation waveforms of the circuit shown in Fig. 6a.

the transient experimental curves versus the simulation curves. The experimental data were sampled directly from oscilloscope outputs and the simulation data are the product of real outputs and a calibration factor from experimental measurements. Both the experimental results and simulation data indicate that there are no obvious effects of relaxation oscillation. In summary, our large-signal model is capable of fitting a wide range of experimental data both in dc and transient cases.

Fig. 6(a) and (b) illustrate the use of our quantum-well laser model as a modulated light source in the simulation of an optoelectronic integrated circuit. Fig. 6(a) shows

the circuit of an optical interconnection, in which the QW laser is driven by a MODFET driver. The laser output is passed through a waveguide to a p-i-n diode followed by a transimpedance receiver. The input and output waveforms are shown in Fig. 6(b). The waveform at the bottom of Fig. 6(b) is the input waveform, the one in the middle is the output from the laser, and the top one is the output from the receiver.

V. AC ANALYSIS AND THE SMALL-SIGNAL MODEL

A small-signal model can be derived from the steady-state solution of rate equations with a small perturbation  $\Delta V e^{j\omega t}$  added to the external applied voltage. For small perturbations, a linearized set of small-signal equations can be derived from (1) and (2).

Suppose that in steady state, a small ac signal is superimposed on the applied voltage, i.e.,  $V = V_0 + \Delta v e^{j\omega t}$ , and let

$$I_r = I_{r0} + \Delta i e^{j\omega t} \quad (31a)$$

$$n_e = n_{e0} + \Delta n e^{j\omega t} \quad (31b)$$

$$g_m = g_{m0} + \Delta g e^{j\omega t} \quad (31c)$$

$$P_{avg} = P_{avg0} + \Delta p e^{j\omega t} \quad (31d)$$

Here  $V_0$  is the dc bias voltage and  $\omega$  is the small-signal angular frequency;  $n_{e0}$ ,  $g_{m0}$ ,  $I_{r0}$ , and  $P_{avg0}$  are the respective steady-state solutions of the charge density equation, the optical gain equation, and rate equations;  $\Delta n$ ,  $\Delta g$ ,  $\Delta i$  and  $\Delta p$  are magnitudes of the corresponding small-signal perturbations. Applying this set of perturbations to (1) and (2) and neglecting higher order terms, the small-signal version of rate equations can be derived as

$$\begin{aligned} j\omega C_n |_{V=V_0} \cdot \Delta v &= \Delta i - G_{st}(g_{m0}\rho + \Delta g P_{avg0}) \\ &\quad - 2G_{sp} B n_{e0} \Delta n \end{aligned} \quad (32)$$

$$\begin{aligned} j\omega C_{op} P &= 2\alpha_{sp} G_{sp} B n_{e0} \Delta n \\ &\quad + \alpha_{st} G_{st}(g_{m0}\rho + \Delta g P_{avg0}) - \frac{\rho}{R_l} \end{aligned} \quad (33)$$

where

$$G_{st} = \frac{4q}{E_{ph}} \Gamma L \quad (34)$$

and

$$G_{sp} = q \cdot (NL, WL) \quad (35)$$

The steady-state solutions  $n_{e0}$ ,  $g_{m0}$ ,  $I_{r0}$ , and  $P_{avg0}$  can either be calculated from (3), (8), (25), and (26), with  $V = V_0$ , or derived from dc simulation results by using the large-signal model. Based upon the definition of a small-signal perturbation,  $\Delta n$  and  $\Delta g$  can be derived by differ-

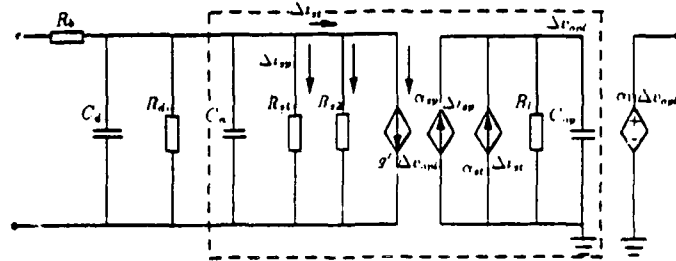


Fig. 7. The small-signal model of a QW laser.

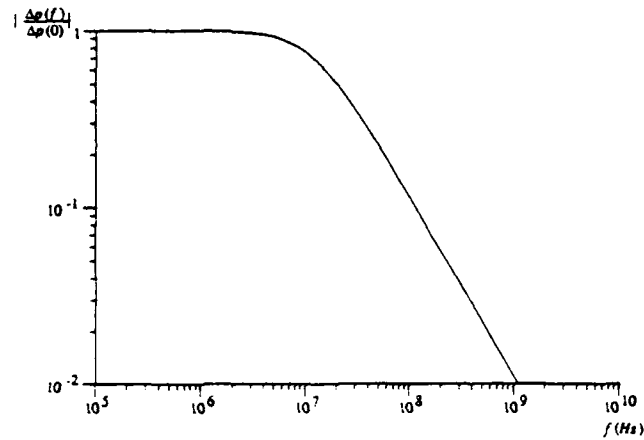


Fig. 8. Modulation characteristics of a QW laser versus frequency.

entiating (3) and (8), and then multiplying them with  $\Delta v$  as follows:

$$\Delta n = \left. \frac{dn_e}{dV} \right|_{V=V_0} \cdot \Delta v \quad (36)$$

and

$$\Delta g = \left. \frac{dg_m}{dV} \right|_{V=V_0} = \Delta v. \quad (37)$$

The small-signal equivalent circuit model can be derived from (32) and (33), using the same technique as used for the large-signal model. Fig. 7 shows the small-signal equivalent circuit model for a quantum-well laser, where  $R_{s1} = dg_m/dV|_{V=V_0} \cdot P_{avg0}$ ,  $g' = G_{st} g_{m0}$  and  $R_{s2} = 2G_{sp} B n_{e0} \Delta n$ . Finally, in the output port the  $P_{avg}$  is multiplied by a constant to provide  $P_{out}$ .

Fig. 7 shows that the topology of this small-signal model is similar to that of the large-signal model, as expected, since both models are derived from rate equations. The spontaneous emission effects of modes other than the lasing mode are neglected in the small-signal model. Further study of the modulation characteristics in the frequency domain of QW lasers could lead to the addition of more parasitics to the small-signal model.

Fig. 8 shows the simulation frequency characteristics of a broad-area graded-barrier quantum-well laser. The curve is generated by using our small-signal model with the package parasitics given in [23]. The parameter set

for the laser in this simulation is the same as for the dc and the transient simulations. The conventional peak at the frequency of relaxation oscillations is not obvious on this curve. This is consistent with the experimental and simulation results for the transient curve shown in Fig. 5(a) and (b). As this laser originally was designed for high-power operation, it may not be suitable for high-frequency modulation due to the large parasitic capacitance.

## VI. SUMMARY

A new large-signal circuit model for quantum-well lasers has been developed, implemented, and validated. With emphasis on physical principles, we incorporated the phenomenon of the recombination process of electron-hole pairs and the lightwave resonance in the active region into our model. The model parameters are readily extracted from the measured experimental data. A small-signal model for ac analysis has also been developed to address the issue of modulation properties of quantum-well lasers. Simulation results demonstrated excellent agreement with experimental data. Our model can be readily implemented into general-purpose circuit simulators, and enables efficient and accurate analysis of integrated optoelectronic circuits.

## APPENDIX

The calculation of the average photon density and the output light power in the laser cavity can be found in many recent publications including [17] and [24]. For the convenience of readers, the calculations are shown here.

Fig. 9 is a simplified figure for a Fabry-Perot resonator. With the assumption of plane wave propagation, the forward-going light intensity in the cavity  $I^+$  and backward-going light intensity  $I^-$  can be calculated from the following differential equations.

$$\frac{dI^+(z)}{dz} = gI^+(z) - \frac{r_{sp}}{z} \cdot E_{ph} \quad (A1a)$$

$$\frac{dI^-(z)}{dz} = -gI^-(z) - \frac{r_{sp}}{z} \cdot E_{ph} \quad (A1b)$$

where

$$r_{sp} = 3Bn_s^2. \quad (A2)$$

For a conventional laser cavity, the following boundary conditions can be applied:

$$I^-(0) = R_1 I^-(0) \quad (A3a)$$

and

$$I^-(L) = R_2 I^-(L). \quad (A3b)$$

The solutions of differential equations (A1a) and (A1b), subject to the boundary conditions given in (A3a) and

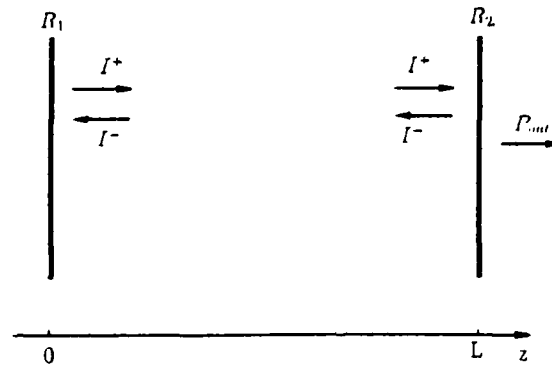


Fig. 9. A simplified configuration of a Fabry-Perot resonator.

(A3b), can be written as

$$I^+(Z) = \frac{r_{sp} E_{ph}}{zg} \left[ \frac{(1 + R_2 e^{gL}) - R_2(1 + R_1 e^{gL})}{1 - R_1 R_2 e^{2gL}} \cdot e^{gz} - 1 \right] \quad (A4a)$$

and

$$I^-(Z) = \frac{r_{sp} E_{ph}}{zg} \left[ \frac{(1 + R_1 e^{gL}) - R_1(1 + R_2 e^{gL})}{1 - R_1 R_2 e^{2gL}} \cdot e^{g(L-z)} - 1 \right]. \quad (A4b)$$

The output power  $P_{out}$  is the forward-going light intensity multiplied by the transmission coefficient and the surface area.

$$P_{out} = (1 - R_2) WNL_z \cdot I^+(L). \quad (A5)$$

Substitution of (A4a) into (A5) leads directly to (17). Also,  $I_{avg}^+$  and  $I_{avg}^-$ , the average light intensities in two directions inside the laser cavity, can be calculated from the following integrals:

$$I_{avg}^+ = \frac{1}{L} \int_0^L I^+(z) dz \quad (A6a)$$

and

$$I_{avg}^- = \frac{1}{L} \int_0^L I^-(z) dz. \quad (A6b)$$

Under the single-mode approximation, the average photon density in the laser cavity is given as

$$S = \frac{2}{E_{ph} c} \cdot (I_{avg}^+ - I_{avg}^-). \quad (A7)$$

The factor of two is due to the existence of two polarizations of light waves. Substituting (A4a) and (A4b) into (A6a) and (A6b), carrying out the integration calculation, and then applying the integral results to (A7) leads to the result in (14).

## ACKNOWLEDGMENT

The authors wish to thank A. T. Yang for setting up the software package iSMILE and for many technical discussions and critical comments, M. E. Givens for providing experimental devices, and Prof. K. Hess for his helpful discussions and critical comments.

## REFERENCES

- [1] A. T. Yang, D. S. Gao, and S. M. Kang, "Computer-aided simulation of optical interconnects," in *Proc. Int. Conf. Comput. Design*, pp. 87-91, 1988.
- [2] R. S. Tucker, "Large-signal circuit model for simulation of injection-laser modulation dynamics," *IEE Proc.*, vol. 128, Pt. 1, no. 5, pp. 180-184, 1981.
- [3] R. S. Tucker and D. J. Pope, "Circuit modeling of the effect of diffusion on damping in a narrow-stripe semiconductor lasers," *IEEE J. Quantum Electron.*, vol. QE-19, no. 7, pp. 1179-1183, 1983.
- [4] R. S. Tucker and I. P. Kaminow, "High-frequency characteristics of directly modulated InGaAsP ridge waveguide and buried heterostructure lasers," *J. Lightwave Technol.*, vol. LT-2, pp. 385-393, Apr. 1984.
- [5] W. Ng and E. A. Sovero, "Network modeling of the modulation response for buried heterostructure injection lasers," *Proc. SPIE*, vol. 466, pp. 36-39, 1984.
- [6] B. Wedding, "SPICE simulation of laser diode modules," *Electron. Lett.*, vol. 23, no. 8, pp. 383-384, 1987.
- [7] N. Holonyak, R. M. Holbas, R. D. Dupuis, and P. D. Dapkus, "Quantum-well heterostructure lasers," *IEEE J. Quantum Electron.*, vol. QE-16, pp. 170-180, Feb. 1980.
- [8] M. K. Kilcoyne, D. Kasemset, R. Asatourian, and S. Beccue, "Optical data transmission between high speed digital integrated circuit chips," *Proc. SPIE*, vol. 625, pp. 127-133, 1986.
- [9] Y. Arakawa and A. Yariv, "Quantum well lasers—Gain, spectra, dynamics," *IEEE J. Quantum Electron.*, vol. QE-22, pp. 1887-1899, Sept. 1986.
- [10] T. K. Yee and D. Welford, "A multimodel rate-equation analysis for semiconductor lasers applied to direct intensity modulation of individual longitudinal modes," *IEEE J. Quantum Electron.*, vol. QE-22, pp. 2116-2122, Nov. 1986.
- [11] D. G. Mclean, M. G. Roe, A. I. D'Souza, and P. E. Wigen, "Picosecond recombination of charged carriers in GaAs," *Appl. Phys. Lett.*, vol. 48, no. 15, pp. 992-993, 1986.
- [12] G. Lasher and F. Stern, "Spontaneous and stimulated recombination radiation in semiconductors," *Phys. Rev. A*, vol. 133, no. 2, pp. A553-A563, 1964.
- [13] N. K. Dutta, "Temperature dependence of threshold current of GaAs quantum well lasers," *Electron. Lett.*, vol. 18, no. 11, pp. 451-453, 1982.
- [14] H. C. Casey and M. B. Panish, *Heterostructure Lasers*. New York: Academic, 1978.
- [15] E. O. Kane, "Band structure of indium antimonide," *J. Phys. Chem. Solids*, vol. 1, pp. 249-261, 1957.
- [16] H. Konavashi *et al.*, "Polarisation-dependent gain-current relationship in GaAs-AlGaAs MQW laser diodes," *Electron. Lett.*, vol. 19, no. 5, pp. 166-168, 1983.
- [17] D. Marcuse, "Computer model of an injection laser amplifier," *IEEE J. Quantum Electron.*, vol. QE-19, pp. 63-73, Jan. 1983.
- [18] I. D. Henning, M. J. Adams, and J. V. Collins, "Performance predictions from a new optical amplifier model," *IEEE J. Quantum Electron.*, vol. QE-21, pp. 609-613, June 1985.
- [19] Y. Arakawa and A. Yariv, "Theory of gain, modulation response, and spectral linewidth in AlGaAs quantum-well lasers," *IEEE J. Quantum Electron.*, vol. QE-21, pp. 666-674, Sept. 1985.
- [20] A. T. Yang and S. M. Kang, "iSMILE: A novel circuit simulation program with emphasis on new device model development," in *Proc. 19th ACM IEEE Design Automat. Conf.*, pp. 650-653, 1989.
- [21] M. E. Givens *et al.*, "Operational and design considerations for broad area graded barrier quantum-well heterostructure lasers grown by metalorganic chemical vapor deposition for high power applications," *Electron. Integrat. Opt.*, vol. 7, no. 4, pp. 443-452, 1988.
- [22] K. Y. Lau *et al.*, "High-speed digital modulation of ultraviolet threshold current AlGaAs single quantum-well lasers without bias," *Appl. Phys. Lett.*, vol. 51, no. 2, pp. 94-97, 1987.
- [23] W. I. Way, "Large signal nonlinear distortion prediction for a single-mode laser diode under microwave intensity modulation," *J. Lightwave Technol.*, vol. LT-5, pp. 305-315, Mar. 1987.
- [24] M. J. Adams *et al.*, "Analysis of semiconductor laser optical amplifiers," *IEE Proc.*, vol. 132, Pt. 1, no. 1, pp. 58-63, 1985.



David S. Gao received the B.S. degree from Rutgers University, New Brunswick, NJ, in 1983 and the M.S. degree from the University of Illinois, Urbana-Champaign, in 1986, both in electrical engineering.

Currently, he is working towards the Ph.D. degree at the University of Illinois, Urbana-Champaign. From 1983 to 1984, he was a design engineer at IBM. His current research interests include device modeling, simulation, optoelectronic and microwave integrated circuit design,

and interconnection technology.

Mr. Gao is a member of Tau Beta Pi and Eta Kappa Nu.



S. M. (Steve) Kang (S'73-M'75-SM'80-F'90) received the Ph.D. degree in electrical engineering from the University of California at Berkeley in 1975.

Until 1985 he was with AT&T Bell Laboratories at Holmdel and Murray Hill, NJ and also served as a faculty member at Rutgers University, New Brunswick, NJ. At AT&T Bell Laboratories, he initially worked on system engineering aspects of large-scale network planning. As Supervisor of High-End Microprocessor Design, he was responsible for the development of AT&T's 32000-series VLSI microprocessors and peripheral chips. In 1985, he joined the University of Illinois, Urbana-Champaign, where he is Professor with the Department of Electrical and Computer Engineering and Research Professor of the Coordinated Science Laboratory, and Associate Director of the NSF Engineering Research Center for Compound Semiconductor Microelectronics.

Dr. Kang has served as Administrative Vice President, Secretary and Treasurer, AdCom member, IEEE Standard Board Liaison Representative for the CAS Society and on the editorial boards of IEEE TRANSACTIONS ON CIRCUITS AND SYSTEMS, *IEEE Circuits and Devices Magazine*, *IEEE Design & Test of Computers*, and *International Journal on Circuit Theory and Applications*. He also has served on technical and program committees of ISCAS, ICCAD, and MWSCAS. He has received best paper awards from 1987 ICCD and 1979 MWSCAS. He was Guest Editor and Guest Coeditor of *IEEE Design & Test of Computers* (1987) and *International Journal of Circuit Theory and Applications* (1988), respectively. He is President-Elect of IEEE Circuit and Systems Society for 1990.



Robert P. Bryan was born in Lisle, IL, on August 23, 1965. He received the B.S. degree in electrical engineering with highest honors and the M.S. degree in electrical engineering from the University of Illinois, Urbana-Champaign, Urbana, in 1986 and 1988, respectively.

Currently, he is working towards the Ph.D. degree in electrical engineering as an AT&T Doctoral Fellow at the Center for Compound Semiconductor Microelectronics at the University of Illinois. His research concentrates on the design and development of high power laser arrays on nonplanar substrates and the characteristics of MeV implants into compound semiconductors.

Mr. Bryan is a member of Sigma Xi.



**James J. Coleman** (S'73-M'76-SM'80) attended the University of Illinois at Urbana-Champaign where he received the B.S., M.S., and Ph.D. degrees in electrical engineering in 1972, 1973, and 1975, respectively.

At Bell Laboratories, Murray Hill, NJ (1976-1978), he studied the materials properties of InGaAsP grown by liquid phase epitaxy (LPE) and helped to develop proton-isolated room temperature CW lasers operating at wavelengths near 1.3  $\mu\text{m}$ . At Rockwell International, Anaheim, CA

(1978-1982), he contributed to the development of the MOCVD growth method and to the processing and testing of various CW room temperature, low-threshold AlGaAs-GaAs laser devices, such as the self-aligned laser and the narrow diffused stripe laser. By extension of the MOCVD growth process to large numbers of ultrathin (10-200 Å) layers and to all binary AlAs-GaAs structures, he was able to make unique quantum-well hetero-

structures and superlattices which show two-dimensional optical and electronic transport effects. Since 1982, he has been a Professor with the Department of Electrical Engineering, University of Illinois, Urbana-Champaign. He and his students are involved in the study of optical processes and electronic transport in various structures such as quantum-well heterostructures, superlattices, strained layer InGaAs-GaAs lasers and laser arrays. He has authored or coauthored more than 160 technical papers and holds two patents.

Prof. Coleman has served on the program committees of the 1983, 1984, 1988, and 1989 International Electron Devices Meetings, the 1984 International Semiconductor Laser Conference, the 1986 International Conference on Metalorganic Vapor Phase Epitaxy, and the 1987 Southwest Optics Conference. He was the Guest Editor of a Special Issue of the *IEEE JOURNAL OF QUANTUM ELECTRONICS* on Quantum-Well Heterostructures and Superlattices. He was the recipient of a Beckman Research Award in 1982. He is a member of the American Physical Society, the Optical Society of America, and Sigma Xi.

## TEMPERATURE DEPENDENCE OF COMPOSITIONAL DISORDERING OF GAAS-ALAS SUPERLATTICES DURING MEV KR IRRADIATION

R. P. Bryan, L. M. Miller, T. M. Cockerill, J. J. Coleman, J. L. Klatt and R. S. Averback  
Materials Research Laboratory  
University of Illinois  
Urbana, IL 61801

### ABSTRACT

The influence of the specimen temperature during MeV Kr irradiation on the extent of compositional disordering in GaAs-AlAs superlattices (SLs) has been determined. We have investigated whether radiation-enhanced diffusion (RED) could be employed to reduce the dose required to completely disorder a SL by ion implantation. Metalorganic chemical vapor deposition grown GaAs-AlAs SLs were implanted with 0.75 MeV Kr to a dose of  $2 \times 10^{16} \text{ cm}^{-2}$  at various sample temperatures ranging from 133 K to 523 K. The extent of disordering induced by the irradiations was determined by Rutherford backscattering spectrometry and secondary ion mass spectrometry. For low temperature irradiations (133 K to 233 K), complete intermixing of the SL is observed. However, the extent of intermixing of the SL *decreases* with increasing specimen temperature between room temperature and 523 K. We propose two possible explanations to interpret these results: (i) that the amount of ion beam mixing decreases with increasing temperature; and (ii) that the RED coefficient is negative which suggests the existence of a miscibility gap in the GaAs-AlAs SL system.

### INTRODUCTION

Compositional disordering of III-V compound semiconductor epitaxial structures has great promise for the microfabrication of unique optical and electronic devices. In recent years, considerable interest has been shown in efforts directed towards fabricating buried heterostructure (BH) lasers [1] by compositional disordering of the active region of the device. The authors have previously reported [2] the fabrication of index-guided BH lasers in which we utilize the compositional disordering and semi-insulating characteristics [3] of MeV oxygen implanted AlGaAs layers. A single oxygen implant into a sample through a stripe mask results in lateral confinement of both the optical field and injected carriers (see Fig. 1). High dose oxygen implants ( $10^{17} \text{ cm}^{-2}$ ) are necessary [3], though, to induce the compositional disordering required to confine the optical field and, thereby, achieve index-guided laser operation. However, we observe that low dose implants ( $\sim 10^{14} \text{ cm}^{-2}$ ) are sufficient [2] to compensate the layers. Therefore, the transverse straggle of the implant leads to a large compensated region under the implantation mask which results in a substantial increase in the threshold current of very narrow stripe width lasers. We have thus considered using radiation-enhanced diffusion to decrease the dose required to induce the compositional disordering of the AlGaAs heterostructure.

During an implantation, the temperature [4] of the sample significantly affects the diffusion of defects and, therefore, the extent of mixing. Three temperature regimes [4-7] are distinguishable in the chemical interdiffusion coefficient during implantation (see Fig. 2). At high temperatures, thermal diffusion is the most significant mixing mechanism but the diffusion coefficient decreases rapidly with decreasing temperature due to a high activation energy. At intermediate sample temperatures, radiation-enhanced diffusion dominates; it is also exponentially dependent on the sample temperature but the activation energy for the process is less than that of the thermal diffusion process. At lower sample temperatures, mixing is dominated by ion beam mixing which is usually assumed to be nearly independent of temperature.

Ion beam mixing [5-6,8] in the low temperature regime is a result of the diffusion which occurs during the dissipation of the energy transferred during collisions between the implanted ion and the target nuclei, *i.e.* a result of the mixing within the displacement cascades. Early in the cascade evolution, atoms are displaced from their lattice sites by collisions with energies greater than  $\sim 5 \text{ eV}$ . Later, when the initial recoil energy becomes partitioned among all atoms in the volume of the cascade, a thermal spike condition develops and diffusion takes place within the hot spike. Although questions about thermal spike dynamics remain, it is recognized [4-5,8] that

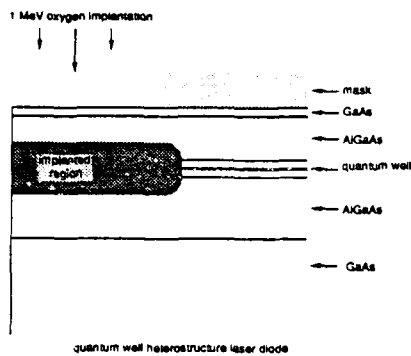


Fig. 1. Schematic of an index-guided buried heterostructure laser diode fabricated by exploiting the characteristics of MeV oxygen implantation.

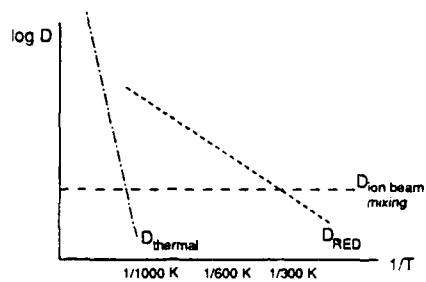


Fig. 2. An Arrhenius plot illustrating the typical temperature dependence of the chemical interdiffusion coefficient for an irradiated sample. At high temperatures, thermal diffusion dominates, whereas at low temperatures ion beam mixing is dominant. At intermediate temperatures, defects generated by the irradiation enhance the normal diffusion leading to a significantly higher diffusion coefficient.

atomic motion occurs while the atoms are highly excited, with atomic energies on the order of 1 eV. Because the atomic rearrangements occur with such high energies relative to the ambient lattice temperature, the system can be driven far from equilibrium.

In addition to creating atomic disorder, displacement cascades also produce point defects, *i.e.* vacancies and interstitial atoms. At low sample temperatures, because of the disordering and defects, some materials will become amorphous. At elevated sample temperatures, these defects are mobile and cause atomic diffusion, usually called radiation-enhanced diffusion (RED). Since this diffusion process takes place long after the thermal spike has cooled and extends well beyond the original boundaries of the displacement event, RED tends to drive the system towards equilibrium. Although ion beam mixing and radiation-enhanced diffusion both occur during high temperature irradiations, the latter dominates [7] at sufficiently high temperatures. The transition between low and high temperature mixing occurs in the temperature range where both vacancies and interstitials become mobile, above room temperature in most cases. Finally, at sufficiently high implant temperatures, the thermally generated population of defects becomes significant and the mixing due to thermal diffusion dominates over the other intermixing mechanisms.

This work focuses on the influence of the sample temperature on the extent of intermixing during implantation. We have investigated whether RED could be employed to reduce the dose required to completely disorder a SL. Furthermore, we studied the transition temperature range between mixing dominated by ion beam mixing and by RED. We will show the unexpected result [9] that the mixing efficiency decreases with increasing sample temperature between room temperature and 523 K, the highest temperature employed in this work. We propose two explanations for this result: (i) that the amount of ion beam mixing decreases with temperature; and (ii) that the radiation-enhanced diffusion coefficient is negative between 300 K and 523 K, which implies the existence of a miscibility gap in the coherent phase diagram of the GaAs-AlAs superlattice system (wavelength  $\sim 400$  Å) with a critical temperatures greater than 523 K.

## EXPERIMENT

The samples used for these experiments were GaAs-AlAs superlattice (SL) structures grown [10] by atmospheric pressure metalorganic chemical vapor deposition (MOCVD) at 800°C. The substrates are (100) GaAs doped with silicon at a carrier concentration of  $2 \times 10^{18} \text{ cm}^{-3}$ . The epitaxial structure consists of a  $0.25 \text{ } \mu\text{m}$  GaAs undoped buffer layer underlying a 50 period undoped SL consisting of alternating layers of 200 Å GaAs and 200 Å AlAs. As a consequence of the growth temperature, the superlattice has a background p-type carrier concentration of  $\sim 1 \times 10^{18} \text{ cm}^{-3}$ . The specimens were irradiated with 0.75 MeV  $\text{Kr}^+$  at the Van de Graaff Accelerator facility in the Materials Research Laboratory at the University of Illinois. Various sample temperatures were investigated ranging from 133 K to 523 K. The dose of Kr for the irradiation was  $2 \times 10^{16} \text{ cm}^{-2}$  for all temperatures. The ion beam current on the sample was kept constant at 120 nA for each irradiation. The beam was wobbled over an aperture plate to provide homogeneity on the  $0.1 \text{ cm}^2$  test spots scribed on the sample. The background pressure in the irradiation chamber was below  $6 \times 10^{-8}$  Torr for all irradiations. The extent of intermixing of the SL layers was determined in all samples by Rutherford backscattering spectrometry (RBS) using 2 MeV  $\text{He}^+$  and checked in selected cases by secondary ion mass spectroscopy (SIMS). All specimens were analyzed at room temperature. The range of the 0.75 MeV  $\text{Kr}^+$  in GaAs is  $\sim 320 \text{ nm}$ , and since only the first six periods of the SL (240 nm) could be used for RBS analysis, the effect of implanted Kr and gradients in the damage distribution can be neglected.

## RESULTS

A typical Rutherford backscattering spectrum from an as-grown GaAs-AlAs SL sample is illustrated in Fig. 3. The backscattering geometry is shown in the inset. At high energies, the oscillations in the yield are due to the changing Ga concentration with depth into the SL, whereas, the oscillations at lower energies, channels 475-625, are due to the changing Al concentration with depth. The attenuation of these oscillations is a consequence of the loss of resolution with depth arising from straggling and lateral spread of the analysis beam [11]. Rutherford backscattering spectra of the Kr implanted GaAs-AlAs SL samples are shown in Fig. 4. The spectra are basically flat for the implants conducted with the sample temperature below room temperature, which indicate that the SL becomes completely disordered by the irradiation. At room temperature, some oscillatory structure is observed after the irradiation indicating only partial mixing of the layers. At increasingly higher sample temperatures, the amplitude of the oscillations increases. At 523 K, the amount of disordering is far less than at low temperatures, although evidence for partial disordering is still clearly visible.

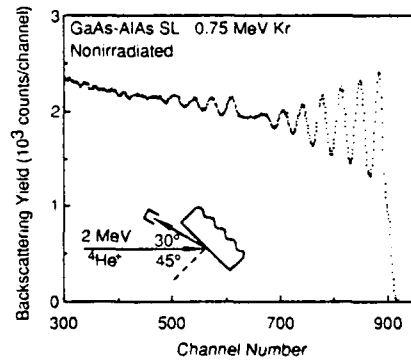


Fig. 3. RBS spectra for a nonirradiated GaAs-AlAs SL sample.

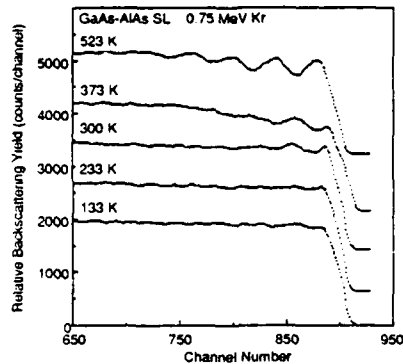


Fig. 4. RBS spectra for GaAs-AlAs SL samples irradiated with Kr to a dose of  $2 \times 10^{16} \text{ cm}^{-2}$  at various implant temperatures. The extent of mixing decreases with increasing sample temperature.

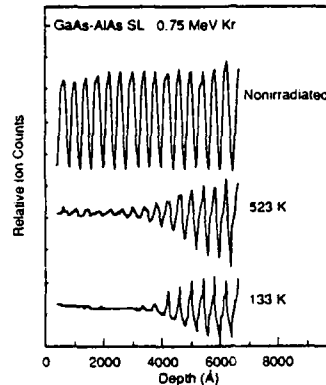


Fig. 5. SIMS depth profiles of Al for a nonirradiated SL sample and for samples which have been irradiated with Kr to a dose of  $2 \times 10^{16} \text{ cm}^{-2}$  at 133 K and 523 K.

The depth profiles of Al concentration, as obtained by SIMS, for the nonirradiated sample and for samples irradiated at 133 K and 523 K are illustrated in Fig. 5. Although SIMS can not be employed for quantitative compositional analysis, it does reveal the interdiffusion quite clearly. The specimen irradiated at low temperatures shows complete disordering from the surface to approximately the projected range of the Kr ions, 320 nm. At this position the deposited damage energy density decreases rapidly with depth and, therefore, the ion beam mixing rapidly decreases. The interdiffusion in the specimen irradiated at 523 K, however, shows only partial intermixing, with no obvious dependence on depth until the end of the Kr ion range.

## DISCUSSION

We propose two explanations for the observed decrease in the extent of intermixing of the SL layers for samples implanted at room temperature and above (see Fig. 6): (i) that the amount of ion beam mixing decreases with increasing temperature; and (ii) that the radiation-enhanced diffusion coefficient is negative between 300 K and 523 K.

Although the amount of ion beam mixing [5-6,8] for an irradiation is generally assumed to be temperature independent, it is possible that the mixing may be smaller in a crystalline phase compared to that in an amorphous phase. Implantation often induces an amorphous phase during low temperature implants but not at higher temperatures where defects are mobile and self-annealing occurs. GaAs is known to behave in this manner. In the crystalline phase, the thermal conductivity is higher than in the amorphous phase and, also, there is a possibility of focusing collisions which dissipate energy from the displacement cascades at supersonic speeds. Consequentially, the temperature and duration of the thermal spike may be reduced, which would lead to less mixing during the thermal spike in crystalline samples compared to that in amorphous samples. Therefore, less disordering would be observed in the higher temperature implants, during which the sample remains crystalline, compared to the lower temperature implants, during which the sample would become amorphous. However, the authors are not aware of any system, metallic or semiconductor, in which the amount of ion beam mixing has been shown to decrease with increasing temperature, regardless of phase transitions. Nevertheless, this does not preclude the possibility. Investigations are underway to compare the amount of ion beam mixing for the crystalline and the amorphous phases of GaAs and AlAs.

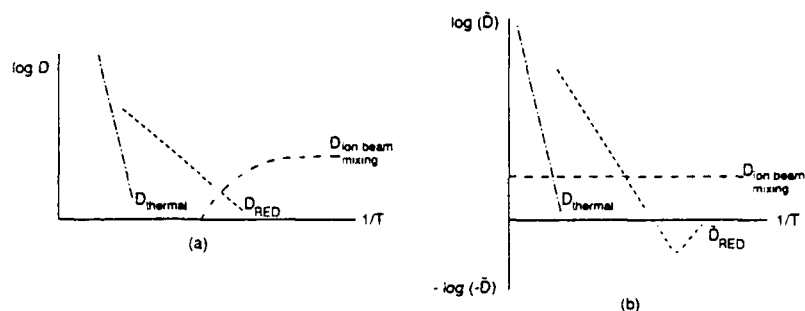


Fig. 6. Arrhenius plots illustrating the possible temperature dependence of the chemical interdiffusion coefficient for a GaAs-AlAs SL sample. In Fig. 6(a), the amount of ion beam mixing decreases with increasing temperature due to an amorphous to crystalline phase change. In Fig. 6(b), the SL is assumed to have a miscibility gap in the phase diagram which leads to a negative radiation-enhanced diffusion coefficient for temperature below the critical temperature.

An alternate explanation for the decrease in the mixing efficiency with increasing temperature is that the total interdiffusion coefficient,

$$D_{\text{total}} = D_{\text{ion beam mixing}} + D_{\text{RED}}(T), \quad (1)$$

decreases due to a negative RED coefficient (see Fig. 6). A negative RED coefficient implies [12] that the defect motion leads to demixing of the system rather than increased mixing. Motion of the defects follows gradients in the chemical potential and, therefore, it is controlled by the thermodynamics of the system, *i.e.*,

$$J = D \nabla \mu, \quad (2)$$

where  $J$  is the defect current and  $\mu$  is the chemical potential. Accordingly, a negative RED coefficient indicates that the heat of mixing,  $\Delta H_{\text{mix}}$ , contribution to the Gibbs free energy is positive and greater than the entropy contribution,  $-T\Delta S_{\text{mix}}$ , thereby resulting in a higher Gibbs free energy for the mixed state compared to the demixed state. Since the GaAs-AlAs SL system completely intermixes [13] due to thermal diffusion above  $\sim 1250$  K, the negative RED coefficient implies the existence of a miscibility gap in the GaAs-AlAs SL system. Recent data [14] has indicated that Ne irradiation at 973 K results in complete mixing of a GaAs-AlAs SL. Thus the critical temperature for the miscibility gap would be between 523 K and 973 K. The existence of a miscibility gap in the GaAs-AlAs system has been the subject of several theoretical investigations, with several researchers predicting no miscibility gap [15-16] and others predicting a miscibility gap with critical temperatures ranging [17-19] between 59 K and 405 K. To our knowledge, experimental evidence for a miscibility gap in bulk  $\text{Al}_x\text{Ga}_{1-x}\text{As}$  or GaAs-AlAs SL has not been reported prior to this study. Presumably, this is because the critical temperature of the miscibility gap is below 973 K and normal thermal diffusion at these temperatures is negligible. Only by enhancing the diffusion coefficient at these temperatures by irradiation could this region of the phase diagram be explored.

## SUMMARY

In summary, we have studied the influence of the sample temperature during MeV Kr irradiation on the extent of compositional disordering in GaAs-AlAs SLs to determine the possibility of using RED to reduce the dose required to induce complete intermixing of GaAs-AlAs SLs by ion implantation. The superlattice is observed to completely intermix during low

temperature irradiations where the mixing is dominated by ion beam mixing. The mixing efficiency, however, decreases with increasing sample temperature above room temperature. At 523 K, the amount of disordering is far less than at low temperatures, although evidence for partial disordering is still visible. We proposed two explanations for the decreasing mixing efficiency with increasing implant temperature. The amount of ion beam mixing may be less for the high temperature implants for which the sample remains crystalline compared to the low temperature implants during which the sample become amorphous. Alternatively, the decreased mixing may be a result of a negative radiation-enhanced diffusion coefficient. The negative RED coefficient implies the existence of a miscibility gap extending to temperatures above 523 K in the GaAs-AlAs superlattice phase diagram.

#### ACKNOWLEDGEMENTS

The authors are grateful to Mr. B. Clymer for technical assistance in performing the ion irradiations and, especially, to Elaine Chapin for helping in preparing this manuscript. This work was supported in part by the Naval Research Laboratory (N00014-88-K-2005), the National Science Foundation (DMR 86-12860 and CDR 85-22666), SDIO/IST (DAAL03-87-K-0013), and the Department of Energy Basic Energy Sciences (DE-AC02-76ER01198). R. P. Bryan is supported in part by an AT&T Doctoral Fellowship.

#### REFERENCES

- [1] P. Gavrilovic, D. G. Deppe, K. Meehan, N. Holonyak, Jr., J. J. Coleman, and R. D. Burnham, *Appl. Phys. Lett.* **47**, 130 (1985).
- [2] R. P. Bryan, J. J. Coleman, L. M. Miller, M. E. Givens, R. S. Averback, and J. L. Klatt, *Appl. Phys. Lett.* **55**, 94 (1989).
- [3] R. P. Bryan, M. E. Givens, J. L. Klatt, R. S. Averback, and J. J. Coleman, *J. Electron. Mater.* **18**, 39 (1989).
- [4] R. S. Averback, *Nucl. Instrum. Methods Phys. Res. Sect. B* **15**, 675 (1986).
- [5] H. Wiedersich, *Nucl. Instrum. Methods Phys. Res. Sect. B* **7/8**, 1 (1985).
- [6] R. S. Averback, T. Diaz de la Rubia, and R. Benedek, *Nucl. Instrum. Methods Phys. Res. Sect. B* **33**, 693 (1988).
- [7] G. Martin, *Phys. Rev. B* **30**, 1424 (1984).
- [8] W. L. Johnson, Y. T. Cheng, M. Van Rossum, and M.-A. Nicolet, *Nucl. Instrum. Methods Phys. Res. Sect. B* **7/8**, 657 (1985).
- [9] R. P. Bryan, L. M. Miller, T. M. Cockerill, J. J. Coleman, J. L. Klatt, and R. S. Averback, *Phys. Rev. B* **41**, 3889 (1990).
- [10] L. M. Miller and J. J. Coleman, *CRC Crit. Rev. Solid State Mater. Sci.* **15**, 1 (1988).
- [11] J. S. Williams and W. Möller, *Nucl. Instrum. Methods* **157**, 213 (1978).
- [12] R. S. Averback, D. Peak, and L. J. Thompson, *Appl. Phys. A* **39**, 59 (1986).
- [13] W. D. Laidig, N. Holonyak, Jr., J. J. Coleman, and P. D. Dapkus, *J. Electron. Mater.* **11**, 1 (1982).
- [14] K. K. Anderson, J. P. Donnelly, C. A. Wang, J. D. Woodhouse, and H. A. Haus, *Appl. Phys. Lett.* **53**, 1632 (1988).
- [15] A.-B. Chen and A. Sher, *Phys. Rev. B* **32**, 3695 (1985).
- [16] G. B. Stringfellow, *J. Crystals Growth* **27**, 21 (1974).
- [17] S.-H. Wei and A. Zunger, *Phys. Rev. Lett.* **61**, 1505 (1988).
- [18] A. Balzarotti, P. Letardi, and N. Motta, *Solid State Commun.* **56**, 471 (1985).
- [19] V. T. Bublik and V. N. Leikin, *Phys. Stat. Sol. A* **46**, 365 (1978).

# InGaAs-GaAs-AlGaAs gain-guided arrays operating in the in-phase fundamental array mode

K. J. Beermink, J. J. Alwan, and J. J. Coleman

Compound Semiconductor Microelectronics Laboratory and Materials Research Laboratory,  
University of Illinois, 208 North Wright Street, Urbana, Illinois 61801

(Received 1 August 1990; accepted for publication 1 October 1990)

We compare the operation of single-stripe gain-guided InGaAs-GaAs-AlGaAs strained-layer quantum well heterostructure lasers emitting at wavelengths  $> 1.0 \mu\text{m}$  to five-element gain-guided arrays with  $8 \mu\text{m}$  stripe width and center-to-center spacings  $S$  from 14 to  $30 \mu\text{m}$ . Arrays with large interelement spacings exhibit a twin-lobed far-field pattern corresponding to the highest order supermode with  $180^\circ$  phase shift between adjacent elements. Devices with smaller interelement spacing exhibit a single lobe in the far field suggestive of in-phase operation. Pulsed  $L$ - $I$  characteristics show kink-free operation of arrays with  $S = 15 \mu\text{m}$  to  $730 \text{ mW}$  per uncoated facet at  $1.8 \text{ A}$ .

The use of InGaAs strained-layer active regions in the GaAs-AlGaAs materials system has resulted in the fabrication of a wide variety of injection lasers with emission wavelengths in the range  $0.9$ – $1.1 \mu\text{m}$ ,<sup>1–12</sup> including high-power arrays.<sup>8–11</sup> Excellent lifetimes for InGaAs-GaAs-AlGaAs lasers have also been achieved,<sup>3–12</sup> and several differences, mainly advantageous, have been reported for these strained-layer devices compared to their GaAs-AlGaAs counterparts. For example, the carrier-induced antiguiding in gain-guided InGaAs-GaAs-AlGaAs strained-layer lasers, an important part of this work, has been shown to be stronger than for similar GaAs-AlGaAs devices.<sup>13,14</sup> In this letter, we compare the operation of single-stripe gain-guided InGaAs-GaAs-AlGaAs strained-layer quantum well heterostructure lasers to five-element gain-guided arrays with  $8 \mu\text{m}$  stripe width and center-to-center spacings from 14 to  $30 \mu\text{m}$ . Arrays with large interelement spacings exhibit a twin-lobed far-field pattern corresponding to the highest order supermode with  $180^\circ$  phase shift between adjacent elements. Devices with smaller interelement spacing exhibit a single lobe in the far field suggestive of in-phase operation.

The structures described in this work were grown by metalorganic chemical vapor deposition (MOCVD) at atmospheric pressure in a vertical geometry reactor using trimethylindium, trimethylgallium, trimethylaluminum, and arsine. Silane and diethylzinc were used for  $n$ - and  $p$ -type dopants, respectively. The structure consists of a  $0.25\text{-}\mu\text{m}$ -thick GaAs:  $n^+$  buffer layer grown on a (100) GaAs:  $n^+$  substrate,  $1.5\text{-}\mu\text{m}$ -thick  $n$ - and  $p$ -type  $\text{Al}_{0.20}\text{Ga}_{0.80}\text{As}$  confining layers, an undoped strained-layer quantum well centered in a  $0.2\text{-}\mu\text{m}$ -thick GaAs carrier collection layer, and a  $0.2 \mu\text{m}$  GaAs:  $p^+$  contact layer. For the array with  $14 \mu\text{m}$  center-to-center spacing, the active region consists of a  $70 \text{ \AA}$   $\text{In}_{0.33}\text{Ga}_{0.67}\text{As}$  quantum well with emission at  $1.09 \mu\text{m}$ . All other devices contain a  $70 \text{ \AA}$   $\text{In}_{0.25}\text{Ga}_{0.75}\text{As}$  quantum well and lase at  $1.01 \mu\text{m}$ . Standard photolithographic techniques were used to pattern oxide-defined stripe devices, with either single stripes or five-stripe arrays of  $8\text{-}\mu\text{m}$ -wide stripes with center-to-center spacing  $S$  of 14, 15, or  $30 \mu\text{m}$ . After thinning the wafers to  $\sim 125 \mu\text{m}$ , a Ge/Au contact was evaporated onto the  $n$

side and alloyed at  $400^\circ\text{C}$  for 10 s. This was followed by the deposition of a nonalloyed Cr/Au contact on the  $p$  side. The wafers were cleaved into bars of cavity length  $L = 510 \mu\text{m}$ , and at least four devices of each spacing were tested under pulsed conditions ( $1.5 \mu\text{s}$ ,  $2 \text{ kHz}$ ) at room temperature without heat sinking.

The far-field pattern for a single-stripe device with a stripe width of  $8 \mu\text{m}$  and  $L = 510 \mu\text{m}$  is shown in Fig. 1 for four values of drive current. Note that the curves are offset in the vertical direction for clarity. As seen in the figure, the far field consists of two lobes centered about the facet normal which move apart as the current is increased. This is the result of the unusually strong index antiguiding formed by the injected carriers under the stripe,<sup>13–15</sup> with leaky waves on either side of the stripe being responsible for the two lobes in the far field.<sup>14,16</sup> Since the coupling of gain-guided arrays<sup>17,18</sup> occurs via leaky waves rather than by evanescent field coupling as in index-guided arrays, this strong antiguiding behavior should enhance coupling of neighboring array elements. The inclusion of antiguiding in the analysis of gain-guided arrays<sup>19</sup> results in the prediction that below some critical spacing (which depends on the amount of antiguiding), the antiguiding can lead to array operation in the in-phase array mode. Above this critical spacing, the arrays are predicted to operate in the

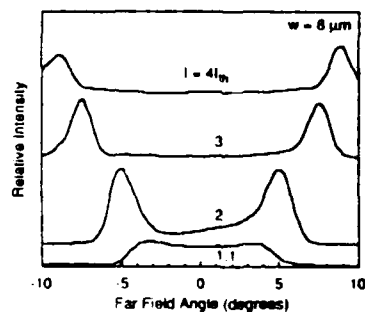


FIG. 1. Far-field pattern of an InGaAs-GaAs-AlGaAs strained-layer gain-guided laser with  $8 \mu\text{m}$  stripe width and a  $510 \mu\text{m}$  cavity at 1.1, 2, 3, and 4 times threshold. The strong antiguiding in these lasers results in the double-lobed far field.

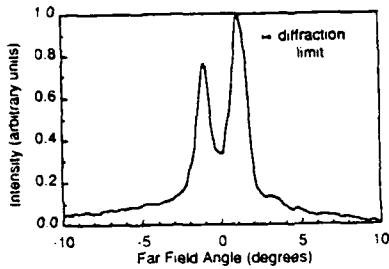


FIG 2. Far-field pattern at  $1.1I_{th}$  of a five-element gain-guided array of  $8 \mu\text{m}$  stripes on  $30 \mu\text{m}$  centers.

highest order mode with a  $180^\circ$  phase shift between neighboring elements.

In Fig. 2 we show the far-field pattern of a five-element array with  $S = 30 \mu\text{m}$  at  $1.1 I_{th}$ . This twin-peaked pattern suggests operation with  $180^\circ$  phase difference between adjacent elements. The lobe separation of  $2.2^\circ$  is slightly higher than the calculated value of  $1.9^\circ$  from diffraction theory. The lobe's full widths at half maximum (FWHM) of  $1.0^\circ$  and  $1.3^\circ$  correspond to 2.3 and 3.0 times the diffraction limit, respectively. Operation of the array in this  $180^\circ$  phase mode is similar to GaAs-AlGaAs gain-guided arrays, and is consistent with the calculations of Ref. 19 for large element spacing. The far-field pattern of a device with  $S = 14 \mu\text{m}$  is shown in Fig. 3 for three different drive levels above threshold. The single lobe in the far field is suggestive of array operation with all emitters in phase, and is in contrast to previously reported results for a similar ten-stripe array with  $4 \mu\text{m}$  emitters on  $12 \mu\text{m}$  centers which operated with a double-lobed far field.<sup>10</sup> In that case, the emitters were defined by hydrogenation, which limits the current spreading. Thus the regions between stripes are more lossy than in the case of oxide-defined stripes, and the hydrogenated devices operate in the out-of-phase mode. Although sufficient current spreading to allow operation in the in-phase mode is present in the devices in this work, note that the near fields indicate strongly coupled emitters rather than a uniformly pumped region. The FWHM of  $1.8^\circ$  at  $1.25I_{th}$  and  $2.3^\circ$  at  $3I_{th}$  correspond to 2.0 and 2.6 times the diffraction limit, respectively. Arrays with  $S = 15 \mu\text{m}$  also exhibited a narrow, single lobe in the far field. Operation of the arrays in this in-phase mode agrees with

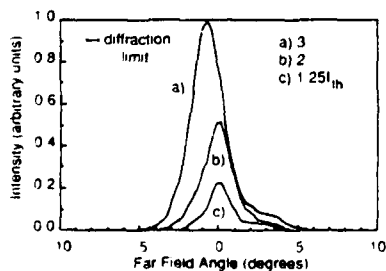


FIG 3. Far-field pattern at  $1.25$ ,  $2$ , and  $3I_{th}$  for a five-element gain-guided array of  $8 \mu\text{m}$  stripes on  $14 \mu\text{m}$  centers.

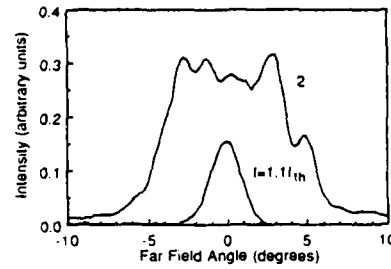


FIG 4. Far-field pattern at  $1.1$  and  $2I_{th}$  of a single-stripe broad-area device with  $50 \mu\text{m}$  stripe width and  $510 \mu\text{m}$  cavity length. The far field is unstable, and at  $2I_{th}$  has spread to  $\sim 10^\circ$  FWHM

the calculations of Ref. 19 including strong antiguiding for a gain-guided array of elements spaced below the critical distance.

It has been shown that, due to the strong coupling between elements, gain-guided arrays do not operate as arrays of individual emitters.<sup>18,20,21</sup> Rather, the array modes are best described as modes of the entire waveguide, and the gain-guided arrays are more correctly viewed as broad-area devices with perturbations in gain. This may, in fact, be the case here for the devices with  $S = 14 \mu\text{m}$ , especially given the strong antiguiding present in the individual  $8 \mu\text{m}$  stripe devices (Fig. 1) which leads to very strong coupling of the elements; however, there are differences between the operation of these arrays and broad-area devices. The far-field pattern of a single-stripe device with  $w = 50 \mu\text{m}$  is shown in Fig. 4 for two drive levels. The transverse modes of such broad-area devices are typically unstable, due in part to the tendency to lase on filaments. This is seen in Fig. 4, where the far-field pattern is unstable with drive current, and at  $2I_{th}$  the far field has spread to  $\sim 10^\circ$  FWHM. In comparison, the FWHM of the array in Fig. 3, with a similar total width ( $64 \mu\text{m}$ ), is only  $2.3^\circ$  at  $3I_{th}$ . Clearly, the stability of the far field is much greater for the array than for the broad-area single-stripe device. The  $L-I$  characteristics for a  $w = 50 \mu\text{m}$  device and for an array with  $S = 15 \mu\text{m}$  are plotted in Fig. 5. The array operated with a kink-free characteristic up to the limit of our current source, emitting  $730 \text{ mW}$  per uncoated facet at  $1.8 \text{ A}$ . In contrast, the single-stripe device characteristic is nonlinear with the appearance of several kinks. These characteristics are typical of all array spacings and single-stripe devices tested. Although the arrays of closely spaced

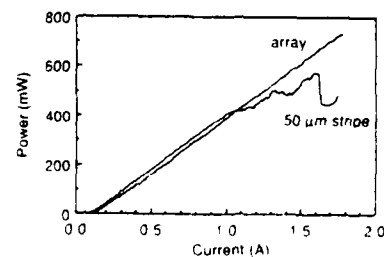


FIG 5. Power vs current characteristics of a  $50\text{-}\mu\text{m}$ -wide single-stripe device and a five-element gain-guided array of  $8 \mu\text{m}$  stripes on  $15 \mu\text{m}$  centers. These plots are typical of all single stripe and arrays tested

stripes with leaky modes seemingly approach broad-area device behavior, the improved stability of the far field and the linearity of the  $L-I$  characteristic are evidence of the superior performance of the arrays.

In summary, arrays with  $8\ \mu\text{m}$  stripe widths and large spacing ( $S = 30\ \mu\text{m}$ ) exhibited a twin-peaked far-field pattern corresponding to the highest order supermode with  $180^\circ$  phase shift between adjacent elements. Devices with smaller spacing ( $S = 14$  and  $15\ \mu\text{m}$ ) exhibited a single lobe in the far field suggestive of in-phase operation. Pulsed  $L-I$  characteristics showed kink-free operation of arrays with  $S = 15\ \mu\text{m}$  to  $730\ \text{mW}$  per uncoated facet at  $1.8\ \text{A}$ . The far-field pattern and the linearity of the  $L-I$  characteristic of the in-phase arrays were superior to those of single-stripe broad-area devices with widths similar to the total array width.

The authors wish to thank R. P. Bryan and M. K. Suits for helpful discussions and technical assistance. This work was supported by the Naval Research Laboratory (N00014-88-K-2005), the National Science Foundation (DMR 89-20538 and ECD-89-43166), and the Charles Stark Draper Laboratory (DLH 285419). K. J. Beernink is supported in part by a NDSEG fellowship. J. J. Alwan is supported in part by an Amoco fellowship.

<sup>1</sup>W. D. Laidig, P. J. Caldwell, Y. F. Lin, and C. K. Peng, *Appl. Phys. Lett.* **44**, 653 (1984).

<sup>2</sup>S. E. Fischer, D. Fekete, G. B. Feak, and J. M. Ballantyne, *Appl. Phys. Lett.* **50**, 714 (1987).

<sup>3</sup>K. J. Beernink, P. K. York, J. J. Coleman, R. G. Waters, J. Kim, and C. Wayman, *Appl. Phys. Lett.* **55**, 2167 (1989).

<sup>4</sup>K. J. Beernink, P. K. York, and J. J. Coleman, *Appl. Phys. Lett.* **55**, 2585 (1989).

<sup>5</sup>P. K. York, K. J. Beernink, G. E. Fernández, and J. J. Coleman, *Appl. Phys. Lett.* **54**, 499 (1989).

<sup>6</sup>P. K. York, S. M. Langsjoen, L. M. Miller, K. J. Beernink, J. J. Alwan, and J. J. Coleman, *Appl. Phys. Lett.* **57**, 843 (1990).

<sup>7</sup>J. S. Major, Jr., L. J. Guido, K. C. Hsieh, N. Holonyak, Jr., W. Stutius, P. Gavrilovic, and J. E. Williams, *Appl. Phys. Lett.* **54**, 913 (1989).

<sup>8</sup>J. N. Baillargeon, P. K. York, C. A. Zmudzinski, G. E. Fernández, K. J. Beernink, and J. J. Coleman, *Appl. Phys. Lett.* **53**, 457 (1988).

<sup>9</sup>J. S. Major, Jr., D. C. Hall, L. J. Guido, N. Holonyak, Jr., P. Gavrilovic, K. Meehan, J. E. Williams, and W. Stutius, *Appl. Phys. Lett.* **55**, 271 (1989).

<sup>10</sup>J. S. Major, Jr., W. E. Plano, A. R. Sugg, D. C. Hall, N. Holonyak, Jr., K. C. Hsieh, *Appl. Phys. Lett.* **56**, 105 (1990).

<sup>11</sup>D. P. Bour, P. Stabile, A. Rosen, W. Janton, L. Elbaum, and D. J. Holmes, *Appl. Phys. Lett.* **54**, 2637 (1989).

<sup>12</sup>R. G. Waters, P. K. York, K. J. Beernink, and J. J. Coleman, *J. Appl. Phys.* **67**, 1132 (1990).

<sup>13</sup>C. Shieh, J. Mantz, H. Lee, D. Ackley, and R. Engelmann, *Appl. Phys. Lett.* **54**, 2521 (1989).

<sup>14</sup>K. J. Beernink, J. J. Alwan, and J. J. Coleman (unpublished).

<sup>15</sup>W. Steifer, R. D. Burnham, and D. R. Scifres, *IEEE J. Quantum Electron.* **QE-18**, 856 (1982).

<sup>16</sup>D. E. Ackley, *IEEE J. Quantum Electron.* **QE-18**, 1910 (1982).

<sup>17</sup>E. Kapon, C. Lindsey, J. Katz, S. Margalit, and A. Yariv, *Appl. Phys. Lett.* **44**, 389 (1984).

<sup>18</sup>J. P. Hohimer, G. R. Hadley, and A. Owyong, *Appl. Phys. Lett.* **48**, 1504 (1986).

<sup>19</sup>G. Agrawal, *J. Appl. Phys.* **58**, 2922 (1985).

<sup>20</sup>W. K. Marshall and J. Katz, *IEEE J. Quantum Electron.* **QE-22**, 827 (1986).

<sup>21</sup>J. Buus, *Electron. Lett.* **22**, 1296 (1986).

# In-phase operation of high-power nonplanar periodic laser arrays

R. P. Bryan, T. M. Cockerill, L. M. Miller, T. K. Tang, T. A. DeTemple, and J. J. Coleman  
*Compound Semiconductor Microelectronics Laboratory, University of Illinois, 208 North Wright  
Street, Urbana, Illinois 61801*

(Received 29 May 1990; accepted for publication 17 October 1990)

The transformation of nonplanar periodic laser array modes from weakly locked out-of-phase to locked in-phase operation is investigated. A comparison study of near-field and far-field patterns is made for devices with differing mesa widths and heights. Data are presented which show that the mesa height and width can be adjusted to force in-phase operation. An array of 19 elements shows an essentially single-lobed far-field pattern centered at  $0^\circ$  with full width at half maximum of  $1.6^\circ$ , to output powers of more than 500 mW/uncoated facet.

Recently there has been considerable interest in developing high-power arrays<sup>1-5</sup> which may be used in such applications as pumping of solid-state lasers, long distance communication, lidar, high-speed modulation, and optical recording. In many applications, the optical output power needs to be a nearly diffraction limited single-lobed beam. However, coherent semiconductor laser arrays typically operate with each element locked out of phase which leads to a double-lobed far-field pattern. Several array structures including leaky waveguide arrays,<sup>3</sup> Y-coupled arrays,<sup>1,6,7</sup> diffraction-coupled arrays,<sup>8</sup> and offset stripe arrays<sup>9</sup> have been developed which exhibit stable, single-lobed far-field patterns. However, in general, these methods require some combination of multiple growths and sophisticated or complex processing. We report in this letter a relatively simple procedure to obtain high-power, in-phase operation of wide aperture laser arrays which require only simple processing and a single metalorganic chemical vapor deposition (MOCVD) growth. Index-guided laser structures grown on patterned substrates<sup>10</sup> can be formed into high power, wide aperture laser arrays<sup>11,12</sup> made possible by the incorporation of a nonplanar active region in the form of a regular pattern of mesas and grooves to suppress lateral lasing and amplified spontaneous emission. We have investigated the characteristics and, in particular, the far-field pattern of devices with various mesa heights and widths. By varying the width and the height of the mesas, we are able to transform the array elements from being weakly locked out of phase to being locked in phase. Consequently, we obtain a single-lobed far-field pattern from the laser array. Stable, near-diffraction-limited operation is obtained to over five times threshold with more than 500 mW/per facet of optical power for devices  $150\ \mu\text{m}$  wide and  $380\ \mu\text{m}$  long.

The laser device configuration utilized for this study is similar to nonplanar periodic laser arrays reported previously.<sup>10,11</sup> The laser structure is an AlGaAs-GaAs graded barrier quantum well heterostructure with a  $50\ \text{\AA}$  quantum well grown by MOCVD. The first step in forming the array is wet chemical etching of a periodic pattern of mesa stripes into a GaAs substrate. We have investigated devices with shallow and deep mesas ( $0.3\ \mu\text{m}$  and  $0.6\ \mu\text{m}$  etch depth respectively) as well as wide and narrow mesas ( $3.1\ \mu\text{m}$  and  $2\ \mu\text{m}$  width at the active region, respectively). The center-to-center spacing between mesas was kept constant

at  $8\ \mu\text{m}$ . Following etching, the devices are completed by a single MOCVD growth of the entire laser structure and contact metallization. In selected devices,  $150\text{-}\mu\text{m}$ -wide oxide defined stripes were incorporated in order to accurately control the width and therefore the number of elements of the device. A schematic of the array structure and a scanning electron micrograph of the cross section are shown in Fig. 1 of the narrow, shallow mesa array. The MOCVD growth on a corrugated substrate forms a nonplanar active region which provides<sup>10,11</sup> definition of the individual emitters of the array, formation of a step in the effective index of refraction for stable mode operation, and suppression of the lateral lasing and the amplified spontaneous emission, thereby allowing high-power operation of wide aperture devices.

As reported previously,<sup>12</sup> the far-field patterns of devices with wide, deep mesas are very broad and double lobed. In order to determine the parameters which lead to the transformation from weakly locked out-of-phase to stable in-phase operation, we compared the far-field pattern of devices with different widths and heights of the mesas. For the comparison, the length and the width of the devices were kept relatively constant at  $380$  and  $560\ \mu\text{m}$ , respectively. Figure 2(a) shows the far-field pattern for a nonplanar laser array with mesas  $0.6\ \mu\text{m}$  high and  $3.1\ \mu\text{m}$  wide. The far-field pattern consists of two broad lobes at approximately  $\pm 10^\circ$ . The full width at half maximum (FWHM) for each is  $\sim 12^\circ$  with no null at  $0^\circ$ . These patterns indicate that the emitters of the device are weakly locked out of phase. In the far field of the wide ( $3.1\ \mu\text{m}$ ), shallow ( $0.3\ \mu\text{m}$ ) mesa devices we observe a reduction of the width of the lobes as shown in Fig. 2(b). The far-field pattern is also double lobed with a narrower FWHM ( $\sim 5^\circ$ ) for these devices and the minimum at zero is more pronounced. For narrow ( $2\ \mu\text{m}$ ), shallow ( $0.3\ \mu\text{m}$ ) mesa devices the far-field pattern narrows to a predominantly single-lobed pattern. The FWHM for the main lobe is  $2.2^\circ$  with sidemodes spaced at  $5.8\text{--}6.0^\circ$  as shown in Fig. 2(c).

By reducing the mesa width at the active region from  $3.1$  to  $2\ \mu\text{m}$  and reducing the etch depth to only  $0.3\ \mu\text{m}$ , the far-field pattern switches from being a double-lobed pattern to a sharply peaked single-lobed pattern as seen in Fig. 2. Limiting the number of elements to nineteen with  $150\ \mu\text{m}$  oxide defined stripes further reduces the FWHM of the far-field pattern to  $1.6^\circ$  as shown in Fig. 3. Although

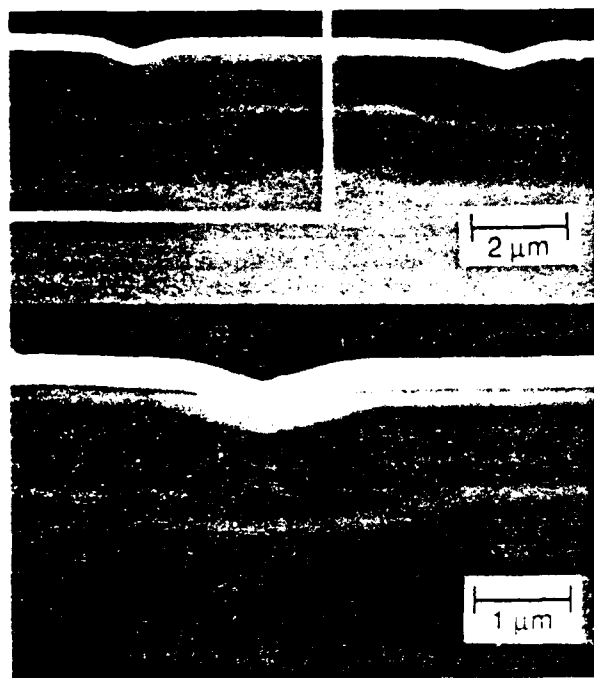
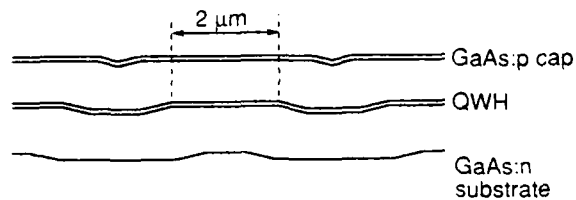


FIG. 1. Schematic and scanning electron micrograph image of the cross section of a nonplanar periodic laser array. The nonplanar active region inhibits lateral lasing and amplified spontaneous emission while still providing the necessary coupling and gain for phase-locked operation. The mesa width is  $3 \mu\text{m}$  at the substrate and narrows to  $2 \mu\text{m}$  at the active region. The center-to-center spacing between mesas is  $8 \mu\text{m}$ .

this is approximately four to five times the diffraction limit, it is more than a factor of 15 smaller than the diffraction limit expected for a single element. The broadening of the main lobe is likely due to the simultaneous operation of several lower order modes and incomplete locking of the phase over all the elements in the array which may arise due to processing variations across the wide device. The average threshold current density of the in-phase arrays is

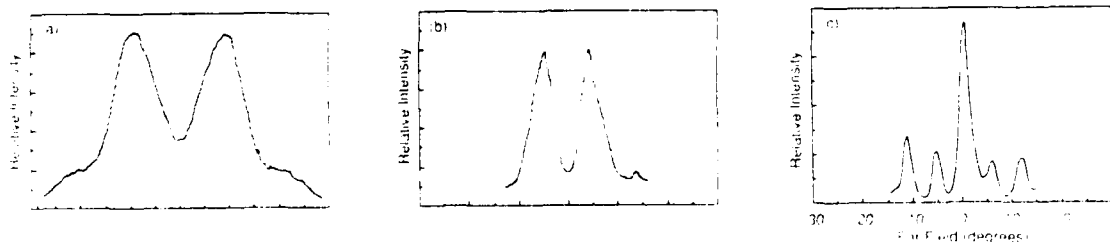


FIG. 2. Far-field patterns for nonplanar laser arrays with a cavity length of  $380 \mu\text{m}$  and width of  $560 \mu\text{m}$  for: (a) a device with mesas  $0.6 \mu\text{m}$  high and  $3.1 \mu\text{m}$  wide having a doubled-lobed far-field pattern with a FWHM of  $\sim 12^\circ$ ; (b) a wide, shallow ( $0.3 \mu\text{m}$ ) mesa device in which the phase locking between emitters becomes stronger but the far field is still double lobed; and (c) a device having a narrow mesa ( $2 \mu\text{m}$ ) and a  $0.3 \mu\text{m}$  mesa height showing an essentially single-lobed far-field pattern with a FWHM of  $2.2^\circ$ .

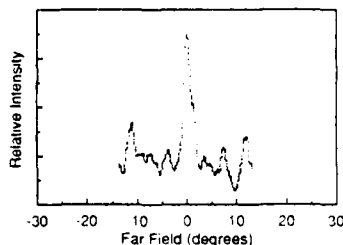


FIG. 3. Far-field patterns for nonplanar laser arrays with a cavity length of  $\sim 380 \mu\text{m}$  and width of  $150 \mu\text{m}$  at five times threshold. The width of the mesas is  $2 \mu\text{m}$  at the active region and the height of the mesas is  $0.3 \mu\text{m}$ . The far-field patterns is essentially single lobed with a FWHM of  $1.6^\circ$  for output powers of more than  $500 \text{ mW}$ .

$264 \text{ A/cm}^2$  and the average external efficiency is  $33\%$ . We obtained in-phase operation at nearly the diffraction limit to over five times the threshold current and over  $500 \text{ mW}$  of optical power per uncoated facet. We do not observe significant broadening of the far field with increasing intensity to over  $500 \text{ mW}$  indicating that the optical mode pattern is very stable.

To determine the dominant mechanisms for the different device structures discussed above, we examined the near-field properties of the devices. As previously reported,<sup>10,11</sup> two emission spots are observed on each mesa of the wide, deep mesa devices. This characteristic is also observed for the wide, shallow mesa and the narrow, shallow mesa devices. Although there is some evidence that the emission pattern on the mesa is that of a first-order mode,<sup>12</sup> an alternative explanation is that a localized, fundamental mode forms near each edge of the mesa. We have performed passive waveguide measurements on the wide, deep mesa devices which support the two localized modes theory. For a  $\text{TEM}_{10}$  mode beam launched into a mesa, the transmitted intensity profile consists of two spots near the edge of the mesa as is also observed in the near-field profiles of the device when lasing. If the mesa consists of a single waveguide, then the passive waveguide measurements should have resulted in a single, fundamental mode detected near the center of the mesa. Further evidence supporting the two localized modes per mesa theory is a recent report<sup>13</sup> which indicates that structurally induced strain effects in AlGaAs-GaAs rib waveguide lasers yield two localized modes on the rib, one near each edge of the

rib. As a consequence of the proximity, the two modes are expected to be phase locked; however, they may be locked in phase or out of phase depending on which configuration has the highest gain. Previous reports<sup>12</sup> on the wide, deep mesa devices have noted that the emission intensity between the mesas is substantially reduced compared to the emission from on top of the mesas. From the near-field patterns of the shallow mesa devices, strong emission intensity was detected between the mesas. These data indicate that there is greater spreading of the fields in the shallow mesa devices compared to deep mesa devices and a corresponding greater coupling between elements. The very broad but double-lobed far-field emission pattern, shown in Fig. 2(a), for the wide, deep mesas indicates that the two emission spots on the mesas are locked out of phase and that the coupling between the mesas is weak. The out-of-phase operation of the spots on top of the mesa indicates that the region of the mesa between the emission spots has low gain, possibly resulting from carrier diffusion from the center to the edges of the mesa.<sup>14</sup> The lack of significant emission from the grooved region indicates that this is also a low gain region. For this configuration the out-of-phase mode will have higher gain than the in-phase mode. For the wide, shallow mesas the two fundamental modes on the mesas are still expected to be locked out of phase. However, for these devices there is stronger coupling between each mesa. Evidence of the coupling between the mesas is the presence of the far-field lobes at  $\pm 6^\circ$  which indicates sources or a pair of sources on  $8 \mu\text{m}$  centers. Also, the FWHM of the lobes is narrower due to the strong coupling between the mesas as seen in Fig. 2(b). Finally, for the narrow, shallow mesa devices we expect the two fundamental modes on the mesas to be strong, as in the case of the wide, shallow mesa devices. The high emission intensity between the mesas suggests, however, that there is significant gain in this region. The near-field patterns show that there are lasing spots spaced approximately  $4 \mu\text{m}$  apart on both the mesas and grooves for this structure. These spots may lase in phase or out of phase depending on which mode has the higher overall gain. The far-field pattern for these devices corresponds to emitters operating in phase spaced  $4 \mu\text{m}$  apart as shown in Fig. 2(c). This indicates that the in-phase mode has a higher gain for this structure. The behavior of the narrow, shallow mesa devices is similar to that of broad-area devices which operate with in-phase coupled filaments;<sup>15</sup> however, the periodicity in our devices is explicitly controlled by built-in variations in the lateral index of refraction profile rather than carrier diffusion. Although the beam was not diffraction limited, we found that by reducing the number of emitters (Fig. 3)

we more closely approached the diffraction limit as expected since the intermodal discrimination should be inversely proportional to the number of emitters.<sup>16</sup> Of course, processing variations across the device and strong but incomplete coupling between the mesas also contribute to broadening of the beam.

In summary, we have demonstrated nonplanar periodic laser arrays which do not require sophisticated processing or multiple growths but which operate with a nearly diffraction limited single beam to over 500 mW of optical power for devices  $150 \mu\text{m}$  wide and  $380 \mu\text{m}$  long. By comparing the far-field patterns of several devices in which the width of the mesas and the depth of the wet chemical etch were varied, we found that reducing the mesa width and depth transforms the devices from operating weakly locked out of phase to locked in phase. These devices hold great promise for use in applications such as optical recording and communication where high-power single beams are necessary and where the advantages of minimal processing are attractive.

This work has been supported in part by SDIO/IST (DAAL03-89-K-0080), the Naval Research Laboratory (N00014-88-K-2005), and the National Science Foundation Engineering Research Center for Compound Semiconductor Microelectronics (ECD 89-43166). R. P. Bryan is supported in part by an AT&T Doctoral Fellowship.

- <sup>1</sup> D. F. Welch, P. S. Cross, D. R. Seifres, W. Streifer, and R. D. Burnham, *Appl. Phys. Lett.* **49**, 1672 (1986).
- <sup>2</sup> F. Zhao, G. Du, X. Zhang, and D. Gao, *J. Appl. Phys.* **66**, 5637 (1989).
- <sup>3</sup> D. Botez, L. Mawst, P. Hayashida, G. Peterson, and T. J. Roth, *Appl. Phys. Lett.* **53**, 464 (1988).
- <sup>4</sup> D. R. Seifres, R. D. Burnham, C. Lindstrom, W. Streifer, and T. L. Paoli, *Appl. Phys. Lett.* **42**, 645 (1983).
- <sup>5</sup> H. Temkin, R. A. Logan, J. P. van der Ziel, C. L. Reynolds, Jr. and S. M. Tharaldsen, *Appl. Phys. Lett.* **46**, 467 (1985).
- <sup>6</sup> K. L. Chen and S. Wang, *Electron. Lett.* **21**, 347 (1985).
- <sup>7</sup> D. F. Welch, P. Cross, D. R. Seifres, W. Streifer, and R. D. Burnham, *Electron. Lett.* **22**, 293 (1986).
- <sup>8</sup> J. Katz, S. Margalit, and A. Yariv, *Appl. Phys. Lett.* **42**, 554 (1983).
- <sup>9</sup> E. Kapon, C. P. Lindsey, J. Katz, S. Margalit, and A. Yariv, *Appl. Phys. Lett.* **45**, 200 (1984).
- <sup>10</sup> D. R. Seifres, R. D. Burnham, and W. Streifer, *Electron. Lett.* **18**, 549 (1982).
- <sup>11</sup> C. A. Zmudzinski, M. E. Givens, R. P. Bryan, and J. J. Coleman, *Appl. Phys. Lett.* **53**, 350 (1988).
- <sup>12</sup> C. A. Zmudzinski, M. E. Givens, R. P. Bryan, and J. J. Coleman, *IEEE J. Quantum Electron.* **QE-25**, 1539 (1989).
- <sup>13</sup> M. Zediker (unpublished data).
- <sup>14</sup> S. M. Lee, S.-L. Chuang, R. P. Bryan, and J. J. Coleman, *IEEE J. Quantum Electron.* (in press).
- <sup>15</sup> D. Mehuys, R. J. Lang, M. Mittelstein, J. Salzman, and A. Yariv, *IEEE J. Quantum Electron.* **Q1**, 23 (1969) (1987).
- <sup>16</sup> J. K. Butler, D. E. Ackley, and D. Botez, *Appl. Phys. Lett.* **44**, 293 (1984).